Mitochondrial lysophosphatidic acid generating enzymes glycerol-3-phosphate acyltransferase 1 and acylglycerol kinase are associated with ovarian cancer cell migration.

Dissertation
zur Erlangung des akademischen Grades des Doktors der Naturwissenschaften (Dr. rer. nat.) an der Fakultät für Chemie und Chemische Biologie der Technischen Universität Dortmund

Anastasia Gonscharow (M.Sc.)
März 2025

1. Gutachter: Prof. Dr. Jan G. Hengstler
2. Gutachter: PD Dr. Leif Dehmelt

Abstract

Metastasis remains the primary cause of mortality in ovarian cancer, particularly in high-grade serous ovarian cancer (HGSOC), which is recognized as the most prevalent and aggressive subtype. The process of tumor metastasis is closely associated with metabolic reprogramming, including alterations in glycerophospholipid pathways. Our previous research demonstrated that high expression of the mitochondrial enzyme glycerol-3-phosphate acyltransferase 1 (GPAM), which catalyzes the first step in triglyceride synthesis, is associated with poor prognosis in ovarian cancer. Recent unpublished data further revealed that higher GPAM expression is significantly higher in omental metastases compared to primary tumor tissues from ovarian cancer patients. Early work demonstrated that silencing GPAM in various cancer cell lines significantly reduced *in vitro* cell migration, an important factor in tumor metastasis. Conversely, overexpressing GPAM in HEK293 cells enhanced their migratory capacity. *In vivo*, the downregulation of GPAM in the ovarian cancer clear cell line ES2 was associated with reduced tumor growth in a subcutaneous xenograft mouse model. GPAM catalyzes the production of the bioactive signaling lipid, lysophosphatidic acid (LPA) through the acylation of glycerol-3-phosphate (G3P), and *in vitro* studies in breast cancer cells demonstrated an association between intracellular LPA levels and the migratory capacity of the cells. In addition to GPAM, intracellular LPA can also be produced by a number of other enzymes, including acylglycerol kinase (AGK) which is increasingly linked to different cancer types. Altogether, these previous findings motivated the present study, which aims to investigate the roles of intracellular LPA-producing enzymes, GPAM and AGK in cancer-related processes in HGSOC.

In this study, a panel of ovarian cancer cell lines was used to characterize the basal expression of GPAM and AGK, along with intracellular lipid profiles and the migratory capacity of the cells, in order to identify suitable models for functional analysis. Five HGSOC cell lines were selected for further investigation. Silencing GPAM and AGK using siRNA consistently resulted in a significant reduction in cell migration in all cell lines. Moreover, OVCAR8 cells exhibited disrupted spheroid formation and outgrowth following the silencing of both GPAM and AGK. Stable overexpression of AGK enhanced both cell migration and spheroid formation, implicating AGK in promoting cancer-relevant phenotypes. Different endpoints were investigated to determine the underlying mechanism by which GPAM and AGK regulate these processes. Interestingly, targeted lipidomic analysis with mass spectrometry did not reveal consistent changes in intracellular levels of LPA or its downstream metabolites, phosphatidic acid (PA) and diacylglycerol (DAG) following the silencing of GPAM and AGK, suggesting that the observed effects on cellular behavior are not be directly mediated by alterations in lipid levels. Gene expression analysis with RT-qPCR indicated cell line-specific compensatory changes in other LPA-producing enzymes, including GPAT isoforms; however, these changes were inconsistent across the cell lines and could not explain the observed alterations in lipid profiles. Furthermore, protein expression of classical epithelial-to-mesenchymal transition (EMT) markers such as E-cadherin, N-cadherin, and vimentin, along with RhoA GTPase activity in the OVCAR8 cells showed no changes upon modulation of GPAM and AGK expression. However, silencing both GPAM and AGK in OVCAR8 cells resulted in reduced phosphorylation of key signaling proteins Akt, ERK and GSK3β. Finally, due to their mitochondrial location and previous studies suggesting potential roles for both GPAM and AGK in maintaining mitochondrial integrity, initial studies were performed to investigate the effect of changes in expression of GPAM and AGK on mitochondrial function using the Seahorse Mitochondrial Stress Test assay. Interestingly, a consistent increase in the non-mitochondrial oxygen consumption rate following the silencing of both GPAM and AGK, alongside a reduction in cells overexpressing AGK was observed. Furthermore, the results revealed significant alterations in respiratory function in cells with deregulated AGK expression. In conclusion, this study establishes GPAM and AGK as crucial regulators of HGSOC cell migration, spheroid formation, and mitochondrial function, independent of changes in intracellular lipid levels or EMT markers.

Zusammenfassung

Metastasen bleiben die Hauptursache für die Sterblichkeit bei Eierstockkrebs, insbesondere bei hochgradigem serösem Eierstockkrebs (HGSOC), der als der häufigste und aggressivste Subtyp bekannt ist. Der Prozess der Tumormetastasierung ist eng mit der metabolischen Umprogrammierung verbunden, einschließlich Veränderungen in der Verstoffwechselung der Glycerophospholipiden. Unsere vorherige Forschung hat gezeigt, dass eine hohe Expression des mitochondrialen Enzyms Glycerol-3-phosphat-Acyltransferase 1 (GPAM), das den ersten Schritt in der Triglyceridsynthese katalysiert, mit einer schlechten Prognose bei Eierstockkrebs assoziiert ist. Neuere unveröffentlichte Daten haben zudem gezeigt, dass die GPAM-Expression in omentalen Metastasen signifikant höher ist im Vergleich zu primären Tumorgeweben von Eierstockkrebspatientinnen. Frühere Arbeiten haben gezeigt, dass die Herunterregulierung von GPAM in verschiedenen Krebszelllinien die Zellmigration, ein wichtiger Faktor bei der Tumormetastasierung, signifikant reduzierte. Im Gegensatz dazu erhöhte die Überexpression von GPAM in HEK293-Zellen deren Migrationsfähigkeit. *In vivo* war die Herunterregulierung von GPAM in der Eierstockkrebs-Zelllinie ES2 mit einem reduzierten Tumorwachstum in einem subkutanen Xenograft-Mausmodell assoziiert. GPAM katalysiert die Produktion des bioaktiven Signallipids, Lysophosphatidsäure (LPA), durch die Acylierung von Glycerol-3-phosphat (G3P), und *in vitro*-Studien in Brustkrebszellen zeigten eine Assoziation zwischen intrazellulären LPA-Spiegeln und der Migrationsfähigkeit der Zellen. Neben GPAM kann auch eine Reihe anderer Enzyme, einschließlich der Acylglycerolkinase (AGK) intrazellulär LPA produzieren. Desweiteren wird das Enzym AGK zunehmend mit verschiedenen Krebsarten in Verbindung gebracht wird. Insgesamt motivierten diese vorherigen Ergebnisse die vorliegende Studie, die darauf abzielt, die Rollen der intrazellulären LPA-produzierenden Enzyme GPAM und AGK in krebsbezogenen Prozessen bei HGSOC zu untersuchen.

In dieser Studie wurde zunächst ein Panel von Eierstockkrebszelllinien verwendet, um die basale Expression von GPAM und AGK sowie die intrazellulären Lipidprofile und die Migrationsfähigkeit der Zellen zu charakterisieren, um geeignete Modelle für die funktionale Analyse zu identifizieren. Fünf HGSOC-Zelllinien wurden für weitere Untersuchungen ausgewählt. Die Herunterregulierung von GPAM und AGK mittels siRNA führte in allen Zelllinien konsistent zu einer signifikanten Reduktion der Zellmigration. Darüber hinaus zeigten OVCAR8-Zellen nach dem Stilllegen von sowohl GPAM als auch AGK eine gestörte Sphäroidbildung und -ausbreitung. Die stabile Überexpression von AGK erhöhte sowohl die Zellmigration als auch die Sphäroidbildung, was auf die Rolle von AGK bei der Förderung krebsrelevanter Phänotypen hinweist. Verschiedene Endpunkte wurden untersucht, um den zugrunde liegenden Mechanismus zu untersuchen, durch den GPAM und AGK die Migration sowie die Sphäroidbildung und -ausbreitung regulieren. Interessanterweise ergab die gezielte Lipidomik-Analyse mit Massenspektrometrie keine konsistenten Veränderungen der intrazellulären LPA-Spiegel oder von assoziierten Metaboliten, Phosphatidsäure (PA) und Diacylglycerol (DAG), nach dem Stilllegen von

GPAM und AGK, was darauf hindeutet, dass die beobachteten Effekte auf das Zellverhalten möglicherweise nicht direkt durch Veränderungen der Lipidspiegel vermittelt werden. Die Analyse der Genexpression mit RT-qPCR zeigte zelllinien-spezifische kompensatorische Veränderungen in anderen LPA-produzierenden Enzymen, einschließlich GPAT-Isoformen; jedoch waren diese Veränderungen zwischen den Zelllinien inkonsistent und konnten die beobachteten Veränderungen in den Lipidprofilen nicht erklären. Darüber hinaus zeigte die Proteinexpression klassischer Marker für den epithelial-mesenchymalen Übergang (EMT) wie E-Cadherin, N-Cadherin und Vimentin sowie die Aktivität der RhoA-GTPase in den OVCAR8-Zellen keine Veränderungen bei der Modulation der GPAM- und AGK-Expression. Das Stilllegen von sowohl GPAM als auch AGK in OVCAR8-Zellen führte jedoch zu einer reduzierten Phosphorylierung wichtiger Signalmoleküle wie Akt, ERK und GSK3β. Schließlich wurden aufgrund ihrer mitochondrialen Lage und früherer Studien, die potenzielle Rollen für sowohl GPAM als auch AGK bei der Aufrechterhaltung der mitochondrialen Integrität vorschlugen, erste Studien durchgeführt, um den Effekt des Stilllegens von GPAM und AGK und der Überexpression von AGK auf die mitochondriale Funktion mithilfe des Seahorse Mitochondrial Stress Test-Assays zu untersuchen. Interessanterweise wurde eine konsistenten Anstieg der nicht-mitochondrialen Sauerstoffverbrauchsrate nach dem Stilllegen von sowohl GPAM als auch AGK, zusammen mit einer Reduktion in Zellen, die AGK überexprimieren, beobachtet. Zusätzlich zeigten die Ergebnisse signifikante Veränderungen in der respiratorischen Funktion in Zellen mit deregulierter AGK-Expression. Zusammenfassend etabliert diese Studie GPAM und AGK als entscheidende Regulatoren der Zellmigration, Sphäroidbildung und mitochondrialen Funktion bei HGSOC, unabhängig von Veränderungen der intrazellulären Lipidspiegel oder EMT-Markern.

List contents

Abstract I

Abstract I

Zusammenfassung III

1 Introduction 1

1.1 Glycerophospholipid structure and metabolism 1

1.2 Lysophosphatidic acid 3

1.2.1 Lysophosphatidic acid metabolism 4

1.2.2 Extracellular lysophosphatidic acid functions 6

1.2.3 Intracellular lysophosphatidic acid functions 8

1.3 Mitochondrial lysophosphatidic acid producing enzymes 10

1.3.1 Glycerol-3-phosphate O-acyltransferase 1 12

1.3.2 Acylglycerol kinase 13

1.4 Ovarian Cancer - a highly metastatic disease 15

1.4.1 Ovarian cancer risk factors and treatment strategies 15

1.4.2 Ovarian cancer classification 16

1.4.3 Metastasis formation in epithelial ovarian cancer 18

1.5 Aim of the study 20

2 Materials 21

2.1 Instruments 21

2.2 Consumables 22

2.3 Reagents & kits 22

2.4 Buffers 24

2.5 Lentiviral vectors 25

2.6 Cell lines 28

2.7 siRNA 29

2.8 Primer 29

2.9 Antibodies 30

3 Methods 31

3.1 Molecular biological methods 31

3.1.1 Bacterial transformation 31

3.1.2 Plasmid purification 31

3.1.3 Generation of lentiviral particles 31

3.2 Cell biological methods 32

3.2.1 Cultivation of cells 32

3.2.2 Transient inhibition of gene expression via RNA interference 33

3.2.3 Antibiotic kill-curve 33
3.2.4 Generation of stable constitutive AGK expressing cells lines 34
3.2.5 Single cell cloning 34
3.3 3D cell culture methods 35
3.3.1 Formation of cell spheroids 35
3.3.2 Spheroid outgrowth 35
3.4 *In vitro* assays 36
3.4.1 Migration Assays 36
3.4.1.1 Wound closure assay 36
3.4.1.2 Transwell migration assay 36
3.4.2 Viability assay 37
3.4.3 Colony formation assay 37
3.4.4 Mitochondria Stress Kit 37
3.5 Gene expression analysis 38
3.5.1 RNA isolation 38
3.5.2 Synthesis of complementary DNA 38
3.5.3 Quantitative real-time Polymerase Chain Reaction 39
3.6 Protein expression analysis 39
3.6.1 Protein extraction and quantification 39
3.6.2 Sodium dodecyl sulfate polyacrylamide gel electrophoresis 40
3.6.3 Semi-dry protein transfer 40
3.6.4 Western blot analysis 41
3.7 Targeted lipidomics analysis 41
3.8 Active Rho-GTPase Pulldown Assay 42
3.9 Statistical data analysis 43

4 Results 44
4.1 Selection of cell models from a panel of ovarian cancer (OC) cell lines 44
4.1.1 OC cell lines differ in basal GPAM and AGK expression 45
4.1.2 OC cell lines differ in their basal intracellular phospholipid content 46
4.1.3 OC cell lines differ in their ability to migrate and form colonies 48
4.2 Silencing GPAM and AGK attenuates OC cell migration 51
4.2.1 Establishing GPAM and AGK knockdowns in selected OC cell lines 51
4.2.2 GPAM and AGK knockdown decrease cell migration of OC cells 53
4.2.3 GPAM and AGK knockdown has no consistent effect on colony formation 57
4.2.4 Combined GPAM and AGK knockdown has no synergistic effect on cell migration 58
4.2.5 GPAM and AGK knockdown disrupt spheroid formation and outgrowth . . 61
4.3 AGK overexpression leads to enhanced migration 63

- 4.3.1 Generation of AGK overexpressing OVCAR8 clones 63
- 4.3.2 Stable AGK overexpressing OVCAR8 clones exhibit enhanced migration 66
- 4.3.3 Spheroid formation and outgrowth is affected by AGK overexpression . . 66

4.4 Migration changes upon manipulating GPAM and AGK expression are independent of intracellular lipid levels 69
- 4.4.1 Intracellular G3P levels are unaffected by GPAM and AGK knockdown . 70
- 4.4.2 Silencing GPAM and AGK leads to cell specific changes in intracellular LPA levels 71
- 4.4.3 Silencing GPAM and AGK leads to cell specific changes in PA and DAG levels 72
- 4.4.4 AGK overexpressing clones exhibit overall reduced lipid levels 77
- 4.4.5 Expression of LPA-producing enzymes is not consistently affected by silencing GPAM or AGK. 77

4.5 Investigating mechanisms of GPAM and AGK in cell migration regulation 81
- 4.5.1 Impact of GPAM and AGK expression on signaling proteins 81
- 4.5.2 Impact of GPAM and AGK expression on EMT marker 82
- 4.5.3 Impact of GPAM and AGK expression on RhoA GTPase activation 84

4.6 Impact of GPAM and AGK expression on mitochondrial function 86

5 Discussion **90**

5.1 Modulating GPAM and AGK expression influences ovarian cancer cell migration but has no consistent effect on colony formation *in vitro* 91

5.2 GPAM and AGK expression influence spheroid formation and outgrowth 93

5.3 Exploring mechanisms by which GPAM and AGK may regulate the migration of ovarian cancer cells 94
- 5.3.1 No common alterations in intracellular lipid levels 94
- 5.3.2 Role of GPAM and AGK in cell migration signaling pathways 96
- 5.3.3 Non-mitochondrial OCR affected by GPAM and AGK expression changes 98
- 5.3.4 Future perspectives 100

Appendix **A1**

A Transition data for measurement of lipids. **A1**

B Intracellular lipids levels in the cell line panel. **A3**

C Scratch assay for OVCAR8 upon AGK knockdown **A6**

D Western Blot for signaling proteins **A7**

E List of Acronyms **A8**
Abbreviations A10
List of figures A11
List of tables A13
References A14

Acknowledgments **A32**

Eidesstatliche Versicherung (Affidavit) **A32**

1 Introduction

Ovarian cancer (OC) remains one of the most lethal gynecological malignancies worldwide, characterized by late-stage diagnosis, high rates of recurrence, and limited therapeutic options [1]. One of the biggest challenges in OC therapy remains metastasis - the spread of cancer cells from the primary tumor to surrounding tissues and distant organs [2–4]. Therefore, understanding the molecular mechanisms driving OC progression and metastasis is crucial for the identification of novel therapeutic targets. Cancer cells have increased bioenergetic and biosynthetic requirements, and in order to meet these demands, the cells rewire their metabolic pathways to promote and maintain cellular processes that drive tumor growth and metastasis [5, 6]. Among the various metabolic alterations, lipid metabolism has emerged as a critical player in tumorigenesis [7]. For example, the bioactive glycerophospholipid, lysophosphatidic acid (LPA) has been implicated in various cancer-related processes, including proliferation, migration, invasion, and survival [8], primarily regulated by the binding of extracellular LPA to G-protein coupled receptors (GPCRs) on the cell’s surface to activate intracellular signaling pathways. Our previous work demonstrated that transfecting LPA into cancer cells led to increased intracellular levels that were associated with enhanced migration [9]. Furthermore, the mitochondrial glycerol-3-phosphate acyltransferase 1 (GPAT1/GPAM), a key enzyme involved in the biosynthesis of intracellular LPA, was found to be associated with poor clinical outcomes in OC [9]. Specifically, elevated expression of GPAM in the primary tumors is associated with shorter overall survival, suggesting that intracellular LPA production may play an important role in driving OC aggressiveness. Accordingly, silencing GPAM in cancer cells resulted in decreased cell migration, further underscoring its role in promoting metastatic behavior [9]. However, the specific mechanisms by which intracellularly-derived LPA contributes to OC progression remain to be understood. Therefore, this thesis aims to elucidate the role of intracellular LPA and its metabolizing enzymes in regulating tumor-promoting processes linked to OC metastasis.

1.1 Glycerophospholipid structure and metabolism

Glycerophospholipids are the major components of biological membranes, characterized by a glycerol backbone linked to one or two hydrophobic fatty acid chains and a phosphate group (Fig. 1A). The attachment of an additional head group, such as choline, ethanolamine, serine, glycerol or inositol to the phosphate enables the formation of various glycerophospholipid species, more specifically phosphatidylcholine (PtdCho), phosphatidylethanolamine (PE), phosphatidylserine (PS), phosphatidylglycerol (PG) and phosphatidylinositol (PI) (Fig. 1B). Glycerophospholipids are obtained from dietary sources, but they can also be synthesized through various metabolic pathways within cells. For instance, the *de novo* synthesis pathway for many glycerophospholipids begins with the esterification of glycerol-3-phosphate (G3P) by GPATs, leading to the production of LPA. This intermediate can then be further acylated by

1-acylglycerol-3-phosphate-O-acyltransferases (AGPATs) or lysophospholipid acyltransferases (LPATs) to form phosphatidic acid (PA). Subsequently, PA may be dephosphorylated by phospholipid phosphatases (PLPPs) to yield diacylglycerol (DAG), which provides the glycerol background for all glycerophospholipids (Fig. 2A) [10, 11]. Breakdown of glycerophospholipids is mediated by numerous phospholipases, enzymes that hydrolyze specific bonds within phospholipid molecules leading to the production of different lipid and water soluble metabolic products (Fig. 2C). Moreover, glycerophospholipids can undergo remodeling through the Lands' cycle, which involves the action of phospholipase A (PLA) and LPATs that deacylates and acylates phospholipids and lysophospholipids, respectively to facilitate changes in fatty acid composition (Fig. 2B). This dynamic reorganization and remodeling of phospholipids generates a diverse array of lysophospholipids and glycerophospholipids that are essential for maintaining the structural integrity and functionality of cellular membranes.

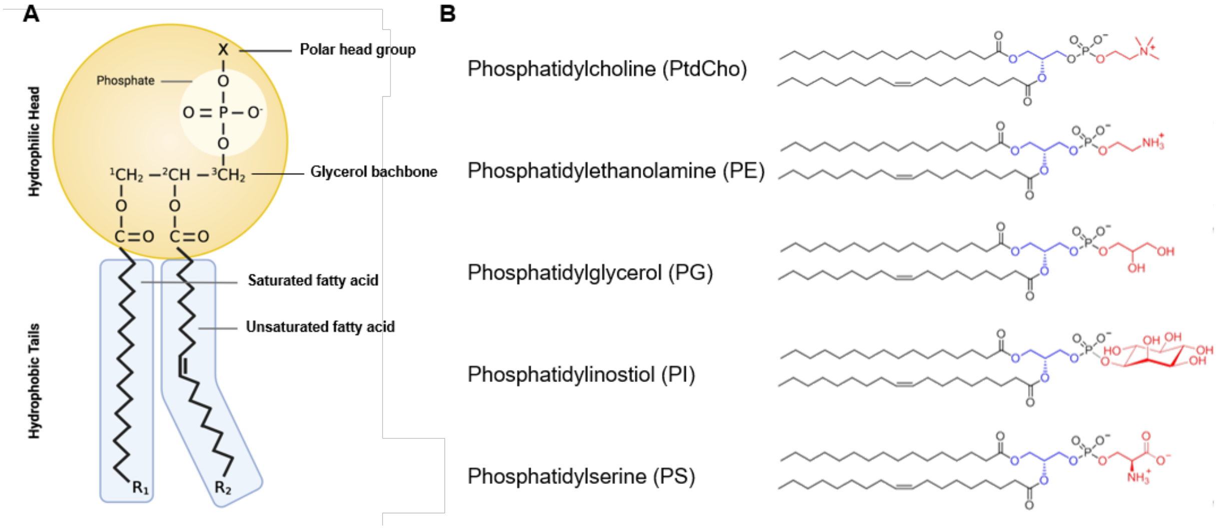

Figure 1: **Glycerophospholipid structure.** **A** Glycerophospholipids are characterized by a backbone of glycerol, to which two fatty acid chains are attached at the sn-1 and sn-2 positions. These fatty acid chains can vary in both chain length and degree of unsaturation. At the sn-3 position, a phosphate group is linked, which can carry different polar head groups. **B** The specific type of phospholipid is determined by the head group attached to the phosphate. Common classifications include phosphatidylcholine (PtdCho), phosphatidylethanolamine (PE), phosphatidylglycerol (PG), phosphatidylinositol (PI) and phosphatidylserine (PS).

As major components of the plasma membrane, glycerophospholipids greatly contribute to the maintenance of membrane structure and function maintaining membrane integrity and fluidity, which is influenced by the saturation status of their fatty acid chains [12]. In addition to their structural role, glycerophospholipids act as energy sources, as the fatty acids released from them can undergo β-oxidation, thereby contributing to energy production [13]. Furthermore, glycerophospholipids serve as precursors to several important lipid mediators, such as DAG, PA and LPA that play a vital role in activating signaling pathways that regulate various cellular functions [14]. Consequently, proper regulation of glycerophospholipid metabolism is essential for maintaining cellular homeostasis. However, cancer cells frequently undergo extensive reprogramming of their phospholipid metabolic pathways, including increased lipid uptake and storage as well as increased *de novo* synthesis, to support rapid proliferation, enhance membrane fluidity, and facilitate signaling pathways that promote invasion and survival [15–17]. Proteins involved in the biosynthesis, breakdown, transport, and trafficking of phospholipids, along with their metabolic products have been frequently reported to be deregulated in cancer [18]. For example, the expression of phospholipases is often upregulated in various cancer types. Phospholipase C (PLC), which hydrolyzes glycerophospholipids to produce DAG, has been associated with worse survival outcomes in breast cancer patients [19]. DAG, a bioactive signaling lipid, activates conventional protein kinase C (PKC) family members to regulate processes such as gene transcription, protein secretion, cell proliferation, migration, and inflammation [20, 21]. Similarly, phospholipase D (PLD), which hydrolyzes phospholipids to generate PA, is frequently linked to progression in various cancer types, including breast, colorectal and ovarian carcinomas [22–25]. PLD plays a significant role in cancer metastasis by interacting with Rho family GTPases to regulate cytoskeletal reorganization during cell movement, thereby promoting cancer metastasis [24, 26, 27]. PA has also been shown to activate the mammalian target of rapamycin (mTOR) mediated signaling pathways which enhance cancer cell survival [22, 28, 29]. The deacylation of PA by PLAs, results in the generation of another well-characterized bioactive signaling lipid, LPA that regulates a number of cancer-relevant cellular processes, including proliferation, migration, and survival, best characterized by its binding to extracellular LPA receptors (LPARs) [30, 31]. However, in our previous work, it could be shown that intracellular derived LPA is also linked to migration of cancer cells by an unknown mechanism and is therefore in focus of this thesis [9].

1.2 Lysophosphatidic acid

LPA is a the simplest glycerophospholipid, comprising only one acyl or alkyl chain attached to either the sn-1 or sn-2 position of the glycerol phosphate backbone (Fig. 3). Based on the saturation of its fatty acid chains, LPA can be categorized into two main groups: those containing saturated fatty acids (16:0 and 18:0) and those with unsaturated fatty acids (16:1, 18:1, 18:2, and 20:4) [30, 32] (Fig. 3). LPA is produced both intra- and extracellularly via distinct metabolic pathways and it is primarily known for its structural role influencing membrane curvature and as a precursor of *de novo* phospholipid synthesis [33]. Furthermore, extracellular LPA is increasingly recognized for its bioactive properties [34], more specifically for its role as a signaling lipid that activates intracellular signaling pathways upon binding to GPCRs on the cell surface to mediate a wide array of cellular responses [35]. This signaling capability positions LPA as a critical player in numerous physiological and pathophysiological processes, including wound healing, metabolic regulation, and cancer progression. LPA is present in all eukaryotic tissues and biological fluids, and is proposed to be secreted by various cell types such as adipocytes, fibroblasts, peritoneal mesothelial cells and cancer cells under defined conditions [31, 36, 37]. In serum, physiological LPA concentration ranges between 0.7 and 80 nM and can reach up to 10 µM in plasma during inflammatory responses or wound healing, thus acting as a significant growth factor primarily produced by thrombin-activated platelets [38] as well as in several medical conditions, such as obesity and sepsis [39, 40]. Moreover, elevated LPA in plasma and malignant ascites have been reported in OC patients [41, 42].

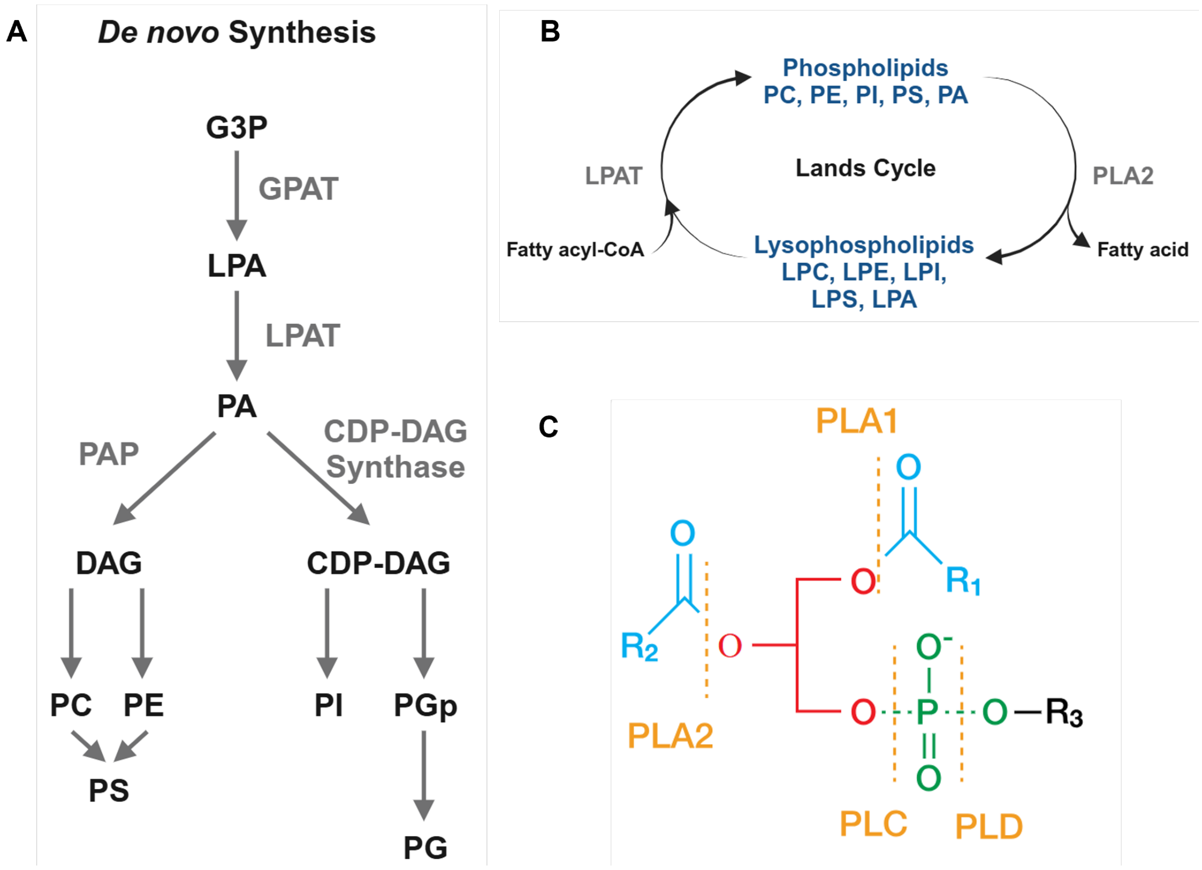

Figure 2: **Glycerophospholipid metabolism.** **A** Pathway illustrating the *de novo* phospholipid synthesis. **B** Schematic of phospholipid remodeling through the Lands cycle. **C** Sites of cleavage by the different phospholipases. CDP, cytidine diphosphate; DAG, diacylglycerol; G3P, glycerol-3-phosphate; GPAT, glycerol-3-phosphate acyltransferase; (L)PA, (lyso)phosphatdic acid; (L)PC, (lyso)phosphatidylcholine; (L)PE, (lyso)phosphatidylethanolamine; (L)PG, (lyso)phosphatidylglycerol; (L)PI, (lyso)phosphatidylinositol; (L)PS, (lyso)phosphatidylserine; LPAT, lysophospholipid acyltransferase; PAP, phosphatidate phosphatase; PLA1/2, phospholipase A1/2; PLB, phospholipase B; PLC, phospholipase C; PLD, phospholipase D

1.2.1 Lysophosphatidic acid metabolism

LPA is metabolized both intra- and extracellularly via a complex and highly regulated network of enzymes (Fig. 4). Its production both in and out of cells is regulated by distinct enzymes via different metabolic pathways using lysophospholipids and glycerophospholipids as substrates. The primary enzyme responsible for the production of extracellular LPA is lysophospholipase D (lysoPLD, ENPP2), commonly referred to as autotaxin (ATX), which catalyzes the hydrolysis of lysophospholipids, such as lysophosphatidylcholine (LPC), to produce LPA and the associated head group, for example choline [43]. These lysophospholipids are derived from membrane phospholipids through the action of PLAs or via the oxidative modification of low-density lipoproteins (LDL) [44, 45]. LPA can also be produced directly from PA through deacylation by PLAs both in the extracellular environment and inside the cell [46]. PA itself is derived from the hydrolysis of glycerophospholipids or via the phosphorylation of DAG by the mitochondrial enzyme AGK or the cytosolic diacylglycerol kinase (DAGK) [47]. Notably, AGK can also phosphorylate monoacylglycerol (MAG), leading to the direct formation of LPA [48]. In addition to AGK, intracellular LPA can be metabolized by several other enzymes, for example, through the enzymatic activity of one of four GPAT enzymes [30, 49]. In mammals, four LPA-producing GPAT isoforms have been identified and are distinguished by their substrate preferences, sensitivity to N-ethylmaleimide (NEM), and subcellular localization: GPAT1/GPAM and GPAT2 are found in the mitochondrial outer membrane, while GPAT3 and GPAT4 are localized to the endoplasmic reticulum (ER) membrane [10]. Finally, two members of the glycerophosphodiester phosphodiesterase (GDE) family, specifically GDE4 (GDPD4) and GDE7 (GDPD3), exhibit lysoPLD activity enabling them to generate intracellular LPA from lysophospholipids [50].

LPA degradation is mediated by a number of enzymes localized both extracellularly and inside the cell, such as PLPPs, as well as enzymes located inside the cell, such as AGPATs/LPATs. PLPPs are a family of membrane-associated enzymes of which seven have been identified to date. While they all have specific substrates, PLPP1-3 (LPP1-3) are best characterized for their ability to dephosphorylate LPA to produce MAG, as well as PA to DAG, thus regulating LPA levels within cells and in the extracellular environment [51]. For example, by reducing LPA concentrations in the extracellular space, PLPPs serve as negative regulators of LPA signaling, thereby attenuating the biological effects mediated by LPARs [52]. Moreover, altered expression of PLPPs has been implicated in cancer progression; for example, downregulation of PLPP1 and PLPP3 has been observed in various cancers, including ovarian, breast, and prostate cancers [53, 54]. This downregulation may lead to enhanced LPA signaling, promoting tumor growth, metastasis, and angiogenesis [55]. The AGPATs are integral membrane proteins, localized to the ER, Golgi and mitochondrial membranes where they catalyze the transfer of an acyl group from acyl-CoA to LPA, resulting in decreased intracellular LPA concentrations while increasing PA levels for the biosynthesis of glycerophospholipids [56]. Thus AGPATs are vital for maintaining the balance of lipid species within cells, significantly influencing key biological functions, including membrane biosynthesis and cellular processes that are regulated by LPA's role as a signaling molecule [14, 57]. AGPAT isoforms have been shown to enhance proliferation and chemoresistance in cancer cells, correlating with the increased risk of tumor development and aggressive phenotypes in hepatocellular carcinoma (HCC), as well as colorectal and OC [58–60].

Figure 3: **Major lysophosphatidic acid (LPA) species.** Lysophosphatidic acid (LPA) is characterized by three main components: a glycerol backbone, a phosphate group, and a single fatty acid chain. The fatty acid chain can vary in saturation and length, resulting in various species of LPA. The most prevalent species found in mammals 16:0, 16:1, 18:0, 18:1 and 20:4 LPA are shown.

1.2.2 Extracellular lysophosphatidic acid functions

LPA in the extracellular environment exerts a wide array of cellular effects through its binding and activation of GPCRs, specifically known as LPARs. To date, six LPARs (LPAR1-6) have been identified that are expressed on the membrane of various cell types. Each receptor activates several G proteins (Gαi, Gα12/13 and Gαq) leading to the activation of diverse downstream signaling pathways (Fig. 5) [35]. Depending on the length and saturation of the fatty acid chain, different LPA species can exert specific biological activities as they are recognized by different LPARs [61]. The major signal transduction pathways activated by LPA binding to LPARs include the mitogen-activated protein kinase (MAPK) and the extracellular signal-regulated kinase (ERK), phosphoinositide 3-kinase (PI3K)/Akt, PLC and DAG that results in increased intracellular calcium levels and the activation of PKC, and the cAMP-dependent protein kinase A (PKA) [35]. LPA-mediated activation of these pathways stimulates several cellular processes, such as cell proliferation, cell-cell interactions, migration, growth and inhibition of apoptosis [35, 62, 63]. Furthermore, LPA activates the Ras homolog family member A (RhoA) signaling [64]. This small GTPase regulates cytoskeletal dynamics, cell migration and adhesion through its downstream effector, Rho-associated protein kinase (ROCK) [65]. Therefore, due to its regulation of cellular processes mediated by different pathways, the deregulation of LPA-mediated signaling has been linked to different pathologies, including cancer [66, 67].

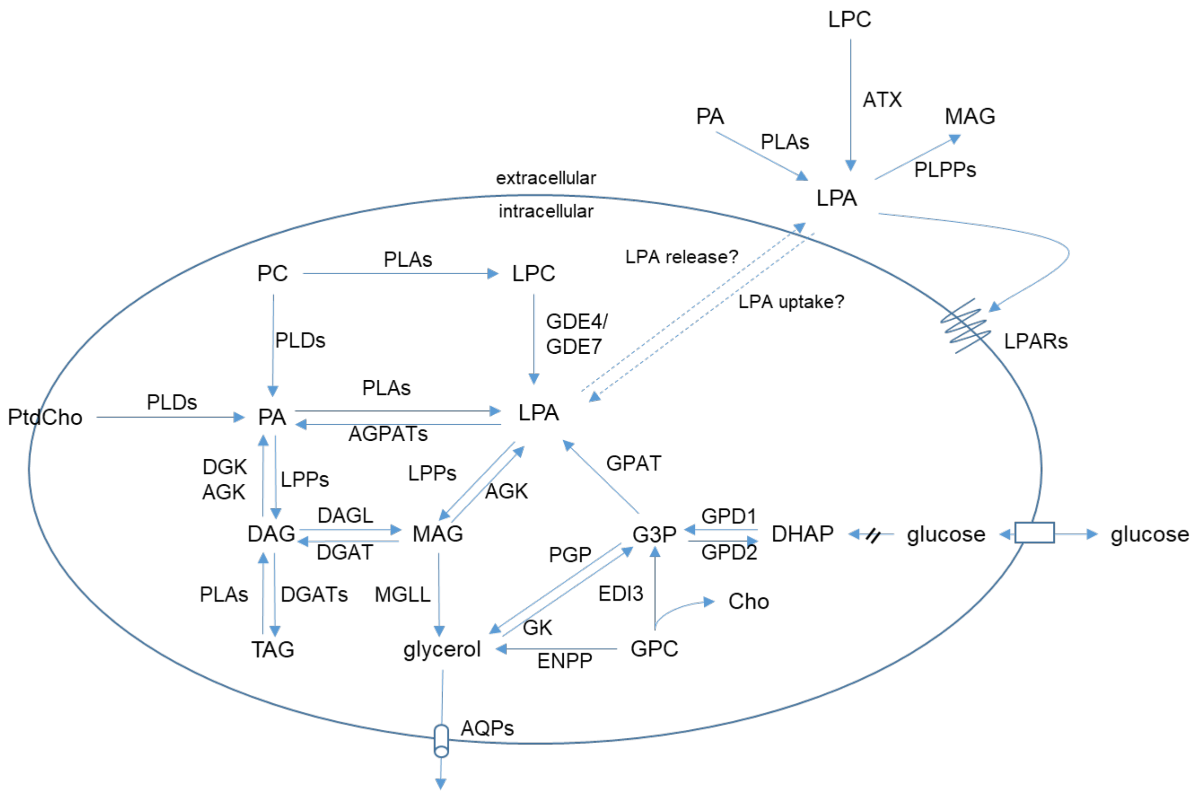

Figure 4: **LPA metabolism.** Lysophosphatidic acid (LPA) is synthesized through both extracellular and intracellular mechanisms. AGK, acylglycerol kinase; AGPAT, 1-acylglycerol-3-phosphate O-acyltransferase; ATX, autotaxin; AQP, aquaporin; DAG, diacylglycerol; DAGL, diacylglycerol lipase; DGAT, diacylglycerol O-acyltransferase; DGK, diacylglycerol kinase; ENPP, ectonucleotide pyro-phosphatase/ phosphodiesterase; G3P, glycerol 3-phosphate; GDE, glycerophosphodiesterase; GPAT, glycerol 3-phosphate acyltransferase; GPC, glycerophosphocholine; LPA, lyso-phosphatidic acid; LPAR, LPA receptor LPC, lysophosphatidylcholine; MAG, monoacylglycerol; MGLL, monoglyceride lipase; PA, phosphatidic acid; PC, phosphocholine; PLA, phospholipase A; PLD, phospholipase D; PLPP, phospholipid phosphate phosphohydrolase; PtdCho, phosphatidylcholine

Studies have shown that the expression of specific LPARs, particularly LPAR1, LPAR2, and LPAR3 is increased in several cancer types, including ovarian and breast cancers, and is linked to increased tumor aggressiveness, poorer patient outcomes and increased metastatic potential [68, 69]. The upregulation of LPA signaling was reported to enhance cytoskeletal reorganization necessary for motility, epithelial-to-mesenchymal transition (EMT), the production of proteolytic enzymes that degrade the extracellular matrix, allowing cancer cells to invade the surrounding tissues [70]. Moreover, LPARs have been implicated in the modulation of tumor microenvironmental factors, which can further support metastatic spread [71]. Given the crucial role of LPA signaling in cancer progression, recent research has focused on developing LPAR inhibitors as potential therapeutic agents. These inhibitors work by blocking the binding of LPA to its receptors, thereby preventing the activation of downstream signaling pathways. For instance, LPAR1 antagonists such as Ki16425 and Debio-0719 have been studied for their potential to inhibit metastasis in breast cancer [72, 73]. Furthermore, ATX inhibitors were shown to effectively disrupt the signaling cascade by limiting the pathological processes mediated by the ATX-LPA axis. Pharmacologicaly targeting ATX has shown potential in preclinical studies to reduce tumor growth and fibrosis, highlighting its role as a critical regulator of cancer progression and a viable target for therapeutic intervention [74].

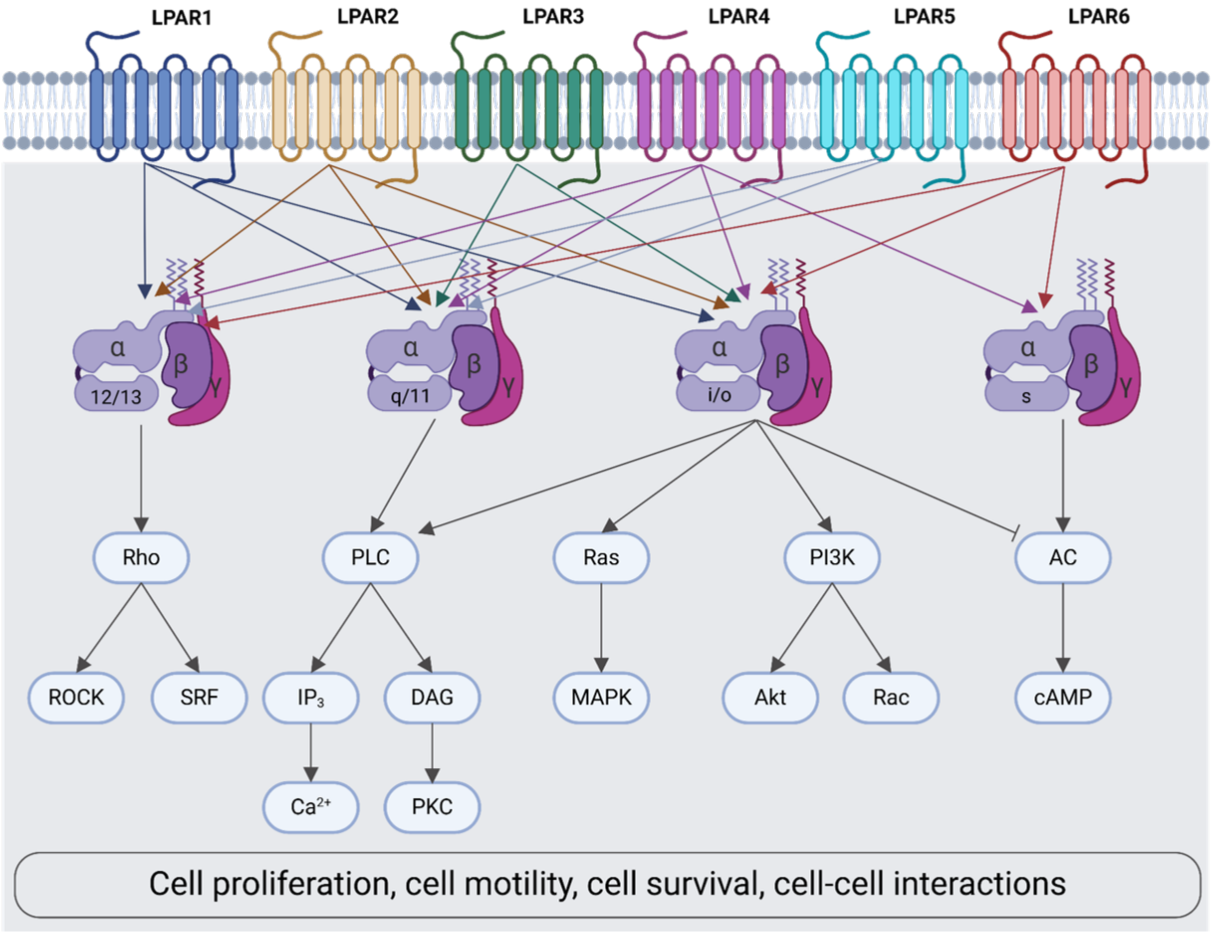

Figure 5: **LPA receptor signal transduction.** Lysophosphatidic acid (LPA) exerts its biological effects by signaling through six specific transmembrane G protein-coupled receptors (GPCRs), known as LPAR1–6, as well as other GPCRs, such as P2Y10 and GPR87. These receptors activate diverse intracellular signaling pathways, leading to a wide range of cellular responses, including cytoskeletal reorganization, cell migration, proliferation, survival, and cell–cell communication. Created with BioRender.com.

1.2.3 Intracellular lysophosphatidic acid functions

LPA produced in the cell is an important intermediate in membrane biosynthesis. It is frequently stated that intracellular LPA is secreted or exported from cells [36, 48], although no comprehensive studies have been reported so far. To date there is no direct evidence that intracellularly-derived LPA has a signaling function, and it is also less studied compared to extracellularly generated LPA. It is unknown whether extracellular LPA can be taken up by cells and enter the cytosol. This suggests a clear distinction in roles on cellular signaling and behavior between extracellularly generated LPA and that produced inside the cell. Studies have reported that intracellular LPA is a ligand of the peroxisome proliferator-activated receptor gamma (PPARγ) [75–77], a nuclear receptor that upon ligand binding in the cytoplasm, translocates to the nucleus where it binds PPAR-response-element (PPRE) on genes related to lipid metabolism, glucose homeostasis, and cellular differentiation to regulate expression (Fig. 6). The authors could show that LPA, but not PA, was able to displace the binding of the PPARγ agonist, rosiglitazone from the ligand-binding pocket of PPARγ. In addition, LPA binding increased the expression a PPAR-responsive element reporter, and the expression of CD36 a known PPARγ-target gene and fatty acid transporter, which was accompanied by lipid accumulation. Later work by the group demonstrated that overexpressing the LPA producing enzyme, GPAM increased intracellular LPA levels, which was associated with an increase in CD36 expression [76]. In the same study, addition of exogenous LPA, PA or a membrane-permeable DAG had no effect on PPARγ activation, suggesting a specific role for the intracellularly generated LPA by GPAM.

Actin-modulating proteins, such as villin and gelsolin were also shown to be regulated by intracellular LPA [78]. Villin is an actin-binding protein specific to epithelial cells that is recruited to the membrane to help regulate processes requiring dynamic actin-rearrangements such as membrane trafficking and cell migration [79]. When bound to phosphatidylinositol 4,5-bisphosphate (PIP2), villin has been shown to inhibit actin depolymerization and enhance actin cross-linking [80]. Interestingly, villin can interact directly with intracellular LPA, exhibiting a higher affinity for its binding sites compared to PIP2 [79]. This interaction leads to the displacement of PIP2, which in turn inhibits the actin-regulating functions of villin, thus promoting increased actin polymerization and altered dynamics of actin reorganization [79]. The second protein, gelsolin was also predicted to bind LPA at its PIP2-binding site leading to weak gelsolin-actin interaction and alterations in actin organization that influences various cellular processes, including cell motility, shape, and division [81]. In addition to its role in regulating cytoskeletal dynamics, LPA was also shown to have a role in regulating mitochondrial structure and function. For example, LPA generated by GPAM was reported to be essential for mitochondrial fusion in *C. elegans* [82]. Expression of GPAM mutants led to fragmented mitochondria; in contrast, injection of exogenous LPA as well as the inhibition of LPATs both resulted in an increase in LPA levels in cells and rescued the elongated structure of mitochondria [82]. Further studies showed that the mitochondrial carrier homologue 2 (MTCH2) is involved in mitochondrial fusion by modulating GPAM-derived LPA, highlighting a connection between lipid metabolism and mitochondrial dynamics [83, 84].

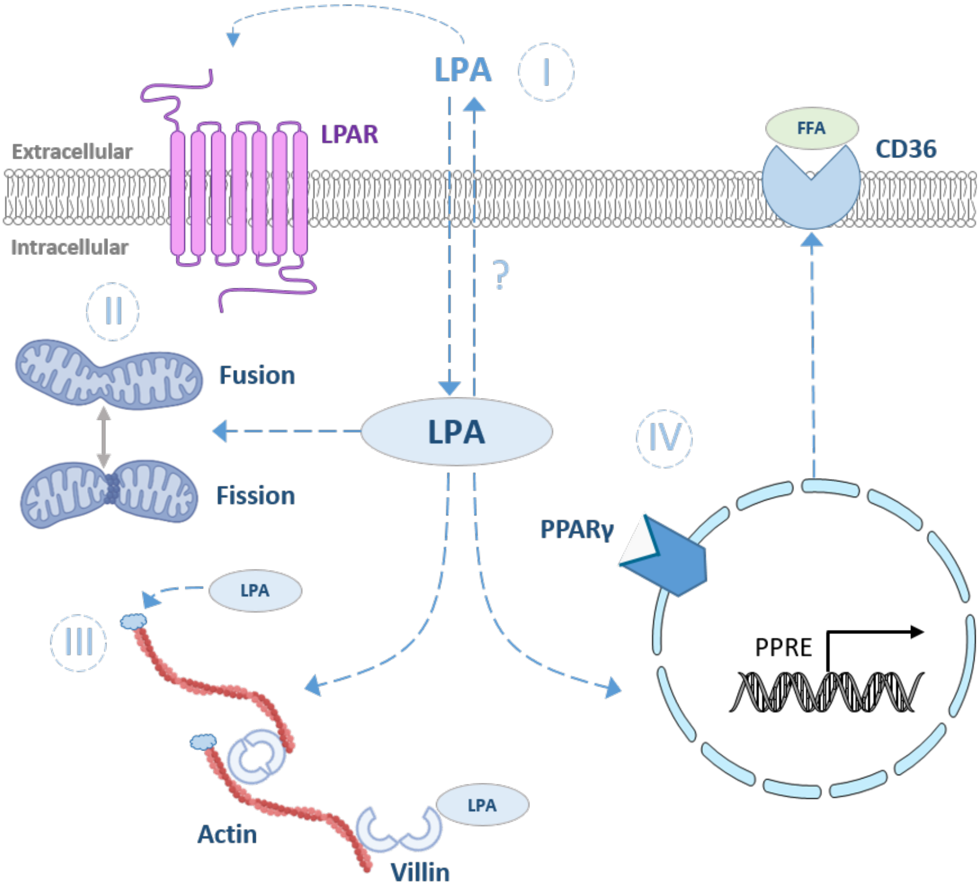

Figure 6: **Intracellular LPA signaling.** Reported mechanisms by which intracellular lysophosphatidic acid (LPA) may exert its signaling effects include: (I) export to the extracellular environment followed by binding to cell surface LPA receptors, (II) regulation of mitochondrial fusion and fission dynamics, (III) direct interactions with intracellular proteins such as actin and villin, (IV) activation of the peroxisome proliferator-activated receptor gamma (PPARγ), which binds to the PPAR-response element (PPRE) and induces the expression of targets like the CD36 receptor. Created with BioRender.com.

1.3 Mitochondrial lysophosphatidic acid producing enzymes

The LPA-metabolizing enzymes, GPAM and AGK are located in the outer (MOM) and inner (MIM) mitochondrial membranes, respectively (Fig. 7). Understanding how these mitochondrial enzymes affect lipid homeostasis and cellular function, and how they impact cancer-related processes, such as cell migration, may allow for the identification of novel therapeutic targets that could disrupt cancer cell metabolism and inhibit tumor growth and metastasis. Given the central role of mitochondria in cancer cell metabolism and survival, targeting mitochondrial LPA-generating enzymes could provide a means to modulate mitochondrial function and integrity, potentially leading to new therapeutic strategies. Mitochondria are essential organelles often referred to as the “powerhouse” of the cell because they generate the majority of cellular ATP through oxidative phosphorylation (OXPHOS) [85]. However, their role extends beyond energy production and includes the citric acid cycle (TCA cycle), fatty acid β-oxidation, and amino acid metabolism [86]. Mitochondria play a role in maintaining calcium homeostasis, which is important for various cellular processes, including motility [86]. Calcium dysregulation can affect actin dynamics, focal adhesion turnover, and cell contractility, driving the expression of malignant cancer phenotypes, such as migration, invasion, and metastasis [87, 88]. Furthermore, mitochondria form a highly dynamic intracellular network, undergoing continuous fusion and fission processes to maintain function and integrity [89]. These processes are crucial for cell movement, as they allow mitochondria to interact with the cytoskeleton and be recruited to areas of the cell that require high energy during movement, such as the leading edge of migrating cells where lamellipodia are formed [90, 91]. Additionally, by releasing pro-apoptotic factors such as cytochrome C, mitochondria are involved in the regulation of cell death and autophagy, and are significant sources of reactive oxygen species (ROS), which play an important role in cell signaling, and can lead to damage if not tightly regulated [92, 93].

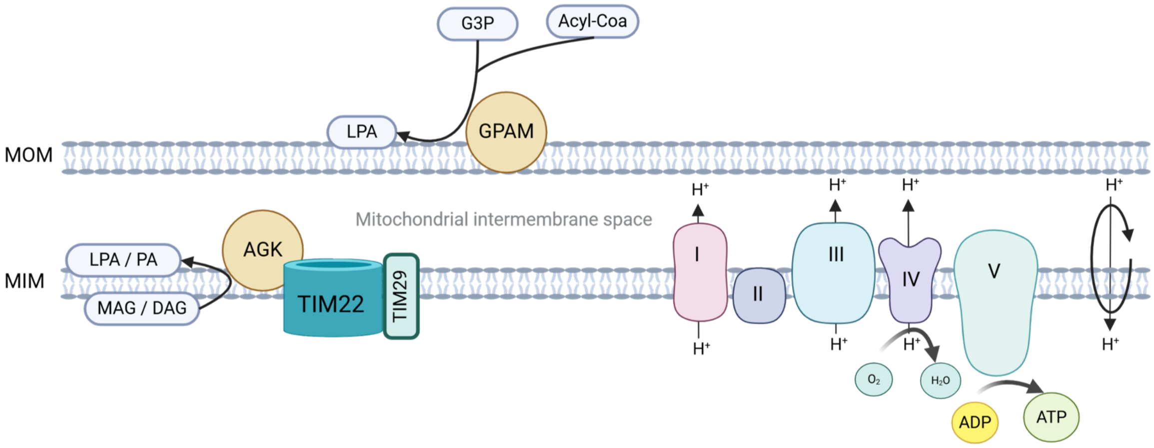

Figure 7: **Mitochondrial localization of GPAM and AGK.** The figure depicts the mitochondrial localization of glycerol-3-phosphate acyltransferase (GPAM) and acylglycerol kinase (AGK), highlighting their roles in mitochondrial lipid metabolism. GPAM is localized to the outer mitochondrial membrane (MOM) and catalyzes the initial step in glycerolipid biosynthesis by converting glycerol-3-phosphate (G3P) and acyl-CoA into lysophosphatidic acid (LPA). AGK, on the other hand, is part of a protein complex with TIM22 and TIM29 at the inner mitochondrial membrane (MIM). It contributes to protein biogenesis and mitochondrial lipid metabolism by phosphorylating monoacylglycerol (MAG) and diacylglycerol (DAG) to produce LPA and phosphatidic acid (PA), respectively. Additionally, the protein complexes of the respiratory chain (I-V), which are essential for oxidative phosphorylation, are also localized within the MIM. ADP, adenosine diphosphate; ATP, adenosine triphosphate. Created with BioRender.com

1.3.1 Glycerol-3-phosphate O-acyltransferase 1

GPAM, also known as GPAT1, is a mitochondrial enzyme of the glycerophosphate acyltransferase family, which catalyzes the first and committed step in the synthesis of glycerophospholipids by converting G3P into LPA, preferably utilizing acyl-CoA with saturated fatty acids such as 16:0-CoA as a substrate [10]. GPAM is highly expressed in tissues that are important for lipid biosynthesis, such as liver and adipose tissue, with moderate expression found in all peripheral tissues [82]. GPAM's central role is to control the balance between fatty acid storage and consumption by directing the flow of fatty acids towards triglyceride (TAG) biosynthesis, which can either be stored in lipid droplets or utilized as an energy source through β-oxidation [94]. GPAM also competes with carnitine palmitoyltransferase 1 (CPT1) for acyl-CoAs, thereby diminishing the flux of fatty acids into the mitochondria for ATP production through oxidative phosphorylation. Loss of GPAM in hepatocytes was reported to lead to increased fatty acid β-oxidation *in vitro* and *in vivo* [94]. Moreover, GPAM knockout mice were shown to have reduced liver mass, lower TAG levels and altered glycerophospholipid composition in liver [95]. Thus, GPAM regulates processes relevant for fatty acids storage and usage, which is important for the maintenance of metabolic flexibility.

While GPAM is well-known for its role in energy metabolism, only a few studies have highlighted its emerging significance in cancer biology. The study by Brockmöller et al. [96] explored GPAM's role in breast cancer and revealed increased levels of G3P, the substrate of GPAM, in cancer compared to normal tissues. Higher levels of phospholipids, in particular PtdCho were measured in tumors positive for GPAM. These findings led the authors to conclude that GPAM alters lipid metabolism in cancer cells, particularly through the deregulated synthesis of phospholipids, such as PtdCho. Such changes in lipid composition may affect cancer cell behavior, including membrane dynamics, and potentially influence processes, such as migration and invasion [96]. Indeed, previous work in our group demonstrated that silencing GPAM reduced migration in MCF7 and MDA-MB-231 breast and ES-2 clear-cell ovarian cancer cells; in contrast, overexpressing GPAM in HEK293 cells led to increased migration. Furthermore, downregulation of GPAM in MCF7 cells led to reduced intracellular LPA levels while transfecting LPA into parental MCF7 cells increased its levels inside the cell, which was associated with enhanced migration [9]. *In vivo* studies revealed that downregulating GPAM expression in the ovarian cancer cell line ES2 led to a notable decrease in tumor growth in a xenograft mouse model [9]. Additionally, it was observed that high GPAM expression was found to be associated with shorter overall survival in ovarian cancer patients, highlighting the potential of GPAM as a therapeutic target in ovarian cancer [9]. Moreover, recent RNA sequencing analysis in our research group revealed that GPAM expression is higher in omental metastases compared to matched primary tumors of ovarian cancer patients (unpublished data). Altogether, the findings suggest that understanding intracellular glycerophospholipid metabolism, especially that of intracellular LPA, may offer new therapeutic strategies in ovarian cancer.

A recent study by Irifune et al. [97] reported higher GPAM expression indicative of enhanced intracellular LPA generation in acute myeloid leukemia (AML) cells compared to healthy CD34+ hematopoietic stem/progenitor cells. The authors reported that inhibition of GPAM with the small molecule inhibitor, FSG67 induced mitochondrial fission and increased oxidative stress. The impaired mitochondrial function led to the suppression of oxidative phosphorylation resulting in decreased ATP production and elevated ROS. The oxidative damage to lipids led to cell death via ferroptosis, showing the effectiveness of GPAM inhibition in this tumor model. In another study using a leukemic mouse model, treatment with FSG67 significantly prolonged the survival of mice compared to untreated control mice [97]. Therefore, the few studies currently available support targeting GPAM as a viable therapeutic approach to disrupt tumor growth and progression in cancer cells.

1.3.2 Acylglycerol kinase

The mitochondrial LPA-metabolizing enzyme AGK catalyzes the phosphorylation of MAG and DAG to produce LPA and PA, respectively. AGK exhibits a slight preference for substrates containing a 18:1 fatty acid, but also phosphorylates other species (16:0, 18:0 and 20:4) [48]. AGK was identified as a component of the mitochondrial translocase within the inner membrane 22 (TIM22) protein complex [98], which is responsible for the assembly, import and insertion of transmembrane proteins into the inner mitochondrial membrane. Deregulation of AGK has been shown to be associated with defective mitochondrial protein biogenesis and import [99]. Its deregulation was also shown to result in an imbalance in lipid turnover in cells leading to various metabolic disorders and diseases, such as Sengers syndrome, diabetes, and cardiovascular diseases [99, 100]. Additionally, AGK has been increasingly recognized for its role in cancer progression and metastasis with multiple studies reporting its increased expression in various tumor types, including prostate, esophageal and oral squamous cell carcinoma (ESCC, OSCC), breast, renal and ovarian cancer, where elevated levels correlate with poor prognosis, advanced clinical stage, and reduced overall survival [48, 101–105].

Several molecular mechanisms have been proposed to elucidate AGK's role in cancer progression. For example, the overexpression of AGK in prostate cancer cells has been linked to increased intra- and extracellular concentrations of LPA, which enhanced the activation of LPA receptors through LPA binding [48]. This interaction increased the activation of ERK 1/2, promoting cell growth and migration. Conversely, downregulation of AGK resulted in a reduction of intra- and extracellular LPA and PA levels by approximately 30%, which suppressed the epidermal growth factor receptor (EGFR) transactivation and resulted in decreased cell migration [48]. Notably, it has been hypothesized that the source of extracellular LPA originates from the secretion of LPA generated intracellularly by AGK [48]. However, preliminary findings in our group do not support this export of LPA from cells, suggesting a different mechanism in OC cells (data not shown). Additionally, AGK expression in ESCC has been implicated in activating oncogenic pathways, such as the Janus kinase 2 (JAK2), resulting in constitutive activation of the signal transducer and activator of transcription 3 (STAT3) pathway, which drives oncogenesis by promoting cell proliferation, survival, and immune evasion [101]. Furthermore, AGK was reported to contribute to tumor growth through the promotion of angiogenesis and the inhibition of apoptosis by the activation of the nuclear factor kappa-light-chain-enhancer of activated B cells (NF-κB) signaling pathway, which is known to regulate genes involved in inflammation, cell survival, and immune responses [106]. In breast cancer cells, the overexpression of AGK has been associated with increased rates of cell proliferation and tumor growth, primarily due to enhanced cell cycle progression mediated by the transcription factor FOXO1 [103]. Similarly, the upregulation of AGK in OSCC cells has been shown to promote cell proliferation, cell cycle progression and cyclin D1 and p21 expression; whereas knocking down AGK resulted in the opposite effects, highlighting its significant role in regulating these cellular processes [102]. AGK has also been shown to phosphorylate and inactivate both glycogen synthase kinase-3 beta (GSK3β) and phosphatase and tensin homolog (PTEN), resulting in enhanced activation of the PI3K-AKT pathway in renal cell carcinoma (RCC) cells and CD8+ T cells, respectively [104, 107]. In RCC, the overexpression of AGK promoted cell cycle progression and furthermore increased migration and invasion through the promotion of EMT [104]. Recent study has additionally highlighted AGK's role in mitochondrial function and integrity, thus promoting non-alcoholic steatohepatitis (NASH) progression [108]. It was demonstrated that AGK-deficient hepatocytes exhibit a lower mitochondrial membrane potential, decreased and disintegrated mitochondrial cristae structure, and reduced ATP production along with maximum respiration, as indicated by the oxygen consumption rate (OCR) [108]. In another recent study linking AGK to OC, it was reported that AGK plays a crucial role in maintaining mitochondrial cristae morphogenesis through its interaction with ribosomal protein L39 (RPL39) [105]. Using OC cell models in which AGK was overexpressed and silenced, the authors demonstrated an association between AGK expression and increased cell proliferation that was independent of its kinase activity [105]. Furthermore, silencing AGK in OVCAR3 cells led to reduced number of cristae in the mitochondria compared to the overexpressed cells, as well as decreased expression of OPA1, which regulates mitochondrial fusion, suggesting that AGK may be important for maintaining mitochondrial structural integrity [105]. Interestingly, there was no significant change in ATP levels or mitochondrial respiration upon silencing or overexpression, suggesting that AGK may not influence mitochondrial function, however more in depth studies are needed [105]. Taken together, there is a significant correlation between high AGK expression and cancer progression of diverse carcinoma, as well as poor prognosis for the patients.

1.4 Ovarian Cancer - a highly metastatic disease

After lung, breast, colon and pancreatic cancer, epithelial ovarian cancer (EOC) is one of the deadliest cancers, responsible for 5% of all cancer-related deaths in women [109, 110]. Patients with EOC often remain symptom-free for years, and the few symptoms reported, such as bloating, fatigue, abdominal swelling and pain, increased urinary urgency and weight loss, are unspecific, resulting in late detection often when the disease has already progressed [111]. Additionally, the lack of early diagnostic methods accounts for the fact that only 5% of OC patients are diagnosed at early FIGO (Fédération Internationale de Gynécologie et d'Obstétrique) stages I or II [1]. Early-stage OC can be treated with surgical intervention, often involving the removal of the affected ovary or both ovaries along with chemotherapy. However, most patients are diagnosed with advanced-stage disease (FIGO stage III and IV), when the tumor has already metastasized, resulting in significantly poorer prognosis with a 5-year survival rate below 30% [112, 113].

1.4.1 Ovarian cancer risk factors and treatment strategies

The risk of getting OC increases with age, and the disease is more common after menopause [114]. Additionally, genetic, hormonal, and environmental risk factors [112], as well as the cumulative number of ovulatory cycles are associated with increased susceptibility to ovarian cancer [115, 116]. Thus, the use of oral contraceptives, having a child at a young age, multiple pregnancies, or breastfeeding for an extended period of time have all been shown to be protective against OC [117, 118]. A significant genetic risk factor for developing ovarian cancer is a family history of ovarian and breast cancer, particularly associated with hereditary breast and ovarian cancer syndrome, which is linked to mutations in the BRCA1 and BRCA2 genes. These mutations can dramatically elevate the likelihood of developing ovarian cancer. Women with these genetic mutations face a 10% to 40% higher chance of developing ovarian cancer by the age of 70 [118]. Additionally, women with Lynch syndrome, a genetic disorder characterized by defects in DNA mismatch repair genes, have an increased risk of developing diverse cancer types, including endometrial and ovarian cancers [119].

The treatment strategy for OC is primarily determined by the stage at which the disease is diagnosed. When diagnosed at an early stage (stage I), first-line treatment involves debulking surgery to remove the cancerous tissue, which may include the affected ovary. This is often followed by adjuvant chemotherapy using agents such as carboplatin and paclitaxel [120, 121]. Studies indicate that when ovarian cancer is detected early, cytoreductive surgery combined with conventional chemotherapy can cure 70-90% of patients [122]. For more advanced stages (stages II-IV), treatment may necessitate the removal of both ovaries, fallopian tubes, and the uterus, followed by systemic chemotherapy [123]. In these cases, the prognosis is generally poorer, with survival rates significantly lower than in early-stage diagnoses [124]. Targeted therapies have emerged as effective options, particularly for cancers with BRCA1/2 mutations. Poly(ADP-ribose) polymerase (PARP) inhibitors, such as olaparib, niraparib, and rucaparib, exploit defective DNA repair pathways in cancer cells leading to cell death [125]. Additionally, bevacizumab, a monoclonal antibody that targets vascular endothelial growth factor (VEGF), is used to inhibit angiogenesis, thereby reducing the tumor's ability to grow and spread [126]. Hormonal therapy, such as tamoxifen is another treatment option for low-grade or hormone-sensitive ovarian cancer subtypes [127]. In some cases, intraperitoneal (IP)-administered chemotherapy, in which drugs are delivered directly into the abdominal cavity, is used to achieve higher local concentrations of chemotherapy agents to help improve outcomes [128].

1.4.2 Ovarian cancer classification

Ovarian neoplasms are broadly categorized into epithelial and non-epithelial cancers. The latter are less common and arise from germ cells, which mature into oocytes, or from endocrine and interstitial sex cord stromal cells responsible for hormone production, such as estrogen and progesterone. Germ cells are implicated in 3-5% of all cases of malignant ovarian carcinoma, while sex cord-stromal cells contribute to approximately 7% [129]. EOC accounts for 90% of all diagnosed OC cases, making it the most predominant form of the disease [129]. It originates from the epithelium that covers the surface of the ovaries and fallopian tube. Five main types of EOC can be distinguished according to their histopathological characteristics: High-grade and low-grade serous carcinoma (HGSC/LGSC), endometrioid carcinoma, clear cell carcinoma, and mucinous carcinomas [130]. The categorization is based on the morphological resemblance to the tissue of the female genital tract from which the tumor cells originate. The predominant EOC subtype, high grade serous, accounts for 70% of EOC cases and originates from the ovarian surface epithelium and fallopian tube. As stated above, the subtype is further divided into HGS and LGS carcinomas, with the former being the more common and aggressive of the two, with a significantly poorer prognosis [131]. Endometrioid EOC, representing around 10% of tumors, resembles endometrial tissue, while clear cell EOC, which accounts for 10% of cases, is similar to low-grade endometrioid EOC and may arise from retrograde menstruation. Finally, mucinous EOC makes up 3% of all cases, but its exact origin remains uncertain [132, 133].

Classification of EOC into one of the four clinical FIGO stages is based on the progression of the tumor at the time of diagnosis, which considers the size of the tumor, whether it has metastasized to neighboring organs and whether the lymph nodes and distant organs are affected [129]. Stage I is limited to one or both ovaries, while stage II involves both ovaries with extension to the uterus, fallopian tubes, or other pelvic tissues. Advanced stages include stage

III, where metastasis occurs to the lymph nodes or tissues in the peritoneal cavity, such as the omentum or small intestine, and stage IV involves distant metastases [129]. Furthermore, tumor grading, which assesses cell differentiation, helps predict the cancer's behavior and likelihood of metastasis. Low-grade tumors (grades I & II) consist of well-to-moderately differentiated cells; whereas, high-grade tumors (grade III) consist of poorly differentiated cells [134]. EOC is further classified into type I and type II based on histological grade, molecular phenotype, and genotype. Type I tumors - mucinous, clear cell, low-grade endometrioid, and LGS carcinomas - are typically diagnosed at the early stages (I or II), grow slowly, and are well-differentiated. These tumors respond poorly to standard chemotherapy but may be treated effectively with hormonal therapy [132, 135]. Conversely, type II ovarian carcinomas, including high-grade endometrioid and high-grade serous carcinomas, are often detected at advanced stages (III or IV). These tumors are aggressive, fast-growing, and prone to rapid metastasis [132]. To minimize the lethal impact of HGS EOC, it is therefore essential to understand and target the processes that are activated during metastasis.

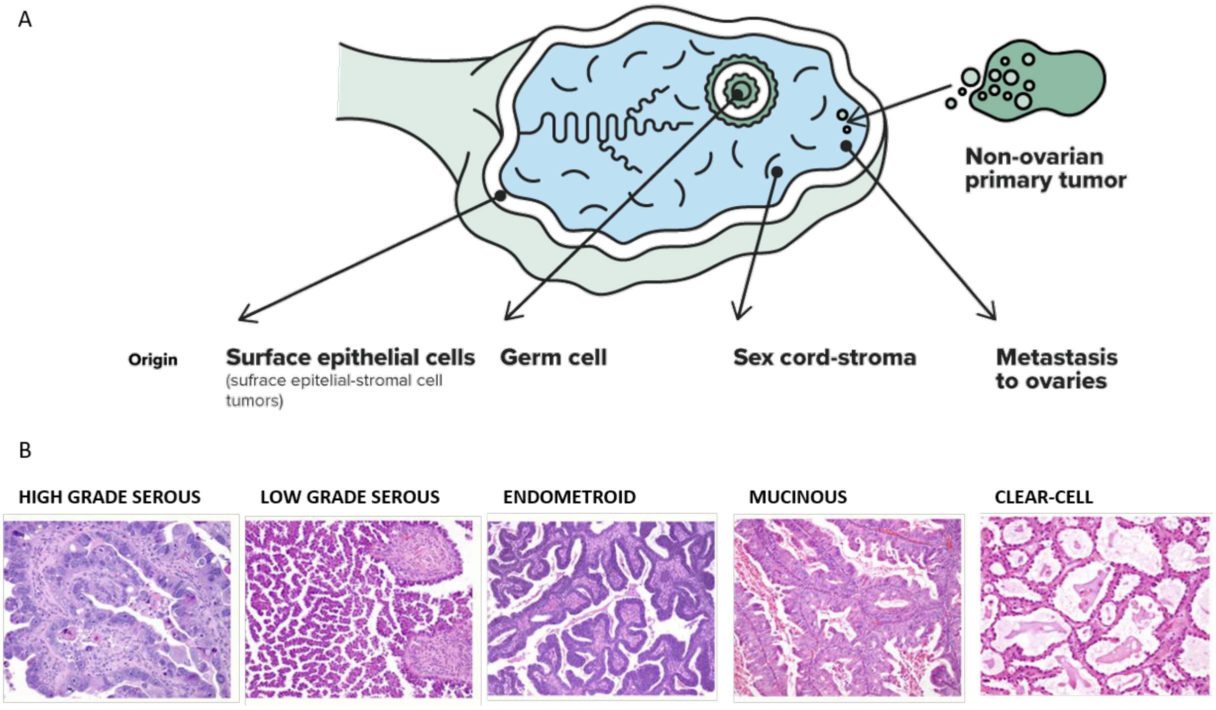

Figure 8: **Potential sources of ovarian carcinoma** **A** Ovarian carcinoma can originate from three primary cellular sources: surface epithelial cells, germ cells, or sex cord-stromal cells. Adapted from Gaba, 2020 [136]. **B** Epithelial ovarian cancer is classified based on tumor histology and grade. The main histological subtypes include high-grade serous carcinoma, low-grade serous carcinoma, endometrioid carcinoma, mucinous carcinoma, and clear-cell carcinoma. Ravindran & Choudhary, 2021 [137].

1.4.3 Metastasis formation in epithelial ovarian cancer

Metastasis of EOC occurs early in its progression through transcoelomic dissemination and is typically first confined to the pelvic organs and walls [138]. Arising from the outer layer of the ovaries, single cancer cells or cell aggregates can shed and spread through the peritoneal cavity [139]. Aggregation into cell spheroids helps cancer cells circumvent anoikis and makes them more resistant to drugs and chemotherapeutic agents [139, 140]. Furthermore, EOC metastasis is often accompanied by an excessive accumulation of abdominal fluid - malignant ascites - which is rich in proteins, metabolites, and signaling molecules, all of which are beneficial for the survival of the disseminated cancer cells, and create a conducive environment for tumor implantation and carcinogenesis at the metastatic site [141]. The adipocyte-rich omentum is a preferred metastatic niche for EOC. Due to its rich supply of fatty acids, as well as secretion of pro-inflammatory cytokines, such as IL-8, the omentum facilitates the colonization and invasion of tumor cells [142]. Spread of EOC outside of the peritoneal cavity is uncommon. However, in advanced stages, EOC can also metastasize via hematogenous or lymphatic pathways to distant organs such as the liver and lungs [143–145]. Circulating tumor cells (CTCs) are also detectable in some patients, indicating systemic dissemination [146].

For cancer cells to detach from the primary tumor and invade surrounding tissues, they must undergo significant morphological and molecular changes through a process known as EMT. EMT is characterized by the loss of epithelial traits, such as cell-cell adhesion, and the acquisition of mesenchymal properties, including enhanced motility and invasiveness [147]. Epithelial cells are defined by the expression of E-cadherin, a key protein that maintains tissue integrity by facilitating cell-cell adhesion [148]. During EMT, cancer cells downregulate E-cadherin expression, weakening their adhesion to neighboring cells and promoting detachment from the ovarian surface [149]. The loss of E-cadherin disrupts adherens junctions, releasing β-catenin into the cytoplasm [150]. In the absence of WNT signaling, cytoplasmic β-catenin is targeted for degradation by GSK3β, preventing its accumulation. However, during EMT, WNT signaling is frequently activated, inhibiting GSK3β and stabilizing β-catenin. Stabilized β-catenin translocates to the nucleus where it drives the transcription of mesenchymal markers such as N-cadherin, vimentin, fibronectin receptors, and matrix metalloproteinases (MMPs) [151]. These molecular changes enhance the cell's ability to bind to fibronectin, a key extracellular matrix (ECM) protein, and remodel the ECM, thereby promoting cell motility and invasion by facilitating the detachment from the primary tumor site and migration through the ECM [149, 152]. Understanding the molecular and cellular mechanisms underlying ovarian cancer metastasis is essential for identifying novel therapeutic targets to prevent or limit disease spread, ultimately improving patient outcomes.

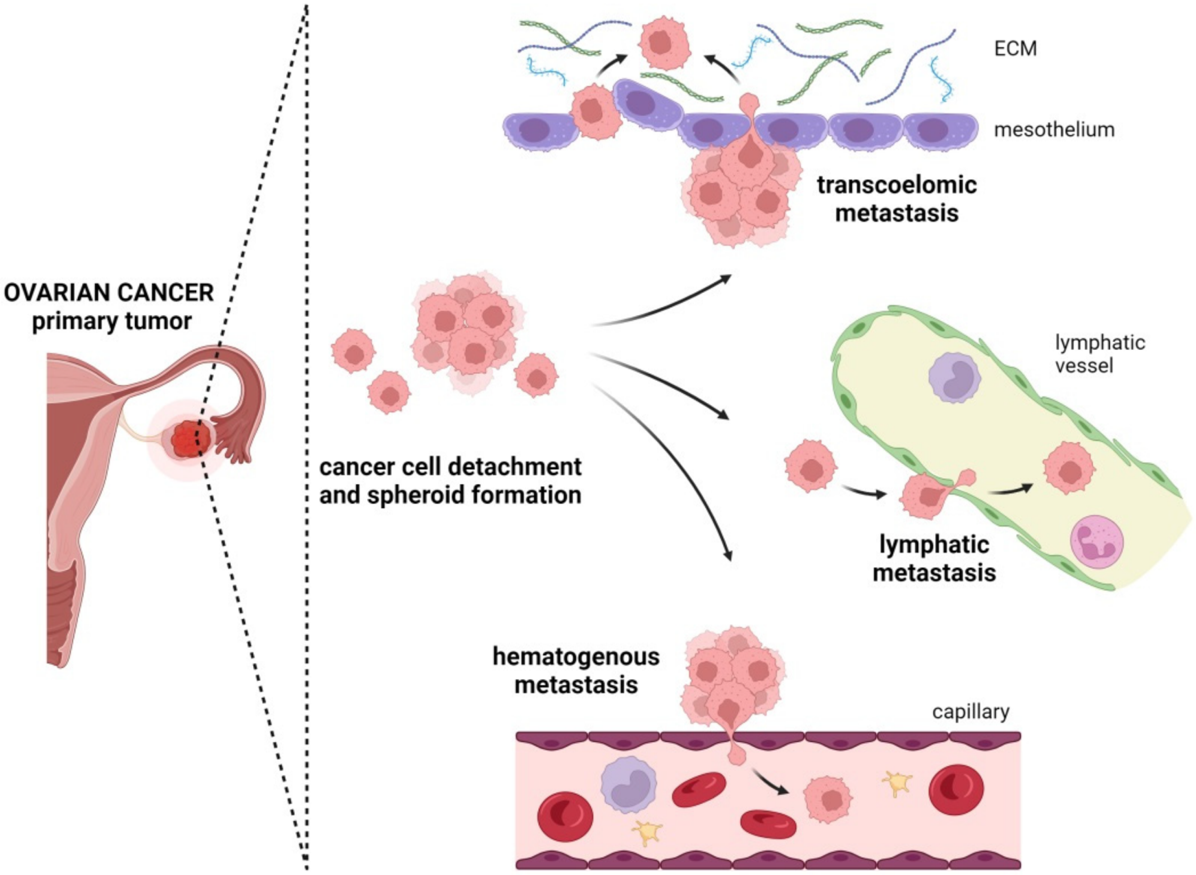

Figure 9: **Metastatic routes of epithelial ovarian cancer.** Metastasis in epithelial ovarian cancer (EOC) occur predominantly via the transcoelomic pathway, which involves several critical steps. First cancer cells dettach from the primary tumor, allowing them to enter the the peritoneal fluid where they can aggregate to form spheroids. Spheroids can then invade the mesothelial layer and extracellullar matrix (ECM), facilitating further spread within the peritoneal cavity. In addition to transcoelomic metastasis, EOC can also disseminate through lymphatic and hematogenous routes, leading to distant metastasis in various organs. Figure adapted from Sliwa et al., 2024 [153].

1.5 Aim of the study

Previous studies on the mitochondrial LPA-producing enzyme, GPAM demonstrated that higher GPAM expression is associated with shorter overall survival in human ovarian cancer. Furthermore, reducing GPAM expression in breast, endometrial and clear cell ovarian cancer cell lines decreased cell migration, and silencing GPAM in the latter also reduced subcutaneous tumor growth in a xenograft mouse model. Interestingly, directly transfecting GPAM's enzymatic product, LPA into MCF7 breast cancer cells significantly increased migration and liquid chromatography mass spectrometry (LC/MS-MS) measurements confirmed that the faster migrating cells did indeed have higher intracellular levels of LPA, indicating a potential link between the two [9]. An increasing number of published studies, have also reported that another mitochondrial LPA-producing enzyme, acyl glycerol kinase is involved in cancer-promoting processes in diverse cancer types [48, 101–103, 105]. However, the role of these two enzymes has not yet been comprehensively studied in high-grade serous ovarian cancer, which is the most common as well as most lethal histotype of ovarian cancer. Therefore, the aim of this PhD thesis is to investigate the mitochondrial LPA-producing enzymes, GPAM and AGK in high-grade serous ovarian cancer cells, focusing on their role in cellular processes, including cell migration and 3D spheroid formation and outgrowth, and the underlying mechanism by comprehensively characterizing changes is intracellular phospholipid levels after gene silencing or overexpression, the effect on known signaling proteins and EMT markers, and cellular energetics.

2 Materials

2.1 Instruments

Table 1: List of used instruments and consumables

Instrument	Company
ABI 7500 Fast Real-Time PCR System	Applied Biosystems
Blotting chamber	Bio-Rad
Blot imager Vilber Fusion Fx7	Vilber
Cell counter CASYTT	OMNI Life Science
Cell culture incubator	Binder
Centrifuge, Avant JNX-26	Beckmann Coulter
Centrifuge 5415R	Eppendorf
Centrifuge Megafuge 1.0R	Thermo Fisher Scientific
Centrifuge MiniSpinplus	Eppendorf
Electrophoresis unit Mini-PROTEAN	Bio-Rad
Fume hood	Waldner
Heating block	Grant-Bio
Inverted Microscope Axiovert 26	Zeiss
Laminar flow hood HERAsafe	Heraeus
Microscope BZ-X800	Keyence
Microscope eclipse TS100	Nikon
Milli-Q® IQ Water Purification System	Millipore
Mini Vortex Mixer	Thermo Fisher Scientific
NanoDrop 2000	Thermo Fisher Scientific
Pipettes (2, 10, 100, 200, 1000µl)	Eppendorf
Pipetting aid	Integra Bioscience
pH meter	Schott
Phase contrast microscope eclipse TS100	Nikon
Plate reader infinite M200 Pro	Tecan
Power pack HC	Bio-Rad
Power pack P25T	Biometra
Shaker KS 260 basic	IKA
Thermal cycler T3000	Biometra
Thermomixer	Eppendorf
Trans-Blot® SD Semi-Dry Transfer Cell®	BioRad
Vacuum pump	Vacuubrand
Water bath for cell culture	GLF
Western Blot System	Biometra

2.2 Consumables

Table 2: List of used consumables

Consumable	Company
CASY cups	OMNI Life Sciences
Cell culture dishes (10, 15 cm)	Sarstedt
Cell culture flasks (T25,T75,T175)	Sarstedt
Cell culture inserts 24 well 8.0 µm pore	CellQArt
Cell culture multiwell plates (6-, 24-, 96-well)	Sarstedt
Cell scraper	Sarstedt
Cryogenic Vials	Sarstedt
Inserts (24-Well, 8.0 µm)	CellQArt
Falcon tubes(15, 50 ml)	Sarstedt
Filter tips (10, 200, 1000 µl)	Eppendorf
Freezing container (Mr. Frosty)	Thermo Fisher Scientific
MicroAmp Optical Adhesive Film	Thermo Fisher Scientific
MicroAmp Optical 96-Well Reaction Plate	Thermo Fisher Scientific
MicroTissues 3D Petri-dish micro-mold	Merck Millipore
Pipet tips (10, 200, 1000 µl)	Sarstedt
PVDF membrane	PerkinElmer
Reaction tubes(1.5, 2, 5 ml)	Sarstedt
RNase-free Microfuge Tubes 1.5 ml	Thermo Fisher Scientific
Serological pipettes (5, 10, 25, 50 ml)	Sarstedt
Tips (10, 100, 200, 1000, 5000 µl)	Sarstedt
Whatman paper 3 mm	VWR

2.3 Reagents & kits

Table 3: List of commercially available reagents, kits & buffers

Name	Producer
Acrylamide (30% (v/v))	Roth
Ammonium persulfate	Sigma Aldrich
Active Rho Pull-Down and Detection Kit	Thermo Fisher Scientific
Agarose	Thermo Fisher Scientific
Bicinchoninic acid assay kit	Thermo Fisher Scientific
Bovine serum albumin (BSA)	Roth
Buffer concentrate A	Roth

Buffer concentrate K	Roth
CASY ton	OMNI Life Sciences
p-Coumaric acid	Sigma Aldrich
Diethylpyrocarbonate-treated (DEPC) water	Invitrogen
Dimethylsulfoxide (DMSO)	Sigma Aldrich
E. Coli (NEB 5-alpha Competent)	New England Biolabs
Ethanol absolute	Roth
Fetal calf serum (FCS)	Gibco
High capacity cDNA RT kit	Roche
Lipofectamine RNAiMax	Invitrogen
Loading buffer 4x	Bio-Rad
β-Mercaptoethanol	Roth
Methanol, HPLC grade	Roth
Milk Powder	Roth
Nonidet P-40 substitute	Roche
NucleoBond® Xtra Maxi kit	Machery-Nagel
Odd-chained Lipidomix mass spec standard	Avanti
Opti-MEM	Gibco
Phosphate buffered saline (PBS) 10x	Sigma Aldrich
Phosphatase-Inhibitor-Cocktail II&III	Sigma Aldrich
Polybrene	Merck Millipore
Precision plus protein dual color	Bio-Rad
Protease-Inhibitor-Cocktail	Sigma Aldrich
Puromycin	Gibco
2-Propanol	Roth
QuantiFast SYBR Green PCR Kit	Qiagen
QuantiNova SYBR Green PCR Kit	Qiagen
RNaseZap™ RNase Decontamination Solution	Thermo Fisher Scientific
RNeasy mini kit	Qiagen
RPMI 1640	PAN Biotech
RT PCR kit Quanti-Tect SYBR Green	Qiagen
Sodium Dodecyl Sulfate (SDS)	AppliChem
Tris	Roth
Tris-HCl	Roth
Tris/Glycine/SDS Buffer (10x)	Bio-Rad
Triton X-100	Sigma Aldrich
Tween20	AppliChem
Trypsin 0.05% / EDTA 0.02% in PBS	PAN Biotech

2.4 Buffers

Table 4: List of prepared buffers & solutions

Buffer/Solution	Composition
Anode buffer	10% (v/v) Buffer concentrate A 20% (v/v) Methanol
APS solution	10% (w/v) Ammonium persulfate
Blocking solution (BSA)	5% (w/v) BSA in 1x TBS-T
Blocking solution (milk)	5 % (w/v) Milk powder in 1x TBS-T
Cathode buffer	10% (v/v) Buffer concentrate K 20% (v/v) Methanol
Crystal violet fixation solution	0.1% (w/v) crystal violet 20% (v/v) Ethanol in ultrapure water
Enhanced chemiluminescent solution (ECL)	2.5 mM Luminol 0.2 mM p-Coumaric acid in 0.1 M Tris
RIPA buffer	50 mM Tris-HCl (pH 7.5) 150 mM NaCl 1% NP-40 0.5% Sodium deoxycholate 0.5% SDS
SDS solution	10% (w/v) SDS in ultrapure water
Separation buffer	3 M Tris in ultrapure water (pH 8.8)
Stacking buffer	0.47 M Tris in ultrapure water (pH 6.8)
Stripping buffer	0.2 M Glycine 0.1% (w/v) SDS 1% (v/v) Tween20 in ultrapure water (pH 2.2)
TBS-T	10% (v/v) TBS (10x) 0.1% (v/v) Tween20
Tris buffered saline (TBS 10x)	0.5 M Tris 1.5 M NaCl in ultrapure water (pH 7.4)

2.5 Lentiviral vectors

Table 5: List of vectors

Name	Lentiviral Vector construction
pLV_AGK	pLV[Exp]-Puro-CMV>hAGK[NM_018238.4](ns):P2A:EGFP
pLV_GFP	EGFP lentiviral control vector pLV[Exp]-EGFP/Puro-CMV>Stuffer300
pMD2.G	VSV-G envelope expressing plasmid
psPAX2	Lentiviral packaging plasmid

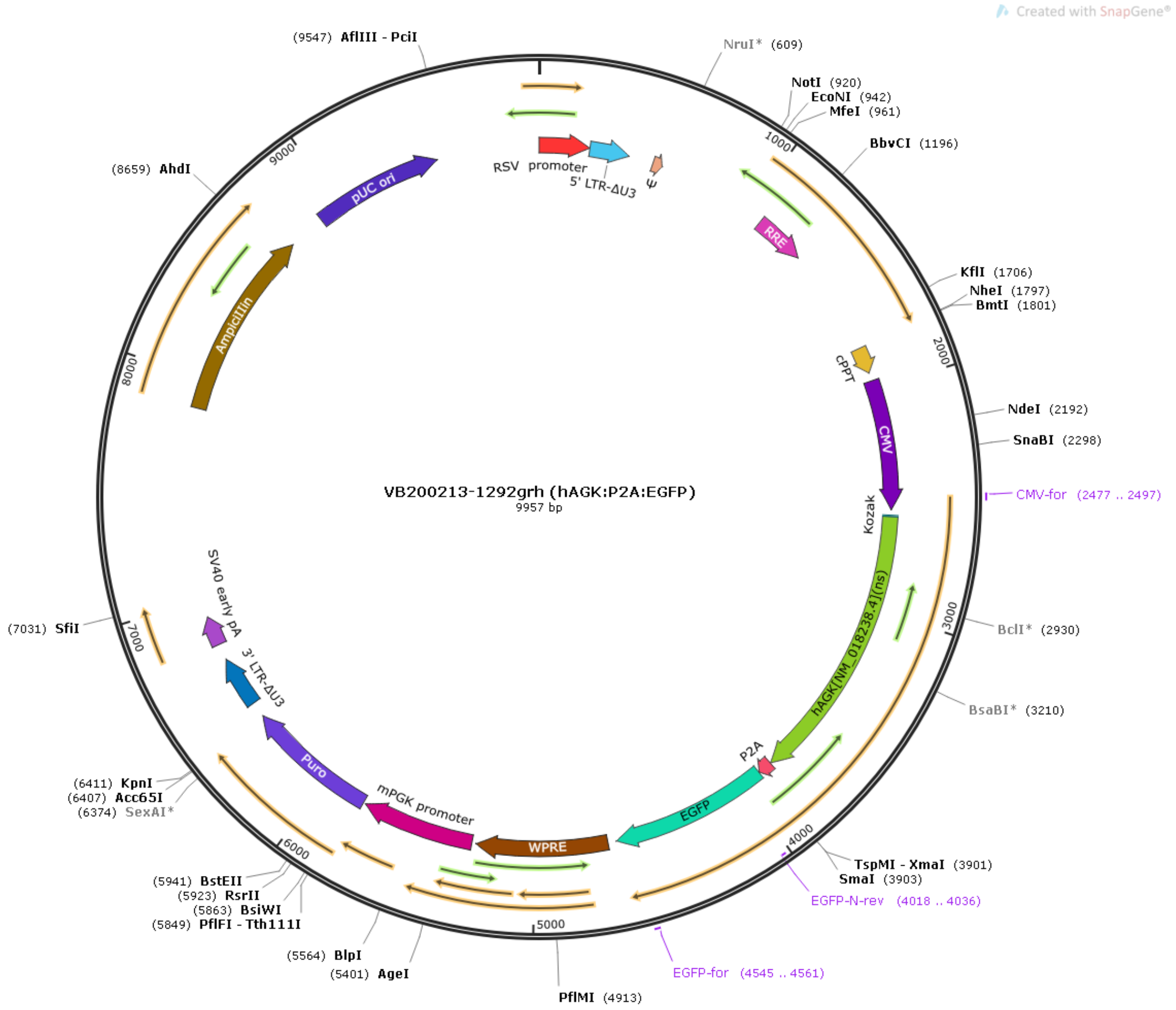

Figure 10: **pLV_AGK vector from Vector Builder.**

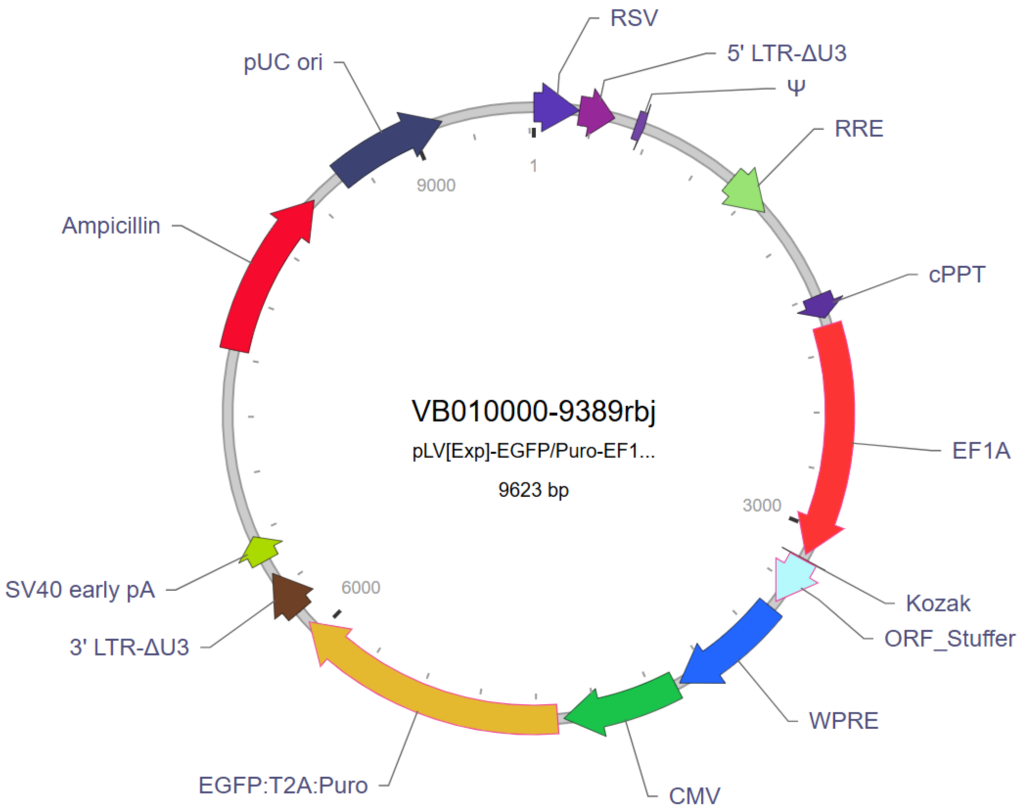

Figure 11: **pLV_GFP vector from Vector Builder.**

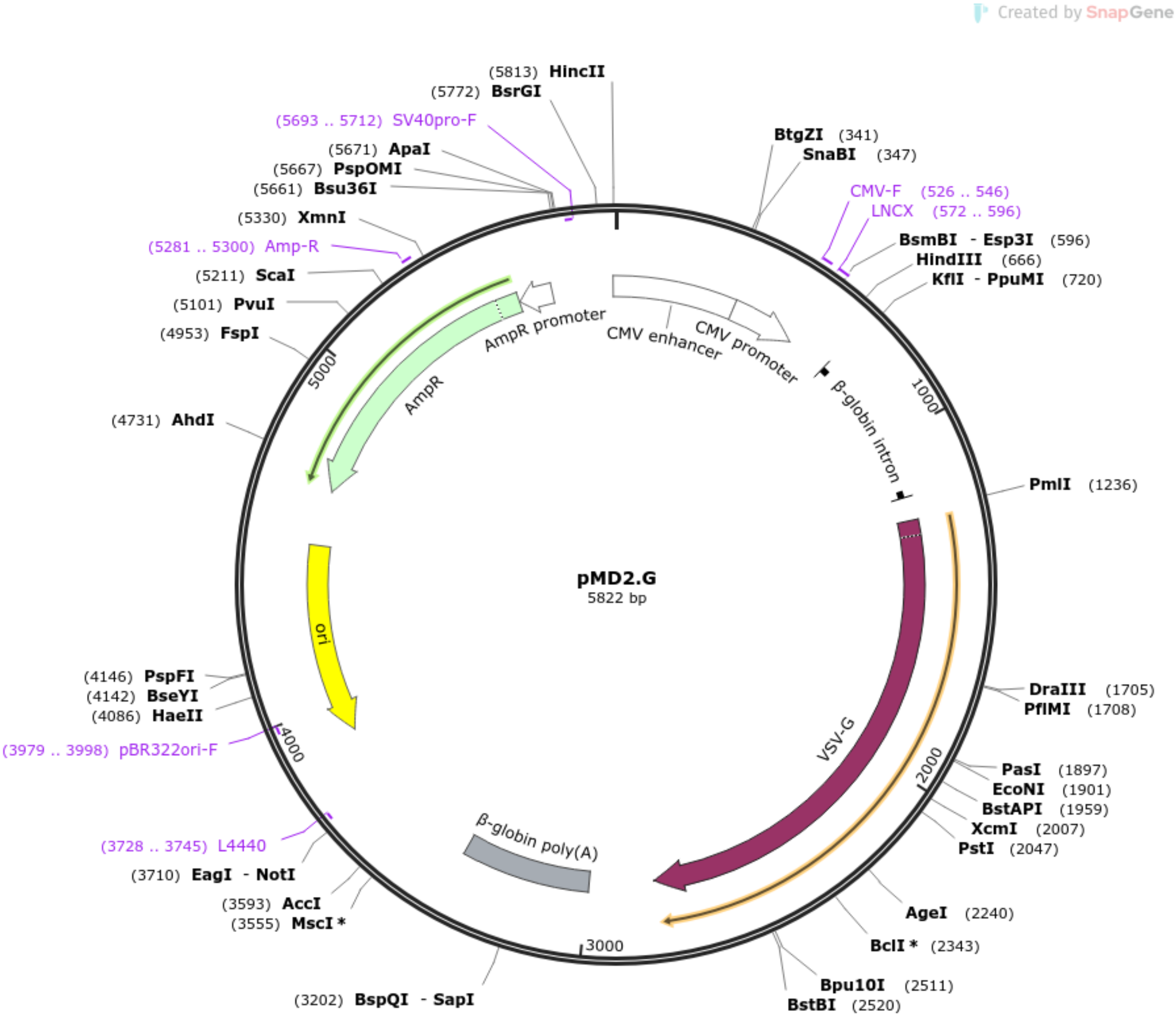

Figure 12: **pMD2.G envelope expressing plasmid from Addgene (Didier Trono Lab).**

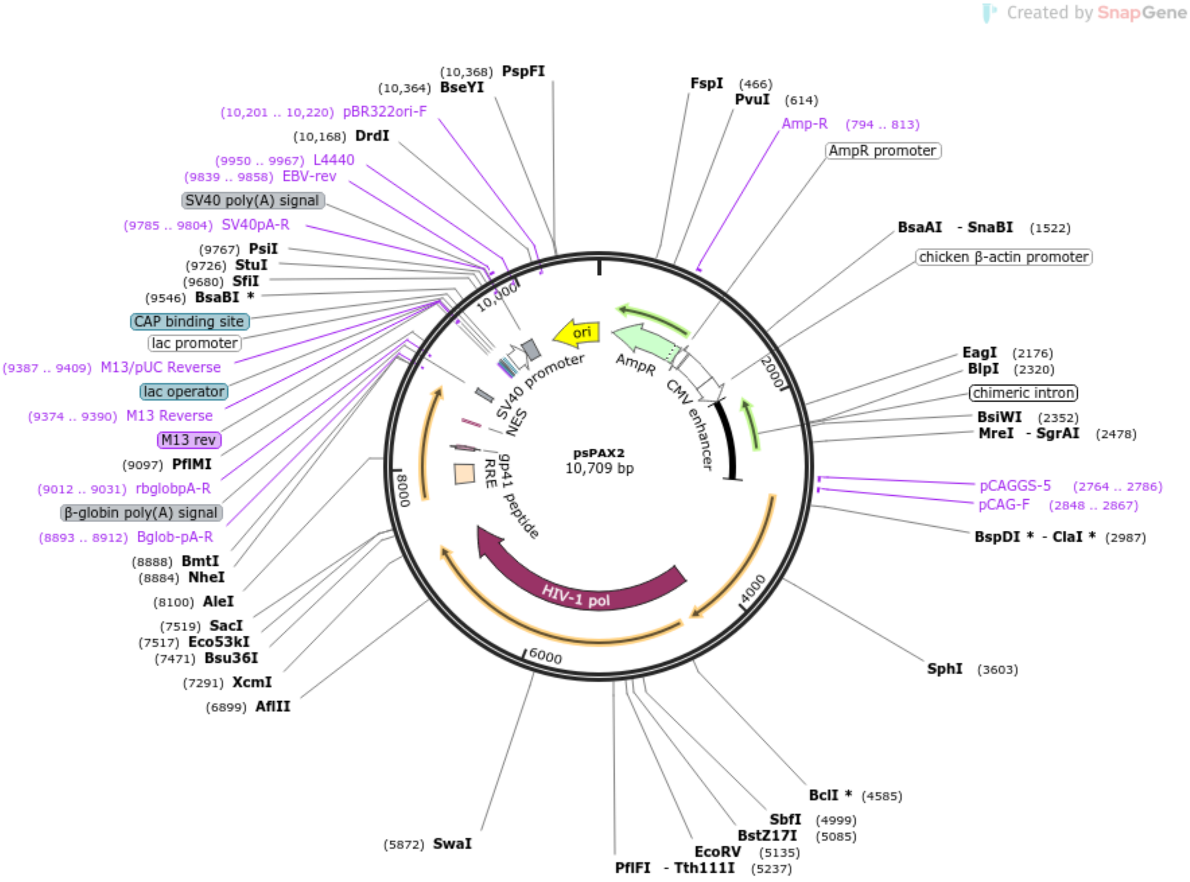

Figure 13: **psPAX2 lentiviral packaging plasmid from Addgene (Didier Trono Lab).**

2.6 Cell lines

Table 6: Commercially available cell lines

Cell lines	Information
COV318	High-grade serous ovarian adenocarcinoma
HOSE6-3	Immortalized normal ovarian epithelial cells
HOSE17-1	Immortalized normal ovarian epithelial cells
Kuramochi	High-grade serous ovarian adenocarcinoma
OAW28	High-grade serous ovarian adenocarcinoma
OAW42	Ovarian serous cystadenocarcinoma
OVCAR3	High-grade serous ovarian adenocarcinoma
OVCAR4	High-grade serous ovarian adenocarcinoma
OVCAR8	High-grade serous ovarian adenocarcinoma.
SKOV3	Ovarian serous cystadenocarcinoma
TOV112D	Ovarian endometrioid adenocarcinoma

Table 7: Cell lines generated as part of this thesis

Cell lines	information
OVCAR8_GFP (OV8_GFP)	Stably Green fluorescence protein (GFP)-expressing cell line was generated by transduction of OVCAR8 cells with the lentiviral pLV_GFP vector
OVCAR8_AGK (OV8_AGK)	Stably AGK-expressing cell line was generated by transduction of OVCAR8 cells with the lentiviral pLV_AGK vector

2.7 siRNA

Target	Assay ID	Product Type
siAGK#1	HSS183238	Stealth siRNA
siAGK#2	HSS124948	Stealth siRNA
siAGK #3	S33575	Silencer® Select
siAGK #4	S224483	Silencer® Select
siAGK #5	S224484	Silencer® Select
siGPAM#1	HSS126649	Stealth siRNA
siGPAM#2	HSS126650	Stealth siRNA
siGPAM#3	S33575	Silencer® Select
siGPAM#4	S224483	Silencer® Select
siNEG #1	465370	Stealth siRNA
siNEG #2	4390843	Silencer

2.8 Primer

Table 8: Quanti-Tect Primer Assays

Target	GeneGlobe ID	Company
ACTB (β-Actin)	QT00095431	Qiagen
AGK	QT01022756	Qiagen
GPAT1/GPAM	QT01668408	Qiagen
GPAT2	QT01668135	Qiagen
GPAT4	QT00042847	Qiagen
GPAT3	QT00016870	Qiagen
GDE4 (GDPD1)	QT00027223	Qiagen
GDE7 (GDPD3)	QT00039991	Qiagen

2.9 Antibodies

Table 9: Antibodies

Target	catalog number	Company
β-Actin	A5316	Sigma Aldrich
Akt	#9272	Cell signaling
Active β-Catenin	#8814	Cell Signaling
AGK	HPA053471	Sigma Aldrich
Anti-mouse	#7076	Cell Signaling
Anti-rabbit	#7074	Cell Signaling
E-cadherin	#3195	Cell Signaling
N-cadherin	#13116	Cell Signaling
Calnexin	#2433S	Cell Signaling
β-Catenin	#8480	Cell Signaling
Erk	#9102	Cell Signaling
GAPDH	#2118	Cell Signaling
GFP	632569	Takara
GPAM	LS-C334872	LS Bio
GSK3β	#9315	Cell Signaling
Phospho-Akt	#9271	Cell Signaling
Phospho-Erk	#9101	Cell Signaling
Phospho-GSK3β	#9323	Cell Signaling
Vimentin	#5741	Cell Signaling

3 Methods

3.1 Molecular biological methods

3.1.1 Bacterial transformation

To prepare large quantities of plasmids containing the DNA of interest, bacteria cells were transformed and cultivated to exponentially amplify the plasmid number. NEB 5-alpha Competent E. coli cells, were first thawed on ice before the addition of 100-200 ng of plasmid DNA. After gentle mixing, the cells were incubated on ice for 30 minutes. Meanwhile, agar plates containing the appropriate antibiotic required for the growth of each plasmid were pre-warmed to 37°C in an incubator. Transformation was conducted using the heat shock method, involving a brief incubation of the cells at 42°C followed by immediate cooling on ice. Afterward, 950 µl of Super Optimal Broth cum glucose (SOC) media (without antibiotic) were added to the transformed bacteria, and the mixture was incubated in a shaking heating block at 37°C for 45 minutes. Following incubation, 200 µl of the transformed cells were spread onto agar plates and incubated upside down overnight at 37°C. The following day, plates were examined for the presence of individual colonies and stored at 4°C until colonies were picked for inoculation.

3.1.2 Plasmid purification

To generate a large quantity of the plasmid of interest, 2 mL of sterile lysogeny broth (LB) media, supplemented with the respective antibiotic as required, were inoculated with one individual transfected bacterial colony from the agar plate (3.1.1). This pre-culture was incubated at 37°C with continuous shaking at 200 rpm for 6-8 hours. After incubation, 300 µL of the pre-culture were added to 250 mL of antibiotic-containing LB-medium in 1000 mL Erlenmeyer flasks covered with aluminum foil and incubated under vigorous shaking at 200 rpm overnight at 37°C. On the following day, 500 µL of the liquid bacterial culture were gently mixed with 250 µL of 100% glycerol by carefully pipetting up and down and frozen at -80°C for long-term storage of the plasmids, which can be used to inoculate new cultures. Plasmid DNA extraction was carried out on the remaining 1 L culture using a commercially available NucleoBond Xtra Maxi kit (Machery-Nagel) following the manufacturer’s protocol. Briefly, bacterial cells were harvested by centrifugation, lysed, and the DNA was purified using a column-based method. The concentration of the extracted plasmid DNA was quantified using a spectrophotometer (NanoDrop One, Thermo Scientific). The plasmids were then stored at -20°C.

3.1.3 Generation of lentiviral particles

To generate lentiviral particles containing the plasmid of interest, a T75 flask was prepared per plasmid by first plating 3 x 10^6 HEK293T cells in full growth medium the day prior to transfection. On the next day, two hours before transfection, a media change was performed. Meanwhile, aliquots of the plasmids containing the gene of interest, as well as the lentiviral packaging (psPAX2) and the lentiviral envelope (pMD2.G) plasmids, as generated in Section 3.1.2, were diluted to an approximate concentration of 1 µg/µl. The volume of all three plasmids, as listed in the table below, were combined with water, calcium chloride ($CaCl_2$), and 2x HEPES-buffered salt solution (HBSS), mixed well by vortexing for 30 seconds, and then added to the flask with the HEK293T cells. After 24 hours of incubation, the transfection medium was discarded and 15 mL of fresh full growth media were added, and the cells were incubated overnight. On the next day, the media was collected and centrifuged at 1500 rpm for 5 minutes. The supernatant (24 h sup) was sterile filtered (0.22 µm), aliquoted à 3 mL, and stored at -80°C. Fresh 15 mL media were added to the flask with the transduced HEK293T cells, and the procedure was repeated after 24 hours and 48 hours to generate the 48 h supernatant and 72 h supernatant, respectively.

Table 10: Pipetting information for the transduction mix.

Component	Amount
Vector plasmid	30 µg
Packaging plasmid (psPAX2)	15 µg
Envelop plasmid (pMD2.G)	6 µg
Water	1280 µl
$CaCl_2$ (2.5 M)	163 µl
2x HBSS	1500 µl

3.2 Cell biological methods

3.2.1 Cultivation of cells

High grade serous ovarian cancer (HGSOC) cell lines (OVCAR4, OVCAR8, Kuramochi, and TOV112D) along with two non-tumorigenic immortalized ovarian epithelial cell lines (HOSE6-3 and HOSE17-1) were kindly provided by Prof. Viola Heinzelmann-Schwarz from the University of Basel. Additionally, COV318 and OAW28 cell lines were purchased from Sigma Aldrich. To ensure authenticity, all cell lines underwent authentication via STR DNA typing following ANSI/ATCC ASN-0002-2011 guidelines by DSMZ (German Collection of Microorganisms and Cell Cultures GmbH), and routine mycoplasma testing was performed using the Venor GeM Classic Mycoplasma Detection Kit (Minerva Biolabs). All cell lines were maintained in RPMI 1640 (Gibco) supplemented with 10% fetal calf serum (Gibco FCS) in a humidified incubator (Binder) set to 5% CO_2 and 37°C under sterile conditions. Work was performed in a laminar flow cabinet (HeraSafe) using sterile materials and solutions. Upon reaching 80-90% confluency, cells were sub-cultured. This involved rinsing adherent cells with 1x PBS, treating with trypsin/EDTA (0.05%/0.02% in PBS), and transferring the detached cells into new culture flasks. Cells were counted using a CASY TT cell counter and diluted to the desired concentration before being plated for the respective assays. For cryopreservation, adherent cells at approximately 70% confluency were detached, pelleted at 133 x g for five min and resuspended in media with 5% DMSO as an antifreeze agent. Frozen cryovials were then transferred to the gas-phase above the liquid nitrogen in the tank for long-term storage. For culturing cryopreserved cells, cryovials were placed in a 37°C water bath for quick thawing. After defrosting, cells were pelleted, resuspended in antibiotic-free medium, and transferred to T25 flasks with fresh medium. Antibiotic-containing medium was added, if needed after 24 hours. Cells were sub-cultured at least twice after thawing before use in experiments.

3.2.2 Transient inhibition of gene expression via RNA interference

RNA interference was used to reduce the expression of genes of interest. Small interfering RNA (siRNA) molecules that bind to specific exons of the target gene were purchased from Thermo Fisher Scientific. For each target gene, at least two different siRNA molecules were used to ensure specificity and efficacy. These siRNA molecules were combined with the transfection reagent Lipofectamine RNAiMAX to facilitate their introduction into cells using the reverse transfection method. The transfection protocol involved the following steps: 500 µl of OptiMEM (a serum-free medium) were pipetted into each well, followed by the addition of the siRNA and gentle shaking to ensure even distribution. Lipofectamine RNAiMAX (5 µl) was then added and allowed to stand for 20 to 30 minutes to form the micellar complexes. The final siRNA concentration used was 20 nM for all genes and cell lines, except for silencing AGK in OAW28 cells, where a higher concentration of 30 nM was required to achieve sufficient reduction in AGK expression at the protein level. For the simultaneous knockdown of two genes, 20 nM of each siRNA oligo was used, followed by the addition of 10 µl Lipofectamine. The appropriate number of cells was then added to each well, so that the cells reached about 80-90% confluency after an incubation period of 72 hours. The effectiveness of the knockdown was subsequently assessed at both the RNA and protein levels to ensure that the siRNA had its intended effect by inhibiting the expression of the target gene. A random siRNA sequence that does not bind specifically to any gene was used as a negative control (siNEG) to ensure that any observed effects were specific to the silenced gene and not due to nonspecific interactions.

3.2.3 Antibiotic kill-curve

To establish stable cell lines via lentiviral transduction, it was essential to determine the minimum antibiotic concentration required to selectively eliminate non-transduced cells. Lentiviral vectors, which were designed for the constitutive expression of AGK (see Table 5), carried a puromycin resistance gene, allowing for selection using puromycin. To determine the minimum effective antibiotic concentration cells were plated in 24-well plates in full growth medium at a density that would achieve a confluence of approximately 70% the next day. Antibiotic dilution series were prepared using stock concentrations of puromycin (10 mg/ml). The antibiotic-containing media were added to the cells after confirmation of confluency, and the cells were monitored for visual toxicity over the following days. The antibiotic-containing media were replaced every two to three days. After one week of treatment, the minimum antibiotic concentration that resulted in cell death was identified and used for subsequent antibiotic selection following transduction experiments.

Table 11: Concentrations of selection antibiotics tested

Antibiotic	**Tested concentrations [µg/ml]**											
Puromycin	0	0.5	1	2	3	4	5	6	7	8	9	10

3.2.4 Generation of stable constitutive AGK expressing cells lines

To generate cell lines with constitutive AGK expression, OVCAR8 cells were transduced with lentiviral particles carrying vectors with a human cytomegalovirus (CMV) immediate early enhancer and promoter. The sequence encoding the AGK gene was linked to the gene sequence for green fluorescence protein (GFP) through a P2A site (ATNFSLLKQAGDVEENPGP), which is a self-cleaving peptide (Fig. 10). This construct allows for the simultaneous expression of multiple proteins from a single open reading frame [154], allowing for the tracking of transduced cells through both the presence of the fluorescence signal and the expression of the gene of interest. To generate a control cell line, a lentiviral vector containing only the GFP sequence was transduced into OVCAR8 cells (Fig. 11). The transduction was performed via the spinfection protocol. Briefly, cells were collected as described in 3.2.1 and diluted with medium to 500,000 cells per ml. Lentiviral supernatant as prepared in section 3.1.3, was mixed with 1 ml of the cell suspension and 0.5 µg Polybrene and added per well of a 24-well plate. The plates were centrifuged at 2500 rpm for 1.5 hours at 30°C. After 24 hours incubation at 37°C and 5% CO_2 in a humidified incubator, transfection media was changed to normal growth media. 72 hours post-transfection, the media was replaced with selection medium containing puromycin at a concentration predetermined in section 3.2.3. Stably transfected cells selected by the antibiotic were expanded for cryopreservation (3.2.1) and gene expression analysis (3.5, 3.6).

3.2.5 Single cell cloning

To obtain monoclonal cell cultures stably expressing the gene of interest following transduction with lentiviral particles (3.2.4), cells underwent antibiotic selection and a monoclonal cell isolation. Specifically, cells were plated sparsely (ca. 10% confluency) onto 15 cm dishes to allow for the formation of colonies from single cells. Plates were then incubated until visible colonies formed; these colonies were then inspected using an inverted microscope. Only well-defined, single colonies were selected and picked using a sterile pipette tip and transferred into a well of a 96-well plate. The growth of cells in each well was monitored regularly, and once the cells in a well reached confluency, they were passaged into larger culture vessels to maintain exponential growth as described above (3.2.1). Positive clones – determined by a fluorescent signal - were then further expanded. Monoclonal cell lines were cryopreserved at early passages and stored in liquid nitrogen for long-term storage.

3.3 3D cell culture methods

3.3.1 Formation of cell spheroids

Cell spheroids were produced using agarose molds with microwells, which served as templates for embedding the cells. To prepare the agarose molds, a 0.5% agarose solution in PBS was prepared and maintained at a constant temperature of 60°C on a hot plate with continuous stirring. Using a pipette, 500 µl of this solution was dispensed into silicone micro-molds (9x9, size L, Merck). After allowing the agarose to solidify for 2 minutes at room temperature, the molds were transferred to a 12-well plate and filled with warm medium to preserve their structure over time. These agarose molds could then be stored for several weeks in medium at 37°C in an incubator. To create the cell spheroids, cells were collected and the cell count for each condition was determined (3.2.1). Cell suspensions were centrifuged for 5 minutes at 133xg. Meanwhile, the agarose molds were transferred to new 12-well plates without medium. The cell pellets were resuspended in the appropriate volume of growth medium to obtain 750,000 cells in 190 µl per agarose mold. Cell suspensions were added to the agar molds and the plates were left under a sterile hood for 12 minutes to allow the cells to settle into the individual microwells of the agarose molds. Subsequently, the wells were carefully filled with growth medium and incubated for 72 hours. After incubation, the spheroids were examined and photographed under a microscope. Spheroid size and shape were evaluated using Fiji software on six randomly photographed spheroids per condition across three biological replicates. The surface area in pixels squared (px^2) and the roundness of the shape were analyzed.

3.3.2 Spheroid outgrowth

The spheroid outgrowth assay models the spread of 3D spheroids on a surface, mimicking the early stages of metastatic dissemination [155]. Spheroids produced as described in 3.3.1 were individually transferred to a 24-well plate with growth medium using a pipette. The plates were incubated for 2 hours to allow the spheroids to adhere to the well surfaces. Microscopic images (10x objective) of the spheroids were then taken, marking this as time point 0 hours (t=0h) for the experiment. The spheroids were then allowed to grow for 24 hours, after which they were photographed again (t=24h). The area of outgrowth at 24 hours and the initial size of the spheroids at 0 hours were quantified using Fiji. The ratio of these two areas was calculated, and the results were normalized to the control. At least two biological replicates with no less than six spheroids were performed for each experiment.

3.4 *In vitro* assays

3.4.1 Migration Assays

3.4.1.1 Wound closure assay

To investigate changes in cell motility, the wound closure assay was performed. Following transient gene silencing as described in section 3.2.2, the cell monolayer was scratched with a 10 µl pipette tip on each side of the outer third of the well to create a wound. This initial scratch was considered as time point 0 hours (t=0h). Cells were carefully rinsed once with 1x PBS to remove detached cells and then fresh full growth media was added to the wells. For each condition, four spots per well were marked and photographed using the Keyence BZX800 microscope, with the stage settings saved to ensure consistent photo positioning. The same spots were photographed every 24 hours (t=24h) until the scratch in the control condition (siNEG) was nearly closed. The area of the gap at each time point was analyzed using the "wound healing tool" for Fiji software. This area was then calculated as the percentage of the initial area of the scratch (t=0h). The average percentage from the four spots photographed was compared to control, which was considered to have a 100% gap closure. The average percentage was calculated from at least three biological replicates.

3.4.1.2 Transwell migration assay

Directed cell migration was analyzed using the transwell migration test, which involves cells migrating through a fine-pored membrane to a chemoattractant, in this case 10% FCS. The cells were collected after gene silencing or overexpression (3.2.2; 3.2.4), counted, and resuspended in serum-free medium. For each condition, one cell culture transwell insert (CellQArt, pore size 8 µm) was used, and 200,000 cells in a volume of 500 µl were added to the insert. After 20 minutes of incubation at 37°C, 600 µl of FCS-containing medium was added to the lower wells with the inserts. Additionally, for each condition, a control well in a 24-well plate was prepared, where 500 µl of the cell suspensions were added to wells with FCS-containing medium. This separate well was used to determine the cell number at the end of the experiment, to account for any effect of gene silencing or overexpression on cell proliferation. Cells were allowed to migrate through the membrane for 24 hours. On the next day, medium was removed from the inserts, and the remaining cells were wiped off the inner membrane with a cotton swab moistened with 1x PBS. The migrated cells on the outer membrane were stained for 20 minutes in a 0.05% (w/v) crystal violet methanol/water solution (1:4 v/v). The inserts were left to dry and photographed at four spots using the Keyence BZX800 microscope. The area of the membrane covered with the stained cells was quantified with Fiji and normalized to the cell number in the control wells to calculate the migration index for at least three independent replicates.

3.4.2 Viability assay

The Cell-Titer Blue (CTB) assay is a widely used method for measuring cell viability by assessing the ability of cells to convert the non-fluorescent chemical compound resazurin into the fluorescent dye resorufin. The fluorescence intensity of resorufin is therefore directly proportional to the number of viable cells present in the sample. To evaluate cell viability after various treatments, cells were seeded into a 96-well plate and allowed to attach for 24 hours. A mixture of CTB reagent (Promega) and full growth medium was then added to the cells, and the plate was returned to the incubator. The cells were monitored periodically until the CTB-medium mixture changed color from blue to purple, indicating the conversion of resazurin to resorufin. Once this color change occurred, 100 µl of the CTB-medium mixture was transferred to a black 96-well plate (Thermo Fisher Scientific), and the fluorescence was measured at Excitation/Emission wavelengths of 540/590 nm using a fluorescence plate reader (SpectraFluor Plus, TECAN). The initial blue-colored CTB-medium mixture (where no cells were present) was used as a reference for normalizing the results.

3.4.3 Colony formation assay

As a general measure of cancer cell behavior, the colony formation assay was used to investigate the altered clonogenic ability following changes in gene expression (3.2.2; 3.2.4). Cells were pretreated and harvested, and 200 cells were resuspended in 3 ml growth medium per well of a 6-well plate. Each condition was plated in triplicate, and the cells were distributed evenly in the well by gentle shaking. The cells were then left in the incubator for 14 days, allowing for colony formation. After this period, the colonies were washed once with 1x PBS to remove any loose cells, and then fixed and stained for 20 minutes in a 0.05% (w/v) crystal violet methanol/water solution (1:4 v/v). Pictures of each well were taken with a digital camera, and the number of colonies was determined using the “Colony Blob Count Tool” plugin for Fiji software.

3.4.4 Mitochondria Stress Kit

To investigate changes in mitochondrial functions, the mitochondria stress test was performed using the Seahorse XF24 Analyzer. Following transient gene silencing or overexpression, OVCAR8 cells were replated into cell culture microplates at a density of 200,000 cells per well in full growth medium and incubated overnight in a 5% CO_2 humidified incubator to allow attachment. The day before the assay, the sensor cartridge was hydrated overnight in Seahorse XF Calibrant buffer at 37°C in a non-CO_2 incubator, as recommended by the manufacturer. On the day of the assay, the growth medium was removed from the cells, and after washing steps, 500 µL of pre-warmed Seahorse XF RPMI medium supplemented with 10 mM glucose, 1 mM sodium pyruvate, and 2 mM glutamine was added to each well. The plate was incubated at 37°C in a non-CO_2 incubator for 1 hour before performing the assay to allow cells to equilibrate and ensure a constant metabolic state before performing the assay. The inhibitors from the Mitochondrial stress kit were prepared and loaded into the ports of the sensor cartridge as recommended by the manufacturer. The assay included oligomycin (1.5 µM final concentration) to inhibit ATP synthase and measure ATP production-related respiration; FCCP (0.5 µM final concentration) to uncouple oxidative phosphorylation and assess maximal respiration capacity and Rotenone/Antimycin A (0.5 µM final concentration) to inhibit mitochondrial complex I and III, respectively, and measure non-mitochondrial respiration. Additionally, Hoechst dye was added to the cells and used to normalize the results to the cell number, allowing for accurate comparison of the data. Three biological replicates, with at least three technical replicates, were performed to ensure the reliability and reproducibility of the results.

3.5 Gene expression analysis

3.5.1 RNA isolation

RNA isolation from cell lines was performed using the RNeasy kit according to the manufacturer's instructions. Briefly, 600 µl of RLT lysis buffer were added to each well of a 6-well plate, and cells were scraped and collected in 2 ml tubes. The cell lysates were then vortexed and either stored at -80°C or processed immediately. For RNA precipitation, the thawed lysates were treated with one volume of 70% ethanol, mixed carefully, and transferred to mini-spin columns. Following the provided protocol, DNase treatment was performed using the RNase-Free DNase set (Qiagen) to remove any residual DNA. Total RNA was then eluted in 30 µl of RNase-free water. The concentration of RNA was determined using a spectrophotometer (NanoDrop One), and the samples were stored at -80°C until further use.

3.5.2 Synthesis of complementary DNA

For gene expression analysis, isolated RNA samples (Section 3.5.1) were reverse transcribed into complementary DNA (cDNA) using the High Capacity cDNA Reverse Transcription Kit according to the manufacturer's instructions. Volumes containing 2 µg RNA samples were diluted in DEPC-treated water and mixed with a master mix containing 10x RT-Buffer, random primers, dNTP mix, and reverse transcriptase. The reaction mixture was adjusted to a total volume of 20 µl and subjected to the specified PCR program (Table 12). Following reverse transcription, the resulting cDNA products were diluted with RNase-free water to a final concentration of 10 ng/µl and stored at -20°C for future use in gene expression analysis.

Table 12: Program for the reverse transcription polymerase chain reaction.

Step	Temperature	Time
Primer annealing	25 °C	10 min
Reverse transcription	37 °C	120 min
Inactivation	85 °C	5 min
Storage	4	∞

3.5.3 Quantitative real-time Polymerase Chain Reaction

Quantitative real-time PCR (qPCR) was used to quantify target gene expression by detecting the fluorescence emitted by a dye that intercalates into double-stranded DNA during its synthesis. In this work, the QuantiNova SYBR Green PCR Kit was employed. Generated cDNA samples (Section 3.5.2) were combined with the Master Mix, which consisted of the specific primer mix (Table 8), SYBR Green reagent, ROX dye, and water, in a 96-well plate. The reaction was performed on an ABI 7500 Fast RT-PCR machine, using the cycling conditions outlined in Table 13. Melting curve analysis was conducted for each run to assess the specificity of the amplified product. Data evaluation utilized the $\Delta\Delta C_T$ method [156], which involved subtracting the cycle threshold (C_T) values of housekeeping genes from those of the target genes. Normalization of the data was achieved by subtracting the calculated ΔC_T values from the control condition. Fold change expression was determined using $2^{-\Delta\Delta C_T}$ values.

Table 13: Program for the quantitative real-time PCR.

Step	Temperature	Time	Cycles
Initiation	50 °C	2 min	1
Activation of DNA polymerase	95 °C	5 min	1
DNA denaturation	94 °C	10 sec	40
Annealing & elongation	60 °C	30 sec	

3.6 Protein expression analysis

3.6.1 Protein extraction and quantification

Total cell lysates were extracted using the radioimmunoprecipitation assay (RIPA) buffer. For each well of a 6-well plate, 200 µl of RIPA buffer, freshly supplemented with 1% (v/v) protease and phosphatase inhibitor cocktails, were used. Cells were incubated on ice for 1 min, collected with a cell scraper in pre-cooled reaction tubes, and then shock-frozen in liquid nitrogen. After thawing on ice, the lysates were vortexed 5 times for 30 seconds with 5-minute pauses on ice to ensure thorough mixing. The lysates were then centrifuged at 4°C and 13,000 x g for 30 min. The resulting supernatant, containing the protein fractions, was collected and stored at -80°C in a new 1.5 ml tube. The protein concentration was determined using the Bicinchoninic Acid (BCA) Protein Assay Kit with a bovine serum albumin calibration standard curve (0 µg/ml - 2 µg/ml) according to the manufacturer's protocol. To determine the protein concentration, 5 µl of the extracted cell lysate was diluted with 20 µl of ddH_2O in a 96-well plate. Then, 200 µl of BCA master mix was added to each well, and the plate was incubated for 20 minutes at 37°C. The absorption at 562 nm was measured using a spectrophotometer. The protein concentrations of the unknown samples were calculated based on the standard curve.

3.6.2 Sodium dodecyl sulfate polyacrylamide gel electrophoresis

According to the concentration determined in Section 3.6.1, equal amounts of approximately 20 µg total protein for each sample were diluted with ddH2O to a final volume of 15 µl. For denaturation, 5 µl of the sodium dodecyl sulfate (SDS) containing 4x Laemmli sample buffer, which had been spiked with 10% (v/v) β-mercaptoethanol prior to use, were added to each sample. The protein samples were then incubated at 95°C for 5 minutes. SDS polyacrylamide gels (10-12.5%) were prepared beforehand using a gel casting apparatus according to the protocol outlined in Table 4. Denaturated protein samples were loaded into the lanes of the gel along with a protein molecular weight marker (Precision Plus Protein Dual Color Standard, Bio-Rad) for reference. Electrophoresis was conducted with the 1x running buffer (Bio-Rad) at a constant voltage of 30 mA per gel until the dye front from the sample buffer reached the bottom of the gel.

3.6.3 Semi-dry protein transfer

Protein transfer from SDS polyacrylamide gels (Section 3.6.2) to polyvinylidene fluoride (PVDF) membranes was conducted using a semi-dry transfer apparatus (Bio-Rad). Three thick sheets of absorbent paper (13.5 x 8.6 cm, Bio-Rad) were pre-treated in the anode buffer (Table 4) and arranged in a chamber. A PVDF membrane, activated in methanol and equilibrated in the anode buffer, was placed atop these papers. The SDS-gel with separated protein samples, equilibrated in the cathode buffer (Table 4), was then placed on the membrane. Another sheet of absorbent paper soaked in cathode buffer was added, and the blotting chamber was sealed. Protein transfer occurred at a set current (0.23 mA per blot sandwich) for 40 minutes. Following transfer, the PVDF membrane was incubated in Tris-buffered saline containing 0.1% Tween-20 (TBS-T) and stored in this solution at 4°C. Alternatively, the membrane could be proceeded further with western blot analysis.

3.6.4 Western blot analysis

To identify the protein of interest, a western blot analysis was conducted using indirect immunodetection of the target antigen immobilized on a PVDF membrane (Section 3.6.3). Membranes were immersed in a 5% bovine serum albumin (BSA) or 5% milk solution in Tris-buffered saline with 0.1% Tween-20 (TBS-T) to block non-specific binding sites for 2 hours at room temperature on an orbital shaker. Subsequently, membranes were transferred to a solution (5% milk/TBS-T or 5% BSA/TBS-T) containing the primary antibody (Table 9), where they were left overnight at 4°C with constant shaking. The following day, membranes were washed three times, 10 minutes each, in TBS-T before being incubated in a solution containing the secondary horseradish peroxidase (HRP) conjugated antibody. After another round of washing, membranes were treated with a chemiluminescent reagent mixture and imaged using an imaging system. For subsequent detection of additional proteins on the same membrane, the membranes were either cut according to the molecular weight of the proteins to be detected or antibodies were removed from the blots by washing in a stripping buffer (Roth) followed by washing and re-blocking before re-probing. For the subsequent analysis of the western blot, band intensities were quantified using Fiji by densitometric analysis, and molecular weights were estimated based on the migration of protein standards. Data obtained were normalized to the expression levels of the loading control (Calnexin, β-actin, or GAPDH) and analyzed to compare protein expression levels between samples or conditions.

3.7 Targeted lipidomics analysis

To investigate basal intracellular metabolite levels in the cell lines, as well as how the downregulation or overexpression of the different genes of interest affects lipid levels, targeted analysis was performed using liquid chromatography mass spectrometry (LC-MS/MS) in the Bioanalytics department at IfADo. For this purpose, cells seeded in 6-well plates 72 hours prior to collection were washed three times with ice-cold 1x PBS, shock-frozen on a thin layer of liquid nitrogen, and collected from the well surface with a cell scraper in 120 µl of 100% methanol containing a mixture of internal standard of defined concentrations. The extracts were collected in 1.5 ml tubes and stored at -80 °C until further processing. The subsequent two-phase extraction was performed according to the SIMPLEX protocol (Simultaneous Metabolite, Protein, Lipid Extraction) [157]. Briefly, cold methyl-tert-butyl-ester (MTBE) was added to the samples, which were then incubated at 4 °C for 1 h under agitation. Phase separation was induced by the addition of aqueous 0.1% ammonium formiate, and samples were centrifuged at 10,000 x g for 5 min. The upper phase (MTBE fraction), which contains most of the lipids, was collected, dried under nitrogen flow, and stored until reconstitution at -20 °C. The lower phase was mixed with 220 µl methanol and incubated for 2 h at -20 °C to achieve complete protein precipitation, followed by centrifugation at 21,000 x g for 5 min. The supernatant (methanol fraction), which contains the lysophospholipids, including LPA, was transferred into a new tube and evaporated to dryness. The MTBE fraction was solubilized in 40 µl 80% acetonitrile/20% methanol with 1 mM phosphoric acid, while the methanol fraction was reconstituted using 40 µl methanol. Both fractions were measured in both positive and negative ion mode. The subsequent LS-MS/MS analysis was performed in the hydrophilic interaction liquid chromatography (HILIC) mode on a 125 x 3 mm PerfectSil Target 100 Si 3 µm column coupled to a QTRAP5500 mass spectrometer operating in the scheduled multiple reaction monitoring (MRM) mode. From each sample, 1 µl were injected, and samples were separated isocratically using 70% solvent A (acetonitrile) and 30% solvent B (50% methanol, 5 mM ammonium formiate, 0.1% formic acid) within 10 min. The settings used for lipid measurement are listed in Fig. S1. The signal intensity of the internal standard contained in the methanol in a known concentration was used to determine the relative concentration of the native metabolite species. The normalized intensity from each replicate was then normalized to the protein amount from the corresponding sample determined via the BCA assay (Section 3.6.1). Cell extracts were collected from at least four biological replicates.

3.8 Active Rho-GTPase Pulldown Assay

To assess the activity of Rho-GTPases under conditions of GPAM and AGK downregulation and constitutive AGK overexpression, the Rho-GTPase pulldown assay was employed. The Active Rho Pulldown and Detection Kit was performed according to the manufacturer’s protocol. Cell lysates were collected by scraping the cells previously plated onto 100 mm dishes with a provided lysis/washing buffer, to which protease inhibitor cocktail was added. After brief vortexing and incubation on ice for 5 min, samples were centrifuged at 16,000 x g at 4°C for 15 min. The supernatant was collected in a new 1.5 ml tube, and the BCA assay for protein quantification was performed (Section 3.6.1). Meanwhile, glutathione S-transferase (GST)-rhotekin Rho-binding domain (RBD) was immobilized onto glutathione agarose beads in columns. Equal amounts of at least 500 µg total protein were then added to the columns with the glutathione resin, and active GTP-bound Rho-GTPases that were present in cell lysates were able to bind RBD and therefore get immobilized. After thorough washing with the lysis/washing buffer, the GST-RBD affinity to the agarose beads was disrupted by adding denaturing SDS-PAGE sample loading buffer, which allowed the entire construct to be eluted from the column. The eluates were then subjected to Western blot analysis (Section 3.6.4) using the provided Anti-Rho antibody. As a loading control, 25 µg of total protein before affinity purification were loaded on the same gel and incubated simultaneously with the Anti-Rho antibody to detect the total levels of Rho GTPases present in the sample. As a positive control for the assay and to test the antibody specificity, one half of an untreated control sample was pre-treated with GTPγS, a stable analogue of GTP that is not sensitive to GTPase activity. As a negative control, the other half of the control sample was incubated with GDP so that the GTP is displaced from the active GTPase form, and therefore does not bind to the RBD domain.

3.9 Statistical data analysis

All cell culture experiments were carried out in at least three independent biological replicates. The visual analysis of the optical density and the calculation of the areas were carried out using the open-source software Fiji [158]. Real-time PCR data analysis was carried out in Excel 2013, while GraphPad Prism 9 was used for generating graphs and conducting statistical analyses. Statistical significance was determined using an unpaired Student's t-test, with significance levels denoted as follows: $p < 0.05$ ($*$), $p < 0.01$ ($**$), $p < 0.001$ ($***$) and $p < 0.0001$ ($****$).

4 Results

4.1 Selection of cell models from a panel of ovarian cancer (OC) cell lines

Due to its heterogeneity, identifying suitable cell culture models that accurately reflect the complexity of ovarian cancer is critical for phenotypic and mechanistic studies. Therefore, to investigate the role of GPAM and AGK in ovarian cancer cell migration and the possible association of this phenotype with intracellular LPA levels, two immortalized non-tumorigenic ovarian epithelial cell lines, HOSE6-3 and HOSE17-1, and ten ovarian cancer cell lines (Fig. 14), mostly derived from patient's ascites and characterized as HGSOC were screened. The screening focused on the expression of relevant genes, intracellular phospholipid levels by targeted LC-MS/MS, and the migratory and colony forming capacity of the different cell lines. All cell lines were maintained under standardized environmental conditions using the same media and growth serum to minimize any potential influence of varying sera or supplements on experimental outcome. Thus, as a first step, it was ensured that all cell lines were viable and maintained their 'normal' morphology in the standardized culture media (Fig. 14).

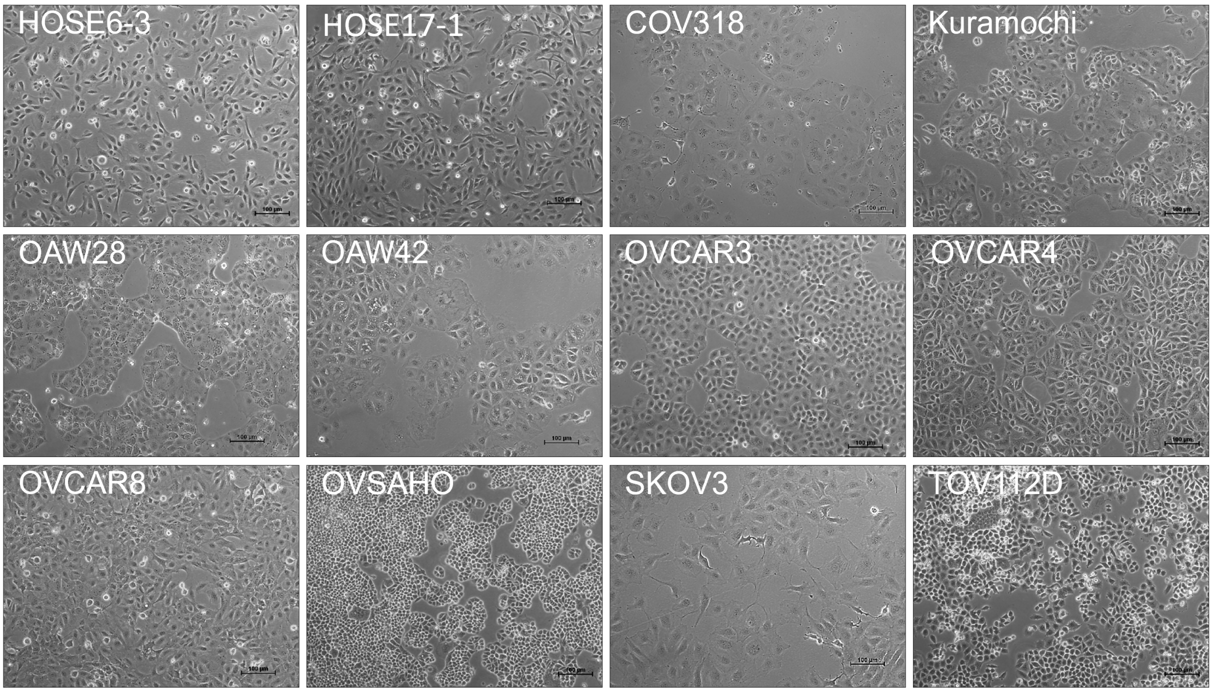

Figure 14: **Morphology of ovarian cancer cell lines.** Representative brightfield images of ovarian cancer cell lines COV318, Kuramochi, OAW28, OAW42, OVCAR3, OVCAR4, OVCAR8, OVSAHO, SKOV3 and TOV112D as well as of the immortalized normal ovarian epithelial cells, HOSE6-3 and HOSE17-1. Cells were cultured in RPMI medium supplemented with 10% fetal calf serum in a humidified incubator at 37°C and 5% CO_2. Cells were photographed with a 10x objective. Scale bar is 100 µm.

4.1.1 OC cell lines differ in basal GPAM and AGK expression

Basal expression of key enzymes involved in LPA metabolism was investigated with real time quantitative PCR to identify the most suitable cell lines to be used for gene silencing (where the gene of interest is expressed) or overexpression (where gene expression is low or undetectable) experiments. Therefore, the basal expression levels of both *GPAM* and *AGK* were investigated in the panel of ovarian cancer cell lines. Expression of both genes are presented as fold change normalized to the non-transformed ovarian epithelial cell line HOSE6-3 relative to the housekeeping gene, *ACTB* (Fig. 15). The two non-transformed cell lines, HOSE6-3 and HOSE17-1 expressed similar levels of both *GPAM* and *AGK*. COV318, OVCAR3 and OVSAHO cells expressed almost 3-fold higher *GPAM* expression compared to HOSE6-3 cells, while expression in OAW28, OAW42, OVCAR4, SKOV3 and TOV112D cells were 1.2-2 times higher (Fig. 15A). In contrast, Kuramochi and OVCAR8 cells expressed approximately 50% less *GPAM* than both non-transformed cell lines (Fig. 15A). Similar to *GPAM*, the highest *AGK* expression was observed in COV318 and OVSAHO cells (3-4 fold) compared to the non-transformed cells. Moreover, most of the other cells lines - except OVCAR8 and SKOV3 - had at least two times higher *AGK* expression compared to HOSE6-3 (Fig. 15B). Despite the variable expression of *GPAM* and *AGK* among the different cell lines, all expressed detectable levels of both genes.

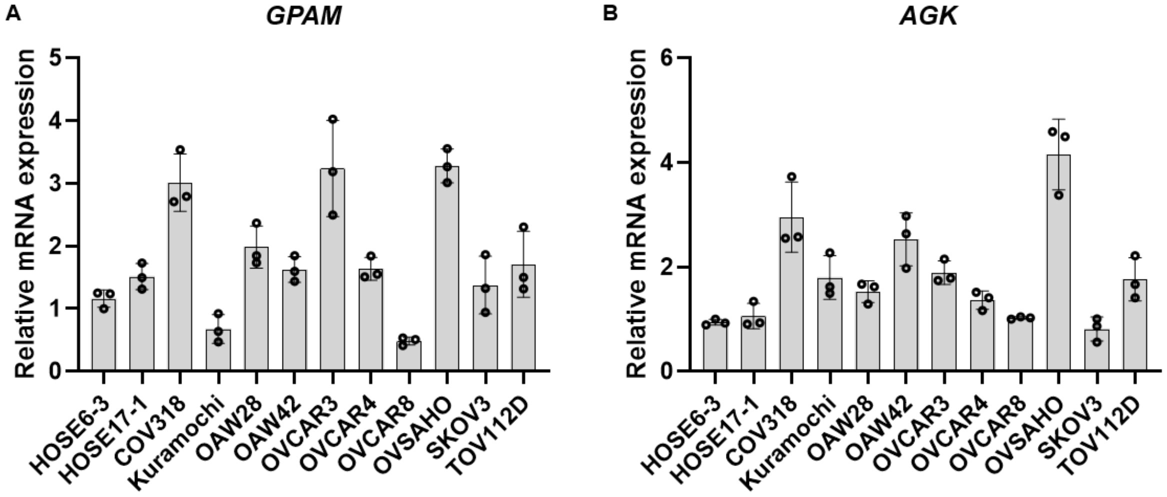

Figure 15: ***GPAM* and *AGK* expression in ovarian cancer cell lines.** **A** *GPAM* and **B** *AGK* expression was evaluated using quantitative PCR in ovarian cancer cell lines, including COV318, Kuramochi, OAW28, OAW42, OVCAR3, OVCAR4, OVCAR8, OVSAHO, SKOV3 and TOV112D cells. Expression levels were normalized to *ACTB* expression and are presented relative to HOSE6-3 cells. Data are presented as mean ± SD of three biological replicates.

4.1.2 OC cell lines differ in their basal intracellular phospholipid content

To characterize the intracellular lipid levels in the cell line panel, an extraction protocol for the simultaneous detection of metabolites, lipids, and proteins via targeted LC-MS/MS was established by IfADo's Bioanalytics central unit (Section 3.7). Using this targeted lipidomics assay, the relative levels of 90 intracellular lipid species were quantified against internal standards and normalized to protein content. These included various species of phospholipids — PA, PE, PS, PC, PI, and PG — as well as the respective lysophospholipids, LPA, LPE, LPS, LPC, LPI, and LPG, in addition to DAG. Selected species of the key signaling lipids LPA, PA, and DAG are presented in Figure 16. The other lipid species analyzed are shown in the Appendix (Fig. S2).

In total, five LPA species could be detected using the established method, namely 16:0, 18:0, 18:1, 18:2 and 20:4 LPA, with varying intracellular levels observed among the different cell lines (Fig. 16A-C, S2). Specifically, LPA levels varied between the two non-transformed cell lines with no LPA species detected in HOSE6-3 cells, while 16:0 and 18:1 LPA could be measured in HOSE17-1 (Fig. 16A,C). Furthermore, all cancer cell lines, except Kuramochi and OVCAR3, had detectable levels of 16:0 LPA; relatively low 16:0 LPA levels were found in COV318 and OVSAHO cells and the highest levels were observed in OVCAR4 and SKOV3 cells (Fig. 16A). In contrast, 18:0 LPA was detected in only half of the HGSOC cell lines, namely Kuramochi, OAW42, OVCAR4, OVCAR8, OVSAHO, and SKOV3 cells (Fig. 16B), while 18:1 LPA was detected in all cell lines, with the highest level observed in OVCAR4 (Fig. 16C). Interestingly, 18:2 and 20:4 LPA species were only detected in OVCAR4 cells (Fig. S2). In contrast, almost all intracellular PA species were detected in all cell lines (Fig. 16 and Fig. S2), except for 18:0-18:2 PA, which was not measurable in HOSE6-3 cells (Fig. 16D), and 36:0 PA in HOSE6-3 and HOSE17-1 cells (Fig. S2). Conversely, HOSE17-1 had twice as much 18:0-18:2 PA compared to the cancer cell lines (Fig. 16E). The DAG species 16:0-16:0 and 18:0-18:2 were highest in HOSE17-1 (Fig. 16G,H), while intracellular levels of the 18:1-18:1 DAG were the highest in OAW42, OVCAR8, and TOV112D cells and moderate in OAW28, OVCAR4, and SKOV3 cells (Fig. 16I). In summary, the levels of the different lipid species measured under the basal conditions were variable among the different cell lines, even between the two non-transformed ovarian epithelial cell lines. Such information is important when selecting the most appropriate cell models to investigate the effect of targeting enzymes that regulate intracellular glycerophospholipid metabolism and how these changes could be linked to cell behavior.

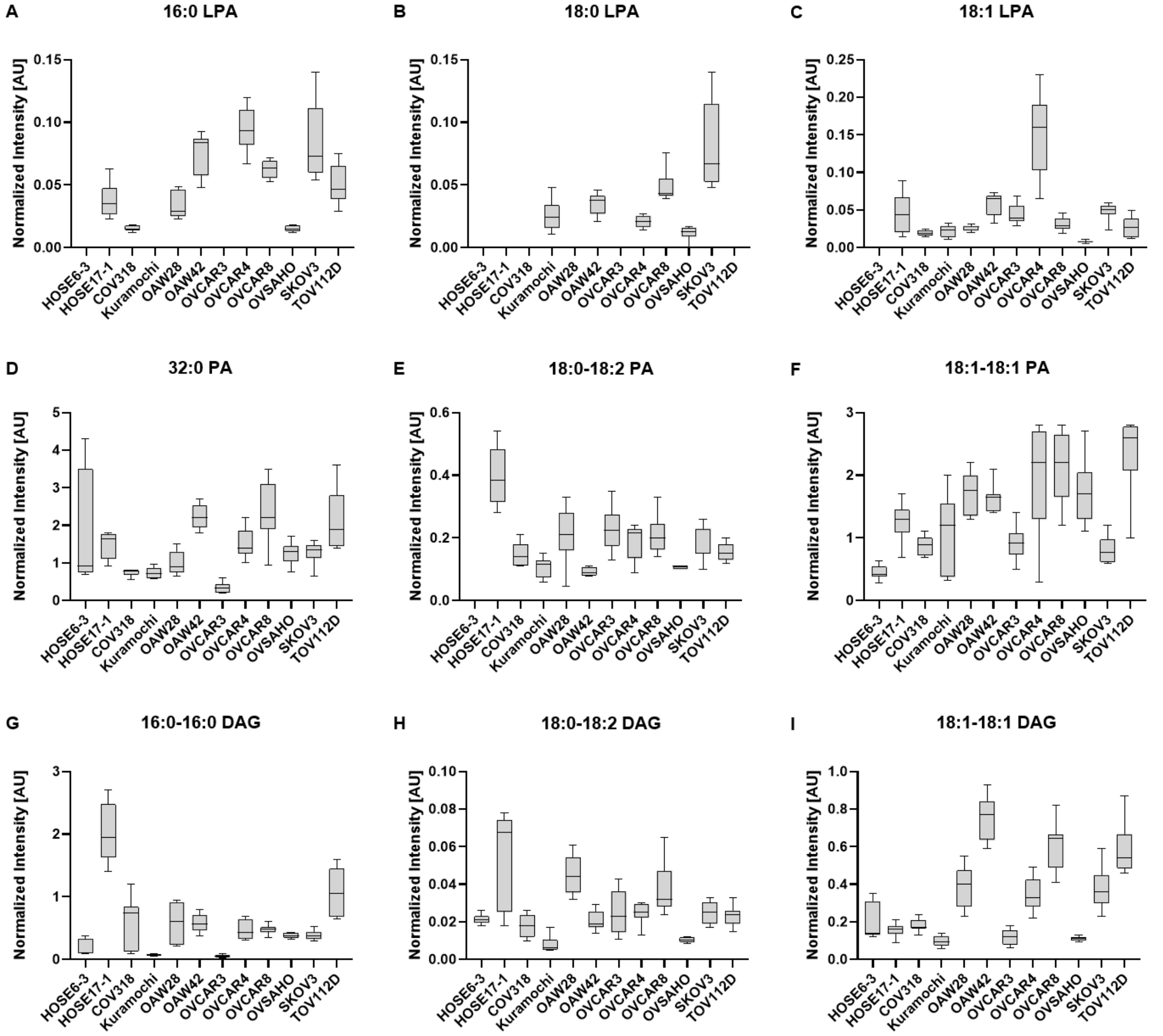

Figure 16: **Intracellular levels of LPA, PA and DAG in ovarian cancer cell lines.** Intracellular levels of selected lipid species, including **A** 16:0, **B** 18:0, **C** 18:1 lysophosphatidic acid (LPA), **D** 32:0, **E** 18:0-18:2, **F** 18:1-18:1 phosphatidic acid (PA), and **G** 16:0-16:0, **H** 18:0-18:2, **I** 18:1-18:1 diacylglycerol (DAG), were quantified in the immortalized ovarian epithelial cell lines HOSE6-3 and HOSE17-1, and the ovarian cancer cell lines COV318, Kuramochi, OAW28, OAW42, OVCAR3, OVCAR4, OVCAR8, OVSAHO, SKOV3, TOV112D. The analysis was performed after the simultaneous metabolite, protein and lipid extraction (SIMPLEX) protocol followed by LC-MS/MS. The area under the curve for the detected peaks was calculated in relation to the corresponding internal standard that was spiked into the sample, and the results were normalized to the protein content. Data are presented as mean ± SD of three biological replicates with three technical replicates each.

4.1.3 OC cell lines differ in their ability to migrate and form colonies

The ovarian cancer cell line panel was also characterized with respect to their migratory capacity and colony forming potential. Migration was evaluated using the wound healing assay and the transwell migration assay, that measures collective migration and chemotaxis, respectively. In the wound healing assay, wound area was measured after 12 hours and 24 hours and was then normalized to the initial scratch size at time 0. The results demonstrated notable differences among the cell lines, with some cell lines closing the scratch more rapidly (within 24h), while others migrated slower as shown in the representative microscopic images (Fig. 17A). More specifically, HOSE17-1 and OAW42 were the fastest migrating cells, closing approximately 70% of the wound after 12 hours and 100% after 24 hours (Fig. 17B,C). In contrast, Kuramochi and OVSAHO were the slowest migrating cell lines with less than 20% closed after 12 hours (Fig. 17B). After 24h, 50% of the wound was closed in the Kuramochi cells, whereas, no change was observed in the OVSAHO cells in which the wound remained 80% open (Fig. 17B). All other cell lines closed approximately 50% of the wound after 12 hours, and except for COV318 and OVCAR4, were fully closed after 24 hours (Fig. 17B,C). The wound healing assay could not be performed in the OAW28 and OVCAR3 cell lines as the cells detached from the surface of the well when the scratch was made.

Similiar to the results obtained with the scratch assay, the transwell assay revealed distinct differences among the cell lines after 24 hours with regard to their ability to migrate through a porous membrane towards FCS as a chemoattractant (Fig. 18A). Importantly, both OAW28 and OVCAR3 cell lines were able to migrate through the membrane and could thus be included in the cell panel for this migration assay. The fastest migration rates were observed for HOSE6-3, HOSE17-1, COV318, Kuramochi, OAW42 and SKOV3 and the slowest for OVSAHO, OAW28 and OVCAR3 cells (Fig. 18B). Interestingly, despite the different aspects of migration evaluated in both assays – collective migration versus chemotaxis - the migratory capacity of the different cell lines were mostly comparable. Major differences were observed in the Kuramochi cells, which were among the slowest in the wound healing assay, but the fastest in the transwell migration assay (Fig. 18B). In contrast, OVCAR8 and TOV112D cells were among the fastest migrating cells in the wound healing assay and slowest in the transwell assay (Fig. 18B).

Colony formation assays provide insight into the proliferative and survival capabilities of cells that are initially seeded as a single cell. In this work, clear differences were observed in the number of colonies formed across the panel of cell lines examined (Fig. 19A). On average, HOSE6-3, HOSE17-1, COV318, Kuramochi, OVCAR3, and OVSAHO formed approximately 50 colonies each. In contrast, OAW28, SKOV3, and TOV112D produced more colonies, which were also larger in size, as determined by visual inspection (Fig. 19A,B). Notably, the highest number of colonies was observed in OAW42, OVCAR4, and OVCAR8 cells (Fig. 19B). These findings highlight the variability in the proliferative capacity and anchorage-independent growth among the different cell lines, suggesting that some exhibit enhanced survival or adaptability under the given conditions.

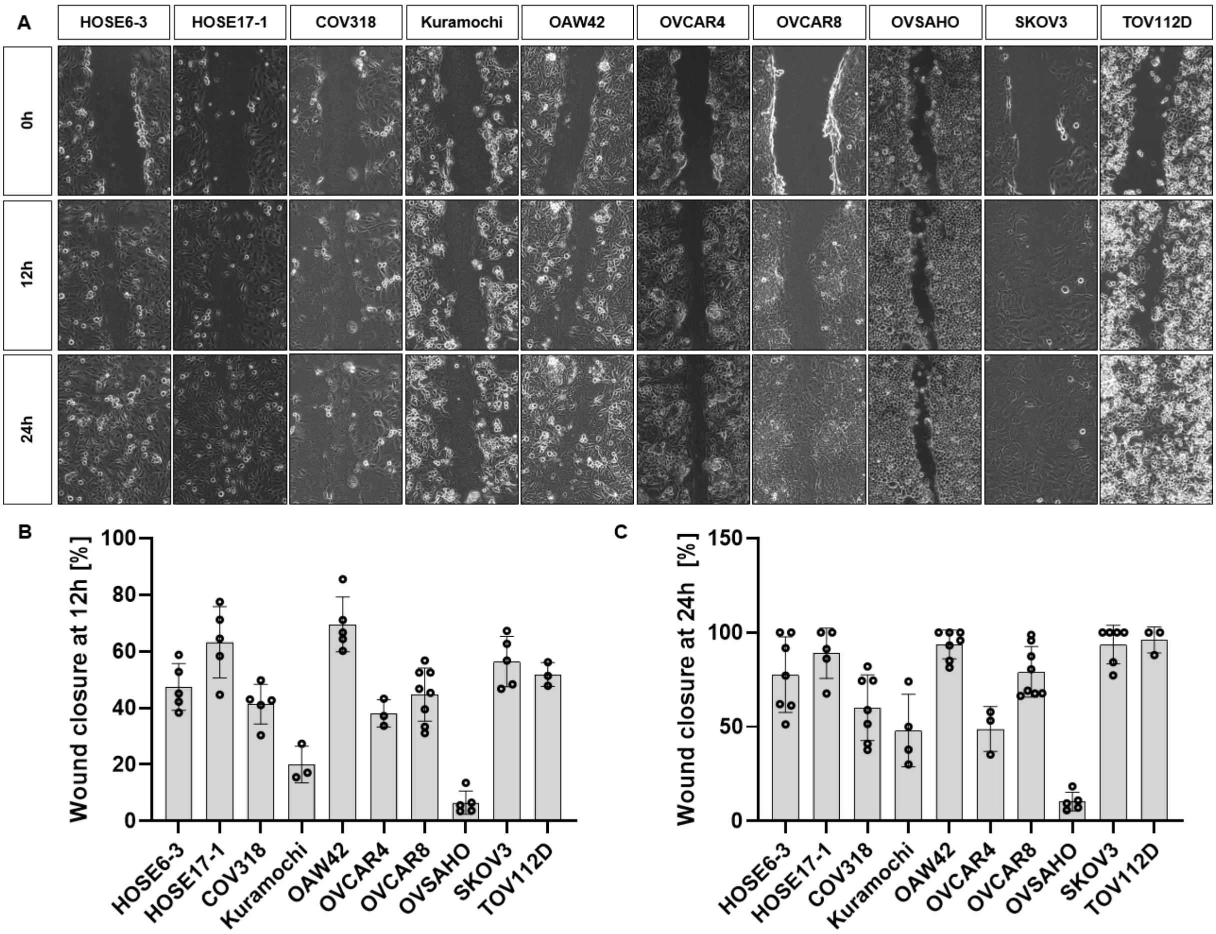

Figure 17: **Migratory ability of ovarian cancer cell lines analyzed by the scratch assay. A** Representative images of wound closure assay in the cell line panel at 0 h, 12 h, and 24 h post-scratch are presented for COV318, Kuramochi, OAW42, OVCAR4, OVCAR8, OVSAHO, SKOV3 and TOV112D. The cell lines OAW28 and OVCAR3 could not be used for the scratch assay, since the cell monolayer detached from the plates after the scratch. **B,C** The ability of the cells to migrate and close the wound was evaluated, showing differences in migration rates across the cell lines. Quantification of wound closure is presented as the percentage of the initial scratch area at each time point. Data are presented as individual data points from at least three biological replicates.

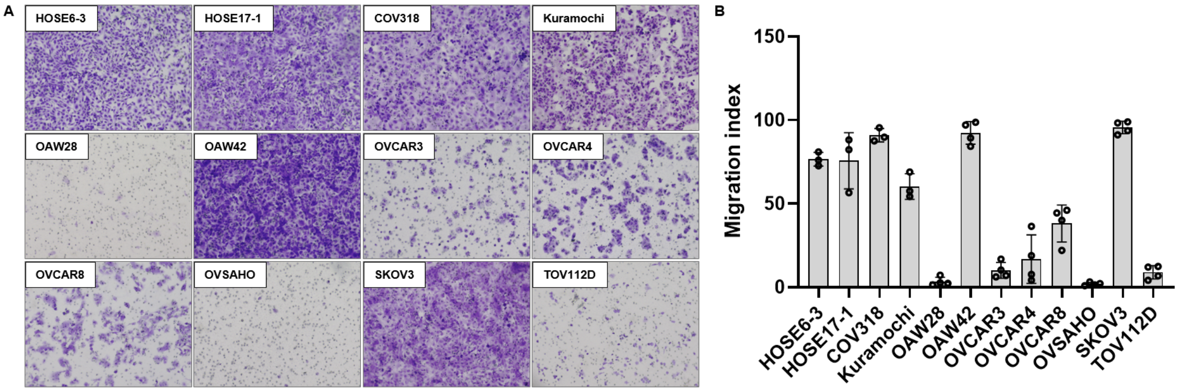

Figure 18: **Migratory ability of ovarian cancer cell lines analyzed by the transwell migration assay.** **A** Representative images of cells that migrated to the underside of the tranwell for HOSE6-3, HOSE17-1, COV318, Kuramochi, OAW28, OAW42, OVCAR3, OVCAR4, OVCAR8, OVSAHO, SKOV3 and TOV112D after 24 h. **B** The number of cells that migrated through the transwell membrane was quantified and normalized to cell number as determined from control wells and presented as migration index. Data are presented as mean ± SD of at least three biological replicates with three technical replicates each.

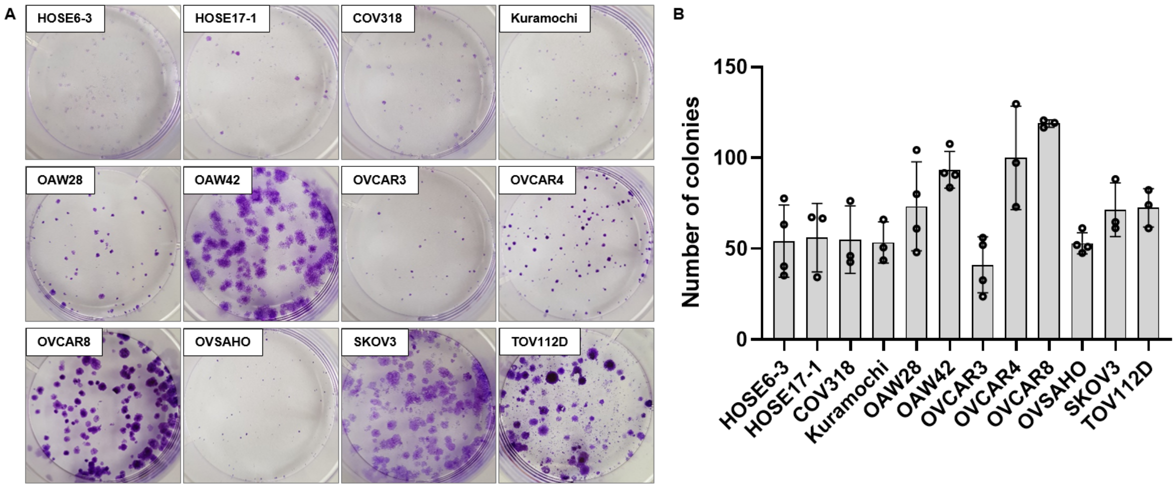

Figure 19: **Colony forming ability of ovarian cancer cell lines.** Colony forming ability of ovarian cancer cell lines was investigated. **A** Representative images of colonies formed by HOSE6-3, HOSE17-1, COV318, Kuramochi, OAW28, OAW42, OVCAR3, OVCAR4, OVCAR8, OVSAHO, SKOV3 and TOV112D cells two weeks post plating. Colonies were stained with crystal violet, wells photographed with a digital camera and **B** the number of colonies was quantified. Data are presented as mean ± SD of three biological replicates with three technical replicates each.

4.2 Silencing GPAM and AGK attenuates OC cell migration

4.2.1 Establishing GPAM and AGK knockdowns in selected OC cell lines

To explore the roles of GPAM and AGK in ovarian cancer, the expression of both genes was downregulated using siRNA in five selected ovarian cancer cell lines: Kuramochi, COV318, OAW28, OVCAR4, and OVCAR8. These cell lines were chosen based on gene expression levels, intracellular phospholipid content, migratory capacity, and colony-forming ability as measured in section 4.1. All selected cell lines are classified as HGSOC cells and exhibit varying expression levels of GPAM and AGK, along with detectable levels of key intracellular phospholipids, particularly PA and LPA. Additionally, these cell lines were found to be suitable for migration assays and demonstrated the ability to form colonies effectively.

GPAM knockdown in the selected cell lines was established using two distinct siRNA sequences for each gene from a subset of commercially available siRNA sequences, labeled in the present work as siGPAM #1-#4. The selection of oligonucleotides for the respective cell lines was based on their ability to induce effective knockdown (at least 70% at RNA level, and 50% at protein level) while maintaining cell viability, which was assessed through visual inspection. RNA was extracted 72 hours post-transfection of cells with siRNA, and the mRNA expression levels of the target gene were quantified using quantitative real time PCR. Expression was normalized to the housekeeping gene *ACTB* and the fold change to the corresponding non-treated control cells was calculated. In all five cell lines tested, *GPAM* RNA expression was successfully downregulated compared to control cells treated with scrambled non-targeting siRNA (siNEG) (Fig. 20A-E). The knockdown achieved with siGPAM #1 and #3 was at least 70%, while siGPAM #2 and #4 resulted in an 80% reduction in expression, with the most significant knockdown observed in OVCAR4 and OVCAR8 cells (Fig. 20D,E).

To confirm that the decrease in mRNA levels led to a reduction in protein levels, western blot analysis using an antibody specifically targeting GPAM was performed, and to ensure equal protein loading, β-Actin expression was analyzed on the same blots (Fig. 20F-J). The results demonstrated that despite variability in knockdown efficiency among the different siRNA oligos, for all cell lines except OAW28, silencing GPAM with siRNA led to a significant decrease in protein levels compared to the siNEG control, as quantified after normalization to β-actin (Fig. 20K-O). Overall, the siRNA-mediated knockdown of GPAM was successful at both the RNA and protein levels across all selected ovarian cancer cell lines, allowing for the study of GPAM on ovarian cancer cell behavior in subsequent experiments.

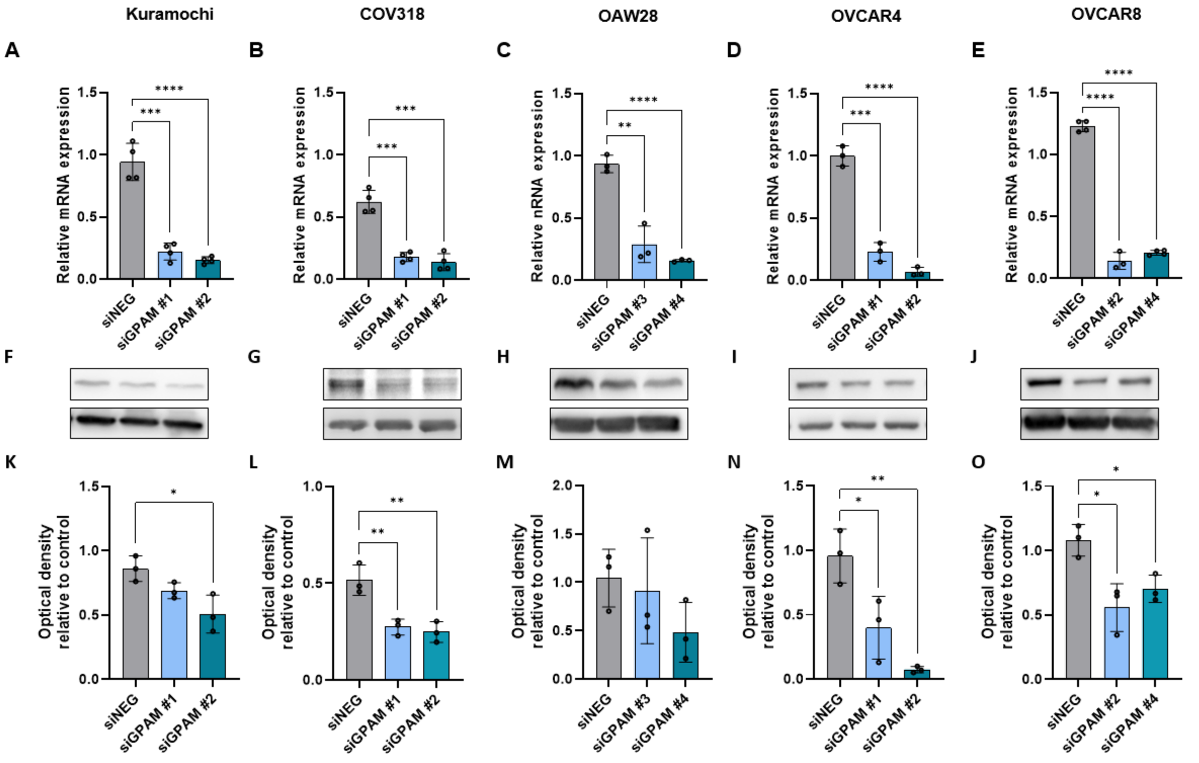

Figure 20: **GPAM expression is decreased in ovarian cancer cells after transfection with siRNA.** GPAM expression was downregulated using two small interfering RNA sequences in five ovarian cancer cell lines. Cells transfected with a scrambled siRNA sequence (siNEG) were used as control cells. Relative mRNA levels of *GPAM* in **A** Kuramochi, **B** COV318, **C** OAW28, **D** OVCAR4 and **E** OVCAR8 cells were investigated using quantitative Real-Time PCR analysis. The relative mRNA expression of *GPAM* was calculated according the $\Delta\Delta C_T$-method, with the C_T-values for *ACTB* as the housekeeping gene and ΔC_T-values of the siNEG as the internal control. The effect of the knockdown on the protein expression of GPAM was determined by western blot analysis. Representative images of the GPAM and β-actin blots with accompanying analysis of GPAM optical density normalized to β-actin are shown for **F,K** Kuramochi, **G,L** COV318, **H,M** OAW28, **I,N** OVCAR4 and **J,O** OVCAR8 cells. Data are mean ±SD from at least three independent biological replicates (* $P < 0.05$; ** $P < 0.01$; *** $P < 0.001$; **** $P < 0.0001$).

Next, AGK was targeted in the same five ovarian cancer cell lines using the siRNA sequences siAGK #1 and #2. The results showed that AGK could be successfully downregulated at RNA level in all cell lines, achieving nearly 80% reduction compared to the siNEG controls, except for OAW28, where the decrease was approximately 60% (see Fig. 21A-E). To assess protein levels, western blot analysis was performed using an antibody specifically targeting AGK, with Calnexin serving as the loading control (Fig. 21F-J). Analysis of the optical band intensities revealed a significant reduction in protein expression of approximately 50% across all transfected cell lines (Fig. 21K-O), with the exception of OVCAR8 cells, in which the knockdwon efficiency was over 90% (Fig. 21O). These findings confirm that AGK knockdown was effective at both the RNA and protein levels in the selected ovarian cancer cell lines providing a valuable tool for subsequent analyses of AGK's role in cancer cell behavior.

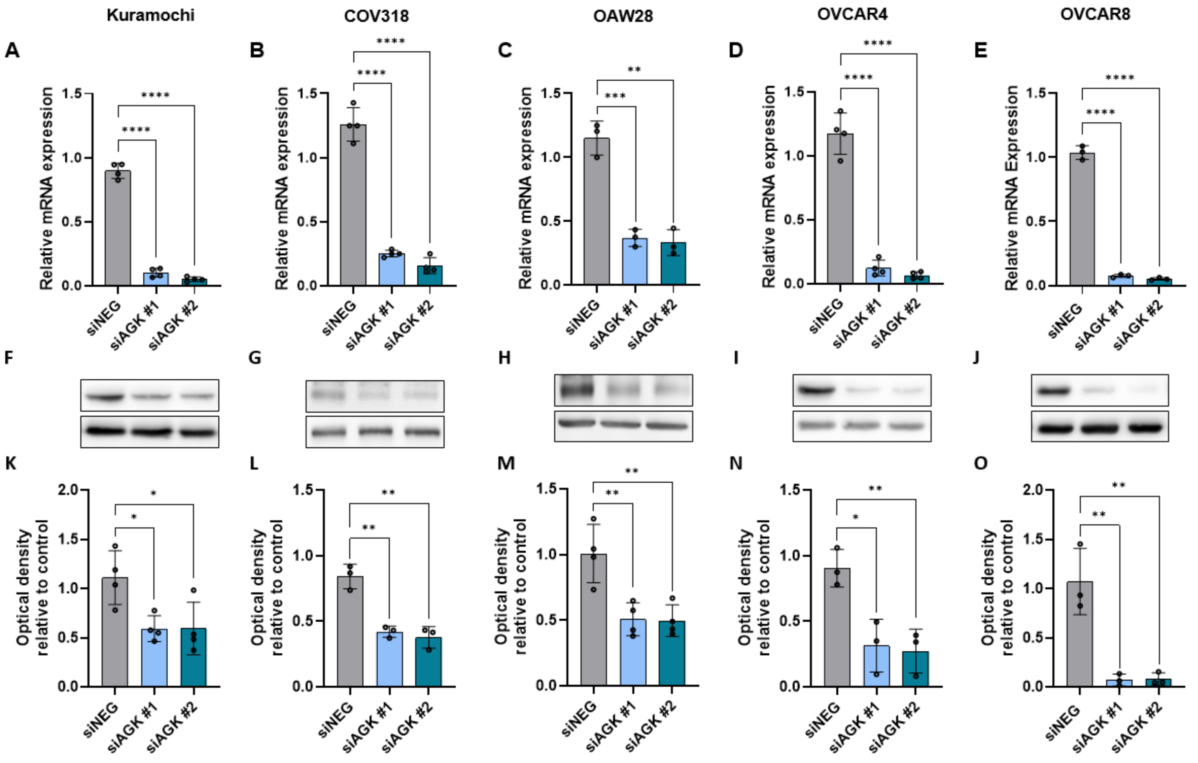

Figure 21: **AGK expression is decreased in ovarian cancer cells after transfection with siRNA.** AGK expression was downregulated using two small interfering RNA sequences (siAGK #1 and #2) in five ovarian cancer cell lines. Cells transfected with a scrambled siRNA sequence (siNEG) were used as control cells. Relative mRNA levels of *AGK* in **A** Kuramochi, **B** COV318, **C** OAW28, **D** OVCAR4 and **E** OVCAR8 cells were investigated using quantitative Real-Time PCR analysis. The relative mRNA expression of *AGK* was calculated according the $\Delta\Delta C_T$-method, with the C_T-values for *ACTB* as the housekeeping gene and ΔC_T-values of the siNEG as the internal control. The effect of the knockdown on the protein expression of AGK was determined by western blot analysis. Representative images of the AGK and β-actin blots with accompanying analysis of AGK optical density normalized to β-actin are shown for **F,K** Kuramochi, **G,L** COV318, **H,M** OAW28, **I,N** OVCAR4 and **J,O** OVCAR8 cells. Data are mean ±SD from at least three independent biological replicates (* $P < 0.05$; ** $P < 0.01$; *** $P < 0.001$; **** $P < 0.0001$).

4.2.2 GPAM and AGK knockdown decrease cell migration of OC cells

The impact of GPAM knockdown on cell migration was determined using the wound healing and transwell migration assays in the five selected HGSOC cell lines. Silencing GPAM in Kuramochi and COV318 cells led to a significant reduction in cell migration assessed by the wound healing assay. In Kuramochi cells, the scratch was 100% closed in the control cells after 72 hours, while the wound remained 30% open with siGPAM #1 and 55% with siGPAM #2 (Fig. 22A,F). Similarly, silencing GPAM in COV318 cells with both oligos led to 30% of the scratch remaining open after 48 hours (Fig. 22B,G). GPAM knockdown in OAW28, OVCAR4 and OVCAR8 cells also led to significant decreases in migration as determined using the transwell assay and presented as a migration index that was calculated in relation to the cell number in the control wells. In OAW28 (Fig. 22C,H) and OVCAR4 (Fig. 22D,I) cells, the migration index was reduced by 50% after silencing GPAM with oligo #1 and almost 90% with oligo #2. More strikingly, silencing GPAM in OVCAR8 cells led to a reduction in migration by 90% with oligo #4 and migration was almost completely attenuated with oligo #2 (Fig. 22E,J).

Downregulation of AGK expression also consistently decreased cell migration across all tested ovarian cancer cell lines, except for OVCAR4 where there were oligo specific effects (Fig. 23A-J). More specifically, the wound closure assay performed in Kuramochi (Fig. 23A,F) and COV318 (Fig. 23B,G) cells revealed closure of approximately 60-70% with siAGK #1 and nearly 50% with siAGK #2, both of which were significantly less than the nearly complete closure observed with the negative control (siNEG) at the same time point. In OAW28 (Fig. 23C,H) and OVCAR8 (Fig. 23E,J) cells, both siRNA sequences led to a significant reduction in the migration index as determined using the transwell assay. However, in OVCAR4 cells, a decrease in migration was only observed with siAGK #2, while cells transfected with siAGK #1 resulted in an increased migration index (Fig. 23D,I). Because of this oligo-specific difference, which may be due to off-target effects in this particular cell line, three additional siRNA oligos (siAGK #4 - #6) were used to silence AGK in OVCAR4 cells. Surprisingly, despite the successful downregulation of AGK expression with all three oligos (Fig. 24A), there was no significant effect on migration (Fig. 24B,C). In OVCAR8 cells, two of this oligos (siAGK #4 and #6) effectively reduced cell migration, aligning with the results obtained from previously utilized oligos (Appendix Fig. S3). However, the absence of a similar effect in OVCAR4 cells indicates that AGK may not be relevant for migration in this particular cell line. Overall, with the exception of OVCAR4, AGK knockdown resulted in a significant reduction in cell migration that was similar to the effect observed after GPAM knockdown. Furthermore, silencing GPAM and AGK had the strongest effect on migration in OVCAR8 cells. These findings highlight the critical role of GPAM and AGK in regulating cell migration, confirming previous results for GPAM in breast cancer and the clear cell ovarian cancer ES2 cells [9], as well as AGK in glioma and renal carcinoma cells [59, 102].

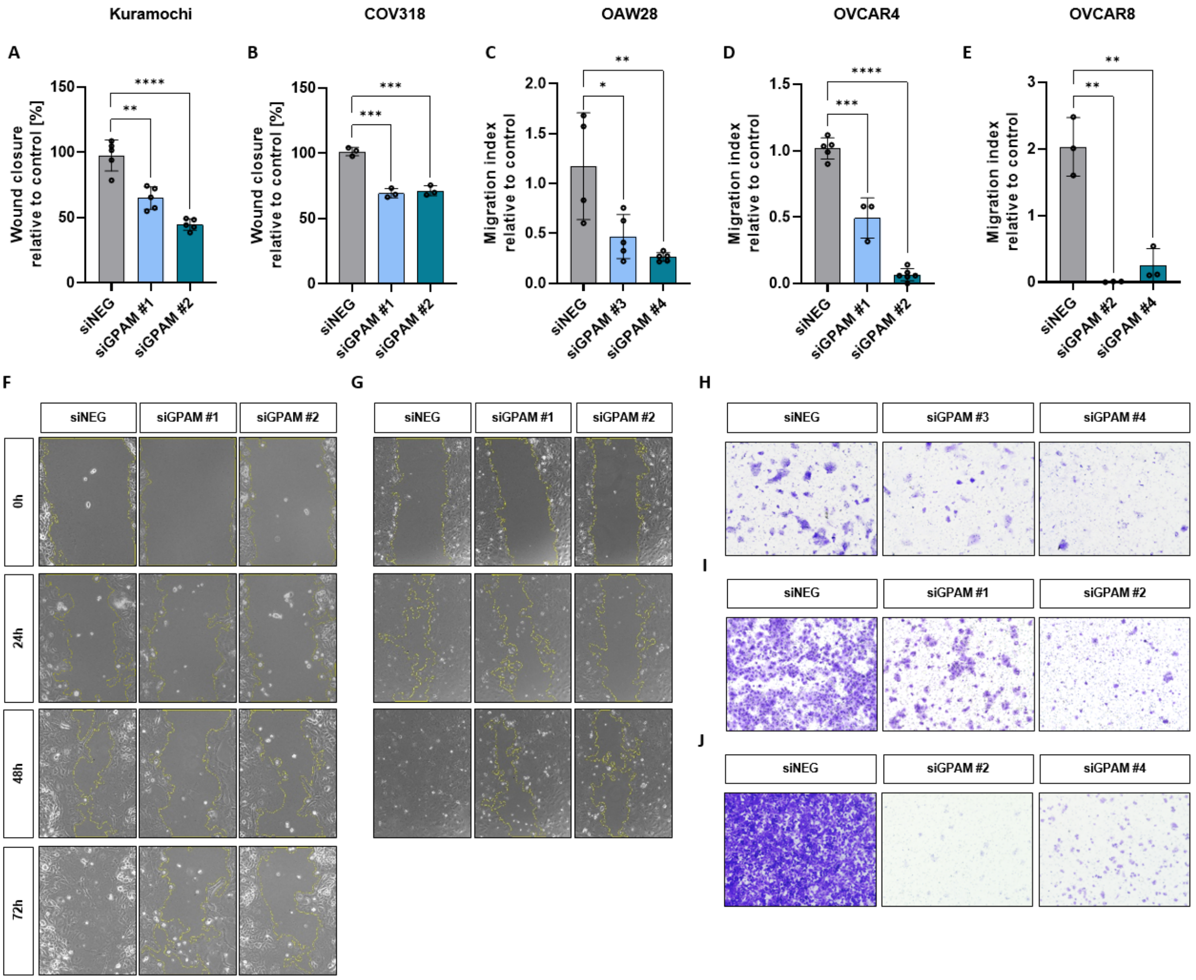

Figure 22: **Silencing GPAM in ovarian cancer cells reduces cell migration.** Cell migration was significantly reduced upon silencing GPAM (siGPAM #1 - #4) compared to the control cells (siNEG) as shown with the wound healing assay for **A,F** Kuramochi and **B,G** COV318 and with the transwell migration assay for **C,H** OAW28, **D,I** OVCAR4 and **E,J** OVCAR8 cells in the graphs and in the representative images. Quantification of the scratch assay was performed as the percentage of the wound closure at the timepoint when the scratch in the siNEG condition closed (72 h for Kuramochi and 48 h for COV318 cells) compared to the initial scratch's size. Each data point represents three to four measurements. For the transwell assay, the migration index was calculated as the percentage of the blue-colored pixels compared to the total pixel amount and normalized to the cell number from control wells for each condition. The mean migration indices were calculated from two inserts per condition and four images per insert and normalized to the siNEG control from each experiment. Microscopic images were acquired using Keyence BX800 microscope with the 10x objective. Data are mean ±SD from at least three independent biological replicates with at least three technical replicates each (** $P < 0.01$; *** $P < 0.001$; **** $P < 0.0001$).

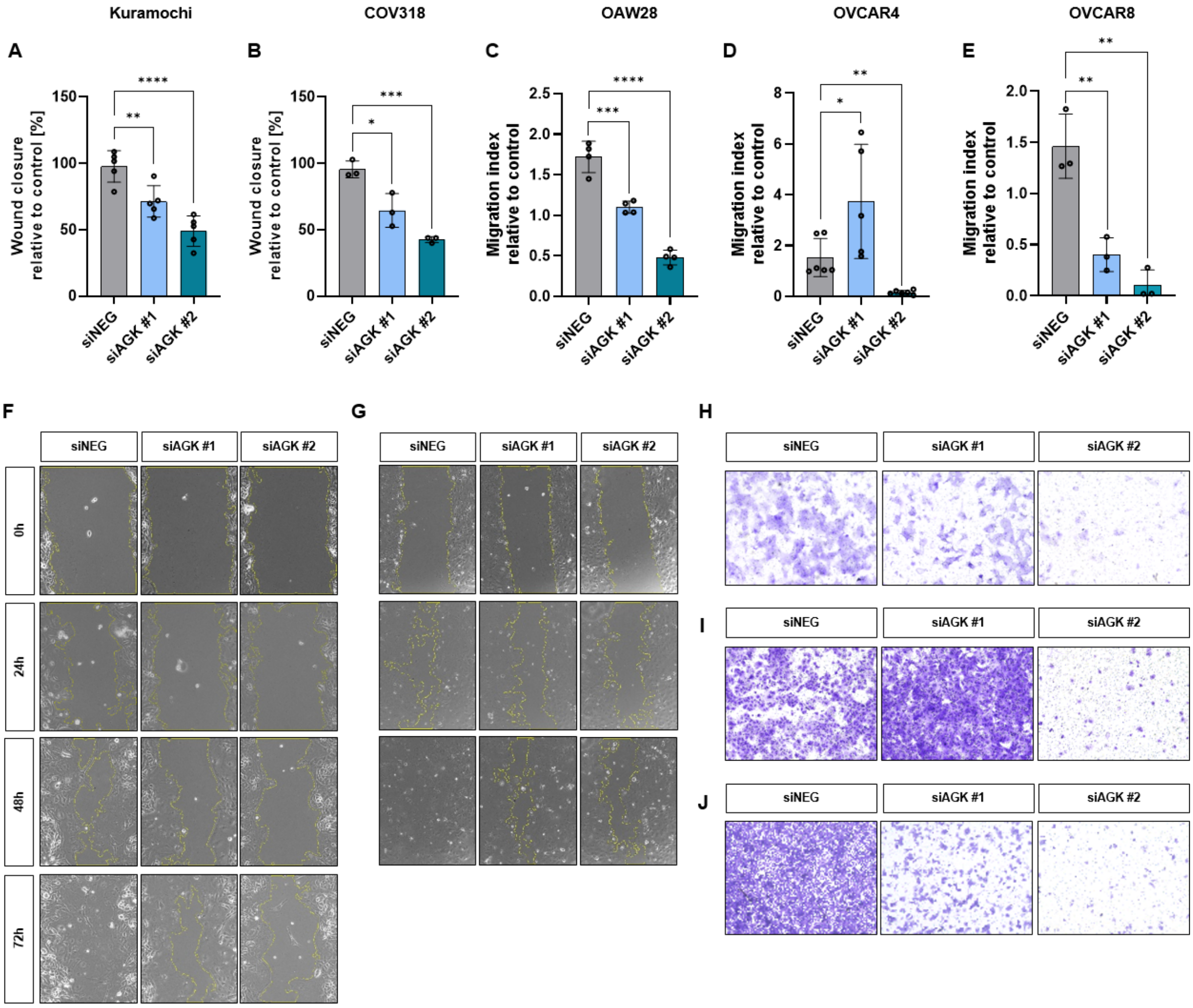

Figure 23: **Silencing AGK in ovarian cancer cells reduces cell migration.** Cell migration was significantly reduced upon silencing AGK (siAGK #1 and #2) compared to the control cells (siNEG) as shown with the wound healing assay for **A,F** Kuramochi and **B,G** COV318 and with the transwell migration assay for **C,H** OAW28, **D,I** OVCAR4 and **E,J** OVCAR8 cells in the graphs and in the representative images. Quantification of the scratch assay was performed as the percentage of the wound closure at the timepoint when the scratch in the siNEG condition closed (72 h for Kuramochi and 48 h for COV318 cells) compared to the initial scratch's size. Each data point represents three to four measurements. For the transwell assay, the migration index was calculated as the percentage of the blue-colored pixels compared to the total pixel amount and normalized to the cell number from control wells for each condition. The mean migration indices were calculated from two inserts per condition and four images per insert and normalized to the siNEG control from each experiment. Microscopic images were acquired using Keyence BX800 microscope with the 10x objective. Data are mean ±SD from at least three independent biological replicates with at least three technical replicates each (* $P < 0.05$; ** $P < 0.01$; *** $P < 0.001$; **** $P < 0.0001$).

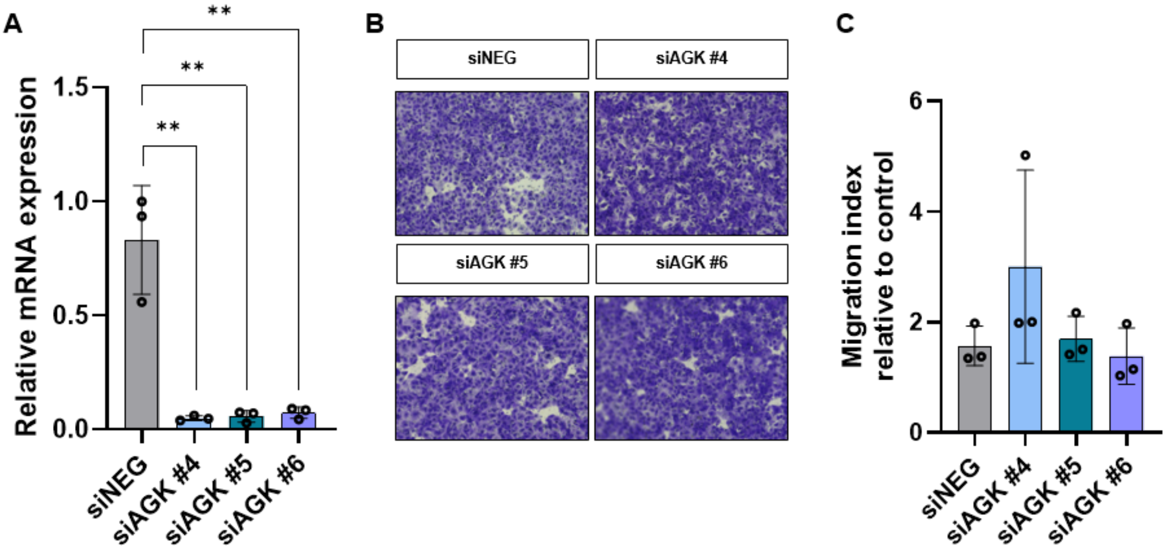

Figure 24: **Silencing AGK does not affect cell migration in OVCAR4 cells** **A** AGK mRNA levels were downregulated in OVCAR4 cells using three additional siRNA oligonucleotides - siAGK #4 - #6. **B,C** Transwell migration assay of the siAGK treated cells and the control cells transfected with scrambled siRNA (siNEG) was performed. The migration index was calculated as the percentage of the blue-colored pixels compared to the total pixel amount and normalized to the cell number from control wells for each condition. The mean migration indices were calculated from two inserts per condition and four images per insert. Microscopic images were acquired using Keyence BX800 microscope with the 10x objective and quantified as described before. Data are mean ±SD from at least three independent biological replicates with at least two technical replicates each (** P < 0.01).

4.2.3 GPAM and AGK knockdown has no consistent effect on colony formation

The impact of silencing GPAM and AGK on the colony-forming ability of ovarian cancer cells was evaluated in the same panel of HGSOC cells for migration above with variable results. Silencing GPAM led to reduced number of colonies in Kuramochi (Fig. 25A,F), COV318 (Fig. 25B,G), and OVCAR4 (Fig. 25D,I) cells, but with only one of the two oligos used. Interestingly, knocking down GPAM appear to result in more colonies in OVCAR8 cells; however, only one oligo was significant (Fig. 25E,J). GPAM silencing had no effect on colony number in OAW28 cells (Fig. 25C,H). In contrast to GPAM where its silencing did influence colony number in specific cell lines, knocking down AGK in the same cells had no effect, with the exception of Kuramochi where less colonies were measured, albeit significant with only one of the two oligos used (Fig. 26A,F). The findings indicate that while the migration capacity of the different ovarian cancer cell lines was consistently reduced following GPAM and AGK knockdown, there was no consistent effect on colony formation, highlighting the complexity of their roles in cancer cell behavior.

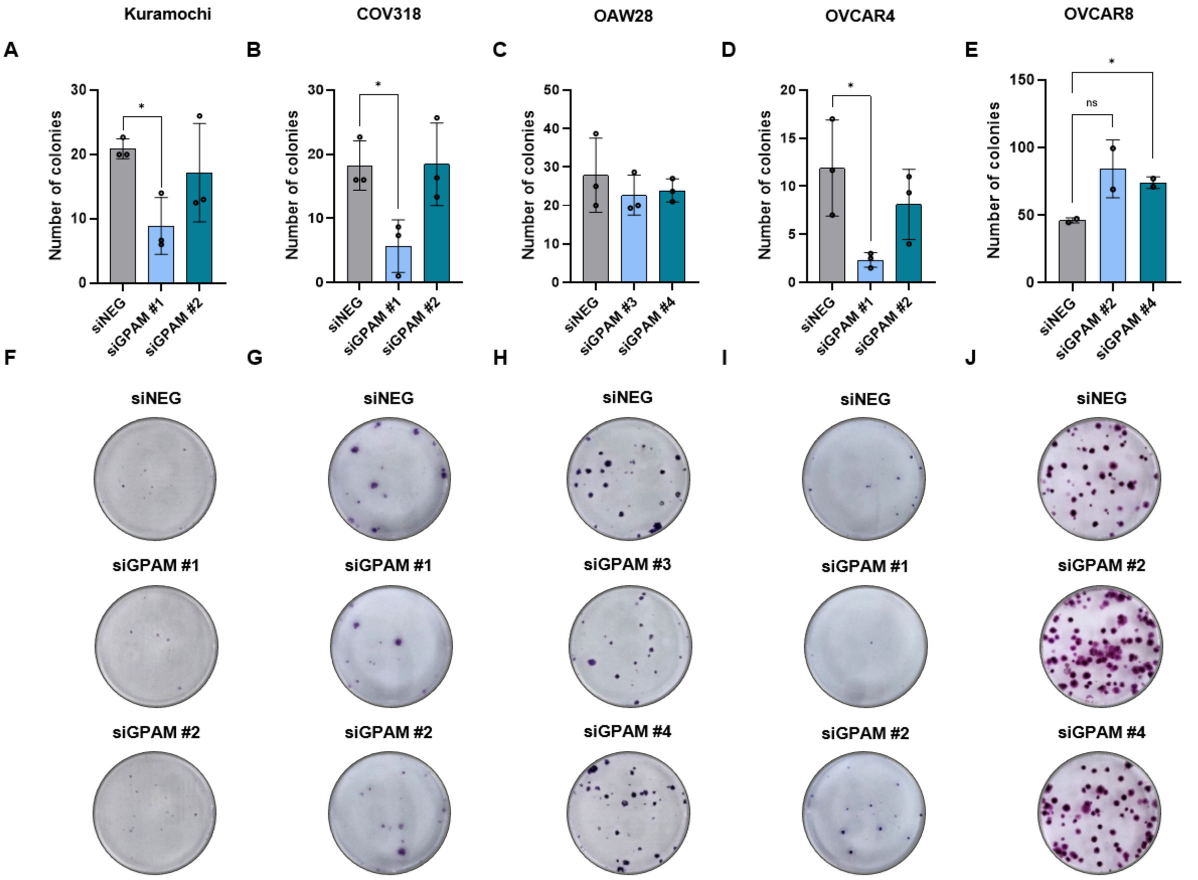

Figure 25: **Silencing GPAM has no consistent effect on colony formation in ovarian cancer cell lines.** The colony formation assay was conducted for a period of two weeks upon silencing GPAM using siRNA (siGPAM #1-#4) in comparison to control cells, that were transfected with scrambled siRNA (siNEG). Analysis of the number of colonies as well as representative images of colonies are presented for **A,F** Kuramochi, **B,G** COV318, **C,H** OAW28, **D,I** OVCAR4 and **E,J** OVCAR8 cells. Data are mean ± SD of three replicates (* $P < 0.05$).

4.2.4 Combined GPAM and AGK knockdown has no synergistic effect on cell migration

Since the silencing of both GPAM and AGK led to a consistent decrease in migration in all cell lines examined, the simultaneous knockdown of GPAM and AGK was next investigated to determine if this would lead to an additive or synergistic effect on migration. To test this, Kuramochi cells were selected, as silencing GPAM and AGK in this cell line resulted in only a moderate decrease in cell migration of 30% - 50% (Section 4.2.2). In a first step, transfection conditions were established in order to achieve a successful downregulation of both genes (Fig. 27). Interestingly, silencing GPAM, led to a significant upregulation of *AGK* mRNA levels compared to siNEG cells (Fig. 27B). Conversely, silencing AGK led to a significant reduction in GPAM expression, with oligo #1 (Fig. 27A). For the simultaneous knockdown using two oligos for each gene, four conditions were tested to address all possible combinations (siGPAM #1/siAGK #2, siGPAM #1/siAGK #2, siGPAM #2/siGPAM #1 and siGPAM #2/siAGK #2). In all four conditions, expression levels of both genes were successfully downregulated by over

80% (Fig. 27A,B). While the individual knockdowns of GPAM and AGK each led to a significant reduction in migration, the combined double knockdown of both genes showed no overall additive or synergistic effect compared to the migration effect observed after single knockdowns (Fig. 27C,D). All single gene knockdowns resulted in a 40% – 60% reduction in migration compared to the siNEG control. In all combinations of the double knockdown, there was an approximately 50% reduction in cell migration compared to the double negative control (siNEG 2x). These results suggest that this is the maximum effect on cell migration that can be achieved in this cell line under these conditions.

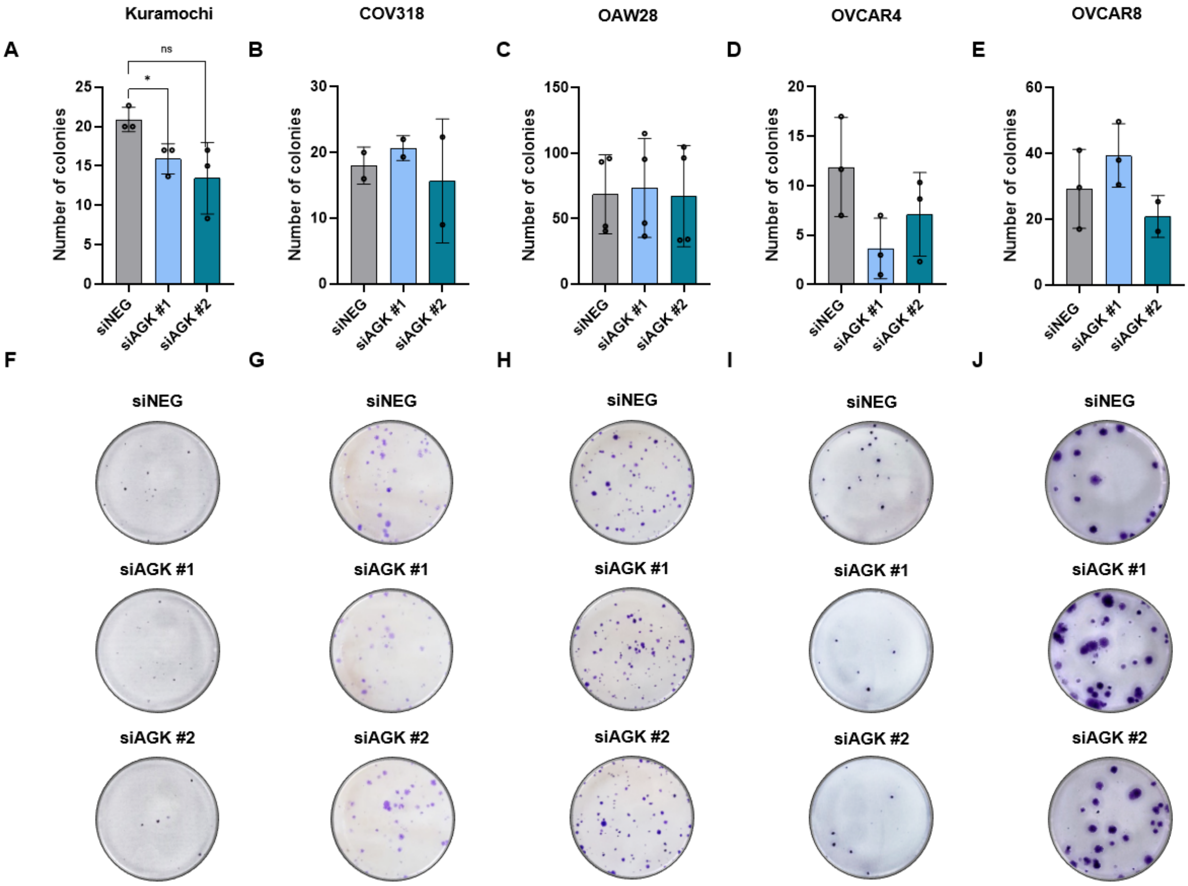

Figure 26: **Silencing AGK has no consistent effect on colony formation in ovarian cancer cell lines.** The colony formation assay was conducted for a period of two weeks upon downregulation of AGK using siRNA (siAGK #1 and #2) in comparison to control cells, transfected with scrambled siRNA (siNEG). Analysis of the number of colonies as well as representative images of colonies are presented for **A,F** Kuramochi, **B,G** COV318, **C,H** OAW28, **D,I** OVCAR4 and **E,J** OVCAR8 cells. Data are presented as mean ± SD of three replicates (* $P < 0.05$).

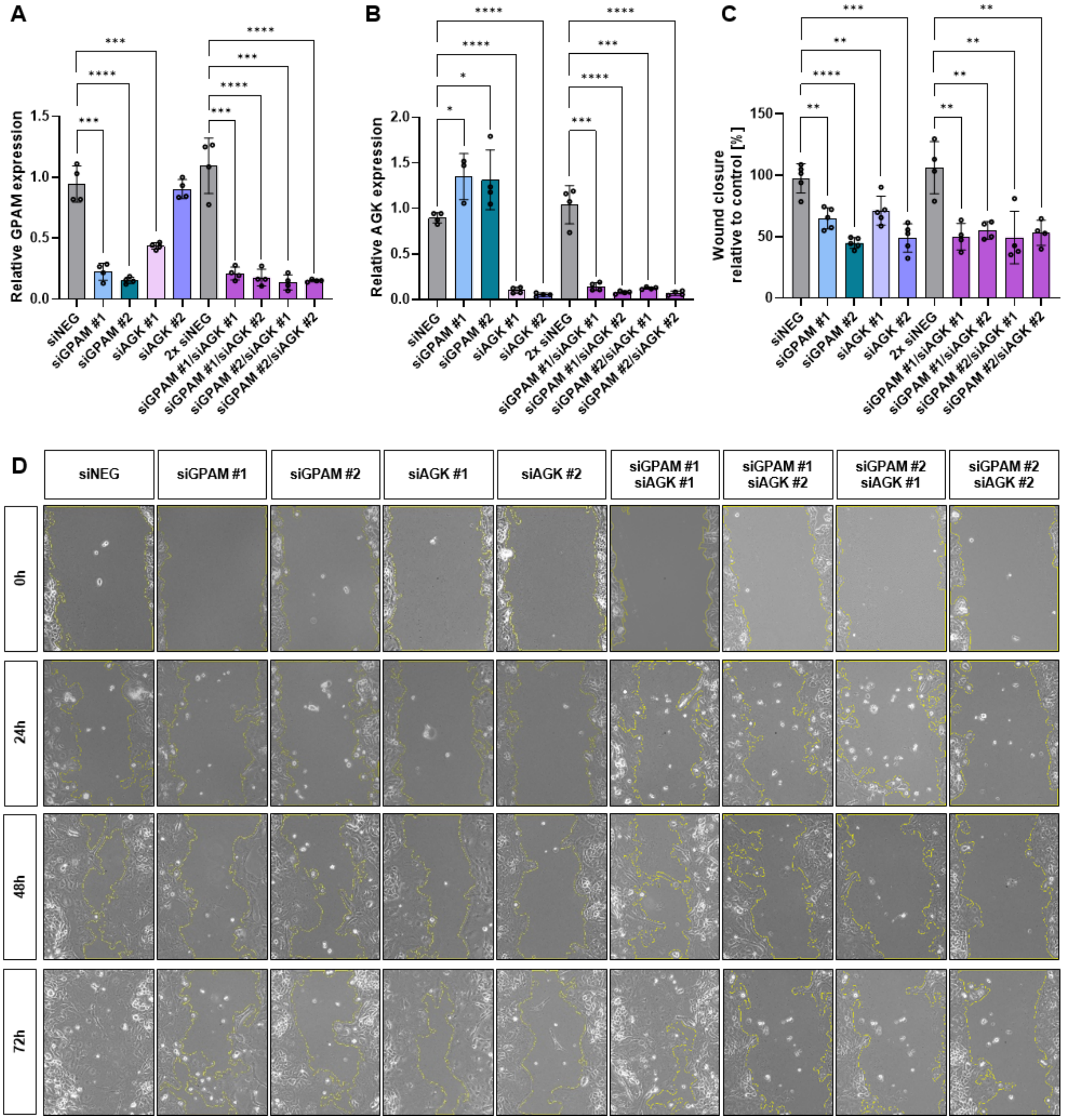

Figure 27: **Simultaneous downregulation of GPAM and AGK has not additive effect on migration in Kuramochi cells.** Kuramochi cells were transfected with two siRNA oligonucleotides targeting GPAM (siGPAM #1 & #2) and AGK (siAGK #1 & #2) individually or in combination of both genes. The cells were also transfected with the control scrambled siRNA oligo or 2x siNEG. Real-time PCR analysis was performed. **A** Relative mRNA levels of GPAM in all conditions, demonstrating efficient knockdown with both oligonucleotides targeting GPAM (siGPAM #1-#2) individually and in combination with AGK siRNA oligos. **B** Relative mRNA levels of AGK in the indicated conditions, showing successful silencing with both oligonucleotides targeting AGK individually and in combination with GPAM knockdown. Gene expression was normalized to β-Actin and presented as fold change relative to control cells. **C** Quantification of gap closure over time, presented as a percentage of the initial scratch area relative to control-treated cells (siNEG, 2x siNEG). **D** Representative images of the scratch assay showing the initial scratch (0 h) and remaining open gap after 24, 48 and 72 hours (outlined in yellow) in Kuramochi cells. Data are mean ±SD from four independent biological replicates (* $P < 0.05$; ** $P < 0.01$; *** $P < 0.001$; **** $P < 0.0001$).

4.2.5 GPAM and AGK knockdown disrupt spheroid formation and outgrowth

Spheroid formation is particularly relevant in the context of ovarian cancer cell migration and metastasis as it mimics the conditions for tumor cell aggregation and spread in vivo [159]. In ovarian cancer, cancer cells can detach from the primary tumor as single cells or in clusters, float in the peritoneal fluid, where they may form larger and more compact cell aggregates which can attach to distant sites in the peritoneal cavity and thus form metastases. These multicellular aggregates are often more resistant to chemotherapies, are less affected by anoikis, and contribute to the spread of the cancer [160].

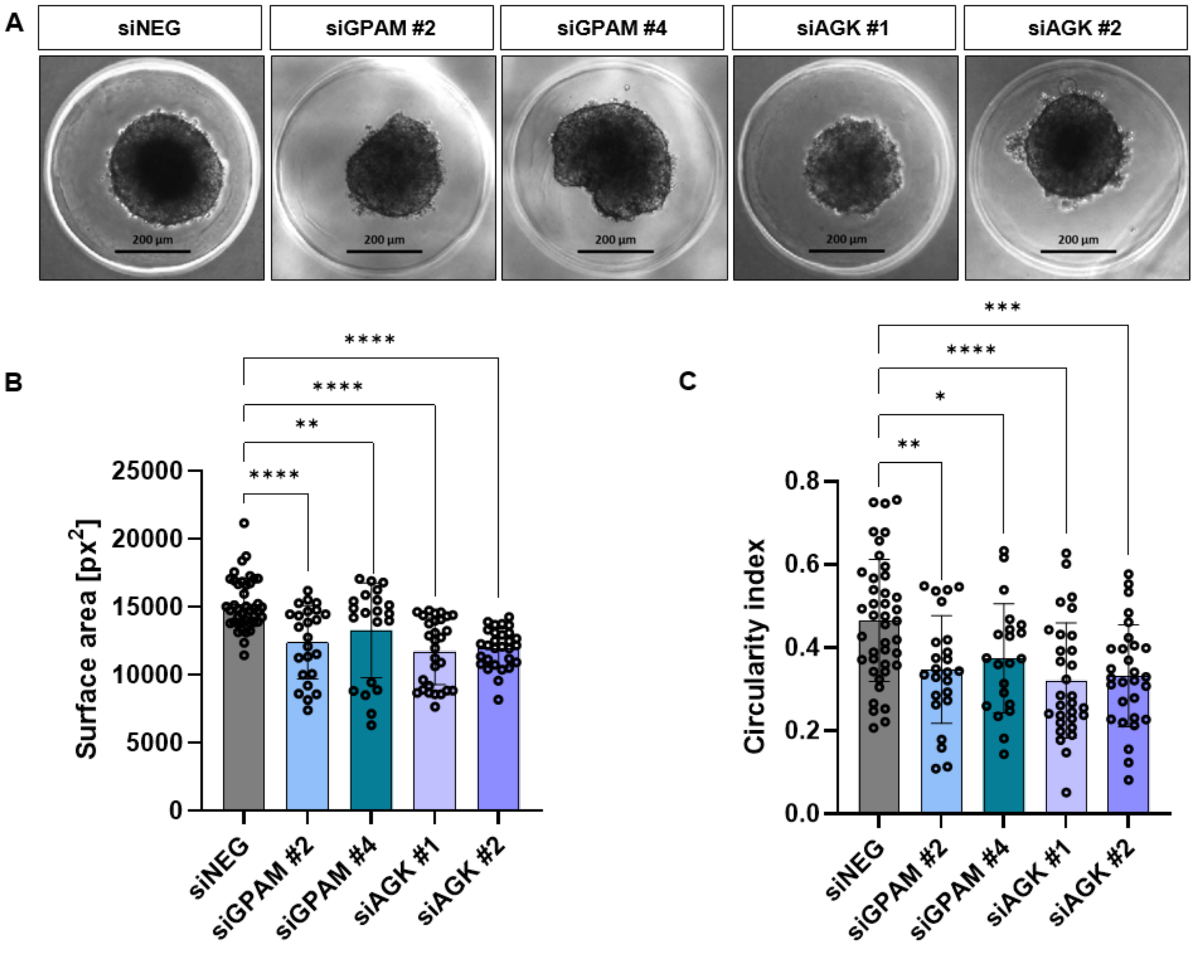

Figure 28: **GPAM and AGK knockdown disrupt spheroid formation.** **A** Representative images of spheroids formed by OVCAR8 cells transfected with control (siNEG), GPAM siRNA (siGPAM #1 and #2) and AGK siRNA (siAGK #1 and #2) illustrating impaired spheroid integrity and structure in knockdown conditions. **B** Quantification of spheroid surface area, showing a significant reduction in spheroid size upon GPAM and AGK knockdown, compared to siNEG control. **C** Shape analysis was performed to evaluate the spheroid morphology, and a significant decrease in spheroid roundness was observed upon knockdown of GPAM and AGK, indicating disrupted spheroid morphology. The spheroids were photographed with a 10x objective. Scale bar in A is 200 µm. Data were collected from at least 20 individual spheroids from three independent biological replicates and are presented as the mean ± SD. (** $P < 0.01$; *** $P < 0.001$; **** $P < 0.0001$).

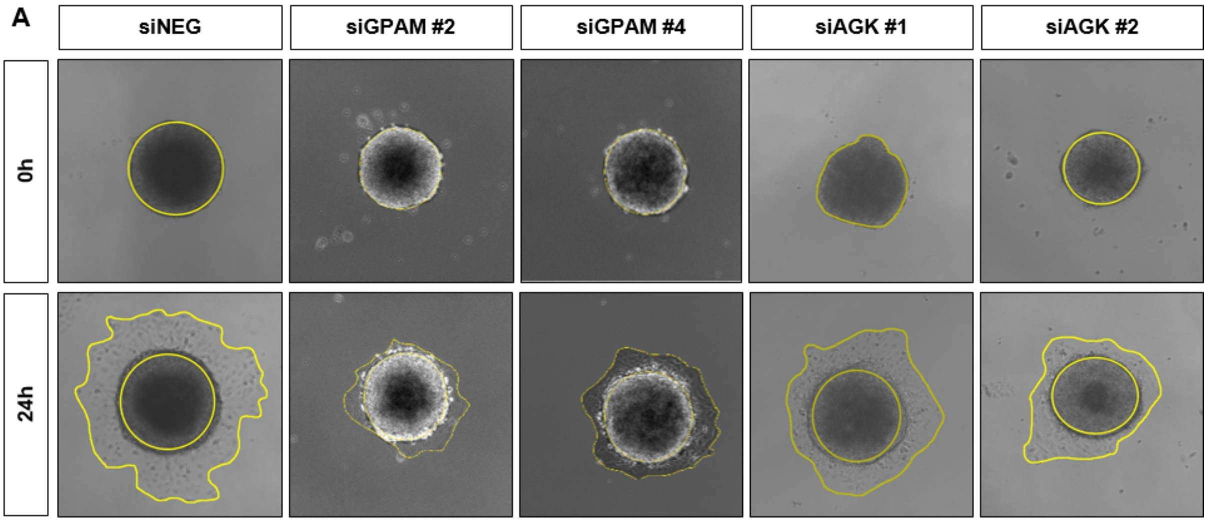

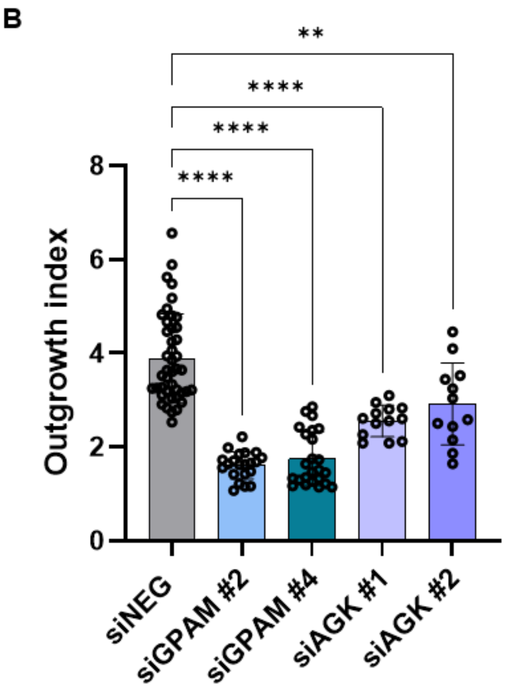

Figure 29: **Spheroid outgrowth is reduced upon GPAM and AGK knockdown.** Spheroids with downregulated GPAM and AGK expression, as well as control spheroids (siNEG) were plated onto a cell culture dish. After allowing the spheroids to attach for 4h, images were taken (timepoint t=0h). After 24h, spheroids were again imaged and the spreading of the outgrowing cells to form a 2D cell monolayer, as outlined in yellow, was evaluated using Fiji. The outgrowth index was calculated by normalizing the outgrowth area to the surface area of the initial spheroid at t=0h. Data were collected from at least 12 individual spheroids from three independent biological replicates and are presented as the mean ± SD. (** $P < 0.01$; **** $P < 0.0001$)

To investigate how GPAM and AGK downregulation affects spheroid formation ability, OVCAR8 cells were selected as silencing both GPAM and AGK in this cell line resulted in the most prominent reduction in cell migration, and OVCAR8 cells were previously used by others to successfully create 3D cell cultures [161]. First, conditions were established to produce reproducibly sized spheroids in control OVCAR8 cells. Next, spheroids were produced using OVCAR8 cells in which GPAM and AGK were silenced and the effect on spheroid size, morphology and outgrowth capabilities investigated. The results indicate that silencing GPAM and AGK led to changes in spheroid size and morphology compared to the spheroids created with non-targeting scrambled siRNA (siNEG) (Fig. 28A). More specifically, image analysis of the surface area showed that the spheroids formed with cells expressing less GPAM and AGK were notably smaller in size - on average 25% smaller than the control spheroids (Fig. 28B). Furthermore, they exhibited a less circular and compact morphology compared to the control (Fig. 28C).

Following spheroid formation, a spheroid outgrowth assay was performed to further examine the migratory and invasive potential of OVCAR8 cells upon silencing GPAM and AGK. In this assay, the spheroids were plated onto a cell culture dish, where they were allowed to attach and initiate outgrowth over time. Imaging was conducted at regular intervals to monitor the expansion of cells from the spheroid structure into a 2D monolayer. Detection of the spheroid surface area after attachment to the plates, marked as timepoint t=0h, as well as the outgrowing area after 24 hours incubation (t=24h), was performed using Fiji and is presented as yellow outlines in the representatives images (Fig. 29A). The outgrowth index was then calculated, by normalizing the outgrowth area to the corresponding initial spheroid size (at t=0h). In comparison to control siNEG spheroids, those with reduced expression of GPAM and AGK exhibited a significantly smaller outgrowth index. GPAM knockdown reduced the outgrowth by approximately 50% with both oligos (Fig. 29B). The effect with AGK knockdown was slightly weaker, with a reduction of about 40% with siAGK #1 and 30% with siAGK #2 (Fig. 29B). Overall, the results suggest that GPAM and AGK may play a crucial role in migration of cells from 3D spheroid structures to 2D monolayers.

4.3 AGK overexpression leads to enhanced migration

4.3.1 Generation of AGK overexpressing OVCAR8 clones

The results thus far indicate that silencing GPAM in several HGSOC cell lines leads to reduced migration, in agreement with the previous findings by our group observed in breast cancer cells and the ES2 clear cell OC cell line [9]. In the same study, overexpressing GPAM was shown to increase migration in HEK293 cells. In the present work, AGK knockdown also consistently led to reduced migration of HGSOC cell lines. Therefore, as a next step, the effect of AGK overexpression on cellular behavior was investigated. To generate stable constitutive AGK expressing cell lines, OVCAR8 cells were infected with lentiviral (LV) particles that were generated in house as described in method section 3.1.3. LV particles carrying the plasmids with AGK sequence coupled to GFP through a P2A site (pLV_AGK, Fig. 10) as well as control plasmids carrying only a GFP-expressing plasmid (pLV_GFP, Fig. 11) were generated in HEK293 cells. Supernatants containing LV particles were then collected from HEK293 cells at 24, 48, and 72 hours post-transfection and subsequently used to transduce OVCAR8 cells, which exhibited the lowest basal expression of AGK among the five previously selected cell lines. The non-infected cells (NIC), with or without the transfection agent polybrene (PB) showed no GFP expression (Fig. 30B), while all cells infected with pLV_GFP and pLV_AGK particles expressed GFP (Fig. 30A). The strongest GFP expression for both the control- and AGK-vectors was observed in cells infected with the 24 hours supernatant (24h sup). The increased AGK and GFP expression was confirmed with Western blot analysis (Fig. 30C), and in line with the GFP signal, cells exposed to the 24h supernatant had the highest AGK and GFP expressions. After selection of the positively transduced cells with puromycin, the surviving cells were expanded and AGK expression analyzed with quantitative real time PCR, which revealed significantly higher *AGK* mRNA levels in pLV_AGK-transduced compared to the pLV_GFP-transduced cells, confirming successful overexpression (Fig. 30D).

As the amount of plasmid taken up by an individual cell can vary, single cell cloning was performed to generate cell lines with a homogeneous genetic background. Seven single cell clones per condition were ‘picked’ and expanded, and once the clones were successfully growing, protein was extracted and AGK expression was tested with Western blot. All control clones expressed GFP and comparably low levels of AGK, therefore one control clone was selected and used in further investigations. For AGK, only two clones generated from the pLV_AGK transduced cells simultaneously expressed GFP and high AGK protein levels (Fig. 31). Therefore, these two clones (A and G) were selected for further expansion, cryopreservation and subsequent analyses. In the further course of the work, these two clones are referred to as OV8_AGK #1 and #2. After selecting the two AGK-overexpressing clones and establishing stable monoclonal cell cultures, the GFP expression in these clones alongside a GFP-transduced control clone was again evaluated. The results indicated that GFP expression remained stable even after antibiotic treatment and the process of monoclonal expansion in all clones (Fig. 32A). Subsequently, AGK expression was assessed using quantitative PCR, which revealed that both AGK-overexpressing clones exhibited significantly higher levels of AGK compared to the control OV8_GFP clone (Fig. 32B). This increase in expression was further corroborated by western blot analysis, which confirmed enhanced protein expression in the AGK-overexpressing clones relative to the control (Fig. 32C, D). These findings demonstrate the successful establishment of stable AGK-overexpressing cell lines OV8_AGK #1 and #2 with robust expression levels.

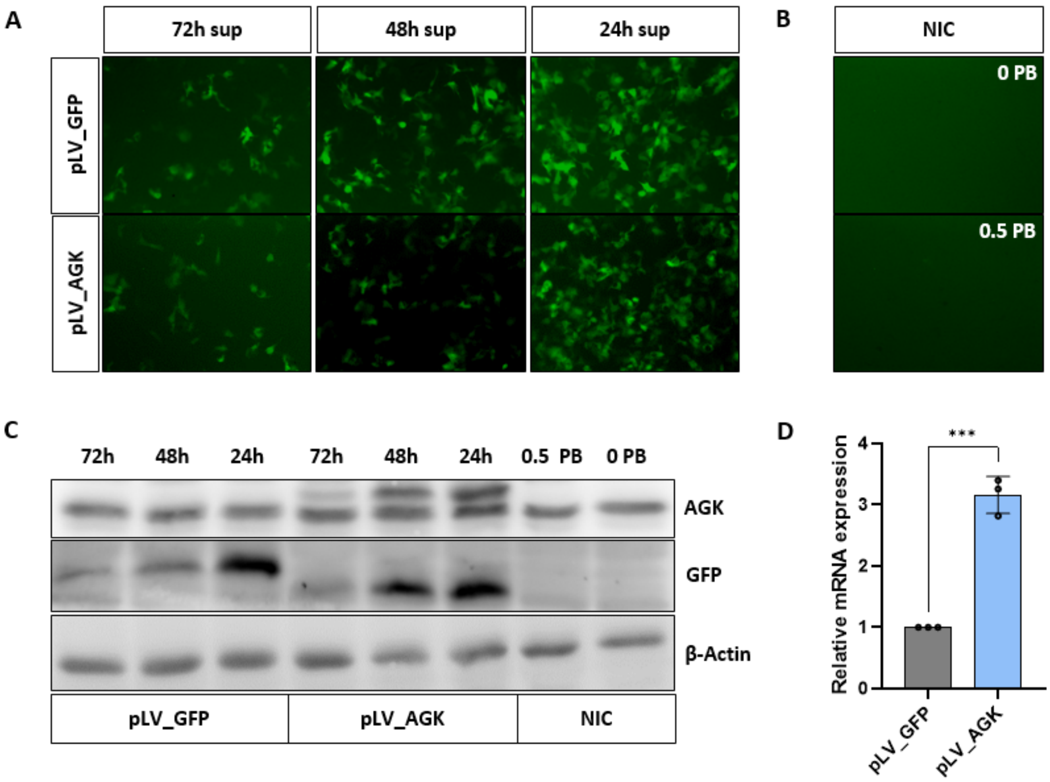

Figure 30: **Generation of constitutive AGK expressing OVCAR8 cells.** OVCAR8 cells were infected with supernatants containing high-titer packed lentiviral (LV) particles collected 24h, 48h and 72h post-transfection of HEK293T cells. The viral particles were packaged with a vector containing the AGK sequence coupled to GFP via a cleavable P2A site. **A** GFP fluorescence in OVCAR8 cells at different times post infection with lentiviral particles with containing pLV-GFP control vector or pLV-AGK overexpressing vector is shown in representative microscopic images. **B** The non-infected control (NIC), with and without the transfection reagent polybrene (PB) showed no fluorescence signal. **C** Total protein lysates were collected 48 hours after infection from all conditions and western blot analysis was conducted. AGK and GFP expression levels were highest in the supernatant (sup) collected 24h post cell infection. **D** AGK mRNA levels in OVCAR8 cells infected with the 24h sup AGK-overexpressing LV particles were significantly higher compared to the control. Quantitative PCR analysis was performed on three independent biological replicates (*** P < 0.001).

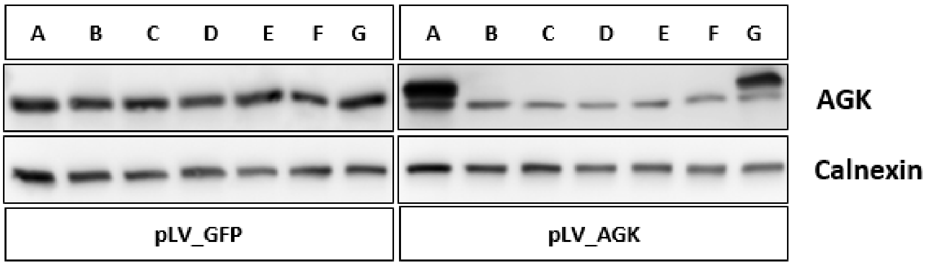

Figure 31: **AGK protein expression in monoclonal OVCAR8 cell cultures.** OVCAR8 cells infected with LV-particles underwent monoclonal selection. **A** AGK protein expression was analyzed in seven GFP-infected clones and seven AGK-infected clones. Only the AGK clones A and G expressed higher AGK levels compared to the control pLV_GFP cells, and were selected for all further analyses where they were referred to as OV8_AGK #1 and OV8_AGK #2. AGK levels were equal in all control clones, therefore clone A was selected for further analyses and renamed OV8_GFP.

4.3.2 Stable AGK overexpressing OVCAR8 clones exhibit enhanced migration

Monoclonal cell selection is a time-intensive process that can potentially alter the fundamental characteristics of cells. To investigate the impact of AGK overexpression on cell viability, proliferation, and single-cell survival, two complementary assays were employed: the CellTiter-Blue (CTB) assay to evaluate cell viability and the colony formation assay to assess the survival and proliferative capacity of individual cells. The results demonstrated that AGK overexpression did not affect cell viability. This was consistent across both the AGK-transduced heterogeneous cell culture (pLV_AGK) (cells transduced with AGK vector but did not undergo single cell cloning) and the two AGK-overexpressing clones when compared to the OV8_GFP control cells (Fig. 33A). Similarly, the colony formation assay revealed no significant changes in the ability of cells to form colonies, with the exception of a modest but statistically significant increase in colony number observed in the OV8_AGK #2 clone (Fig. 33B-C).

The downregulation of AGK resulted in a consistent reduction in cell migration across all five ovarian cancer cell lines tested. To investigate whether AGK overexpression would enhance migratory capabilities, the migratory ability of the OVCAR8 clones was analyzed using the transwell migration assay. Representative images indicate that a greater number of the AGK-overexpressing cells, OV8_AGK #1 and OV8_AGK #2 migrated through the membrane compared to the control cells (OV8_GFP) (Fig. 34A). Notably, no effect on migration was observed with the pLV_AGK transduced cells. The migration index was calculated and normalized to the cell numbers in the control wells to account for variations in proliferation and viability among the different cell populations. This analysis revealed that in both AGK-overexpressing clones, there was a significant increase in migration, highlighting the role of AGK in modulating cell migration in ovarian cancer (Fig. 34B). In conclusion, AGK overexpression enhances cell migration without having an impact on cell viability or the number of colonies, strengthening the potential role of AGK in promoting metastasis-related processes in ovarian cancer.

4.3.3 Spheroid formation and outgrowth is affected by AGK overexpression

Spheroid formation was significantly impaired upon silencing GPAM and AGK in OVCAR8 cells. The resulting spheroids were smaller and less spherical compared to those formed by control cells, indicating that the expression of these enzymes is crucial for maintaining cell-cell contacts within the three-dimensional (3D) structure. To further explore the impact of AGK expression on spheroid formation, the spheroid-forming ability of the AGK-overexpressing OVCAR8 clones was tested. Consistent with previous findings, overexpression of AGK resulted in the formation of significantly larger spheroids compared to the OV8_GFP control (Fig. 35A,B). Additionally, these larger spheroids exhibited a ‘distorted’ shape, i.e., were less rounded, mirroring the morphological changes observed following AGK knockdown (Fig. 35C). These results suggest that higher AGK expression affects the structural integrity and organization of the spheroids.

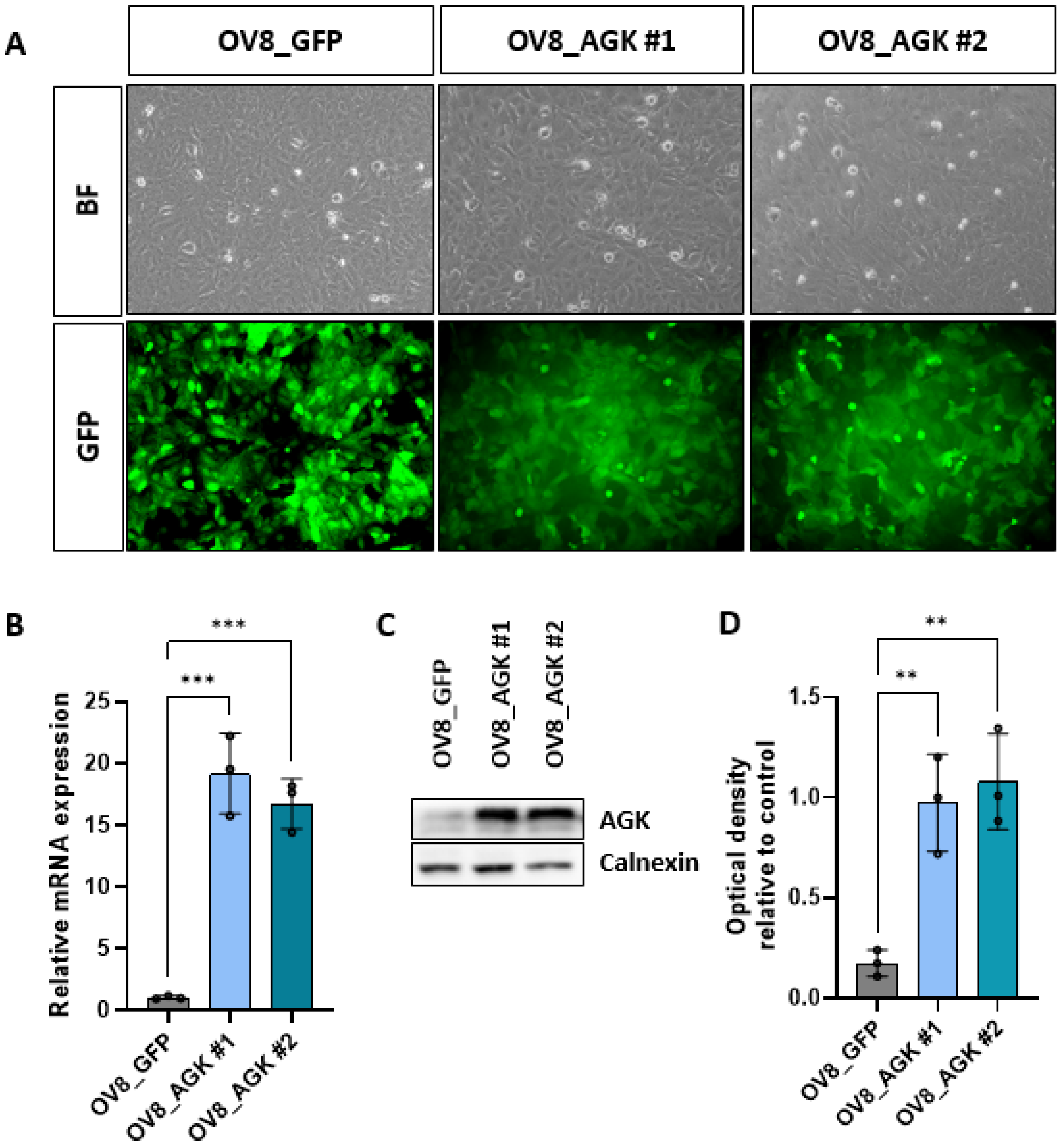

Figure 32: **Generation of monoclonal AGK-overexpressing OVCAR8 cells.** **A** Brightfield and green fluorescence images of the selected control OV8_GFP and two AGK overexpressing OV8_AGK #1 and OV8_AGK #2 cell lines after antibiotic selection and monoclonal expansion. After expansion of the monoclonal cell cultures, significantly higher AGK expression was confirmed at **B** mRNA and **C,D** protein levels in AGK-overexpressing clones (OV8_AGK #1 and #2), compared to the GFP-expressing control cells (OV8_GFP). Data are mean ±SD from three independent biological replicates (** $P < 0.01$, **** $P < 0.0001$).

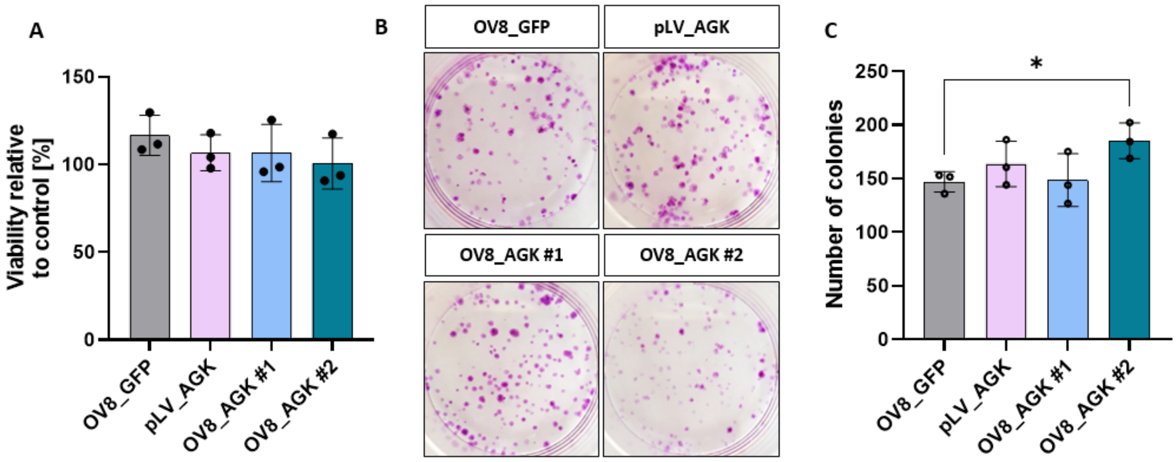

Figure 33: **Cell viability is not affected in AGK-overexpressing OVCAR8 clones.** **A** Cell viability of the AGK-overexpressing OVCAR8 monoclonal (OV8_AGK #1-#2) and heterogenous (pLV_AGK) cultures was investigated using the Cell titer blue assay. **B** Representative images of colonies formed two weeks post plating that were stained with crystal violet solution. **C** Colony number was quantified and normalized to the control cells. Data are mean ±SD from three biological replicates with three technical replicates each (* P < 0.05).

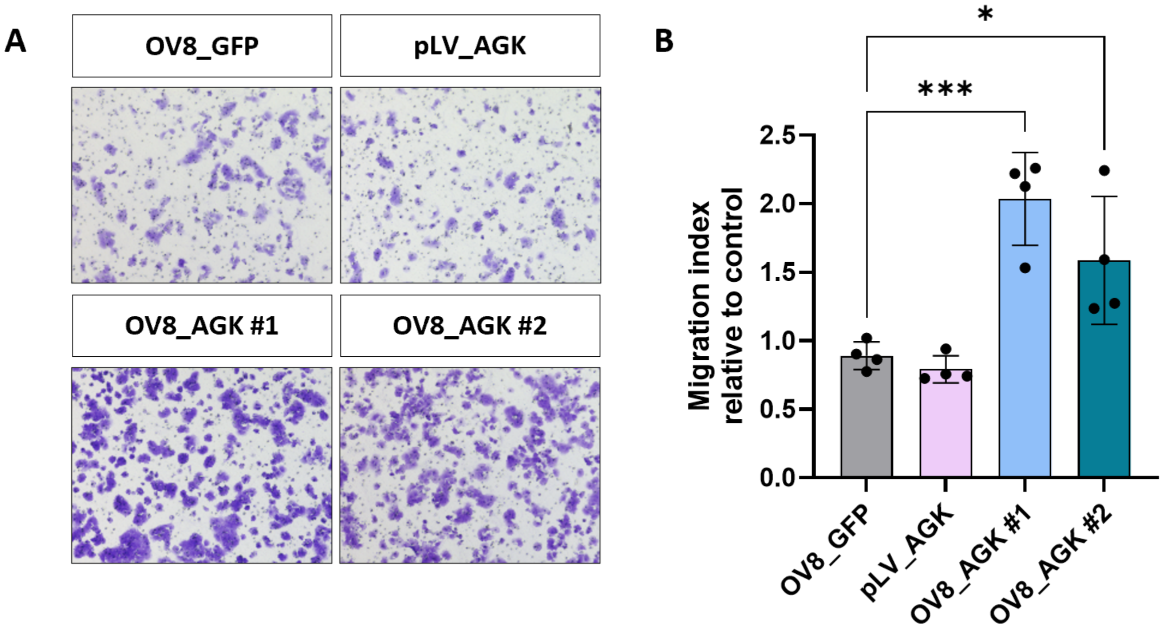

Figure 34: **Cell migration is increased in AGK-overexpressing OVCAR8 clones.** **A** Cell migration of AGK-overexpressing pLV_AGK and AGK-overexpressing clones (OV8_AGK #1-#2) was determined with the transwell migration assay. Monoclonal OVCAR8 GFP-expressing clone was used as control (OV8_GFP). **B** The migration index was calculated as the area of the membrane covered with cells, normalized to the cell number determined from control wells. Data are mean ±SD from four independent replicates (* P < 0.05, *** P < 0.001).

In addition to size, the outgrowth of cells from the spheroid to a 2D monolayer was investigated in response to AGK overexpression. Interestingly, the spheroid outgrowth assay demonstrated that AGK overexpression in OVCAR8 cells led to a reduction in cell outgrowth, similar to the effect observed following GPAM and AGK knockdown (Fig. 35D). Despite the increased size of the AGK-overexpressing spheroids, the expansion of the cells from the spheroid into the surrounding 2D monolayer was significantly diminished, almost by a factor of two (Fig. 35E). These results indicate that while AGK overexpression may enhance spheroid formation and growth, it simultaneously impairs the cells' ability to adhere to the culture plates and exit the 3D structure. The observed reduction in outgrowth is likely due to alterations in spheroid architecture, such as increased cell-cell interactions, rather than a direct impact on the cells' migratory or invasive capabilities. The adverse changes in spheroid size associated with both AGK silencing and overexpression highlight the importance of this enzyme in maintaining structural integrity and facilitating cell-cell contacts within the 3D spheroids.

4.4 Migration changes upon manipulating GPAM and AGK expression are independent of intracellular lipid levels

Our working group's interest in LPA metabolizing enzymes and their role in migration began with early studies showing that, silencing the glycerophosphodiesterase EDI3 (GPCPD1) in the MCF7 breast cancer cell line resulted in decreased cell migration, which was associated with a reduction in intracellular levels of LPA and PA [49]. Further studies demonstrated that silencing GPAM, which esterifies EDI3's product glycerol-3-phosphate (G3P) into LPA, also led to reduced cell migration and a decrease in intracellular LPA levels in MCF7 cells [9]. Moreover, transfecting LPA into MCF7 cells increased intracellular LPA levels and migration, further strengthening the link between intracellular LPA levels and cell movement. Therefore, to investigate whether the effects on cell migration observed upon silencing or overexpressing GPAM and AGK in ovarian cancer cells in this work were also mediated by changes in intracellular LPA levels, targeted LC-MS/MS lipidomics was performed. This targeted assay enables the simultaneous detection of numerous lipid and associated metabolite species within the glycerophospholipid metabolic network, specifically, LPA, PA, DAG, and G3P, all of which are direct precursors or products of GPAM's and AGK's enzymatic reactions.

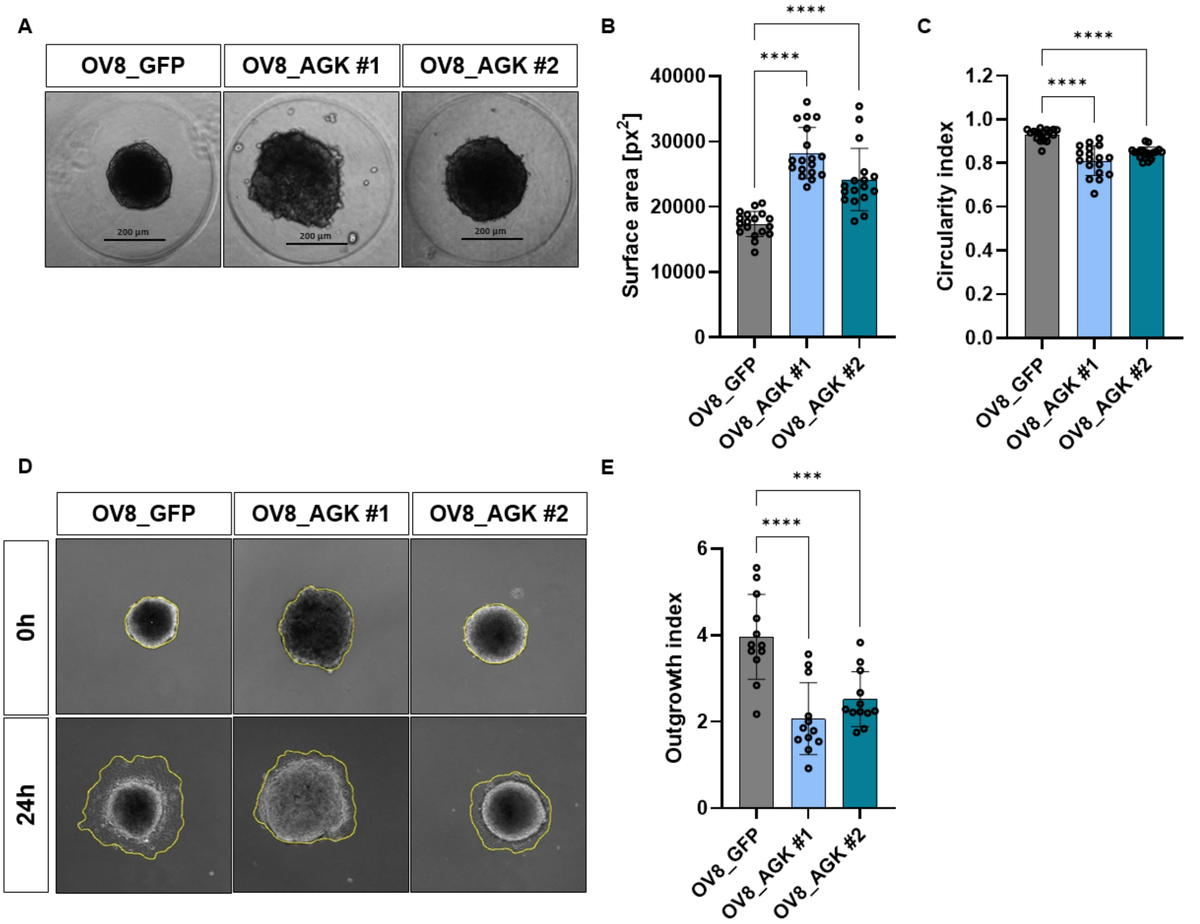

Figure 35: **AGK overexpression disrupts spheroid formation and outgrowth. A** Representative images of spheroids formed by control (OV8_GFP) and AGK-overexpressing clones (OV8_AGK #1 and #2) show disrupted spheroid surface structure. **B** Spheroid surface area of AGK-overexpressing clones in relation to the control spheroids was calculated. **C** Shape analysis was performed to evaluate the spheroid morphology, and a significant decrease in spheroid roundness was observed upon overexpressing AGK, indicating disrupted spheroid morphology. Spheroids were photographed with a 10x objective. Scale bar is 200 µm. **D**Spheroids were plated on a cell culture dish. After allowing the spheroids to attach, the images for timepoint 0h were taken. After 24h, spheroids were again imaged and the spreading of the outgrowing cells into the 2D cell monolayer, was evaluated using Fiji. **E** The outgrowth index was calculated by normalizing the outgrowth area to the surface area of the initial spheroid at timepoint 0h. Data were collected from at least 12-18 individual spheroids from three independent biological replicates and are presented as the mean ± SD. (** $P < 0.01$; *** $P < 0.001$; **** $P < 0.0001$).

4.4.1 Intracellular G3P levels are unaffected by GPAM and AGK knockdown

GPAM catalyzes the esterification of G3P to produce LPA. Consequently, downregulation of GPAM is expected to increase intracellular G3P levels. However, in most cell lines examined here, there was no significant change in G3P levels upon GPAM silencing (Fig. 36A,C,E). Only one of the two oligos used led to a significant increase in G3P in COV318 cells (Fig. 36B), and while both oligos targeting GPAM resulted in a consistent increase in G3P levels in OVCAR4 cells, the effect was not statistically significant (Fig. 36D). Similarly, intracellular G3P levels were assessed following AGK silencing. The loss of LPA production due to AGK knockdown could potentially be compensated by alternative pathways, such as the upregulation of GPAT activity, which might lead to reduced G3P levels. Consistent with the findings for GPAM, no significant changes in G3P levels were observed after AGK silencing across all cell lines (Fig. 36F-H), except for a small but significant decrease with one oligo in OVCAR8 cells (Fig. 36J). The lack of consistent changes in intracellular G3P levels following the downregulation of GPAM and AGK suggests that these enzymes play only a minor role in regulating G3P homeostasis, a central component of glycerophospholipid metabolism.

4.4.2 Silencing GPAM and AGK leads to cell specific changes in intracellular LPA levels

To determine whether the effect of GPAM and AGK knockdown on cell migration and spheroid formation is linked to disruptions in intracellular phospholipid metabolism, different phospholipids, including intracellular LPA (16:0, 18:0 and 18:1) levels were analyzed across the five ovarian cancer cell lines. In Kuramochi, OAW28 and OVCAR4 cells, no changes were observed in any of the measured LPA species upon GPAM knockdown (37A, C, D). In COV318 however, silencing GPAM led to a reduction in 18:1 LPA with both oligos; however, only one was statistically significant (Fig. 37B). Interestingly, other LPA species were not detected in this cell line. In contrast to the expected reduction in LPA, both 16:0 and 18:0 LPA levels increased in the OVCAR8 cells with GPAM knockdown, which was significant with only one oligo (Fig. 37E). Similarly, AGK knockdown produced variable effects on intracellular LPA levels depending on the cell line and LPA species (Fig. 37F-J). In general, silencing AGK had no significant effect on any of the measured LPA species. In OAW28 cells, reductions in 16:0 and 18:0 LPA levels were observed with both oligos, though these changes were not statistically significant (Fig. 37H), and in OVCAR8 cells, a significant reduction in 16:0 and 18:1 LPA levels was observed, but only with oligo #2 (Fig. 37J).

Overall, silencing GPAM or AGK had no consistent effect on intracellular LPA levels under the conditions studied. Instead, intracellular LPA levels remained largely unchanged in most cell lines, suggesting that the downregulation of these enzymes does not significantly affect LPA production or turnover. The lack of a consistent reduction in intracellular LPA may be due to compensatory mechanisms that maintain LPA homeostasis. Thus, further studies are needed to investigate alternative pathways and regulatory mechanisms that contribute to LPA homeostasis in these cells. Nevertheless, the lack of consistent change in intracellular LPA concentration in the tested cell lines suggests that the observed reduction in migration is not directly correlated with the levels of intracellular LPA.

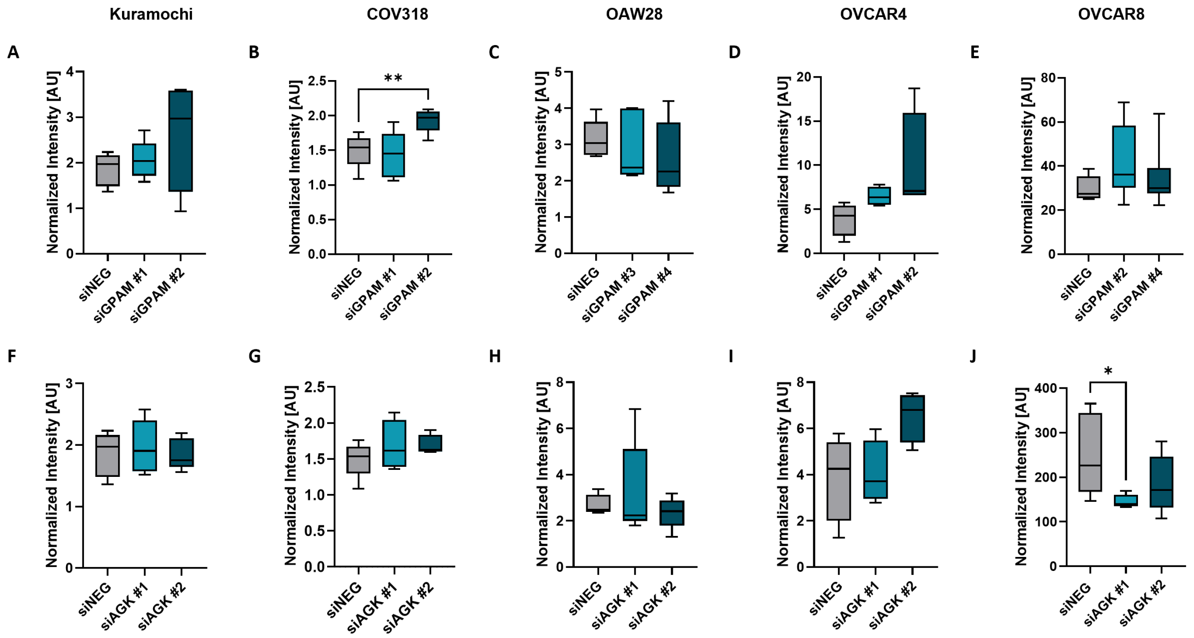

Figure 36: **Intracellular G3P levels upon silencing GPAM and AGK.** Intracellular glycerol-3-phosphate (G3P) levels were determined with targeted LS-MS/MS analysis following silencing GPAM (upper panel) and AGK (lower panel) in **A,F** Kuramochi, **B,G** COV318, **C,H** OAW28, **D,I** OVCAR4 and **E,J** OVCAR8 cells. Data are mean ±SD from at least four independent replicates (* $P < 0.05$; ** $P < 0.01$).

4.4.3 Silencing GPAM and AGK leads to cell specific changes in PA and DAG levels

Since the silencing of GPAM and AGK in the tested ovarian cancer cell lines had no consistent effect on intracellular LPA levels, the levels of LPA-related metabolites were also investigated. LPA is further metabolized to PA through AGPAT activity. PA can also be generated from DAG through DAGK activity and can also be degraded back to DAG by PLPPs. Both PA and DAG are critical signaling lipids involved in several cellular processes, including cell migration [162]. Therefore, intracellular PA and DAG levels were examined to determine whether their levels could be linked to the observed effect on cell migration mediated by GPAM and AGK silencing.

GPAM knockdown resulted in cell line and species-specific changes in intracellular PA levels. More specifically, no significant changes in PA levels were observed in both Kuramochi and OAW28 cells (Fig. 38A,C). However, silencing GPAM led to a significant decrease in 36:1 PA levels in COV318 cells (Fig. 38B) and reduced 34:0 PA levels in OVCAR4 cells, both with oligo #1 (Fig. 38D), as well as a highly significant reduction in 34:0 PA levels in OVCAR8 cells with both oligos (Fig. 38E). Interestingly, there were significant increases in PA levels in OVCAR4 (18:1-18:1) and OVCAR8 (36:1) cells upon GPAM silencing, albeit each with only one oligo (Fig. **??**D,E). Similar to GPAM, AGK knockdown led to cell line and species-specific changes in PA levels that were oligo specific. Specifically, AGK knockdown had no effect on intracellular PA levels in OAW28 cells (Fig. 38H). In Kuramochi cells, AGK knockdown with oligo #2 led to an increase in 36:1 PA and a significant increase in 18:1-18:1 PA levels (Fig. 38F). In contrast, both PA species were significantly decreased in COV318 cells (Fig. 38G), as well as 34:0 PA and 36:1 PA levels in OVCAR8 cells with oligo #2 (Fig. 38J).

Intracellular DAG levels were not affected in COV318 and OAW28 cell lines following GPAM silencing (Fig. 39B, C). In Kuramochi cells, 16:0-18:0 DAG was significantly decreased with oligo #1 (Fig. 39A). Similarly, in OVCAR4 cells, 16:0-18:0 and 16:0-16:0 DAG levels were significantly reduced with the same oligo. However, with oligo #2, a non-significant upregulation of 18:1-18:1 DAG was observed (Fig. 39D). In OVCAR8 cells, 16:0-18:0 and 18:1-18:1 DAG species were significantly increased with both oligos. Additionally, oligo-specific changes in 16:0-16:0 DAG were observed in OVCAR8 cells, with a significant decrease detected with oligo #2 and a significant increase with oligo #4 (Fig. 39E). AGK knockdown had also a cell line- and oligo-specific effect on intracellular DAG levels. In Kuramochi cells, 16:0-16:0 DAG levels were significantly reduced with oligo #2 and 16:0-18:0 DAG levels were significantly decreased with both oligos (Fig. 39F). In COV318 cells, a significant reduction in 18:1-18:1 DAG was observed with oligo #2 (Fig. 39G), similar to the reduction in 16:0-16:0 DAG levels observed in OAW28 cells with the same oligo (Fig. 39H). In OVCAR8 cells, 16:0-16:0 DAG levels were significantly reduced with oligo #2, while 18:1-18:1 DAG levels were significantly decreased with oligo #1 (Fig. 39J). Interestingly, in OVCAR4 cells, 16:0-18:0 DAG levels were significantly reduced with oligo #2. However, 16:0-16:0 DAG levels showed opposing changes: a significant increase with oligo #1 and a significant decrease with oligo #2 (Fig. 39I).

In summary, silencing GPAM and AGK in ovarian cancer cell lines resulted in cell line- and oligo-specific changes in intracellular PA and DAG levels, and no consistent impact on intracellular LPA levels. While PA and DAG are essential signaling lipids involved in processes such as cell migration, the observed changes in their levels did not consistently correlate with the reduced migration observed across the tested cell lines. Specific PA and DAG species, exhibited significant alterations in certain cell lines, but no single lipid species consistently reflected the migration phenotype in all cases, altogether suggesting that the role of GPAM and AGK on cell migration may not be linked to their respective roles in phospholipid biosynthesis.

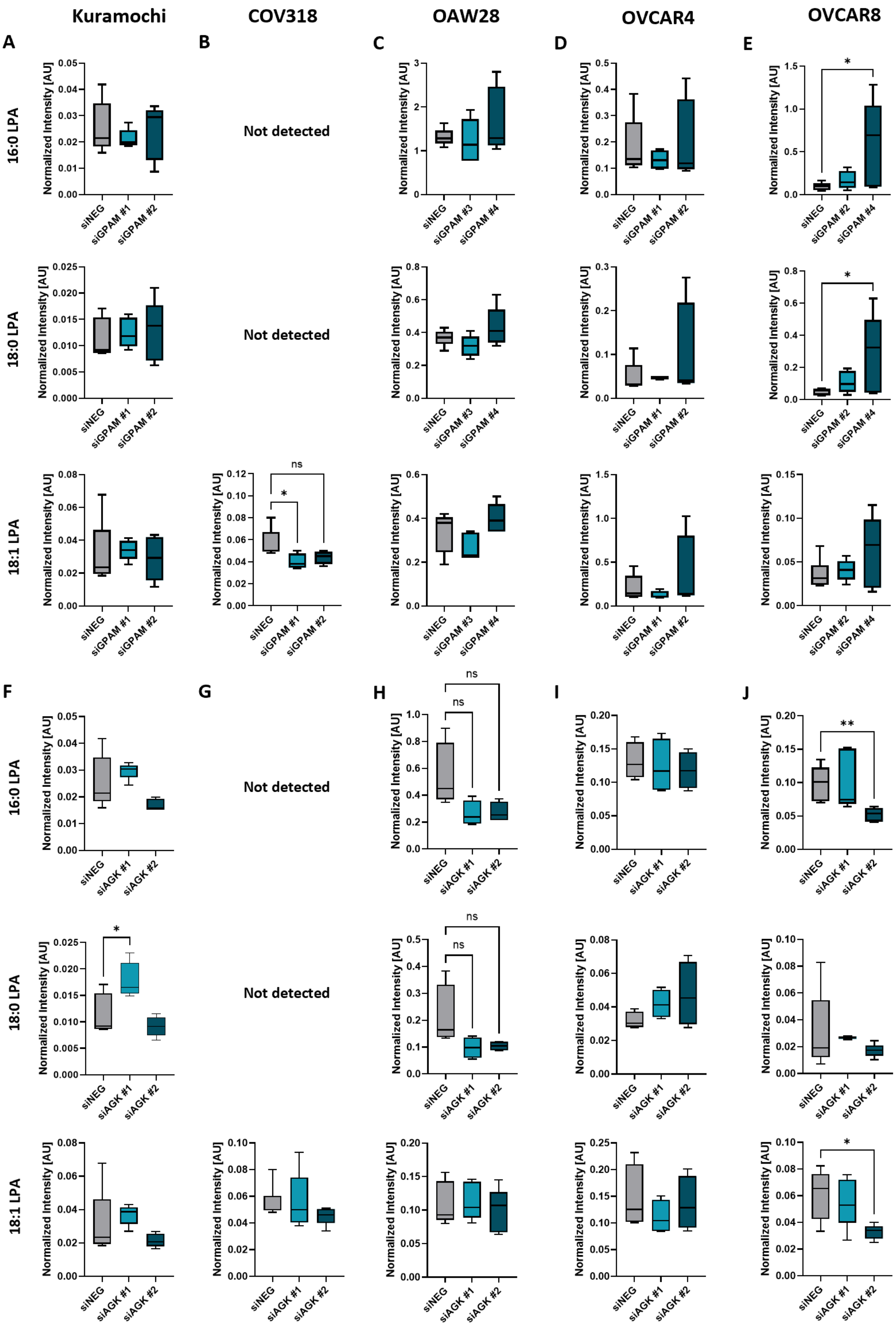

Figure 37: **Intracellular LPA levels upon silencing GPAM and AGK.** Intracellular 16:0, 18:0 and 18:1 lysophosphatidic acid (LPA) levels were determined with targeted LS-MS/MS following silencing GPAM and AGK in **A,F** Kuramochi, **B,G** COV318, **C,H** OAW28, **D,I** OVCAR4 and **E,J** OVCAR8 cells. Data are mean ±SD from at least four independent replicates (* P < 0.05; ** P < 0.01).

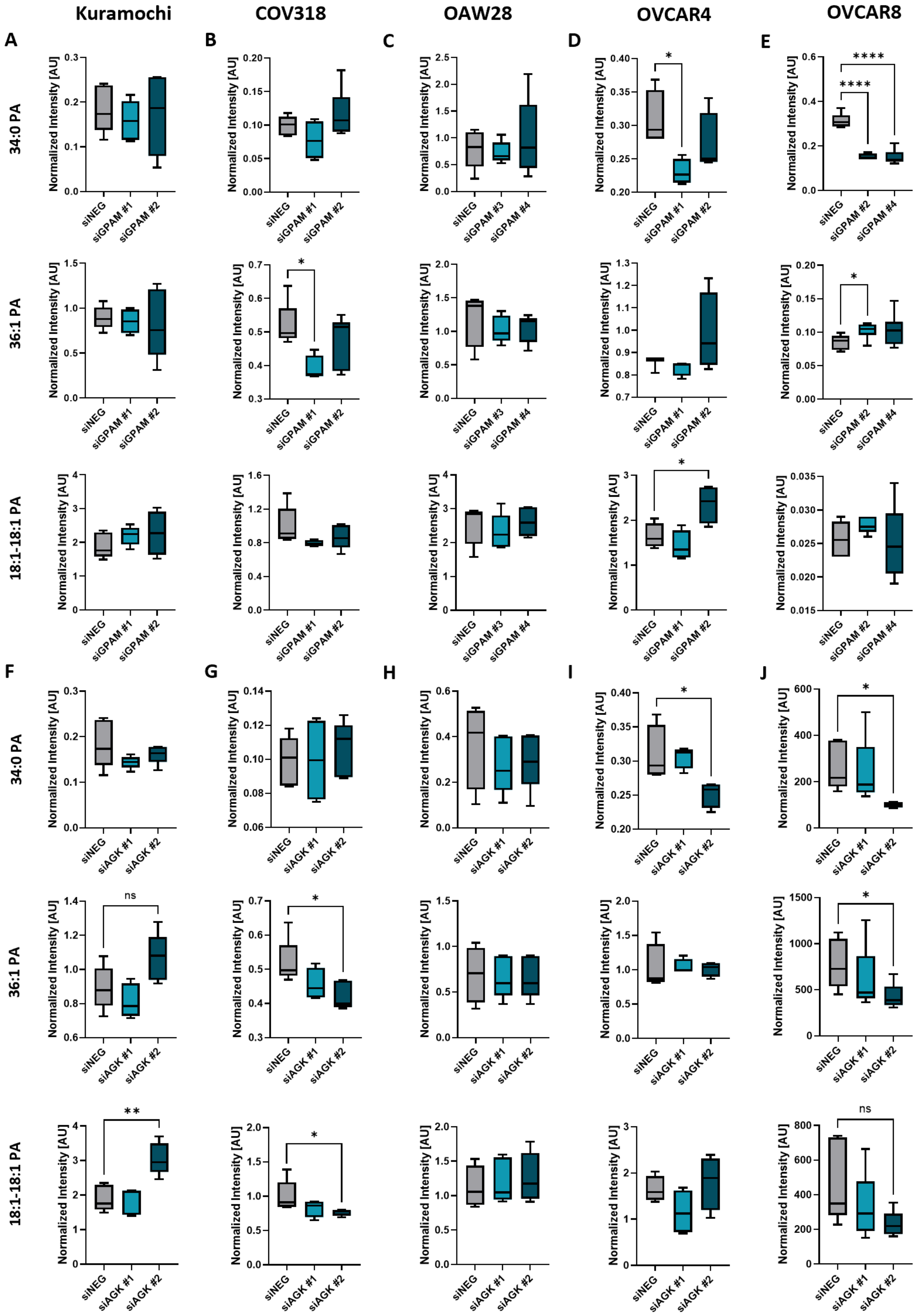

Figure 38: **Intracellular PA levels upon silencing GPAM and AGK.** Intracellular 34:0, 36:1 and 18:1-18:1 phosphatidic acid (PA) levels were determined with LS-MS/MS following silencing GPAM and AGK in **A,F** Kuramochi, **B,G** COV318, **C,H** OAW28, **D,I** OVCAR4 and **E,J** OVCAR8 cells. Data are mean ±SD from at least four independent replicates (* $P < 0.05$; ** $P < 0.01$; **** $P < 0.0001$).

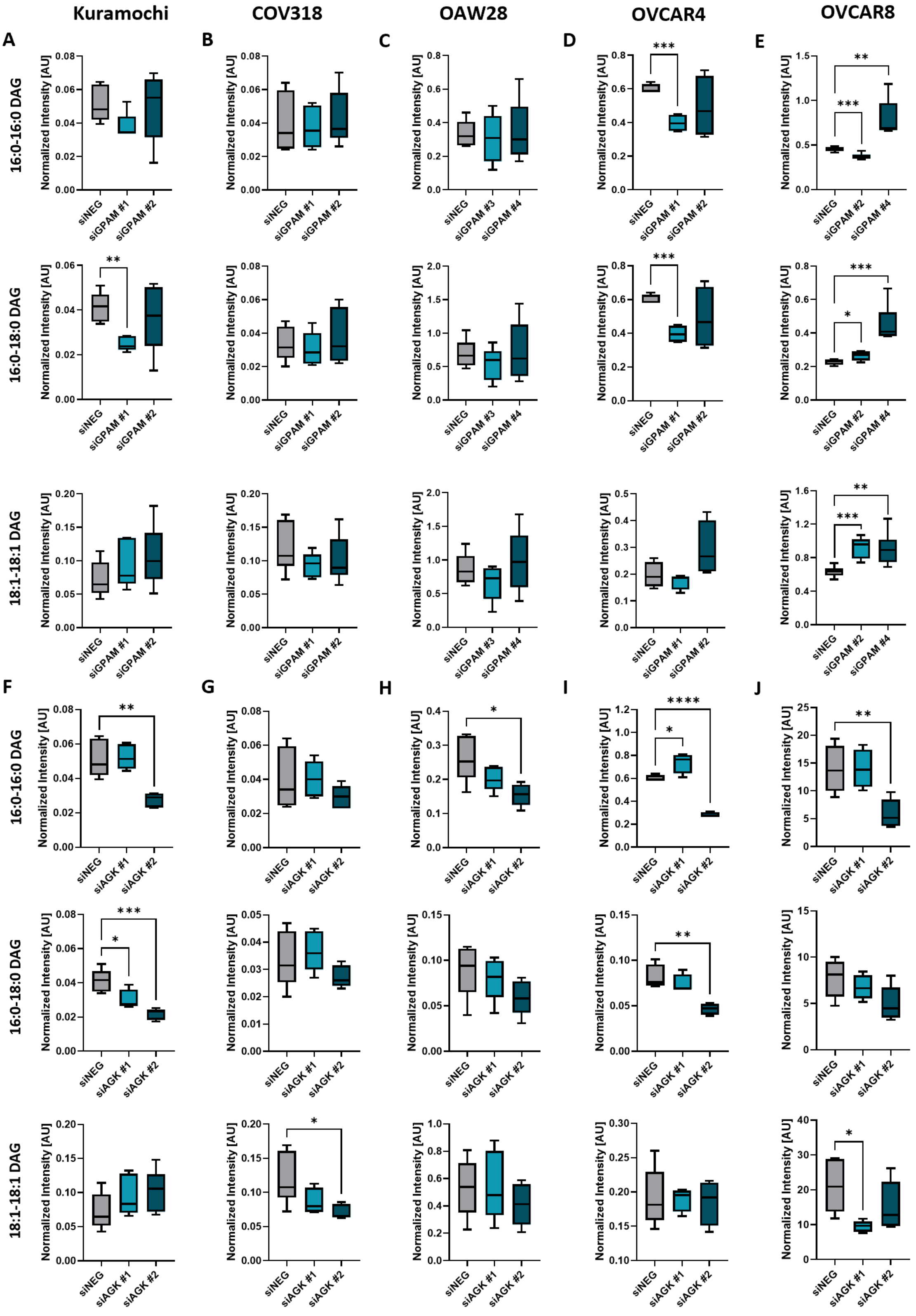

Figure 39: **Intracellular DAG levels upon silencing GPAM and AGK** Intracellular 16:0-16:0, 16:0-18:0 and 18:1-18:1 diacylglycerol (DAG) levels were determined with LS-MS/MS following silencing GPAM and AGK in **A,F** Kuramochi, **B,G** COV318, **C,H** OAW28, **D,I** OVCAR4 and **E,J** OVCAR8 cells. Data are mean ±SD from at least four independent replicates (* $P < 0.05$; ** $P < 0.01$; *** $P < 0.01$; **** $P < 0.0001$).

4.4.4 AGK overexpressing clones exhibit overall reduced lipid levels

AGK overexpression in OVCAR8 clones resulted in an enhanced migration and the formation of larger spheroids. AGK catalyzes the production of LPA and PA from MAG and DAG, respectively. Based on this reaction, it would be expected that AGK overexpression would increase intracellular LPA and PA, while reducing DAG levels due to its conversion into PA. As anticipated, targeted lipidomic analysis revealed that DAG levels were significantly reduced, reflecting enhanced AGK enzymatic activity (Fig. 40C). However, contrary to expectations, no corresponding increase in PA levels was observed (Fig. 40B). Instead, a significant reduction in all measured LPA and PA species was detected compared to the control cell line OV8_GFP (Fig. 40A, B). These findings highlight the complexity of phospholipid metabolism and suggest that AGK's role in promoting migration and spheroid growth may not solely depend on the production of LPA and PA. Further investigations are needed to elucidate the precise mechanisms by which AGK drives these phenotypic changes in ovarian cancer cell lines.

4.4.5 Expression of LPA-producing enzymes is not consistently affected by silencing GPAM or AGK.

In addition to the acylation of G3P by GPAM and phosphorylation of MAG by AGK, LPA can also by generated by three other GPAT enzymes, as well as through the hydrolysis of LPC by GDE4 and GDE7. To investigate whether silencing GPAM and AGK influences the expression of other LPA metabolizing enzymes as a means to compensate for changes in LPA levels in response to GPAM and AGK knockdown, the expression of the three GPATs (GPAT 2-4) and two GDEs were analyzed using quantitative PCR. However, the possibility of mutual compensation between AGK and GPAM was first examined. Interestingly, silencing GPAM led to an upregulation of AGK expression in almost cell lines (Fig. 41) except for OVCAR4, where a downregulation was seen with only one oligo (Fig. 41D). Specifically, increased AGK expression was observed in Kuramochi and OVCAR8 cells with both siGPAM oligos (Fig. 41A,E), and with only one oligo in COV318 and OAW28 cells (Fig. 41B,C). Conversely, silencing AGK resulted in a reduction in GPAM expression in Kuramochi, OAW28 and OVCAR8 cells with oligo #1 (Fig. 41F,H,J), and with both oligos in OVCAR4 cells (Fig. 41I). No changes in GPAM expression were observed in COV318 cells compared to the siNEG control (Fig. 41G). This findings suggest that tgere us sine compensation between GPAM and AGK at RNA level, as the cell attempts to adapt to disruption in the metabolic pathways they regulate.

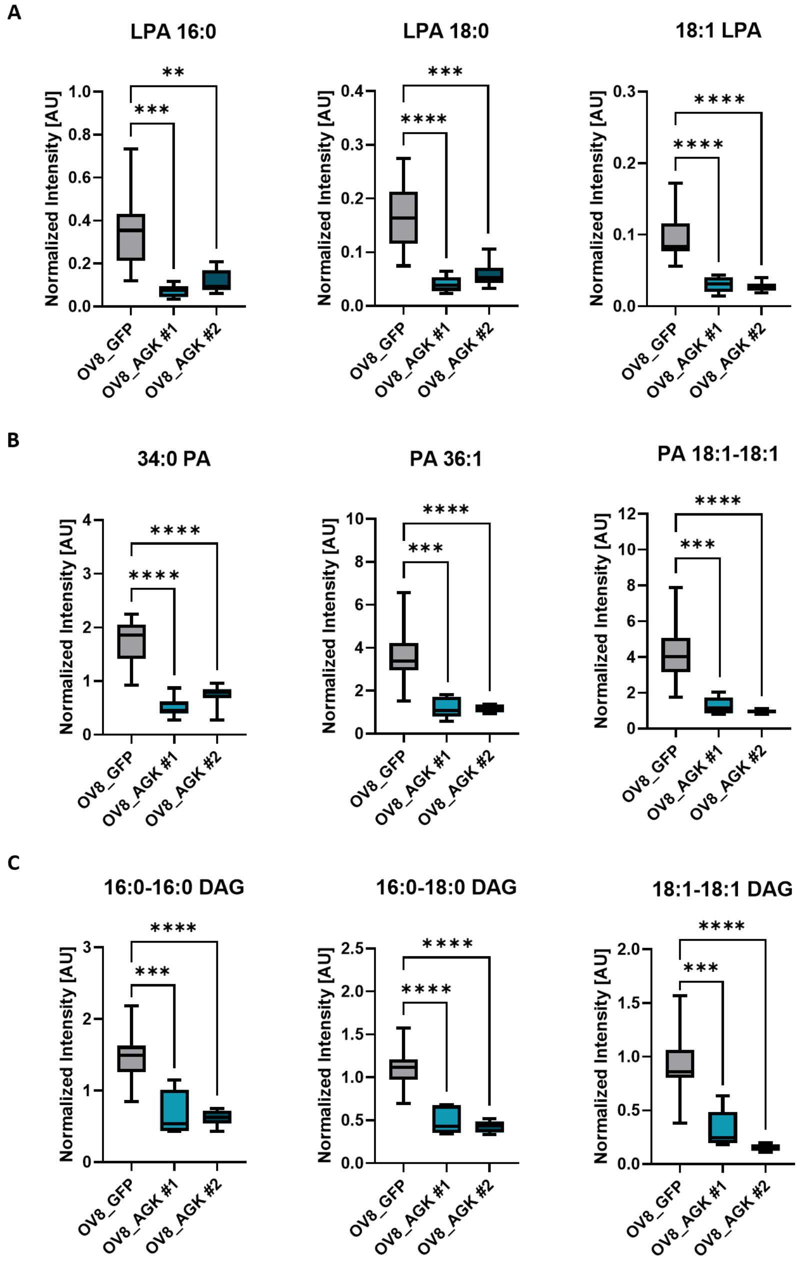

Figure 40: **Intracellular LPA, PA and DAG levels in AGK-overexpressing OVCAR8 clones.** Intracellular **A** 16:0, 18:0, 18:1 LPA, **B** 34:0, 36:1, 18:1-18-1 PA and **C** 16:0-16:0, 16:0-18:0, 18:1-18:1 DAG levels were determined with LS-MS/MS in AGK-overexpressing OVCAR8 cells. Data are mean ±SD from six independent replicates. (** $P < 0.01$, *** $P < 0.001$; **** $P < 0.0001$).

As described earlier, the acylation of G3P to LPA is catalyzed by four different GPATs, including GPAM, potentially explaining the lack of consistent changes in LPA levels upon GPAM silencing. To determine whether *GPAT2, GPAT3* or *GPAT4* expression are altered upon silencing GPAM and AGK, the expression of the three GPATs was measured in the five cell lines. Silencing GPAM led to a reduction in the mRNA expression of *GPAT2* in Kuramochi and OVCAR8 cells

(Fig. 42A,E). In contrast, GPAT2 expression increased in COV318 cells with siGPAM #1, and remained unchanged in OAW28 and OVCAR4 cells. GPAT2 levels were also significantly downregulated in Kuramochi cells after silencing AGK (Fig. 42A,), and except for a small but significant increase with one oligo in OAW28 cells (Fig. 42C), no changes in GPAT2 levels were observed in the other cell lines. The mRNA expression of *GPAT3*, an enzyme located on the endoplasmic reticulum membrane, was reduced in all cell lines after GPAM knockdown, with at least one of the two oligos used (Fig. 42F-J). Silencing AGK had no influence on *GPAT3* expression in all cell lines, except in COV318, where *GPAT3* expression decreased with one siAGK oligo (Fig. 42G). Finally, no significant alterations in *GPAT4* expression were observed in any knockdown condition for both enzymes (Fig. 42K-O). These findings suggest that GPAM and AGK knockdown induces cell line-specific alterations in the expression of other GPAT isoforms, potentially as part of a compensatory mechanism to maintain phospholipid homeostasis in the examined cell lines and may explain some of the cell-line specific effects seen in metabolite levels.

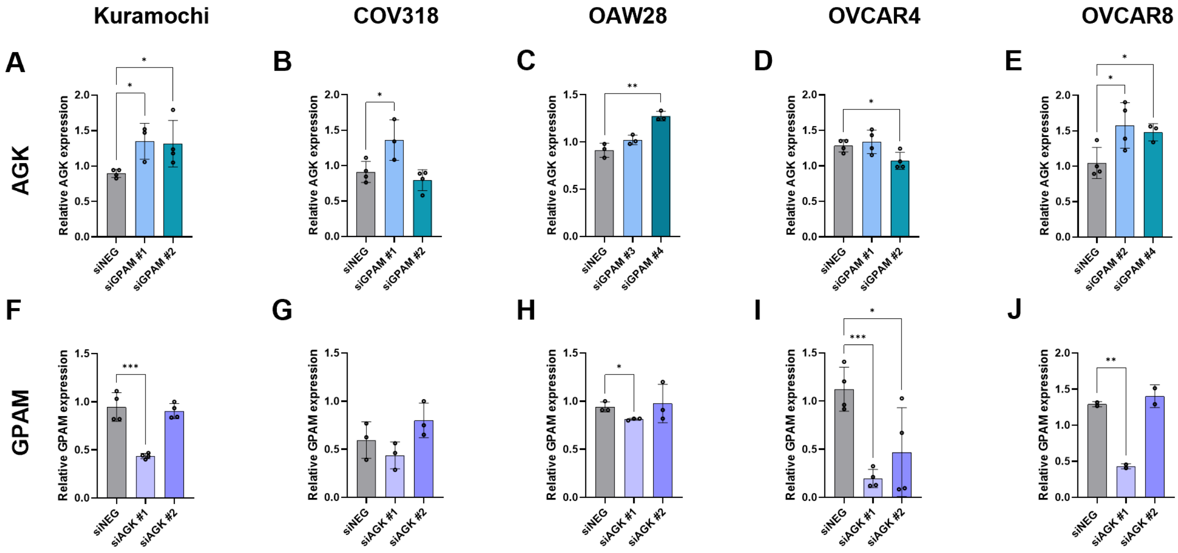

Figure 41: **Reciprocal regulation of GPAM and AGK expression** mRNA expression of the LPA-producing enzymes AGK and GPAM was analyzed in ovarian cancer cells Kuramochi, COV318, OAW28, OVCAR4 and OVCAR8 transfected with siRNA oligos targeting GPAM (siGPAM #1-#4) or AGK (siAGK #1-#2) compared to control cells (siNEG) transfected with scrambled siRNA. Data are mean ±SD of at least three independent biological replicates. (* $P < 0.05$; ** $P < 0.01$; *** $P < 0.001$).

Intracellular LPA can also be produced by two glycerophosphodiesterases, GDE4 and GDE7 that exhibit phospholipase activity to hydrolyze lysophospholipids. The effect of GPAM and AGK silencing on the RNA expression of both enzymes were investigated resulting in varying effects. For example, silencing GPAM in Kuramochi and COV318 cells led to increased *GDE4* expression, but with only one oligo significantly up in Kuramochi cells (Fig. 43A,B). In contrast, GPAM knockdown resulted in reduced *GDE4* expression in OVCAR8 cells with one oligo (Fig.

43E), and no effect in OAW28 cells (Fig. 43C). Silencing AGK led to a significant decrease in *GDE4* levels in COV318, OVCAR4 and OVCAR8 cells (Fig. 43G,D,E), and no change in Kuramochi and OAW28 cells (Fig. 43A,C). With respect to GDE7, silencing GPAM decreased decreased *GDE7* levels in Kuramochi, COV318 and OVCAR4 cell lines, with only one oligo leading to a significant downregulation in the latter two cell lines (Fig. 43F,G,I). Finally AGK silencing only influenced *GDE7* levels in COV318 and OVCAR4 cells (Fig. 43G,I), leading to opposite changes of increased and decreased expression, respectively.

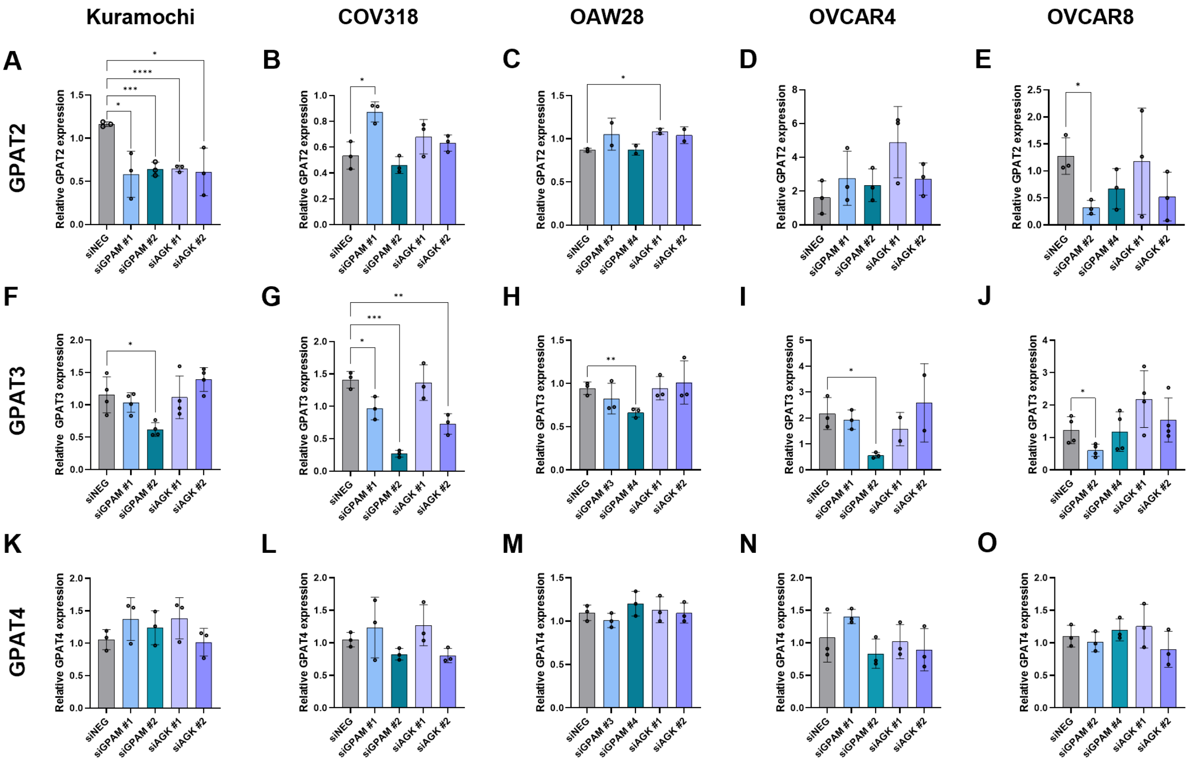

Figure 42: **GPAT expression in response to GPAM and AGK silencing.** The mRNA expression of other GPAT family members were analyzed in ovarian cancer cells Kuramochi, COV318, OAW28, OVCAR4 and OVCAR8 transfected with siRNA oligos targeting GPAM (siGPAM #1-#4) or AGK (siAGK #1-#2) compared to control cells (siNEG) transfected with scrambled siRNA. Data are mean ±SD of at least three independent biological replicates. (* $P < 0.05$; ** $P < 0.01$; *** $P < 0.001$; **** $P < 0.0001$)

Overall, the gene expression changes in response to AGK and GPAM knockdown suggest cell line and oligo-specific mechanisms regulating LPA levels. Notably, when GPAM expression is downregulated, there is a corresponding upregulation of *AGK*. This suggests that cells may adapt to compensate for the absence of GPAM in order to maintain intracellular LPA levels. In contrast, silencing AGK does not lead to a similar response; instead, *GPAM* expression is downregulated. Taken together, the expression patterns of GPAM, AGK, as well as those of GPATs and GDEs following the knockdown of GPAM and AGK, do not clarify why intracellular LPA levels remain mostly unchanged, as noted in the previous section (see section 4.4.3.

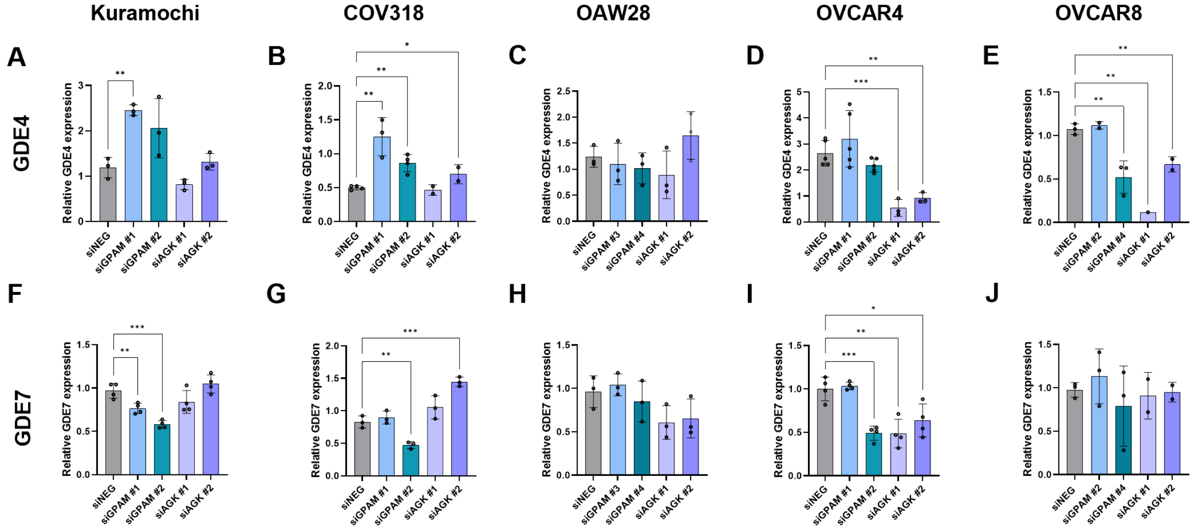

Figure 43: **GDE4 and GDE7 expression in response to GPAM and AGK silencing.** The mRNA expression of the LPA-producing enzymes AGK, GPAM, GPAT2-4, GDE4 and GDE7 was analyzed in ovarian cancer cells Kuramochi, COV318, OAW28, OVCAR4 and OVCAR8 transfected with siRNA oligos targeting GPAM (siGPAM #1-#4) or AGK (siAGK #1-#2) compared to control cells (siNEG) transfected with scrambled siRNA. Data are mean ±SD of at least three independent biological replicates. (* $P < 0.05$; ** $P < 0.01$; *** $P < 0.001$; **** $P < 0.0001$)

4.5 Investigating mechanisms of GPAM and AGK in cell migration regulation

Previous experiments examining the effect of AGK and GPAM on cell behavior have clearly demonstrated an association between the expression of both proteins and cell migration in several ovarian cancer cell lines. In order to elucidate the possible mechanism by which GPAM and AGK are linked to with cellular pathways and contribute to the regulation of migratory behaviors, several experimental approaches were employed using the OVCAR8 cells. Western blot analysis was conducted to evaluate the activation status of key signaling proteins, including Akt, Erk, β-Catenin, and GSK3β. Additionally, changes in the expression of EMT markers such as E-cadherin, N-cadherin, and vimentin were assessed. The analysis also included the activation status of RHO GTPases, which are critical regulators of cell motility [163]. Additionally, a mitochondrial stress test was performed based on two criteria: the mitochondrial localization of both GPAM and AGK, and that previous experiments by others revealed that silencing or inhibiting both enzymes resulted in altered mitochondria structure and function [97, 105].

4.5.1 Impact of GPAM and AGK expression on signaling proteins

Signaling proteins such as Akt, Erk, and GSK3β primarily exert their functions through phosphorylation, which are activated by various signaling pathways, including those initiated by LPA receptors. To investigate the activation status upon modulating GPAM and AGK expression, the expression of these proteins in both their phosphorylated and basal forms, was evaluated via western blot analysis. The detected band intensities were normalized to GAPDH as a loading control, and the ratios between the phosphorylated and non-activated forms were calculated (representative images shown in Appendix S4 and **??**). The experiments presented below focus on the OVCAR8 cells due to the strong reduction in migration, as well as spheroid size and outgrowth in response to GPAM and AGK silencing.

A significant reduction in the phosphorylation levels of Akt (p-Akt) was observed following the knockdown of both GPAM and AGK in OVCAR8 cells (Fig. 44A). Interestingly, AGK overexpression did not produce the opposite effect; instead, it also led to a decrease in Akt activation (Fig. 44E). Similarly, silencing GPAM and AGK resulted in reduced Erk phosphorylation (p-Erk), with the reduction being statistically significant only for siAGK #2 (Fig. 44B). However, no changes in p-Erk levels were observed upon AGK overexpression (Fig. 44F). The phosphorylation status of GSK3β (p-GSK3β) decreased upon silencing GPAM and AGK, with significant reductions observed for siGPAM #2 and siAGK #1 (Fig. 44C). Interestingly, AGK overexpression led to an increase in p-GSK3β levels in OVCAR8 cells, suggesting a reciprocal regulatory mechanism (Fig. 44G). GSK3β phosphorylation is known to play a critical role in modulating diverse cellular processes, including proliferation, cell growth and apoptosis, by altering the activity of its downstream target such as β-catenin. GSK3β phosphorylates β-catenin, marking it for recognition by specific proteins and ultimately leading to its ubiquitination and degradation by the proteasome [164]. To investigate the impact of GPAM and AGK expression on β-catenin signaling, its expression levels and phosphorylation status were analyzed. However, neither GPAM and AGK knockdowns nor AGK overexpression affected significantly the phosphorylation levels of β-catenin (Fig. 44D,H).

4.5.2 Impact of GPAM and AGK expression on EMT marker

Previous findings have demonstrated that silencing GPAM or AGK significantly reduces cell migration, while overexpression of AGK enhances migration in OVCAR8 cells. To explore whether these migration effects are mediated by EMT — a critical process often linked to cancer metastasis — the expression of classical EMT markers, including E-cadherin, N-cadherin, and vimentin, was investigated through western blot analysis in this cell line (Fig. 45). Notably, E-cadherin, an epithelial cell marker, was undetectable in both control siNEG and OV8_GFP conditions, underscoring the mesenchymal and highly migratory phenotype of the OVCAR8 cell line (Fig. 45E). Silencing GPAM and AGK in OVCAR8 cells did not yield significant changes in the expression levels of E-cadherin, such as an increase to indicate a reversal of EMT. In addition, no change in the mesenchymal markers N-cadherin or vimentin were observed (Fig. 45E). Quantitative analysis of band intensities confirmed the absence of substantial differences in these protein levels between control and knockdown conditions (Fig. 45A, D). Interestingly, overexpression of AGK resulted in a significant decrease in N-cadherin expression compared to the OV8_GFP control clone (Fig. 45B), while no significant changes were observed in E-cadherin or vimentin levels (Fig. 45D). These findings suggest that the effects of GPAM and AGK on OVCAR8 cell motility are unlikely to involve the EMT program; rather, their roles in migration may be mediated by alternative pathways. The reduced expression of N-cadherin in AGK-overexpressing clones may indicate a drastic alteration in the general properties of the cell line due to the monoclonal selection process, potentially leading to a less aggressive phenotype and diminished cell-cell adhesion characteristics associated with EMT.

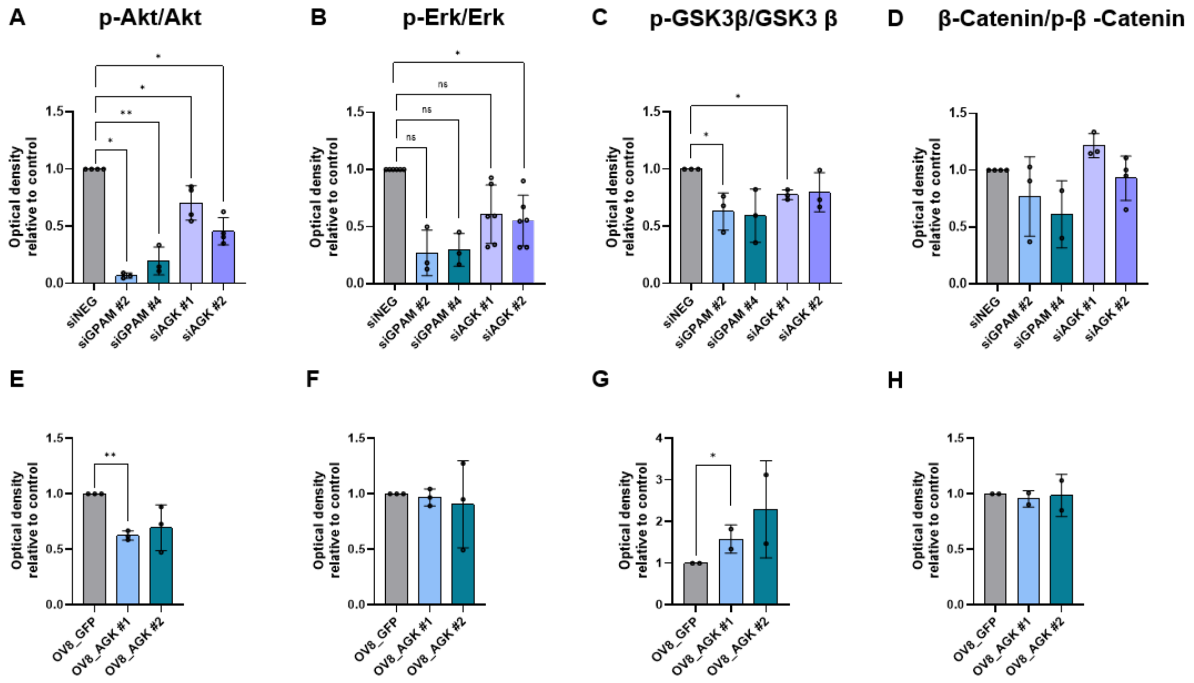

Figure 44: **Expression of signaling proteins in OVCAR8 cells upon GPAM and AGK modulation.** Western blot analysis was conducted to evaluate the basal expression and the phosphorylated status of key signaling proteins, including Akt, Erk, GSK3β and β-Catenin following **A-D** the silencing of GPAM and AGK as well as **E-H** AGK overexpression in OVCAR8 cells. The optical density of the detected bands was quantified using Fiji, and the levels were normalized to the loading control, GAPDH. The ratios of phosphorylated proteins (p-Akt, p-Erk, p-GSK3β, p-β-Catenin) to their non-phosphorylated counterparts were calculated. The data are presented as mean ± SD from two to three independent experiments, with values normalized to the siNEG control for data visualization. For statistical analysis, a paired Student's t-test was performed before normalization (* $P < 0.05$; ** $P < 0.01$).

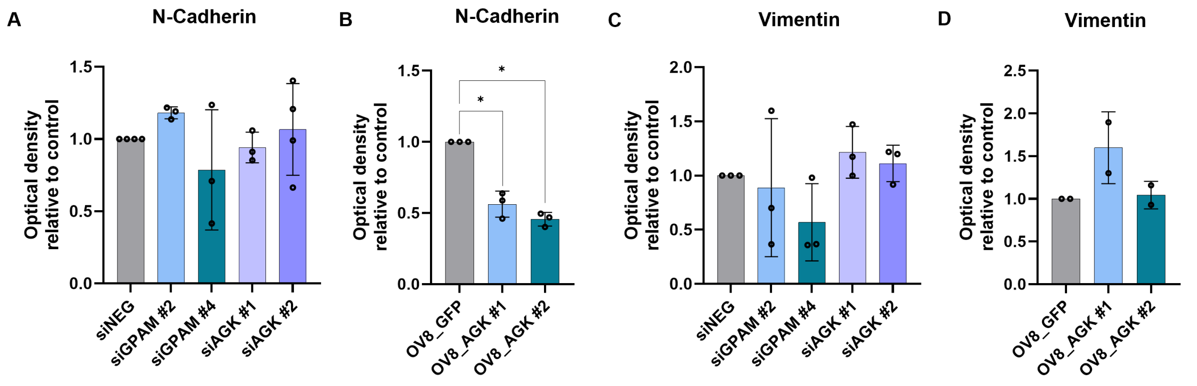

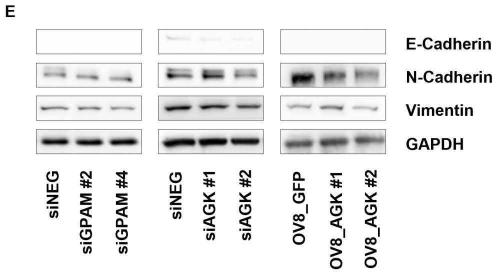

Figure 45: **No effect of GPAM and AGK modulation on EMT marker expression in OVCAR8 cells** Western blot analysis of epithelial-mesenchymal transition (EMT) markers N-cadherin, E-cadherin, and vimentin in OVCAR8 cells following GPAM and AGK silencing or AGK overexpression. **A** Quantification of N-cadherin expression (normalized to GAPDH) upon GPAM and AGK knockdown. **B** N-cadherin expression levels in AGK-overexpressing cells. **C** Vimentin expression quantification following GPAM and AGK knockdown. **D** Vimentin levels in AGK-overexpressing clones. **E** Representative western blot images for all conditions tested. Protein expression was quantified by optical density measurements and normalized to GAPDH. The data are presented as mean ± SD from two to three independent experiments, with values normalized to the siNEG control for data visualization. For statistical analysis, a paired Student's t-test was performed before normalization (* $P < 0.05$)

4.5.3 Impact of GPAM and AGK expression on RhoA GTPase activation

To further investigate the mechanism by which GPAM and AGK expression influences the migratory behavior of ovarian cancer cells, the activation status of RhoA GTPase was analyzed. Rho GTPases are essential regulators of cell migration and invasion, playing a central role in the dynamic reorganization of the actin cytoskeleton, which is crucial for cellular motility. To assess this, the active GTP-bound form of Rho GTPases was extracted using a pull-down method, followed by detection through western blot analysis. This analysis was performed in OVCAR8 cells after GPAM and AGK knockdown, as well as in AGK-overexpressing OVCAR8 clones. The results from the positive control, treated with the non-hydrolysable GTP analog (GTPγS), and the negative GDP-treated controls revealed distinct levels of RhoA activation, confirming the successful establishment of the assay (Fig. 46A, E).

The intensity of the detected bands for active GTP-bound RhoA GTPases in OVCAR8 cells with altered GPAM and AGK expressions was normalized against the baseline levels of RhoA GTPases in the corresponding samples prior to the pull-down extraction. Despite the significant impact of GPAM and AGK on cell migration, no detectable changes in RhoA activation were observed following their silencing (Fig. 46B, C, F, G). Similarly, AGK overexpression did not lead to any significant alterations in RhoA activation status compared to the control group (Fig. 46D, H). For all experimental conditions, the Rho GTPase activity assay was performed in two independent experiments, both yielding consistent and reproducible results. However, to draw statistically robust conclusions, at least one additional replicate would be necessary. These findings suggest that while GPAM and AGK play crucial roles in regulating cell migration, their roles in this process are not mediated via the Rho GTPases. This lack of change in RhoA activation could indicate that other signaling pathways or mechanisms are involved and should be followed-up in future work to understand how AGK and GPAM influence migration.

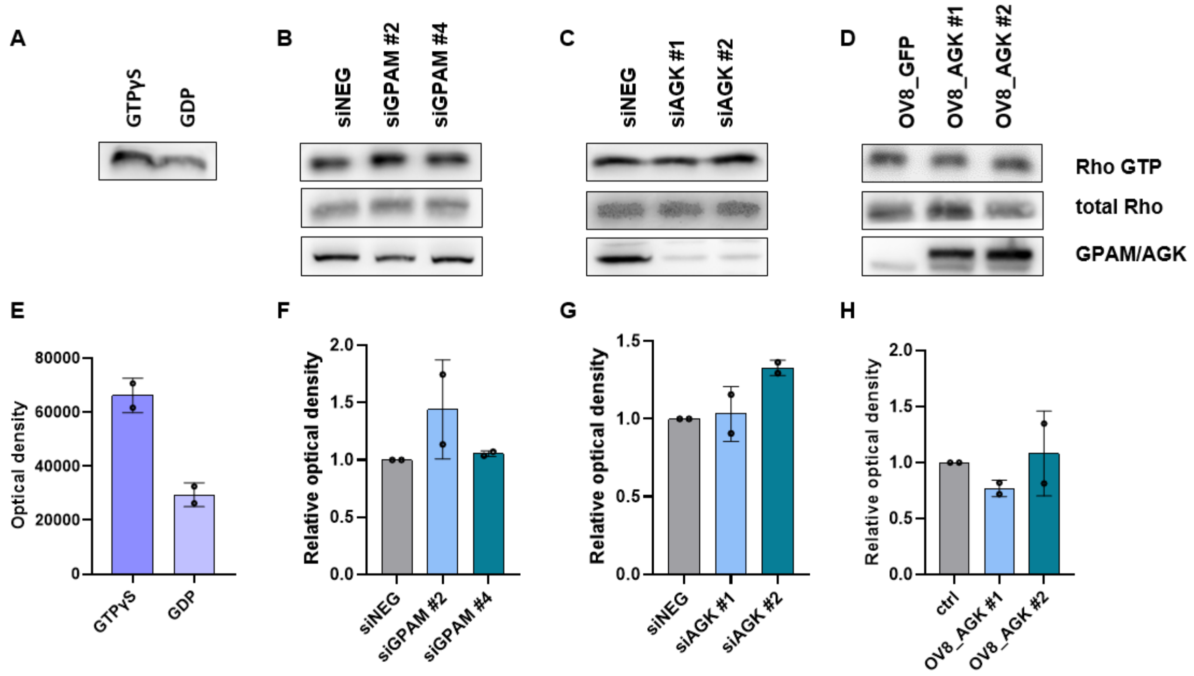

Figure 46: **Impact of AGK and GPAM expression on RhoA GTPase activation** To investigate the activation status of RhoA GTPase, a pull-down assay followed by Western blot analysis was performed. **A, E** To test the effectiveness of the assay, a positive control treated with the non-hydrolyzable GTP analog GTPγS, alongside negative samples treated with GDP were analyzed. The band intensities were quantified using Fiji. Representative Western blot images from the Rho GTPase pull-down assay show the levels of active Rho GTP-bound, total Rho, and the expression of GPAM and AGK in OVCAR8 cells following **B** GPAM and **C** AGK knockdown and **D** AGK overexpression. **F-H** The optical density of the detected bands, normalized to the intensity of the total Rho band in the corresponding sample was quantified. The data represent the average RhoA GTPase activity for each condition from two independent experiments normalized to siNEG control.

4.6 Impact of GPAM and AGK expression on mitochondrial function

Mitochondrial function in response to silencing GPAM and AGK and overexpressing AGK in OVCAR8 cells, was assessed using the Seahorse XF Cell Mito Stress Test Kit (Fig. 47). The oxygen consumption rate (OCR) was measured in real-time after sequential injections of inhibitors targeting proteins in the respiratory chain. Addition of the ATP synthase inhibitor oligomycin led to the expected decrease in OCR, reflecting the inhibition of ATP-linked respiration. Subsequently, the injection of FCCP - a mitochondrial uncoupler - caused an increase in OCR by disrupting the proton gradient across the mitochondrial inner membrane, thus driving the electron transport chain at its maximal capacity. This resulted in the maximal respiration rate. Finally, injection of rotenone (a complex I inhibitor) and antimycin A (a complex III inhibitor) caused a steep decrease in OCR, representing the complete inhibition of mitochondrial respiration and revealing the non-mitochondrial OCR. This profile follows the typical pattern observed in the mitochondrial stress test, and in the present work, the results were normalized by staining the cells with Hoechst dye after the assay to determine the cell number in each well (Fig. 47A,C,E). In addition to the OCR, the extracellular acidification rate (ECAR) was also measured - an important indicator used in mitochondrial stress tests to assess glycolytic activity in cells. The ECAR measures the rate at which protons are released into the extracellular environment, which is primarily a consequence of glycolysis and lactate production (Fig. 47B,D,F). The initial OCR levels in OVCAR8 cells remained unchanged following GPAM knockdown compared to the siNEG control. Measurements taken after the injection of inhibitors also did not reveal any significant alterations in the OCR profiles (Fig. 47A). However, a notable increase in ECAR levels was observed with both siGPAM oligos compared to siNEG (Fig. 47B). In contrast, silencing AGK resulted in a consistent increase in OCR across the entire profile, which was more pronounced with oligo siAGK #1 (Fig. 47C). Interestingly, while the ECAR profile remained unchanged with siAGK #1 compared to siNEG, it increased with siAGK #2 (Fig. 47D). Conversely, a decrease in maximal OCR was observed in clones overexpressing AGK, although the overall OCR profile remained consistent with the control (Fig. 47E). No substantial changes were detected in the ECAR profile when compared to the OV8_GFP control clone (Fig. 47F).

To assess the changes in parameters reflected by the OCR during sequential inhibitor applications, the basal, maximal, ATP-linked, and non-mitochondrial OCR were calculated from the profile. The basal OCR, which indicates oxygen consumption in the absence of inhibitors, remained unchanged following GPAM knockdown in OVCAR8 cells (Fig. 48A). In contrast, AGK knockdown resulted in an increase in basal OCR (Fig. 48E), while its overexpression led to a decrease (Fig. 48I), which was significant for one of the two siRNA oligos and clones investigated, respectively. The maximal OCR, defined as the difference between the OCR after FCCP injection and the non-mitochondrial OCR, showed no impact in response to GPAM silencing (Fig. 48B). However, silencing AGK with oligo #1 led to a significant increase, while both AGK-overexpressing clones exhibited a significant decrease in maximal OCR (Fig. 48F, J). ATP-linked OCR, calculated by subtracting the non-mitochondrial OCR from the OCR measured after oligomycin injection, was unaffected by GPAM knockdown (Fig. 48C). Conversely, and as seen for basal and maximal OCR, silencing AGK with siAGK #1 resulted in a significant increase, while AGK-overexpressing clones demonstrated a significant decrease in ATP-linked OCR (Fig. 48G, K). Interestingly, non-mitochondrial OCR, which reflects mitochondrial inactivity following the injection of rotenone/antimycin A, increased after silencing both GPAM and AGK with both oligos (Fig. 48D, H). In line with this observation, the AGK-overexpressing clone OV8_AGK #2 showed a significant reduction in non-mitochondrial OCR (Fig. 48L). These results indicate that silencing GPAM appear to have no major effect on mitochondrial respiration, whereas slterations in AGK significantly influenced mitochondrial respiration parameters. Furthermore, both proteins influenced non-mitochondrial OCR, overall suggesting a complex interplay between these proteins and cellular bioenergetics in ovarian cancer cells. Therefore, future investigations should focus on elucidating how GPAM and AGK expression mediates their effects on cellular bioenergetics and non-mitochondrial OCR, and whether these changes are linked to the migratory capacity of cells mediated by GPAM and AGK.

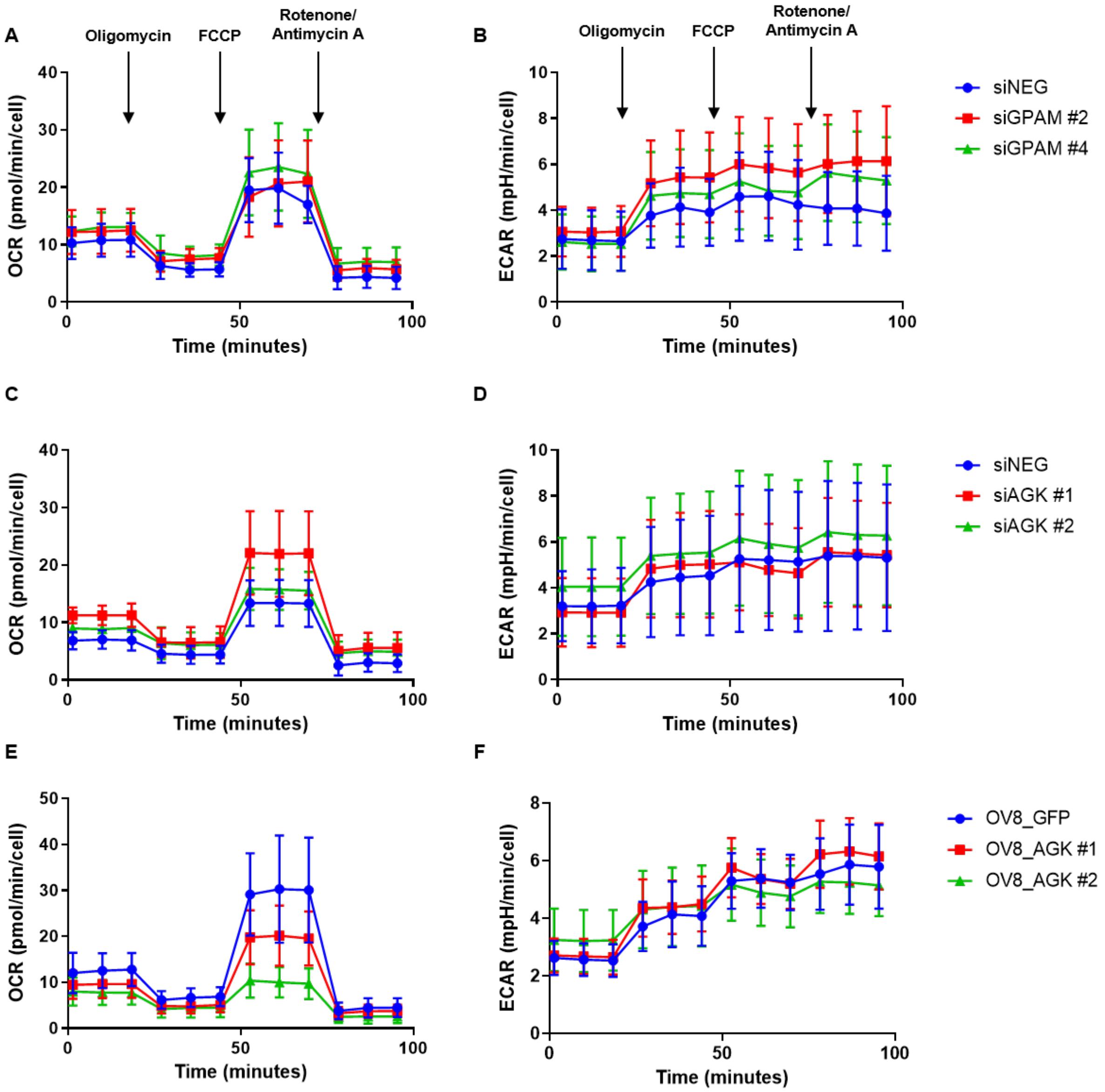

Figure 47: **Mitochondrial stress test in OVCAR8 cells upon GPAM and AGK knockdown and AGK overexpression.** Mitochondrial stress test was performed using the Seahorse XFe24. The results show the oxygen consumption rate (OCR) and the extracellular acidification rate (ECAR) data in pmol/min/cell upon **A, B** GPAM and **C, D** AGK knockdown and **E, F** AGK overexpressing OVCAR8 cells. Each experiment was repeated three independent times, with at least three technical replicates (wells). Each datapoint represent the mean ±SD of three measurements per well.

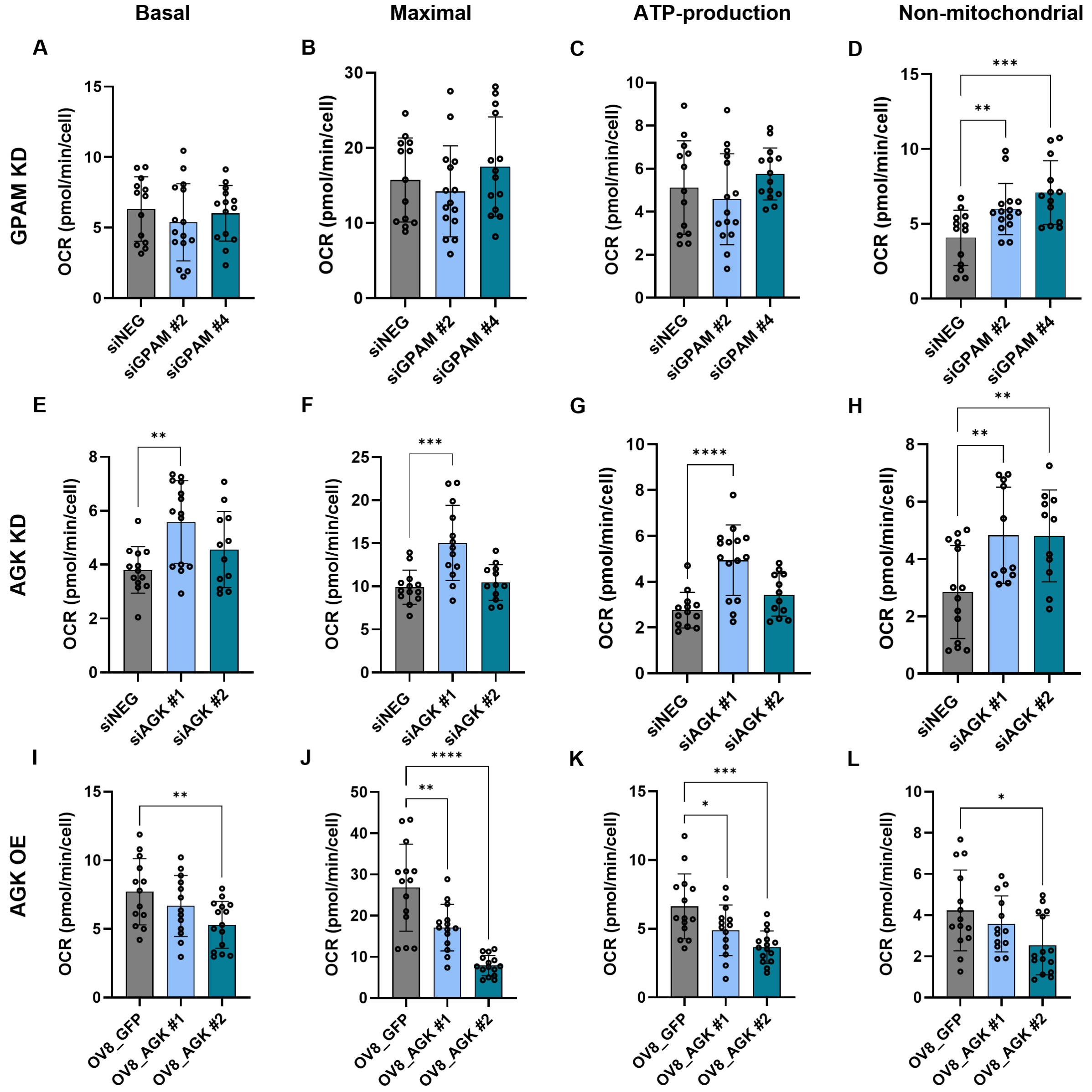

Figure 48: **Mitochondrial respiration function parameters of OVCAR8 cells upon GPAM and AGK knockdown and AGK overexpression.** Mitochondrial parameters derived from the Seahorse XFE24 oxygen consumption rate (OCR) data were evaluated. **A** Basal OCR represents the baseline respiration of cells under normal conditions. **B** Maximal OCR is measured after the addition of FCCP, reflecting the maximum respiratory capacity. **C** ATP-production linked OCR is determined following oligomycin treatment, indicating the portion of respiration coupled to ATP production. **D** Non-mitochondrial OCR is measured after rotenone/antimycin A treatment, reflecting oxygen consumption not associated with mitochondrial activity. Each experiment was repeated three independent times, with at least three technical replicates (wells). Each datapoint represent the mean ±SD of three measurements per well. (* $P < 0.05$; ** $P < 0.01$; *** $P < 0.001$; **** $P < 0.0001$).

5 Discussion

Metastasis is a significant contributor to cancer-related mortality worldwide, and as a result, understanding the underlying mechanism of the disease can contribute to the identification of potential new therapeutic targets [1]. Previous research in the lab that prompted the current PhD thesis identified the mitochondrial LPA-producing enzyme GPAM as a key player in cell migration in a number of different cancer cell lines [9]. Interestingly, several published studies has reported that another mitochondrial LPA-producing enzyme, namely AGK is also involved in cancer-promoting processes in diverse cancer types [48, 101–103, 105], supporting the relevance of intracellularly-produced LPA in regulating cell behavior, by mechanisms still not fully understood. In our earlier work with GPAM, it was shown that silencing GPAM in breast, endometrial and clear cell ovarian cancer cell lines significantly decreased migration, and reduced subcutaneous tumor growth in a xenograft mouse model of the ES2 cells [9]. Moreover, in MCF7 breast cancer cells, silencing GPAM not only decreased migration but also reduced intracellular levels of its enzymatic product, LPA. In addition, overexpressing GPAM in HEK293 cells increased migration, which was associated with higher intracellular LPA levels. When LPA was directly introduced into MCF7 cells via transfection to bypass the binding of extracellularly added LPA to receptors on the plasma membrane, migration also significantly increased compared with cells treated with either LPA or Lipofectamine transfection reagent alone. Higher intracellular LPA levels were indeed detected in the faster migrating cells, altogether, indicating that intracellular LPA may be important for migration. However, the mechanisms by which intracellular LPA mediate an effect on cell migration is not known. Therefore, the aim of this PhD thesis was to further explore the contribution of the mitochondrial, LPA-producing enzymes, GPAM and AGK to cancer-related endpoints, including cell migration and three dimensional spheroid formation and outgrowth, and to study the underlying mechanism by comprehensively characterizing changes in intracellular phospholipid levels after gene silencing or overexpression, as well as mitochondrial function which has been linked to migration in recent literature [86]. Since high GPAM expression was found to be associated with shorter overall survival in human ovarian cancer [9], HGSOC cell lines were used as model systems in the present work. Overall, the results of this PhD thesis corroborate and expand upon previous findings, demonstrating that both GPAM and AGK significantly impact cell migration and spheroid dynamics in HGSOC cells. Interestingly, and contradictory to reported findings in MCF7 cells, the underlying mechanisms appear to be independent of changes in the levels of intracellular lipids such as LPA, which speaks against the hypothesis that the cytoskeletal dynamics that regulate cell migration are dependent on lipid levels changes mediated by the activity of GPAM or AGK.

5.1 Modulating GPAM and AGK expression influences ovarian cancer cell migration but has no consistent effect on colony formation *in vitro*

A central finding of this PhD thesis is the significant influence of GPAM and AGK on the migratory capabilities of ovarian cancer cells. Silencing either enzyme consistently resulted in reduced cell migration across various ovarian cancer cell lines; whereas AGK overexpression led to enhanced migration in OVCAR8 cells, underscoring the essential role of both enzymes in promoting cellular motility. These findings support previous reports on the involvement of GPAM in breast cancer migration, as well as AGK's role in migration in various cancer types, including prostate, esophageal, and hepatocellular carcinoma [9, 48, 101]. Importantly, the silencing of GPAM and AGK in the present work did not affect the overall morphology or viability of the cells, as assessed through visual inspection and comparisons of cell numbers between conditions (data not shown). No morphological change was also observed in the AGK overexpressing OVCAR8 cells compared to the parental cell lines. This indicates that the observed changes in migration are not due to cytotoxic effects but rather reflect specific alterations in migratory pathways. However, to gain a more comprehensive understanding of the effects of silencing these enzymes, further investigations into cell proliferation and viability are warranted. For instance, using bromodeoxyuridine (BrdU) labeling to measure proliferation or CellTiter-Blue (CTB) for cell viability could provide valuable insights. The BrdU assay measures the incorporation of BrdU into newly synthesized DNA, allowing quantification of cell proliferation rates. On the other hand, the CTB assay assesses cell viability based on the metabolic activity of viable cells, providing a clear indication of how silencing GPAM and AGK would affect overall cell health. A more comprehensive approach would clarify whether the observed changes in migration are truly independent of cytotoxic effects or if subtle alterations in cell health might influence migration dynamics. In contrast to the cells in which AGK and GPAM were silenced, the viability of AGK-overexpressing clones was specifically assessed, because it could not be excluded that the lengthy process of monoclonal selection induce significant changes in cell metabolism, leading to changes in viability. Fortunately, the AGK-overexpressing clones did not exhibit any changes in viability when compared to control cells, as shown in figure 33.

Both oligonucleotides targeting GPAM and AGK demonstrated consistent and significant effects on migration. However, an exception was observed in OVCAR4 cells, where downregulation of AGK led to a reduction in migration with only one oligonucleotide, while four other oligos, resulted in either upregulated migration or no change. This discrepancy may arise from several factors that are unique to OVCAR4 cells (variations in receptor expression, intracellular signaling pathways, or compensatory mechanisms). Notably, OVCAR4 cells exhibit the highest intracellular levels of 18:1 LPA, which is generated from monoacylglycerol with an oleoyl group and is the preferred substrate for AGK. This might suggest that AGK's enzymatic activity is particularly critical in OVCAR4 cells in order to maintain the high LPA levels, leading to a direct compensatory response upon AGK knockdown. However, there was no evidence of upregulated expression of other LPA-producing enzymes nor were there changes in intracellular LPA levels upon AGK silencing in this cells.

The simultaneous knockdown of both GPAM and AGK - here only studied in Kuramochi cells - did not produce additive or synergistic effects on migration. This lack of synergy suggests that these enzymes function through overlapping or convergent pathways, potentially regulating a shared process that is critical for cell motility. The absence of a synergistic effect indicates that the two enzymes might be compensating for each other's functions rather than acting independently. In this particular cell line, it was observed that GPAM knockdown led to an upregulation of AGK. Such interactions could be indicative of a functional redundancy between the two enzymes, where the inhibition of one enzyme prompts the upregulation of the other to sustain essential metabolic processes. However, AGK knockdown resulted in a significant decrease in GPAM expression with one oligonucleotide. Given these findings, further investigation into the redundancy and compensatory mechanisms between GPAM and AGK in additional cell lines is warranted.

In contrast to the consistent influence on cell migration, the impact of GPAM and AGK silencing on colony formation was highly dependent on the specific cell line being studied. The capacity of cells to survive as a single cell and replicate indefinitely to establish a colony, i.e. their clonogenicity, serves as a marker of their tumor initiating potential [165]. Silencing GPAM and AGK in panel of ovarian cancer cell lines resulted in significant variations in the colony forming ability of the different cell lines, underscoring the cell line-specific nature of these effects. For instance, in Kuramochi cells, the knockdown of both GPAM and AGK led to a notable reduction in colony numbers with the two oligonucleotides used to silence each gene. In contrast, silencing GPAM and AGK in OVCAR8 cells resulted in an increase in colony numbers either with both oligos or one oligo alone, respectively. Additionally, overexpressing AGK in OVCAR8 cells also resulted in enhanced colony formation, albeit with one of the two clones studied. A drawback of the present work is that only colony number was assessed, while reports have emphasized that colony size can also provide valuable insights [166]. While colony number primarily reflects cytotoxic effects on cells, colony size — by indicating the number of cells per colony — can reveal information on cytostatic effects of the target gene. Thus, a reduction in colony size would suggest a decrease in cell proliferation and growth, independent of changes in colony number. This distinction is crucial for accurately interpreting the effect of targeting both enzymes on ovarian cancer cells and could be addressed in future studies.

5.2 GPAM and AGK expression influence spheroid formation and outgrowth

Three-dimensional (3D) cell culture models have emerged as a crucial tool to study the metastasis of ovarian cancer, particularly due to their ability to more accurately mimic the *in vivo* environment compared to traditional two-dimensional (2D) cultures [159, 161]. During the metastatic process, detached ovarian cancer cells can form aggregates, so called spheroids, which enable them to survive in suspension within the peritoneal fluid, protecting them from immune responses and harsh conditions like nutrient deprivation or chemotherapy [160]. These clusters also enhance the ability of cancer cells to attach to and invade new tissues, particularly in the peritoneal lining and nearby organs [159]. Understanding the molecular mechanisms that regulate spheroid formation can provide insights into how ovarian cancer spreads. In this PhD thesis, an optimized 3D model using the OVCAR8 cell line was established. It was observed that cells with downregulated GPAM and AGK expression formed significantly smaller spheroids compared to the control cells. Furthermore, reduced expression of both enzymes significantly impaired cell's ability to maintain spheroid architecture, resulting in less round and disrupted spheroids. The compromised shape and reduced size may indicate that GPAM and AGK play a potential role in regulating cell-cell interactions to maintain structural integrity within 3D tumor models. AGK overexpression in OVCAR8 cells in contrast enhanced spheroid size but introduced structural irregularities. The disrupted shape could imply that AGK, when deregulated, affects not only cell migration, but also cell-cell adhesion or cell polarity all of which are essential for maintaining spheroid architecture.

GPAM and AGK silencing led to a significant reduction of cells spreading from the 3D spheroids onto cell culture plates in the spheroid outgrowth assay. The area of spreaded cell in the control conditions was four times the size of the initial spheroid, while the spread of the cells upon knockdowns was only twice their original size, indicating a marked reduction in migration of cells detaching from the spheroids. The impaired outgrowth in the knockdown conditions highlights the potential involvement of GPAM and AGK in promoting cell motility, adherence and cell-cell adhesion, all characteristics necessary for efficient cancer cell dissemination in the context of ovarian cancer. Interestingly, the spread into the 2D cell monolayers from the larger spheroids created from AGK-overexpressing cells was also significantly reduced. The increased AGK expression might promote cell adhesion, causing cells to maintain their spheroid form instead of losing the 3D structure and cell-cell contacts. This unexpected outcome highlights the possibility that deregulated AGK expression disrupts cellular adhesion properties, cytoskeletal dynamics, or interactions with the extracellular matrix. The reduced outgrowth, alongside the disrupted spheroid morphology, reinforces the hypothesis that proper regulation of AGK is essential for balancing both the structural integrity of spheroids and their invasive potential, both key factors in ovarian cancer metastasis.

To understand the role of GPAM and AGK in spheroid formation and outgrowth and potentially identify molecular pathways that may be exploited to limit ovarian cancer spread, more in depth analyses are required in future studies. For instance, cell-cell adhesion could be investigated in more detail, as the spheroids form smaller and looser cell aggregates after GPAM and AGK knockdown [167]. To this end, the expression of proteins important for cell-cell contacts, such as cadherins and integrins, could be investigated, either by quantitative PCR or immunohistological (IHC) stainings. Interestingly, integrin β1 has been shown to regulate the formation and adhesion of multicellular spheroids in ovarian cancer [168]. In our previous research, we demonstrated that the downregulation of EDI3, which acts upstream of GPAM to produce its substrate G3P, reduces cell migration, adhesion, and spreading in breast cancer cells, which may be mediated via integrin β1 [169]. Therefore, it would be valuable to investigate how the expression and localization of integrins are affected by the deregulation of GPAM and AGK, as well as during spheroid formation. Furthermore, cells within an organism (as opposed to a cell culture dish) are exposed to an entirely different microenvironment during the metastasis process that is influenced by nutrient gradients, growth hormones, and cell surfaces that all work together to guide migration [170]. Therefore, to better mimic *in vivo* conditions, it has been suggested that spheroids schould be embedded into a 3D matrix of extracellular proteins, such as collagen or fibronectin in order to provide a more realistic 3D environment for migration, rather than the 2D surface used in the current assays [171]. Furthermore, spheroid co-culture with other cells, such as fibroblasts, endothelial cells and adipocytes, would perfectly mimic the *in vivo* situation. For instance, a lipid-rich microenvironment has been shown to promote carcinogenesis and metastasis formation, which is highly relevant considering that ovarian cancer metastasizes primarily to the omentum, an adipose-rich tissue in the abdominal cavity [172–175]. In summary, the findings underscore the importance of AGK and GPAM in maintaining spheroid size and shape, by yet an unknown mechanism. Understanding these process is particularly relevant in the context of ovarian cancer metastasis, where spheroid formation in malignant ascites and subsequent outgrowth into the peritoneal cavity are key steps in disease progression [139, 141].

5.3 Exploring mechanisms by which GPAM and AGK may regulate the migration of ovarian cancer cells

5.3.1 No common alterations in intracellular lipid levels

Surprisingly, the changes in cell migration observed upon silencing GPAM and AGK were not consistently linked to alterations in the intracellular levels of GPAM's and AGK's enzymatic product LPA, nor with downstream lipids PA and DAG. This finding contradicts previous studies that suggested a link between GPAM-mediated migration and intracellular LPA levels in breast cancer cells [9]. Specifically, prior research demonstrated that silencing GPAM resulted in decreased intracellular LPA levels in MCF7 breast cancer cells, while overexpression of

GPAM in HEK293 cells led to increased levels of LPA. Furthermore, transfecting LPA into MCF7 cells significantly increased intracellular LPA levels and increased cell migration. In contrast, results generated as part of the current PhD thesis found, no consistent decrease in LPA levels. Instead, a reduction in 18:1 LPA was only observed in COV318 cells upon silencing GPAM, whereas OVCAR8 cells exhibited an upregulation of 16:0 and 18:0 LPA, albeit with only one oligonucleotide. Silencing AGK resulted in a non-significant decrease in LPA species in OAW28 cells, and a significant reduction was also noted in OVCAR8 cells with one oligonucleotide. Conversely, Kuramochi cells demonstrated increased levels of 18:0 LPA following AGK knockdown with one oligo. These observations suggest that under the experimental conditions employed, the impact of GPAM and AGK on cell migration is not directly linked to the intracellular levels of their enzymatic products. Although some PA and DAG lipid species were altered following the knockdowns, no consistent changes in these lipid species were observed across all tested cell lines. Interestingly, AGK overexpression resulted in a pronounced enhancement of the migratory phenotype in OVCAR8 cells, yet this was paradoxically associated with decreased levels of LPA, PA, and DAG. Altogether, these findings imply that cell motility may be independent of the enzymatic functions of GPAM and AGK, as well as the intracellular levels of the signaling lipids. Instead, they suggest that other processes are deregulated among the cells that are responsible for the altered migration, highlighting the complexity of lipid signaling and its role in cellular behavior.

While LPA generation may not be primarily driven by GPAM or AGK in the studied ovarian cancer cell lines, it is possible that LPA levels are maintained through the activity of other enzymes or via alternative pathways. These other enzymes within the lipid metabolism pathway could be compensating for the loss of GPAM and AGK, ensuring that lipid intermediates like LPA, PA, or DAG continue to be produced at sufficient levels. To begin addressing this possibility, the expression of additional LPA-producing enzymes, including GPAT2-4, GDE4 and GDE7 were analyzed by quantitative PCR. Expression of GPAT2 and GPAT3 were partially reduced upon silencing both GPAM and AGK, while GDE4 and GDE7 expression patterns were variable, depending on cell-line and which gene was targeted. However, to be able to draw any conclusion regarding the potential compensatory effects on overall LPA homeostasis, it would be crucial to analyze the expression and activity of LPA-degrading enzymes, such as PLPPs and AGPATs alongside the activity of LPA-producing enzymes, which was beyond the scope of the present PhD thesis.

Finally, it should also be considered that in this thesis, intracellular metabolites were extracted using the SIMPLEX technique [157, 176], which required more sample preparation steps compared to previously direct LC-MS/MS measurements upon methanol extraction used in the our previously published work [9]. While direct measurement may be advantageous in minimizing potential changes in the metabolome that may occur after the extraction *in vitro*, the technique used here was utilized to be able to capture the entire metabolome. Another limitation of the current metabolomic studies is the reliance on a single time-point conducted 72 hours post-transfection. While the effects on migration remain evident at this time, transient changes in metabolite levels during dynamic cellular processes may be overlooked. Future experiments should incorporate time-course studies to capture these fluctuations. Additionally, employing ^{13}C metabolic flux analysis (^{13}C-MFA) would provide quantitative measures of metabolite conversion rates through metabolic pathways [177] by for example understanding the flow of carbon through metabolic networks and how cells allocate resources under varying conditions. By utilizing stable isotope-labeled substrates, such as ^{13}C-glucose, ^{13}C-glycerol, or ^{13}C-labeled LPA, the carbon flow through metabolic pathways can be traced. Analyzing the labeling patterns in downstream metabolites would allow us to infer pathway activity and quantify intracellular fluxes, potentially shedding light on the roles of GPAM and AGK in phospholipid metabolism. Furthermore, to fully comprehend the role of lipid metabolism in cellular processes such as migration, comprehensive lipid profiling that includes a broader range of lipid species and their precursors might be helpful. Additionally, coupling lipid metabolome with proteomics analysis could provide significant insights into the interplay between lipid metabolism and protein expression that may affect cellular behavior.

5.3.2 Role of GPAM and AGK in cell migration signaling pathways

To investigate the mechanisms underlying the effects of GPAM and AGK silencing on cell migration and spheroid dynamics, their impact on key signaling proteins (Akt, Erk, GSK3β, and β-catenin) and EMT markers (E-cadherin, N-cadherin, and vimentin) were investigated. The phosphorylation status of Akt, Erk, and GSK3β was assessed in OVCAR8 cells, revealing a reduction in p-Akt and p-Erk levels following the knockdown of both GPAM and AGK, suggesting that these proteins may serve as critical upstream regulators of the PI3K/Akt and MAPK/Erk pathways, well-known mediators of cancer cell migration, proliferation, and survival [35]. It was previously shown, that in CD8+ T cells AGK is enhancing the activation of PI3K-mTOR signaling [107]. This effect was mediated via phosporylation of PTEN by AGK, thus leading to its inactivation. However, overexpression of AGK in this work did not lead to increased phosphorylation of Akt or Erk, suggesting a different mechanism in ovarian cancer cells. Nevertheless, the potential regulation of PTEN by AGK should be investigated in future experiments. The significant decrease in p-GSK3β levels upon silencing GPAM and AGK further emphasizes their involvement in regulating cellular signaling pathways. GSK3β is known to play a crucial role in various cellular processes, including cell growth and apoptosis, by modulating β-catenin, which regulates the expression of downstream targets such as cyclin D1 and c-Myc [164]. The observed increase in p-GSK3β levels with AGK overexpression emphasizes further AGK's influence on this signaling pathway. The regulation of β-catenin by

GSK3β has significant implications in cancer, particularly in ovarian cancer. In EOC, aberrant activation of the Wnt/β-catenin pathway has been observed [178]. However, despite the changes in GSK3β phosphorylation, it is noteworthy that neither GPAM nor AGK modulation significantly affected the phosphorylation status of β-catenin. To add on this, β-catenin nuclear localization schould also be investigated. For this immunofluorescence staining and confocal microscopy to visualize and quantify β-catenin's subcellular distribution in control and AGK/GPAM-silenced cells, complemented by western blotting of nuclear fractions to confirm changes in nuclear β-catenin levels could be investigated.

The analysis of EMT markers showed no significant changes in E-cadherin, N-cadherin, or vimentin expression following GPAM and AGK knockdowns in OVCAR8 cells. The significant decrease in N-cadherin expression upon AGK overexpression may indicate a shift in cell adhesion properties, potentially affecting migratory behavior. To further investigate the role of GPAM and AGK in cell migration and their potential relationship with EMT in ovarian cancer cells, future experiments could assess the expression levels of EMT markers in a time-course study. This could help identify any transient changes in expression that may not have been captured in the initial analysis. Furthermore, potential influence on cytoskeletal remodeling dynamics should be investigated. IHC stainings for phalloidin to visualize actin filaments, filamin and focal adhesion proteins would reveal changes in the cytoskeletal organization and cell adhesion that may correlate with migratory behavior. Additionally, staining for α- and β-tubulin can help assess microtubule organization, which are also important for cell shape and motility.

Given the importance of Rho GTPases in cytoskeletal dynamics and cell migration, the activation status of RhoA GTPase following GPAM and AGK downregulation as well as AGK overexpression in OVCAR8 cells was investigated. Despite the impact of GPAM and AGK on cell migration, no detectable changes in the activation of RhoA GTPases were observed upon their modulation, as demonstrated by pull-down assays followed by western blot analysis. These findings imply that GPAM and AGK might impact the cytoskeletal dynamics required for migration, but they do so independently of the classical RhoA GTPase signaling. To follow up on this further, it is important to consider other Rho GTPases, such as Rac1 and Cdc42. While RhoA is often associated with stress fiber formation and cell contraction, Rac1 and Cdc42 play distinct yet complementary roles in regulating the actin cytoskeleton and cellular dynamics [179]. This could provide a broader understanding of the cytoskeletal dynamics involved in the migratory behavior of ovarian cancer cells.

5.3.3 Non-mitochondrial OCR affected by GPAM and AGK expression changes

Given the mitochondrial localization of GPAM and AGK, it was hypothesized that these enzymes might influence cancer cell behavior primarily through their effects on mitochondrial function, rather than via a shared signaling pathway. Mitochondria are essential for ATP production, calcium signaling, and ROS homeostasis, all of which are critical for maintaining cellular homeostasis and motility [180]. Thus, silencing GPAM or AGK may impair mitochondrial function, leading to reduced energy availability, disrupted signaling, and increased oxidative stress, which could alter cytoskeletal organization and decrease cell migration. To investigate this, a mitochondrial stress test was conducted in OVCAR8 cells using a Seahorse metabolic analyzer. Silencing AGK resulted in an increase in OCR, while its overexpression decreased the basal, maximal, and ATP-linked OCR, indicating AGK's crucial role in maintaining mitochondrial respiratory capacity. In contrast, GPAM knockdown had minimal effects on the OCR but appeared to increase the ECAR, suggesting a shift toward glycolytic metabolism. However, the ECAR readout from the Mitochondrial Stress Test provides only a qualitative indication that the overall acifidification in the cells is increased. To determine whether this increase is due to enhanced glycolysis, a more quantitative approach, such as a glycolytic rate assay, should be performed. Notably, non-mitochondrial OCR increased following the downregulation of both GPAM and AGK, while it decreased in AGK-overexpressing OVCAR8 clones. These findings imply that GPAM and AGK's roles extend beyond lipid metabolism, potentially affecting cancer cell behavior through the regulation of cellular bioenergetics.

The non-mitochondrial OCR reflects the residual oxygen consumption rate after inhibiting mitochondrial respiration. Cells utilize oxygen not only for mitochondrial respiration but also for various enzymatic processes that occur outside the mitochondria, which are crucial for numerous physiological functions [181]. One of the key enzymes that consume oxygen outside the mitochondria is prostaglandin-endoperoxide synthase, commonly known as cyclooxygenase (COX) [182]. COX catalyzes the conversion of arachidonic acid into prostaglandins. This reaction involves the incorporation of molecular oxygen into the substrate, leading to the formation of prostaglandin G2 (PGG2), which is subsequently converted to prostaglandin H2 (PGH2). These prostaglandins play significant roles in inflammation, pain, and the regulation of various physiological processes [182]. In cancer cells, COX-2, an inducible isoform of COX, facilitates the production of proangiogenic factors like vascular endothelial growth factor (VEGF), promoting the formation of new blood vessels to supply the growing tumor [183]. Additionally, COX-2-derived prostaglandins can inhibit apoptosis and are linked to increased invasiveness and metastatic potential due to their role in degrading the extracellular matrix [184]. Another important group of oxygen-consuming enzymes are lipoxygenases (LOXs), which are non-heme iron-containing enzymes that catalyze the deoxygenation of polyunsaturated fatty acids (PUFAs) to form fatty acid hydroperoxides. LOXs directly consume molecular oxygen and thus produce various bioactive lipid mediators [185]. For instance, 5-LOX can influence cancer cell proliferation and survival by modulating signaling pathways, with products like 5-HETE stimulating cancer cell growth [186]. Furthermore, LOXs can shape the tumor microenvironment by affecting the expression of cytokines and growth factors, such as TGFβ2, which modulate cellular interactions and promote tumor progression [187]. LOX-derived metabolites, such as 12-HETE produced by 12-LOX, can also promote angiogenesis and metastasis, thus facilitating tumor growth and spread [186]. Lastly, peroxidases play a role in managing oxidative stress within cells [188]. Unlike COX and LOXs, peroxidases do not directly consume molecular oxygen; instead, they utilize hydrogen peroxide (H_2O_2) as an oxidizing agent. By breaking down H_2O_2, peroxidases help regulate ROS levels [189].

While low ROS levels are vital for signaling and defense, their overproduction or inadequate removal can lead to oxidative stress, damaging cells, proteins, lipids, and DNA [190]. Oxidative stress has also been linked to the progression of cancer [191]. Excessive ROS production due to mitochondrial damage can impair cellular structures and signaling pathways, leading to damage to organelles and cytoskeletal proteins, such as actin, which reduces their ability to polymerize and depolymerize [192, 193]. Additionally, ROS can interfere with the signaling pathways that regulate cell motility, such as those involving Rho GTPases [194]. Furthermore, ROS can affect the expression and function of cell adhesion molecules, which are critical for the attachment and detachment of cells during migration. Recent research has also highlighted the role of specific NADPH oxidases, particularly NOX1 and NOX5, in regulating cell migration. NOX1-derived ROS are involved in directional cell migration by affecting the formation of lamellipodia, which are essential for cell movement. Studies have shown that cells lacking Nox1 exhibit reduced migration capabilities, and re-expression of NOX1 or the addition of exogenous H_2O_2 can rescue this phenotype. Thus, the observed increase in non-mitochondrial OCR suggests that oxidative stress or alternative metabolic pathways may be upregulated when GPAM or AGK expression is downregulated.

Mitochondrial dynamics, including fusion and fission, are crucial for regulating mitochondrial morphology, distribution, and function, which in turn can affect cellular motility. Mitochondrial fusion merges two mitochondria into a larger organelle, mediated by mitofusins (MFN1 and MFN2) on the outer membrane and OPA1 on the inner membrane [195]. This process optimizes mitochondrial function, especially under stress. Conversely, mitochondrial fission, regulated by proteins like DRP1 and FIS1, divides mitochondria into separate organelles, facilitating distribution during cell division and the removal of damaged mitochondria through mitophagy [196, 197]. The ability of mitochondria to undergo these dynamic processes allows them to adapt to the cell's energy demands, particularly in regions requiring high energy, such as the leading edge of migrating cells [198]. Mitochondria are transported to these regions along the cytoskeleton by motor proteins like dynein and kinesin, providing localized ATP and metabolites necessary for cell motility [198, 199]. Disruption of mitochondrial dynamics can impair mitochondrial localization, reducing the cell's ability to sustain movement. Additionally, mitochondrial dysfunction can disrupt cytoskeletal structure, impairing the formation of lamellipodia and focal adhesions [180, 200], with lipids playing a critical role in regulating these processes [201]. Interestingly, it has been reported that inhibiting GPAM impairs AML cell propagation by inducing mitochondrial fission, which suppressed OXPHOS and increased ROS levels [97]. In this study the effect on mitochondrial function was shown to be driven by GPAM-generated LPA synthesis, as supplementation of exogenous LPA reversed the effect. LPA was reported to promote mitochondrial fusion by interacting with mitochondrial proteins and influencing lipid composition, modulating the activity of fusion proteins like mitofusins [84]. The upregulated ECAR observed upon GPAM knockdown in this work could indicate increased glycolytic activity to meet the high energy demand of cancer cells. This increase may be due to a disruption in mitochondrial function, as well as increased non-mitochondrial OCR, which together would point to increased ROS levels in the cells, confirming the reported role for GPAM [97]. Furthermore, recent studies indicate that AGK is essential for maintaining mitochondrial cristae morphology that is crucial for proper mitochondrial function and energy production [105]. Upregulated AGK expression has been shown to increase ROS production in EOC cells, potentially contributing to oxidative stress and cancer progression, while also enhancing mitochondrial membrane potential, indicating increased activity [105]. Interestingly, the results observed in the present thesis show rather a decrease in mitochondrial activity upon AGK overexpression, reflected by the decrease in basal, ATP-linked and maximal OCR, which was increased when AGK was downregulated. Notably, AGK's regulation of mitochondrial function was shown to be independent of its kinase activity suggesting that AGK influences mitochondrial homeostasis via an alternative mechanism compared to GPAM [97, 105].

5.3.4 Future perspectives

Based on the results reported in this PhD thesis with the aim to further elucidate the mechanisms behind GPAM and AGK's effects on cell migration as well as their potential as therapeutic targets, a series of experiments should be conducted, focusing on both *in vitro* and *in vivo* models. An important aspect that should be investigated is the reason for alterations in non-mitochondrial OCR, such as measuring ROS levels in cells. To quantify intracellular ROS levels, fluorescent probes such as 2',7'-dichlorofluorescin diacetate (DCF-DA) or CellROX reagents can be employed [202]. The DCF-DA probe is particularly useful as it becomes fluorescent upon oxidation by ROS, allowing for easy detection and quantification [203]. Furthermore, MitoSOX™ Red can be utilized to specifically measure mitochondrial superoxide production [204]. Luminescence-based assays, such as the ROS-Glo™ H_2O_2 assay can be utilized to quantify changes in hydrogen peroxide levels, providing another layer of understanding regarding the specific type of oxidative stress in these cells [205]. Conducting time-course experiments will allow the tracking of ROS changes during cell migration, offering insights into the temporal dynamics of oxidative stress associated with GPAM and AGK expression modulation. Mitochondrial morphology and dynamics using fluorescence microscopy and mitochondria-specific dyes should also be investigated. Mitochondria can exhibit different morphologies, such as fragmented or elongated forms, which are indicative of their functional state. Fragmented mitochondria are often associated with stress and dysfunction, while elongated mitochondria are typically seen in healthy cells. To study mitochondrial morphology and dynamics effectively [206], MitoTracker dyes selectively accumulate in active mitochondria and can be visualized using fluorescence microscopy. These dyes are available complexed to different fluorophores that then allows for multiplexing and co-localization studies. Furthermore, combinations of dyes assessing mitochondrial mass and activity status can help to elucidate how GPAM and AGK affect mitochondrial function and contribute to the overall metabolic landscape of ovarian cancer cells.

Given the critical role of 3D structures in simulating the tumor microenvironment and mimicking ovarian cancer metastasis, as well as the significant influence of GPAM and AGK expression on the size, shape, and outgrowth of spheroids observed in this work, further investigations using 3D cell cultures are also warranted. To assess the mechanism underlying the impact of GPAM and AGK on the 3D structures, it is essential to explore spheroid dynamics more thoroughly, for instance utilizing Matrigel drop invasion assays [207]. Additionally, employing IHC methods will be crucial for examining cell-cell interactions, which are vital regulators of spheroid formation. To further explore the roles of GPAM and AGK in cancer progression, particularly in processes related to metastasis, the mesothelial clearance assay could be performed [208]. This assay allows for the analysis of spheroid invasion into a mesothelial layer, effectively simulating the initial steps of tumor implantation within the metastatic niche *in vitro*. Our laboratory has already established this assay and conducted preliminary tests, demonstrating its feasibility for further investigation. Furthermore, consistent with existing literature and findings from our laboratory, the GPAM inhibitor FSG67 has demonstrated efficacy in inhibiting GPAM activity [97]. Preliminary experiments alongside this research indicate that this inhibitor can reduce cell migration *in vitro* at low concentrations (data not shown). Should these results prove significant, it would be intriguing to investigate how treatment with the inhibitor affects the formation of 3D spheroids and their behavior within the 3D matrix. Finally, while 3D *in vitro* models offer numerous advantages, they also have limitations, particularly in their inability to fully replicate the systemic metastasis processes that occur *in vivo*. To comprehensively determine the effects of GPAM and AGK expression on ovarian cancer metastasis, mouse models are indispensable. Specifically, intraperitoneal (i.p.) metastasis models using luciferase-expressing cells can be employed to monitor tumor growth and spread in living mice. The techniques for generating stable luciferase-positive cell lines and i.p. mouse models are well-established within our facility, providing a solid foundation for further research [209].

Understanding the roles of GPAM and AGK in cell migration *in vitro* and *in vivo* will provide more insight into the mechanisms underlying ovarian cancer progression and metastasis. This knowledge will be crucial for developing targeted therapeutic strategies. For example, in addition to both GPAM and AGK being potential therapeutics themselves, the development of therapeutic strategies based on modulating ROS levels for cancer treatment is a promising and active area of research [210]. These strategies range from increasing ROS to toxic levels in cancer cells to reducing ROS to prevent cancer progression [211]. By understanding the mechanism by which the inhibition of GPAM and AGK potentially through ROS-modulating approaches, we may uncover novel therapeutic avenues that could significantly improve outcomes for ovarian cancer patients.

Appendix

A Transition data for measurement of lipids.

MTBE fraction positive mode (scheduled)

Lipid	Q1 m/z	Q3 m/z	RT [min]	RT window [s]	CE [V]
18:1-18:1 DAG	638,572	339,289	0.90	40.0	26
18:0-18:2 DAG	638,572	341,305	0.90	40.0	26
18:0-18:1 DAG	640,587	341,305	0.90	40.0	26
18:0-18:0 DAG	642,603	341,305	0.90	40.0	26
16:0-18:2 DAG	610,541	313,274	0.90	40.0	26
16:0-18:1 DAG	612,556	313,274	0.90	40.0	26
16:0-18:0 DAG	614,572	313,274	0.90	40.0	26
16:0-16:0 DAG	586,541	313,274	0.90	40.0	26
17:0-17:0 DAG	614,572	327,289	0.90	40.0	26
36:2 PC	786,601	184,100	4.5	180.0	20
36:1 PC	788,616	184,100	4.5	180.0	20
36:0 PC	790,632	184,100	4.5	180.0	20
34:2 PC	758,569	184,100	4.5	180.0	20
34:1 PC	760,585	184,100	4.5	180.0	20
34:0 PC	762,601	184,100	4.5	180.0	20
32:0 PC	734,569	184,100	4.5	180.0	20
17:0-14:1 PC	718,538	184,100	4.5	180.0	20
36:2 PS	788,544	603,535	1.5	80.0	26
36:1 PS	790,559	605,550	1.5	80.0	26
36:0 PS	792,575	607,566	1.5	80.0	26
34:2 PS	760,512	575,503	1.5	80.0	26
34:1 PS	762,528	577,519	1.5	80.0	26
34:0 PS	764,544	579,535	1.5	80.0	26
32:0 PS	736,512	551,503	1.5	80.0	26
17:0-14:1 PS	720,481	535,472	1.5	80.0	26
36:2 PE	744,554	603,535	1.7	70.0	26
36:1 PE	746,569	605,550	1.7	70.0	26
36:0 PE	748,585	607,566	1.7	70.0	26
34:2 PE	716,522	575,503	1.7	70.0	26
34:1 PE	718,538	577,519	1.7	70.0	26
34:0 PE	720,554	579,535	1.7	70.0	26
32:0 PE	692,522	551,503	1.7	70.0	26
17:0-14:1 PE	676,491	535,472	1.7	70.0	26
20:4 Lyso PC	544,340	184,073	6.0	300.0	32
18:3 Lyso PC	518,324	184,073	6.0	300.0	32
18:2 Lyso PC	520,340	184,073	6.0	300.0	32
18:1 Lyso PC	522,355	184,073	6.0	300.0	32
18:0 Lyso PC	524,371	184,073	6.0	300.0	32
17:1 LysoPC	508,340	184,073	6.0	300.0	32
16:1 Lyso PC	494,324	184,073	6.0	300.0	32
16:0 Lyso PC	496,340	184,073	6.0	300.0	32
20:4 Lyso PE	502,293	361,274	2.2	60.0	22
18:3 Lyso PE	476,277	335,258	2.2	60.0	22
18:2 Lyso PE	478,293	337,274	2.2	60.0	22
18:1 Lyso PE	480,308	339,289	2.2	60.0	22
18:0 Lyso PE	482,324	341,305	2.2	60.0	22
17:1 Lyso PE	466,293	325,274	2.2	60.0	22
16:1 Lyso PE	452,277	311,258	2.2	60.0	22
16:0 Lyso PE	454,293	313,274	2.2	60.0	22

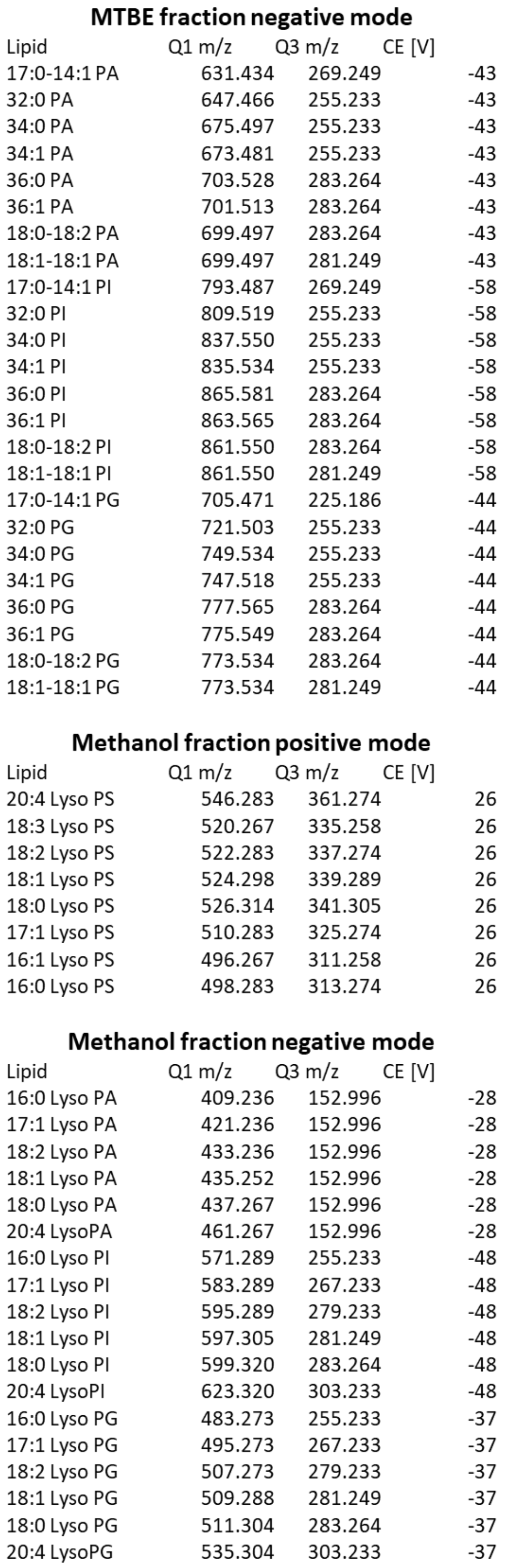

MTBE fraction negative mode

Lipid	Q1 m/z	Q3 m/z	CE [V]
17:0-14:1 PA	631.434	269.249	-43
32:0 PA	647.466	255.233	-43
34:0 PA	675.497	255.233	-43
34:1 PA	673.481	255.233	-43
36:0 PA	703.528	283.264	-43
36:1 PA	701.513	283.264	-43
18:0-18:2 PA	699.497	283.264	-43
18:1-18:1 PA	699.497	281.249	-43
17:0-14:1 PI	793.487	269.249	-58
32:0 PI	809.519	255.233	-58
34:0 PI	837.550	255.233	-58
34:1 PI	835.534	255.233	-58
36:0 PI	865.581	283.264	-58
36:1 PI	863.565	283.264	-58
18:0-18:2 PI	861.550	283.264	-58
18:1-18:1 PI	861.550	281.249	-58
17:0-14:1 PG	705.471	225.186	-44
32:0 PG	721.503	255.233	-44
34:0 PG	749.534	255.233	-44
34:1 PG	747.518	255.233	-44
36:0 PG	777.565	283.264	-44
36:1 PG	775.549	283.264	-44
18:0-18:2 PG	773.534	283.264	-44
18:1-18:1 PG	773.534	281.249	-44

Methanol fraction positive mode

Lipid	Q1 m/z	Q3 m/z	CE [V]
20:4 Lyso PS	546.283	361.274	26
18:3 Lyso PS	520.267	335.258	26
18:2 Lyso PS	522.283	337.274	26
18:1 Lyso PS	524.298	339.289	26
18:0 Lyso PS	526.314	341.305	26
17:1 Lyso PS	510.283	325.274	26
16:1 Lyso PS	496.267	311.258	26
16:0 Lyso PS	498.283	313.274	26

Methanol fraction negative mode

Lipid	Q1 m/z	Q3 m/z	CE [V]
16:0 Lyso PA	409.236	152.996	-28
17:1 Lyso PA	421.236	152.996	-28
18:2 Lyso PA	433.236	152.996	-28
18:1 Lyso PA	435.252	152.996	-28
18:0 Lyso PA	437.267	152.996	-28
20:4 LysoPA	461.267	152.996	-28
16:0 Lyso PI	571.289	255.233	-48
17:1 Lyso PI	583.289	267.233	-48
18:2 Lyso PI	595.289	279.233	-48
18:1 Lyso PI	597.305	281.249	-48
18:0 Lyso PI	599.320	283.264	-48
20:4 LysoPI	623.320	303.233	-48
16:0 Lyso PG	483.273	255.233	-37
17:1 Lyso PG	495.273	267.233	-37
18:2 Lyso PG	507.273	279.233	-37
18:1 Lyso PG	509.288	281.249	-37
18:0 Lyso PG	511.304	283.264	-37
20:4 LysoPG	535.304	303.233	-37

Figure S1: **Transition data for the targeted lipidome analysis.**The LCMS/MS settings used for lipid measurement for all fractions.

B Intracellular lipids levels in the cell line panel.

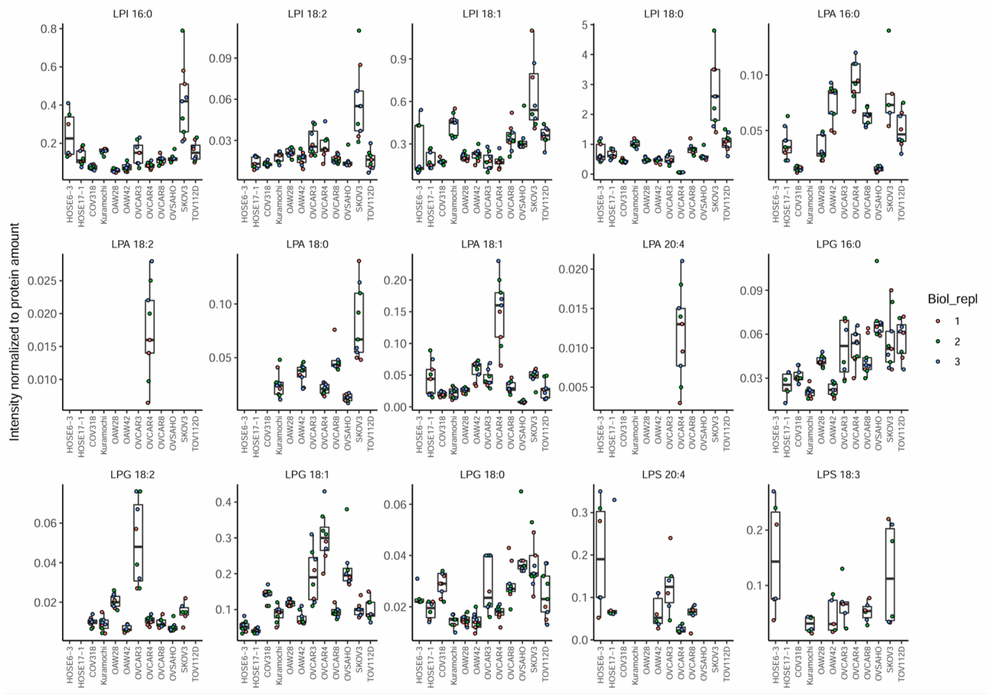

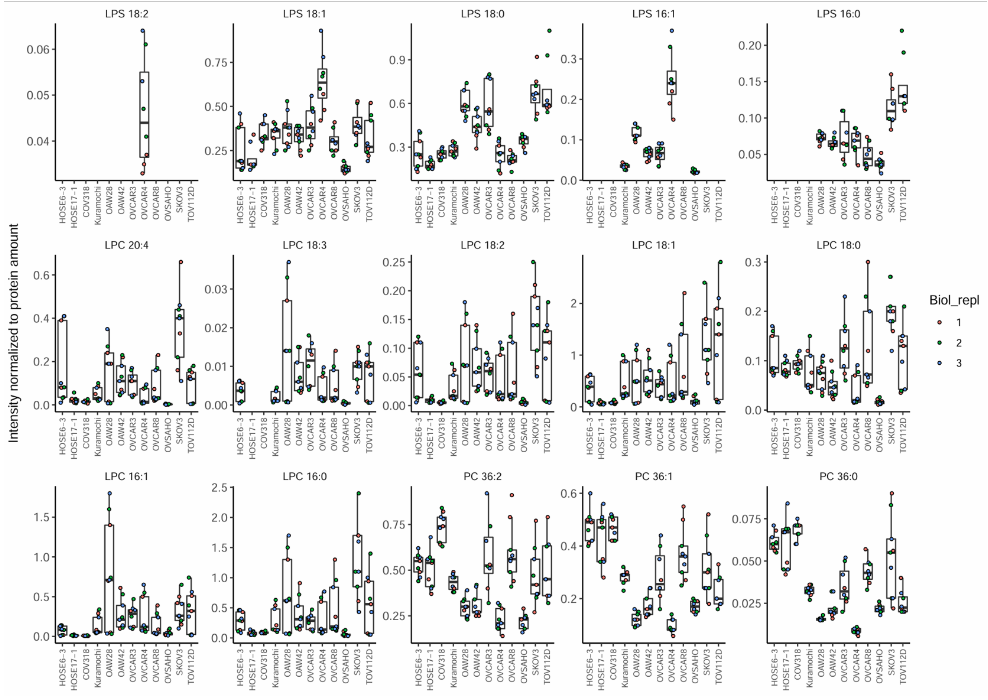

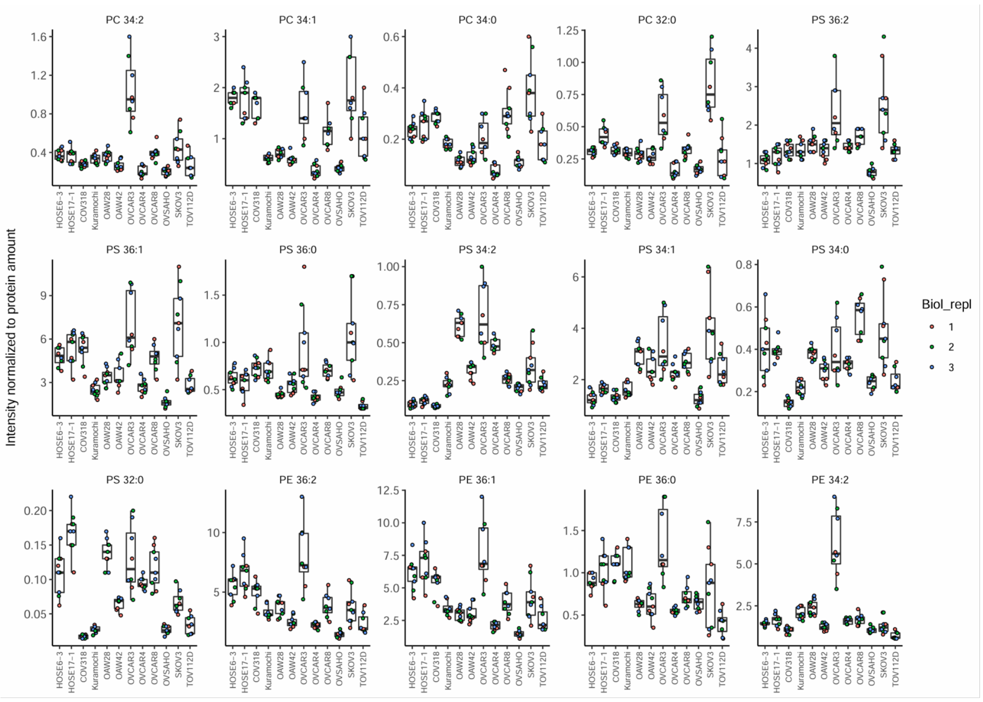
PC 34:2
PC 34:1
PC 34:0
PC 32:0
PS 36:2
PS 36:1
PS 36:0
PS 34:2
PS 34:1
PS 34:0
PS 32:0
PE 36:2
PE 36:1
PE 36:0
PE 34:2
Intensity normalized to protein amount
HOSE6-3
HOSE17-1
COV318
Kuramochi
OAW28
OAW42
OVCAR3
OVCAR4
OVCAR8
OVSAHO
SKOV3
TOV112D
Biol_repl
1
2
3

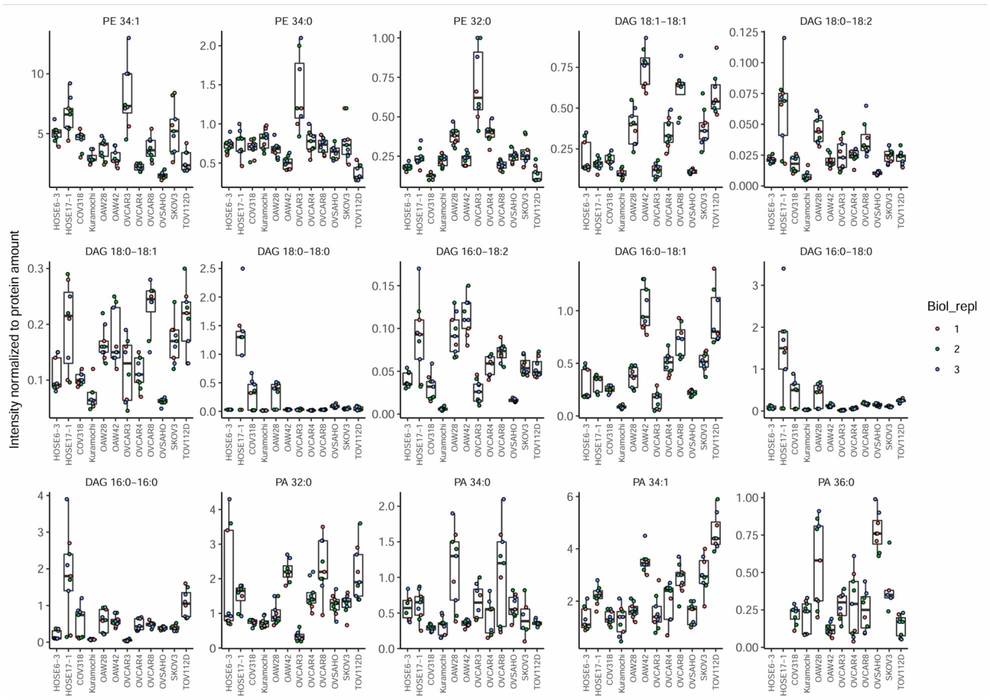
PE 34:1
PE 34:0
PE 32:0
DAG 18:1–18:1
DAG 18:0–18:2
DAG 18:0–18:1
DAG 18:0–18:0
DAG 16:0–18:2
DAG 16:0–18:1
DAG 16:0–18:0
DAG 16:0–16:0
PA 32:0
PA 34:0
PA 34:1
PA 36:0
Intensity normalized to protein amount
HOSE6-3
HOSE17-1
COV318
Kuramochi
OAW28
OAW42
OVCAR3
OVCAR4
OVCAR8
OVSAHO
SKOV3
TOV112D
Biol_repl
1
2
3

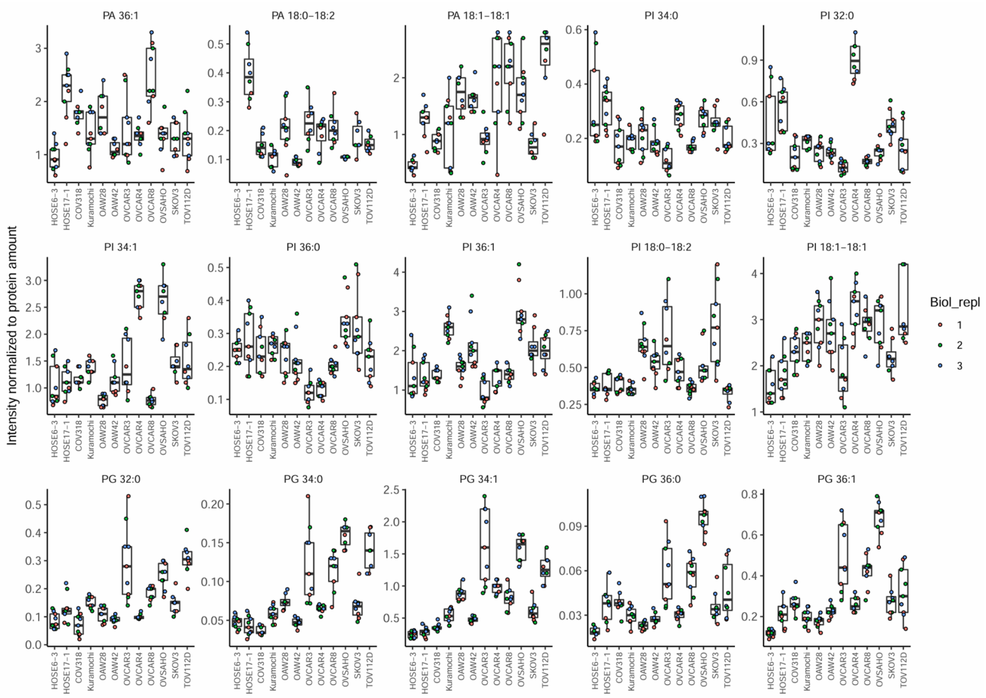

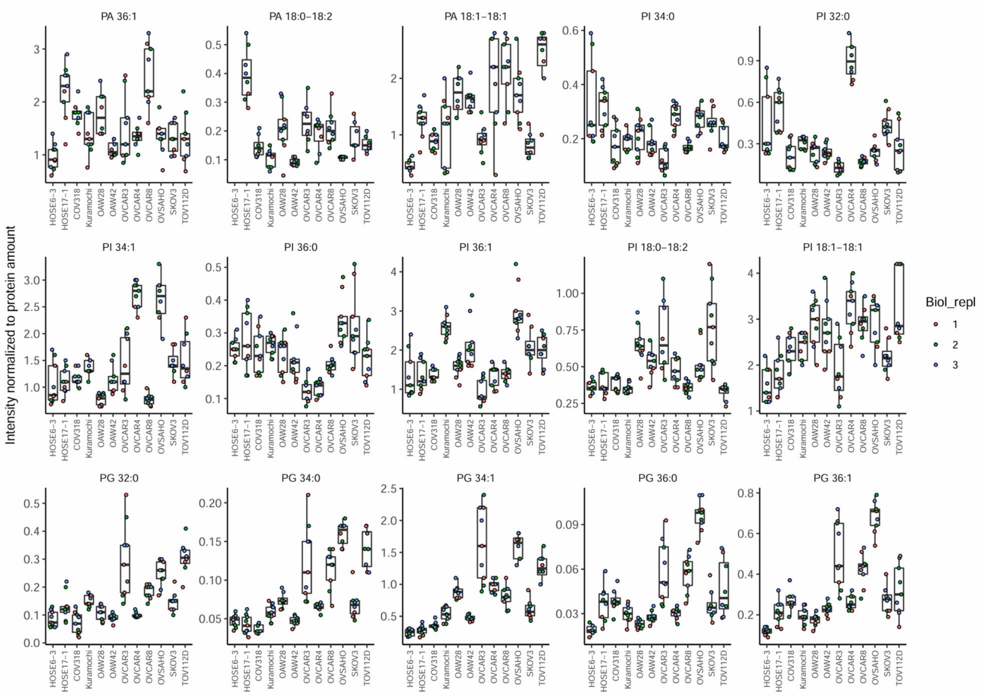

Figure S2: **Analysis of intracellular lipidome in the cell panel.**The analysis was performed after the simultaneous metabolite, protein and lipid extraction (SIMPLEX) protocol followed by LC-MS/MS. The area under the curve for the detected peaks was calculated in relation to the corresponding internal standard that was spiked into the sample, and the results were normalized to the protein content. Data are presented as mean ± SD of three biological replicates (color coded) with three technical replicates each.

C Scratch assay for OVCAR8 upon AGK knockdown

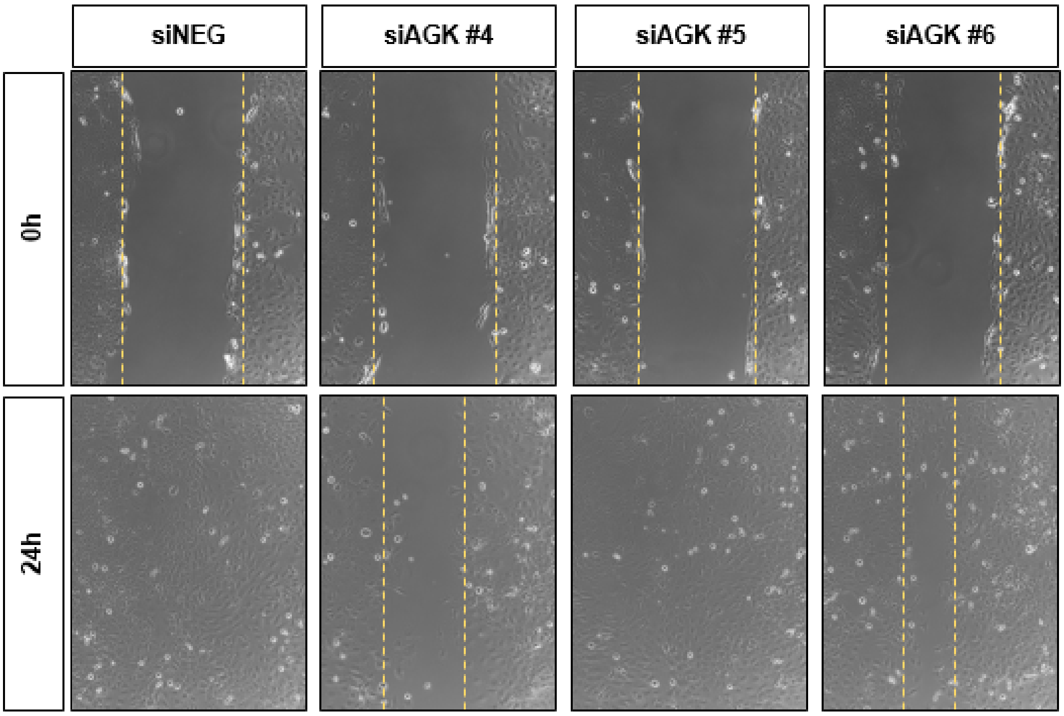

Figure S3: **Migratory ability of OVCAR8 cells upon AGK KD.** Representative images of wound closure in OVCAR8 cells upon silencing AGK with a set of siRNA oligos siAGK #4 - #6. Images were taken at 0 h and 24 h. The scratch is outlined in yellow.

D Western Blot for signaling proteins

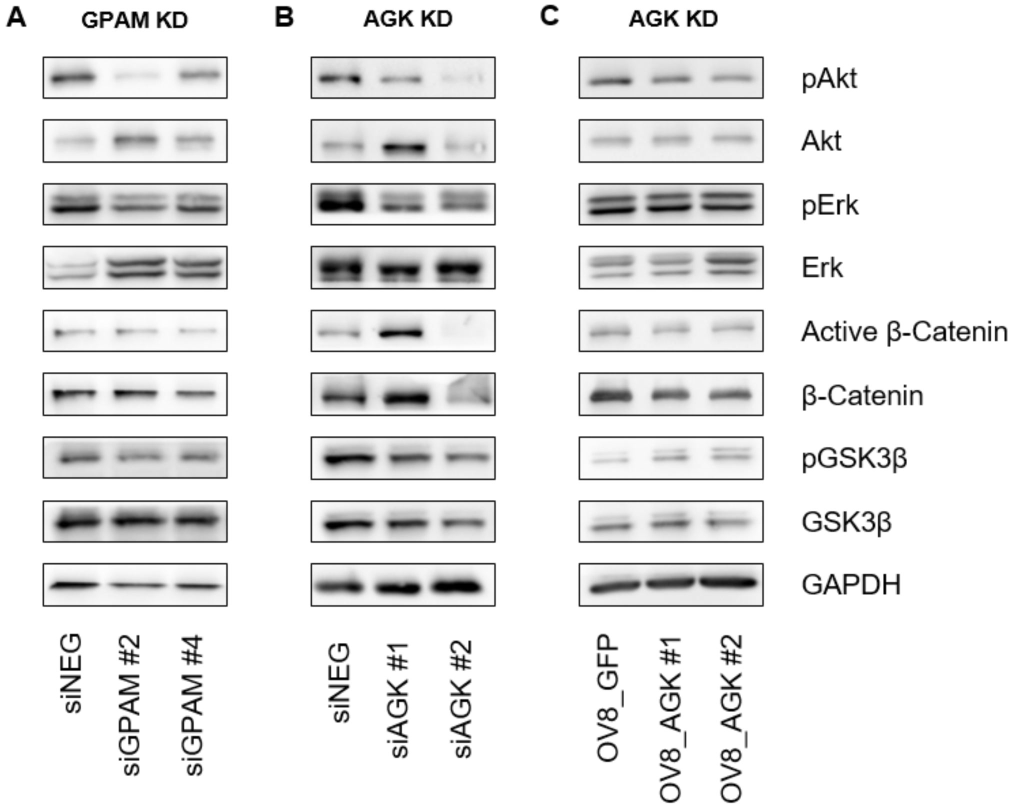

Figure S4: **Western blot analysis of signaling proteins in OVCAR8 cells following silencing of GPAM and AGK, and overexpression of AGK.** Western blot analysis was conducted to evaluate the basal expression and activated phosphorylated status of key signaling proteins, including Akt, Erk, GSK3β and β-Catenin following the silencing of **A** GPAM and **B** AGK as well as **C** AGK overexpression in OVCAR8 cells

E List of Acronyms

ACC	Acetyl-CoA Carboxylase
AGK	Acylglycerol Kinase
AGPAT	Acylglycerol-Phosphate Acyltransferase
AML	Acute Myeloid Leukemia
ATX	Autotaxin
BRCA1/2	Breast Cancer 1/2
CDP-Choline	Cytidine Diphosphate Choline
CHKA	Choline Kinase Alpha
CPT1	Carnitine Palmitoyltransferase 1
CTC	Circulating Tumor Cells
DAG	Diacylglycerol
DAGK	Diacylglycerol Kinase
DHAP	Dihydroxyacetone Phosphate
ECM	Extracellular Matrix
EDI3	Endoplasmic Reticulum Dipeptidase 3
EGFR	Epidermal Growth Factor Receptor
EMT	Epithelial-to-Mesenchymal Transition
EOC	Endometrial Ovarian Cancer
ER	Endoplasmatic Reticulum
ERK	Extracellular Signal-Regulated Kinase
ESCC	Esophageal Squamous Cell Carcinoma
FASN	Fatty Acid Synthase
FIGO	International Federation of Gynecology and Obstetrics
G3P	Glycerol-3-Phosphate
GK	Glucokinase
GDE	Glycerol-3-Phosphate Dehydrogenase
GPAM	Glycerol-3-Phosphate Acyltransferase, mitochondrial
GPAT	Glycerol-3-Phosphate Acyltransferase
GPC	Glycerophosphocholine
GPCPD1	Glycerophosphocholine Phosphodiesterase 1
GPCR	G Protein-Coupled Receptor
GSK3β	Glycogen Synthase Kinase-3 Beta
HCC	Hepatocellular Carcinoma
HGS	High-Grade Serous
HGSOC	High-Grade Serous Ovarian Cancer
IP	Intraperitoneal

JAK2	Janus Kinase 2
LC/MS	Liquid Chromatography Mass Spectrometry
LPA	Lysophosphatidic Acid
LPAR	Lysophosphatidic Acid Receptor
LPAT	Lysophospholipid Acyltransferase
LDL	Low-Density Lipoprotein
LDLR	Low-Density Lipoprotein Receptor
LPC	Lysophosphatidylcholine
lysoPLD	Lysophospholipase D
MAG	Monoacylglycerol
MAPK	Mitogen-Activated Protein Kinase
MIM	Mitofusin Interacting Protein
MTCH2	Mitochondrial Carrier Homolog 2
MOM	Mitochondrial Outer Membrane
MMP	Matrix Metalloproteinase
mTOR	Mammalian Target of Rapamycin
NADPH	Nicotinamide Adenine Dinucleotide Phosphate
NASH	Non-Alcoholic Steatohepatitis
NEM	N-ethylmaleimide
NF-κB	Nuclear Factor kappa-light-chain-enhancer of activated B cells
OC	Ovarian Cancer
OCR	Oxygen Consumption
OSCC	Oral Squamous Cell Carcinoma
OXPHOS	Oxydative Phosphorylation
PA	Phosphatidic Acid
PAP	Phosphatidate Phosphatase
PARP	Poly(ADP-Ribose) Polymerase
PC	Phosphatidylcholine
PE	Phosphatidylethanolamine
PG	Phosphatidylglycerol
PI	Phosphatidylinositol
PI3K	Phosphoinositide 3-Kinase
PIP2	Phosphatidylinositol 4,5-bisphosphate
PKA	Protein Kinase A
PKC	Protein Kinase C
PLA	Phospholipase A
PLC	Phospholipase C
PLD	Phospholipiase D
PLPP	Phospholipid Phosphatase

PPARγ	Peroxisome Proliferator-Activated Receptor Gamma
PPRE	PPAR-Response Element
PTEN	Phosphatase and Tensin Homolog
PtdCho	Phosphatidylcholine
PS	Phosphatidylserine
RCC	Renal Cell Carcinoma
RhoA	Ras Homolog Family Member A
RPL39	Ribosomal Protein L39
ROCK	Rho-Associated Protein Kinase
ROS	Reactive Oxygen Species
STAT3	Signal Transducer and Activator of Transcription 3
TAG	Triglyceride
TCA cycle	Tricarboxylic Acid Cycle
TIM22	Translocase of the Inner Mitochondrial Membrane 22
VEGF	Vascular Endothelial Growth Factor

List of figures

1 Glycerophospholipid structure. 2
2 Glycerophospholipid metabolism 4
3 Major lysophosphatidic acid (LPA) species. 6
4 LPA metabolism. 7
5 LPA signal transduction 8
6 Intracellular LPA signaling. 10
7 Mitochondrial localization of GPAM and AGK. 11
8 Potential sources of ovarian carcinoma. 17
9 Metastatic routes of epithelial ovarian cancer 19
10 pLV_AGK vector from Vector Builder. 25
11 pLV_GFP vector from Vecto rBuilder. 26
12 VSV-G envelope expressing plasmid 27
13 Lentiviral packaging plasmid. 28
14 Morphology of ovarian cancer cell lines. 44
15 *GPAM* and *AGK* expression in ovarian cancer cell lines. 45
16 Intracellular levels of LPA, PA and DAG in ovarian cancer cell lines. 47
17 Migratory ability of ovarian cancer cell lines analyzed by the scratch assay. . . . 49
18 Migratory ability of ovarian cancer cell lines analyzed by the transwell migration assay. 50
19 Colony forming ability of ovarian cancer cell lines. 50
20 GPAM expression is decreased in ovarian cancer cells after transfection with siRNA. 52
21 AGK expression is decreased in ovarian cancer cells after transfection with siRNA 53
22 Silencing GPAM in ovarian cancer cells reduces cell migration 55
23 Silencing AGK in ovarian cancer cells reduces cell migration. 56
24 Silencing AGK does not affect cell migration in OVCAR4 cells 57
25 Silencing GPAM has no consistent effect on colony formation in ovarian cancer cell lines. 58
26 Silencing AGK has no consistent effect on colony formation in ovarian cancer cell lines. 59
27 Simultaneous downregulation of GPAM and AGK has not additive effect on migration in Kuramochi cells. 60
28 GPAM and AGK knockdown disrupt spheroid formation. 61
29 Spheroid outgrowth is reduced upon GPAM and AGK knockdown. 62
30 Generation of constitutive AGK expressing OVCAR8 cells. 65
31 AGK protein expression in monoclonal OVCAR8 cell cultures. 65
32 Generation of monoclonal AGK-overexpressing OVCAR8 cells. 67

33 Cell viability is not affected in AGK-overexpressing OVCAR8 clones. 68
34 Cell migration is increased in AGK-overexpressing OVCAR8 clones. 68
35 AGK overexpression disrupts spheroid formation and outgrowth. 70
36 Intracellular G3P levels upon silencing GPAM and AGK. 72
37 Intracellular LPA levels upon silencing GPAM and AGK. 74
38 Intracellular PA levels upon silencing GPAM and AGK. 75
39 Intracellular DAG levels upon silencing GPAM and AGK 76
40 Intracellular LPA, PA and DAG levels in AGK-overexpressing OVCAR8 clones. . 78
41 Reciprocal regulation of GPAM and AGK expression 79
42 GPAT expression in response to GPAM and AGK silencing. 80
43 GDE4 and GDE7 expression in response to GPAM and AGK silencing. 81
44 Expression of signaling proteins in OVCAR8 cells upon GPAM and AGK modulation 83
45 No effect of GPAM and AGK modulation on EMT marker expression in OVCAR8 cells 84
46 Impact of AGK and GPAM expression on RhoA GTPase activation 85
47 Mitochondrial stress test in OVCAR8 cells upon GPAM and AGK knockdown and AGK overexpression. 88
48 Mitochondrial respiration function parameters of OVCAR8 cells upon GPAM and AGK knockdown and AGK overexpression. 89
S1 Transition data for the targeted lipidome analysis. A2
S2 Analysis of intracellular lipidome in the cell panel. A5
S3 Migratory ability of OVCAR8 cells upon AGK KD. A6
S4 Western blot analysis of signaling proteins in OVCAR8 cells following silencing of GPAM and AGK, and overexpression of AGK. A7

List of tables

1 List of used instruments and consumables 21
2 List of used consumables 22
3 List of commercially available reagents, kits & buffers 22
4 List of prepared buffers & solutions 24
5 List of vectors 25
6 Commercially available cell lines 28
7 Cell lines generated as part of this thesis 29
8 Quanti-Tect Primer Assays 29
9 Antibodies 30
10 Pipetting information for the transduction mix. 32
11 Concentrations of selection antibiotics tested 34
12 Program for the reverse transcription polymerase chain reaction. 39
13 Program for the quantitative real-time PCR. 39

Literatur

1. Liberto JM, Chen SY, Shih IM, Wang TH, Wang TL, Pisanic TR. Current and Emerging Methods for Ovarian Cancer Screening and Diagnostics: A Comprehensive Review. *Cancers (Basel)* **14(12),** 2885 (2022).
2. Chaffer CL, Weinberg RA. A perspective on cancer cell metastasis. *Science* **331,** 1559–1564 (2011).
3. Lengyel E. Ovarian Cancer Development and Metastasis. *The American Journal of Pathology* **177(3),** 1053–1064 (2010).
4. Vaughan S, Coward JI, Bast Jr. RC, Berchuck A, Berek JS, Brenton JD, Coukos G, Crum CC, Drapkin R, Etemadmoghadam D, Friedlander M, Gabra H, Kaye SB, Lord CJ, Lengyel E, Levine DA, McNeish IA, Menon U, Mills GB, Nephew KP, Oza AM, Sood AK, Stronach EA, Walczak H, Bowtell DD, Balkwill FR. Rethinking Ovarian Cancer: Recommendations for Improving Outcomes. *Nature Reviews Cancer* **11(10),** 719–725 (2011).
5. Cantor JR, Sabatini DM. Cancer cell metabolism: one hallmark, many faces. *Cancer Discovery* **2(10),** 881–98 (2012).
6. Koundouros N, Poulogiannis G. Reprogramming of fatty acid metabolism in cancer. *British Journa of Cancer* **122(1),** 4–22 (2020).
7. Fu Y, Zou T, Shen X, Nelson PJ, Li J, Wu C, Yang J, Zheng Y, Bruns C, Zhao Y, Qin L, Dong Q. Lipid metabolism in cancer progression and therapeutic strategies. *MedComm* **2(1),** 27–59 (2020).
8. Mills GB, Moolenaar WH. The emerging role of lysophosphatidic acid in cancer. *Nat Rev Cancer* **3(8),** 582–91 (2003).
9. Marchan R, Büttner B, Lambert J, Edlund K, Glaeser I, Blaszkewicz M, Leonhardt G, Marienhoff L, Kaszta D, Anft M, Watzl C, Madjar K, Grinberg M, Rempel E, Hergenröder R, Selinski S, Rahnenführer J, Lesjak MS, Stewart JD, Cadenas C, Hengstler JG. Glycerol-3-phosphate Acyltransferase 1 Promotes Tumor Cell Migration and Poor Survival in Ovarian Carcinoma. *Cancer Research* **77(17),** 4589–4601 (2017).
10. Yu J, Loh K, Song ZY, Yang HQ, Zhang Yi, Lin S. Update on glycerol-3-phosphate acyltransferases: the roles in the development of insulin resistance. *Nutrition & Diabetes* **34** (2018).
11. Wendel AA, Lewin TM, Coleman RA. Glycerol-3-phosphate acyltransferases: rate limiting enzymes of triacylglycerol biosynthesis. *Biochimica et Biophysica Acta* **1791(6),** 501–506 (2008).
12. Harayama T, Riezman H. Understanding the diversity of membrane lipid composition. *Nature Reviews Molecular Cell Biology* **19(5),** 281–296 (2018).

13. Schulz H. Oxidation of fatty acids in eukaryotes. *Biochemistry of Lipids, Lipoproteins and Membranes.* **5th Edition,** 131–154 (2008).
14. Hishikawa D, Hashidate T, Shimizu T, Shindou H. Diversity and function of membrane glycerophospholipids generated by the remodeling pathway in mammalian cells. *Journal of Lipid Research* **55(5),** 799–807 (2014).
15. Bozzaa PT, Viola JPB. Lipid droplets in inflammation and cancer. *Prostaglandins, Leukotrienes & Essential Fatty Acids* **82(4),** 243–250 (2010).
16. Currie E, Schulze A, Zechner R, Walther TC, Farese RV Jr. Cellular Fatty Acid Metabolism and Cancer. *Cell Metabolism* **18(2),** 153–161 (2013).
17. Snaebjornsson MT, Janaki-Raman S, Schulze A. Greasing the Wheels of the Cancer Machine: The Role of Lipid Metabolism in Cancer. *Cell Metabolism* **31(1),** 62–76 (2020).
18. Cheng M, Bhujwalla ZM, Glunde K. Targeting Phospholipid Metabolism in Cancer. *Frontiers in Oncology* **6(266)** (2016).
19. Cai S, Sun PH, Resaul J, Shi L, Jiang A, Satherley LK, Davies EL, Ruge F, Douglas-Jones A, Jiang WG, Ye L. Expression of phospholipase C isozymes in human breast cancer and their clinical significance. *Oncology reports* **37(3),** 1707–1715 (2017).
20. Eichmann TO, Lass A. DAG tales: the multiple faces of diacylglycerol—stereochemistry, metabolism, and signaling. *Cellular and Molecular Life Sciences* **72,** 3931–3952 (2015).
21. Griner EM, Kazanietz MG. Protein kinase C and other diacylglycerol effectors in cancer. *Nature Reviews Cancer* **7,** 281–294 (2007).
22. Foster DA. Phosphatidic acid signaling to mTOR: Signals for the survival of human cancer cells. *BBA Molecular and Cell Biology of Lipids* **1791(9),** 949–955 (2009).
23. Zhang Y, Frohman MA. Cellular and physiological roles for phospholipase D1 in cancer. *Journal of Biological Chemistry* **289(33),** 22567–22574 (2014).
24. Gomez-Cambronero J. Phospholipase D in cell signaling: from a myriad of cell functions to cancer growth and metastasis. *Journal of Biological Chemistry* **289(33),** 22557–22566 (2014).
25. Iorio E, Ricci A, Bagnoli M, Pisanu ME, Castellano G, Di Vito M, Venturini E, Glunde K, Bhujwalla ZM, Mezzanzanica D, Canevari S, Podo F. Activation of phosphatidylcholine cycle enzymes in human epithelial ovarian cancer cells. *Cancer Research* **70(5),** 2126–35 (2010).
26. Mahankali M, Peng HJ, Henkels KM, Dinauer MC, Gomez-Cambronero J. Phospholipase D2 (PLD2) is a guanine nucleotide exchange factor (GEF) for the GTPase Rac2. *Proc Natl Acad Sci U S A* **108(49),** 19617–22 (2011).

27. Jeon H, Kwak D, Noh J, Lee MN, Lee CS, Suh PG, Ryu SH. Phospholipase D2 induces stress fiber formation through mediating nucleotide exchange for RhoA. *Cellular Signalling* **23(8),** 1320–6 (2011).
28. Fang Y, Vilella-Bach M, Bachmann R, Flanigan A, Chen J. Phosphatidic acid-mediated mitogenic activation of mTOR signaling. *Science* **294(5548),** 1942–1945 (2001).
29. Rizzo MA, Shome K, Watkins SC, Romero G. The Recruitment of Raf-1 to Membranes Is Mediated by Direct Interaction with Phosphatidic Acid and Is Independent of Association with Ras. *Journal of Biological Chemistry* **275(31),** 23911–23918 (2000).
30. Pages C, Simon MF, Valet P, Saulnier-Blache JS. Lysophosphatidic acid synthesis and release. *Prostaglandins & other lipid mediators* **64 (1-4),** 1–10 (2001).
31. Moolenaar WH,van Meeteren LA, Giepmans BNG. The ins and outs oflysophosphatidic acid signaling. *BioEssays* **26(8),** 870–881 (2004).
32. McMahon HT, Gallo JL. Membrane curvature and mechanisms of dynamic cell membrane remodellin. *Nature* **438,** 590–596 (2005).
33. Kooijman EE, Chupin V, Fuller NL, Kozlov MM, de Kruijff B, Burger KN, Rand PR. Spontaneous curvature of phosphatidic acid and lysophosphatidic acid. *Biochemistry* **44(6),** 2097–2102 (2005).
34. Yanagida K, Shimizu T. Lysophosphatidic acid, a simple phospholipid with myriad functions. *Pharmacology Therapeutics* **246** (2023).
35. Geraldo LHM, Leite de Sampaio Spohr TC, Ferreira do Amaral R, Carvalho da Fonseca AC, Garcia C, de Almeida Mendes F, Freitas C, dosSantos MB, Souza Lima FR. Role of lysophosphatidic acid and its receptors in health and disease: novel therapeutic strategies. *Signal Transduction and Targeted Therapy* **6(1))** (2021).
36. Jeon ES, Heo SC, Lee IH, Choi YJ, Park JH, Choi KU, Park DY, Suh DS, Yoon MS, Kim JH. Ovarian cancer-derived lysophosphatidic acid stimulates secretion of VEGF and stromal cell-derived factor-1α from human mesenchymal stem cells. *Experimental & Molecular medicine* **42,** 280–293 (2010).
37. Ren J, Xiao YJ, Singh LS, Zhao X, Zhao Z, Feng L, Rose TM, Prestwich GD, Xu Y. Lysophosphatidic acid is constitutively produced by human peritoneal mesothelial cells and enhances adhesion, migration, and invasion of ovarian cancer cells. *Cancer Research* **66(6),** 3006–14 (2006).
38. Eichholtz T, Jalink K, Fahrenfort I, Moolenaar WH. The bioactive phospholipid lysophosphatidic acid is released from activated platelets. *Biochemical Journal* **291(3),** 677–680 (1993).

39. Michalczyk A, Budkowska M, Dołęgowska B, Chlubek D, Safranow K. Lysophosphatidic acid plasma concentrations in healthy subjects: circadian rhythm and associations with demographic, anthropometric and biochemical parameters. *Lipids in Health and Disease* **16(140)** (2017).

40. Ahn WG, Jung JS, Kwon HY, Song DK. Alteration of Lysophosphatidylcholine-Related Metabolic Parameters in the Plasma of Mice with Experimental Sepsis. *Inflammation* **40(2),** 537–545 (2017).

41. Xu Y, Shen Z, Wiper DW, Wu M, Morton RE, Elson P, Kennedy AW, Belinson J, Markman M, Casey G. Lysophosphatidic acid as a potential biomarker for ovarian and other gynecologic cancers. *JAMA* **280(8),** 719–23 (1998).

42. Fang X, Gaudette D, Furui T, Mao M, Estrella V, Eder A, Pustilnik T, Sasagawa T, Lapushin R, Yu S, Jaffe RB, Wiener JR, Erickson JR, Mills GB. Lysophospholipid growth factors in the initiation, progression, metastases, and management of ovarian cancer. *Annals of the New York Academy of Sciences* **905,** 188–208 (2000).

43. Tokumura A, Kanaya Y, Miyake M, Yamano S, Irahara M, Fukuzawa K. Increased Production of Bioactive Lysophosphatidic Acid by Serum Lysophospholipase D in Human Pregnancy. *Biology of Reproduction* **67(5),** 1386–1392 (2002).

44. Burke JE, Dennis EA. Phospholipase A2 structure/function, mechanism, and signaling. *Journal of Lipid Research* **50,** 237–42 (2009).

45. Sawada N, Obama T, Mizuno M, Fukuhara K, Iwamoto S, Aiuchi T, Makiyama T, Itabe H. Transfer and Enzyme-Mediated Metabolism of Oxidized Phosphatidylcholine and Lysophosphatidylcholine between Low- and High-Density Lipoproteins. *Antioxidants* **9(11)** (2020).

46. Sonoda H, Aoki J, Hiramatsu T, Ishida M, Bandoh K, Nagai Y, Taguchi R, Inoue K, Arai H. A novel phosphatidic acid-selective phospholipase A1 that produces lysophosphatidic acid. *Journal of Biological Chemistry* **277(37),** 34254–63 (2002).

47. Shulga YV, Topham MK, Epand RM. Regulation and functions of diacylglycerol kinases. *Chemical Reviews* **111(10),** 6186–208 (2011).

48. Bektas M, Payne SG, Liu H, Goparaju S, Milstien S, Spiegel S. A novel acylglycerol kinase that produces lysophosphatidic acid modulates cross talk with EGFR in prostate cancer cells. *The Journal of Cell Biology* **169(5),** 801–811 (2005).

49. Stewart JD, Marchan R, Lesjak MS, Lambert J, Hergenroeder R, Ellisc JK, Lau CH, Keun HC, Schmitz G, Schiller J, Eibisch M, Hedberg C, Waldmann H, Lausch E, Tanner B, Sehouli J, Sagemueller J, Staude H, Steiner E, Hengstler JG. Choline-releasing glycerophosphodiesterase EDI3 drives tumor cell migration and metastasis. *PNAS* **109(21),** 8155–8160 (2012).

50. Ohshima N, Kudo T, Yamashita Y, Mariggiò S, Araki M, Honda A, Nagano T, Isaji C, Kato N, Corda D, Izumi T, Yanaka N. New members of the mammalian glycerophosphodiester phosphodiesterase family: GDE4 and GDE7 produce lysophosphatidic acid by lysophospholipase D activity. *Journal of Biological Chemistry* **290(7),** 4260–4271 (2014).
51. Brindley DN, Waggoner DW. Mammalian lipid phosphate phosphohydrolases. *Journal of Biological Chemistry* **273(38),** 24281–4 (1998).
52. Tang X, Brindley DN. Lipid Phosphate Phosphatases and Cancer. *Biomolecules* **10(9),** 1263 (2020).
53. Tang X, Benesch MG, Brindley DN. Lipid phosphate phosphatases and their roles in mammalian physiology and pathology. *Journal of Lipid Research* **56(11),** 2048–60 (2015).
54. Tanyi JL, Morris AJ, Wolf JK, Fang X, Hasegawa Y, Lapushin R, Auersperg N, Sigal YJ, Newman RA, Felix EA, Atkinson EN, Mills GB. The human lipid phosphate phosphatase-3 decreases the growth, survival, and tumorigenesis of ovarian cancer cells: validation of the lysophosphatidic acid signaling cascade as a target for therapy in ovarian cancer. *Cancer Research* **63(5),** 1073–82 (2003).
55. Tanyi JL, Hasegawa Y, Lapushin R, Morris AJ, Wolf JK, Berchuck A, Lu K, Smith DI, Kalli K, Hartmann LC, McCune K, Fishman D, Broaddus R, Cheng KW, Atkinson EN, Yamal JM, Bast RC, Felix EA, Newman RA, Mills GB. Role of decreased levels of lipid phosphate phosphatase-1 in accumulation of lysophosphatidic acid in ovarian cancer. *Clinical Cancer Research* **9(10),** 3534–45 (2003).
56. Yamashita A, Hayashi Y, Matsumoto N, Nemoto-Sasaki Y, Oka S, Tanikawa T, Sugiura T. Glycerophosphate/Acylglycerophosphate acyltransferases. *Biology (Basel)* **3(4),** 801–30 (2014).
57. Karagiota A, Chachami G, Paraskeva E. Lipid Metabolism in Cancer: The Role of Acylglycerolphosphate Acyltransferases (AGPATs). *Cancers (Basel)* **14(1),** 228 (2022).
58. Wen P, Wang R, Xing Y, Ouyang W, Yuan Y, Zhang S, Liu Y, Peng Z. The prognostic value of the GPAT/AGPAT gene family in hepatocellular carcinoma and its role in the tumor immune microenvironment. *Frontiers in Immunology* **10** (2023).
59. Zhang D, Shi R, Xiang W, Kang X, Tang B, Li C, Gao L, Zhang X, Zhang L, Dai R, Miao H. The Agpat4/LPA axis in colorectal cancer cells regulates antitumor responses via p38/p65 signaling in macrophages. *Signal Transduction and Targeted Therapy* **5(24)** (2020).
60. Diefenbach CS, Soslow RA, Iasonos A, Linkov I, Hedvat C, Bonham L, Singer J, Barakat RR, Aghajanian C, Dupont J. Lysophosphatidic acid acyltransferase-beta (LPAAT-beta) is highly expressed in advanced ovarian cancer and is associated with aggressive histology and poor survival. *Cancer* **107(7),** 1511–9 (2006).
61. Aikawa S, Hashimoto T, Kano K, Aoki J. Lysophosphatidic acid as a lipid mediator with multiple biological actions. *Journal of Biochemistry* **157(2),** 81–9. (2015).

62. Yung YC, Stoddard NC, Chun J. LPA receptor signaling: pharmacology, physiology, and pathophysiology. *Journal of Lipid Research* **55(7),** 1192–1214 (2014).
63. Balijepalli P, Sitton CC, Meier KE. Lysophosphatidic Acid Signaling in Cancer Cells: What Makes LPA So Special? *Cells* **10(8),** 2059 (2021).
64. Kranenburg O, Poland M, van Horck FP, Drechsel D, Hall A, Moolenaar WH. Activation of RhoA by lysophosphatidic acid and Galpha12/13 subunits in neuronal cells: induction of neurite retraction. *Molecular Biology of the Cell* **10(6),** 1851–7 (1999).
65. Bhadriraju K, Yang M, Alom Ruiz S, Pirone D, Tan J, Chen CS. Activation of ROCK by RhoA is regulated by cell adhesion, shape, and cytoskeletal tension. *Experimental Cell Research* **313(16),** 3616–23 (2007).
66. Panupinthu N, Lee HY, Mills GB. Lysophosphatidic acid production and action: critical new players in breast cancer initiation and progression. *British Journal of Cancer* **102(6),** 941–6 (2010).
67. Yu S, Murph MM, Lu Y, Liu S, Hall HS, Liu J, Stephens C, Fang X, Mills GB. Lysophosphatidic acid receptors determine tumorigenicity and aggressiveness of ovarian cancer cells. *Journal of the National Cancer Institute* **100(22),** 1630–42 (2008).
68. Cui R, Cao G, Bai H, Zhang Z. LPAR1 regulates the development of intratumoral heterogeneity in ovarian serous cystadenocarcinoma by activating the PI3K/AKT signaling pathway. *Cancer Cell International* **19(201)** (2019).
69. Popnikolov NK, Dalwadi BH, Thomas JD, Johannes GJ, Imagawa WT. Association of autotaxin and lysophosphatidic acid receptor 3 with aggressiveness of human breast carcinoma. *Tumour Biology* **33(6),** 2237–43 (2012).
70. Jeong KJ, Park SY, Cho KH, Sohn JS, Lee J, Kim YK, Kang J, Park CG, Han JW, Lee HY. The Rho/ROCK pathway for lysophosphatidic acid-induced proteolytic enzyme expression and ovarian cancer cell invasion. *Oncogene* **31(39),** 4279–89 (2012).
71. Aiello S, Casiraghi F. Lysophosphatidic Acid: Promoter of Cancer Progression and of Tumor Microenvironment Development. A Promising Target for Anticancer Therapies? *Cells* **10(6),** 1390 (2021).
72. Marshall JC, Collins JW, Nakayama J, Horak CE, Liewehr DJ, Steinberg SM, Albaugh M, Vidal-Vanaclocha F, Palmieri D, Barbier M, Murone M, Steeg PS. Effect of inhibition of the lysophosphatidic acid receptor 1 on metastasis and metastatic dormancy in breast cancer. *Journal of the National Cancer Institute* **104(17),** 1306–19 (2012).
73. International Journal of Oncology. Targeting lysophosphatidic acid receptor type 1 with Debio 0719 inhibits spontaneous metastasis dissemination of breast cancer cells independently of cell proliferation and angiogenesis. *David M, Ribeiro J, Descotes F, Serre CM, Barbier M, Murone M, Clézardin P, Peyruchaud O* **40(4),** 1133–41 (2011).

74. Brindley DN. Lysophosphatidic Acid Signaling in Cancer. *Cancers (Basel)* **12(12),** 3791 (2020).

75. McIntyre TM, Pontsler AV, Silva AR, St. Hilaire A, Xu Y, Hinshaw JC, Zimmerman GA, Hama K, Aoki J, Arai H, Prestwich GD. Identification of an intracellular receptor for lysophosphatidic acid (LPA): LPA is a transcellular PPARγ agonist. *PNAS* **100(1),** 131–136 (2003).

76. Stapleton CM, Mashek DG, Wang S, Nagle CA, Cline GW, Thuillier P, Leesnitzer LM, Li LO, Stimmel JB, Shulman GI, Coleman RA. Lysophosphatidic Acid Activates Peroxisome Proliferator Activated Receptor- γin CHO Cells That Overexpress Glycerol 3-Phosphate Acyltransferase-1. *PLOS one* **6(4)** (2011).

77. Tsukahara T, Yamagishi S, Matsuda Y, Haniu H. Lysophosphatidic acid signaling regulates the KLF9-PPARγ axis in human induced pluripotent stem cell-derived neurons. *Biochemical and Biophysical Research Communications* **1(9),** 223–227 (2017).

78. Meerschaert K, De Corte V, De Ville Y, ÈI Vandekerckhove J, Gettemans J. Gelsolin and functinally similar actin-binding proteins are regulated by lysophosphatidic acid. *The EMBO Journal* **17(20),** 5923–5932 (1998).

79. Tomar A, George SP, Mathew S, Khurana S. Differential Effects of Lysophosphatidic Acid and Phosphatidylinositol 4,5-Bisphosphate on Actin Dynamics by Direct Association with the Actin-binding Protein Villin. *Journal of biological chemistry* **184(51),** 35278–35282 (2009).

80. Kumar N, Tomar A, Parrill AL, Khurana S. Functional dissection and molecular characterization of calcium-sensitive actin-capping and actin-depolymerizing sites in villin. *The Journal of Biological Chemistry* **279(43),** 45036–46 (2004).

81. Davoudian K, Bhattacharya S, Thompson D, Thompson M. Coupled Electrostatic and Hydrophobic Destabilisation of the Gelsolin-Actin Complex Enables Facile Detection of Ovarian Cancer Biomarker Lysophosphatidic Acid. *Biomolecules* **13** (2023).

82. Ohba Y, Sakuragi T, Kage-Nakadai E, Tomioka NH, Kono N, Imae R, Inoue A, Aoki J, Ishihara N, Inoue T, Mitani S, Arai H. Mitochondria-type GPAT is required for mitochondrial fusion. *The EMBO Journal* **32,** 1265–1279 (2013).

83. Labbe K, Mookerjee S, Le Vasseur M, Gibbs E, Lerner C, Nunnari J. The modified mitochondrial outer membrane carrier MTCH2 links mitochondrial fusion to lipogenesis. *Journal of Cell Biology* **220(11)** (2021).

84. Goldman A, Mullokandov M, Zaltsman Y, Regev L, Levin-Zaidman S, Gross A. MTCH2 cooperates with MFN2 and lysophosphatidic acid synthesis to sustain mitochondrial fusion. *EMBO Reports* **25,** 45–67 (2024).

85. Smeitink J, van den Heuvel L, DiMauro S. The genetics and pathology of oxidative phosphorylation. *Nat Rev Genet* **2(5),** 342–52 (2001).

86. Kuznetsov AV, Ausserlechner MJ. Research of Mitochondrial Function, Structure, Dynamics and Intracellular Organization. **24(1),** 886 (2023).

87. Chen YF, Chen YT, Chiu WT, Shen MR. Remodeling of calcium signaling in tumor progression. *Journal of Biomedical Science* **20(1),** 23 (2013).

88. Martin-Romero FJ, Lopez-Guerrero AM, Pascual-Caro C, Pozo-Guisado E. The Interplay between Cytoskeleton and Calcium Dynamics. Cytoskeleton - Structure, Dynamics, Function and Disease. *InTech* (2017).

89. Adebayo M, Singh S, Singh AP, Dasgupta S. Mitochondrial fusion and fission: The fine-tune balance for cellular homeostasis. *FASEB* **35(6)** (2021).

90. Cunniff B, McKenzie AJ, Heintz NH, Howe AK. AMPK activity regulates trafficking of mitochondria to the leading edge during cell migration and matrix invasion. *Molecular Biology of the Cell* **27(17),** 2662–74 (2016).

91. Libring S, Berestesky ED, Reinhart-King CA. The movement of mitochondria in breast cancer: internal motility and intercellular transfer of mitochondria. *Clinical Experimental Metastasis* **41(5),** 567–587 (2024).

92. Abate M, Festa A, Falco M, Lombardi A, Luce A, Grimaldi A, Zappavigna S, Sperlongano P, Irace C, Caraglia M, Misso G. Mitochondria as playmakers of apoptosis, autophagy and senescence. *Seminars in Cell Developlemtal Biology* **98,** 139–153 (2020).

93. Sullivan LB, Chandel NS. Mitochondrial reactive oxygen species and cancer. *Cancer Metabolism* **2(17)** (2014).

94. Wendel AA, Cooper DE, Ilkayeva OR, Muoio DM, Coleman RA. Glycerol-3-phosphate Acyltransferase (GPAT)-1, but not GPAT4,Incorporates Newly Synthesized Fatty Acids into Triacylglycerol and Diminishes Fatty Acid Oxidation. *Journal of Biological Chemistry* **288(38),** 27299–27306 (2013).

95. Lewin TM, de Jong H, Schwerbrock NJ, Hammond LE, Watkins SM, Combs TP, Coleman RA. Mice deficient in mitochondrial glycerol-3-phosphate acyltransferase-1 have diminished myocardial triacylglycerol accumulation during lipogenic diet and altered phospholipid fatty acid composition. *Biochimica et Biophysica Acta* **1781(6-7),** 352–8 (2008).

96. Brockmöller SF, Bucher E, Müller BM, Budczies J, Hilvo M, Griffin JL, Orešič M, Kallioniemi O, Iljin K, Loibl S, Darb-Esfahani S, Sinn BV, Klauschen F, Prinzler J, Bangemann N, Ismaeel F, Fiehn O, Dietel M, Denkert C. Integration of metabolomics and expression of glycerol-3-phosphate acyltransferase (GPAM) in breast cancer: Link to patient survival, hormone receptor status and metabolic profiling. *Journal of Proteome Research* **11(2),** 850–860 (2011).

97. Irifune H, Kochi Y, Miyamoto T, Sakoda T, Kato K, Kunisaki Y, Akashi K, Kikushige Y. GPAM mediated lysophosphatidic acid synthesis regulates mitochondrial dynamics in acute myeloid leukemia. *Cancer Science* (2003).

98. Vukotic M, Nolte H, König T, Saita S, Ananjew M, Krüger M, Tatsuta T, Langer T. Acylglycerol Kinase Mutated in Sengers Syndrome Is a Subunit of the TIM22 Protein Translocase in Mitochondria. *Molecular Cell* **67(3),** 471–483 (2017).

99. Kang Y, Stroud DA, Baker MJ, De Souza DP, Frazier AE, Liem M, Tull D, Mathivanan S, McConville MJ, Thorburn DR, Ryan MT, Stojanovski D. Sengers Syndrome-Associated Mitochondrial Acylglycerol Kinase Is a Subunit of the Human TIM22 Protein Import Complex. *Molecular Cell* **67(3),** 457–470 (2017).

100. Mayr JA, Haack TB, Graf E, Zimmermann FA, Wieland T, Haberberger B, Superti-Furga A, Kirschner J, Steinmann B, Baumgartner MR, Moroni I, Lamantea E, Zeviani M, Rodenburg RJ, Smeitink J, Strom TM, Meitinger T, Sperl W, Prokisch H. Lack of the mitochondrial protein acylglycerol kinase causes Sengers syndrome. *The American Journal of Human Genetics* **90(2),** 314–20 (2012).

101. Chen X, Ying Z, Lin X, Lin H, Wu J, Li M, Song L. Acylglycerol kinase augments JAK2/STAT3 signaling in esophageal squamous cells. *The Journal of Clinical Investigation* **123(6),** 2576–89 (2013).

102. Liu G, Ren X, Gao C, Zhang W. Acylglycerol kinase promotes the proliferation and cell cycle progression of oral squamous cell carcinoma. *Molecular Medicine Reports* **12(2),** 2225–30 (2015).

103. Wang X, Lin C, Zhao X, Liu A, Zhu J, Li X, Song L. Acylglycerol kinase promotes cell proliferation and tumorigenicity in breast cancer via suppression of the FOXO1 transcription factor. *Molecular Cancer* **13(106)** (2014).

104. Zhu Q, Zhong AL, Hu H, Zhao JJ, Weng DS, Tang Y, Pan QZ, Zhou ZQ, Song MJ, Yang JY, He JY, Liu Y, Li M, Hu WM, Yang CP, Xiang T, Chen MY, Ma G, Guo L, Xia JC. Acylglycerol kinase promotes tumour growth and metastasis via activating the PI3K/AKT/GSK3β signalling pathway in renal cell carcinoma. *Journal of hematology oncology* **13(1)** (2020).

105. Sun F, Wei Y, Liu Z, Jie Q, Yang X, Long P, Wang J, Xiong Y, Li Q, Quan S, Ma Y. Acylglycerol kinase promotes ovarian cancer progression and regulates mitochondria function by interacting with ribosomal protein L39. *Journal of experimental and clinical research* **41(1),** 238 (2022).

106. Cui Y, Lin C, Wu Z, Liu A, Zhang X, Zhu J, Wu G, Wu J, Li M, Li J, Song L. AGK enhances angiogenesis and inhibits apoptosis via activation of the NF- κB signaling pathway in hepatocellular carcinoma. *Oncotarget* **5(23),** 12057–69 (2014).

107. Hu Z, Qu G, Yu X, Jiang H, Teng XL, Ding L, Hu Q, Guo X, Zhou Y, Wang F, Li HB, Chen L, Jiang J, Su B, Liu J, Zou Q. Acylglycerol Kinase Maintains Metabolic State and Immune Responses of CD8+ T Cells. *Cell Metabolism* **30(2),** 290–302 (2019).

108. Ding N, Wang K, Jiang H, Yang M, Zhang L, Fan X, Zou Q, Yu J, Dong H, Cheng S, Xu Y, Liu J. AGK regulates the progression to NASH by affecting mitochondria complex I function. *Theranostics* **12(7),** 3237–3250 (2022).

109. Rosen DG, Yang G, Liu G, Mercado-Uribe I, Chang B, Xiao XS, Zheng J, Xue FX, Liu J. Ovarian cancer: pathology, biology, and disease models. *Frontiers in Bioscience* **14(6),** 2089–102 (2009).

110. Webb PM, Jordan SJ. Global epidemiology of epithelial ovarian cancer. *Nature Reviews. Clinical oncology* **21(5),** 389–400 (2024).

111. Goff BA, Mandel LS, Drescher CW, Urban N, Gough S, Schurman KM, Patras J, Mahony BS, Andersen MR. Development of an ovarian cancer symptom index: possibilities for earlier detection. *Cancer* **109(2),** 221–7 (2007).

112. Cho KR & Shih IM. Ovarian Cancer. *Annual Review of Pathology: Mechanisms of Disease* **4(1),** 287–313 (2009).

113. Wild CP, Weiderpass E, Stewart BW, editors. World Cancer Report: Cancer Research for Cancer Prevention. accessed 10.04.2024. `http://publications.iarc.fr/586` (2020).

114. Khazaei Z, Namayandeh SMM, Beiranvand R, Naemi H, Bechashk SM, Goodarzi E. Worldwide incidence and mortality of ovarian cancer and Human Development Index (HDI): GLOBOCAN sources and methods 2018. *Journal of Preventive Medicine and Hygiene* **62,** 237–249 (2012).

115. Tung KH, Wilkens LR, Wu AH, McDuffie K, Nomura AMY, Kolonel LN, Terada KY, Goodman MT. Effect of anovulation factors on pre- and postmenopausal ovarian cancer risk: revisiting the incessant ovulation hypothesis. *American Journal of Epidemiology* **161,** 321–329 (2005).

116. Mallen A, Soong TR, Townsend MK, Wenham RM, Crum CP, SS Tworoger. Surgical prevention strategies in ovarian cancer. *Gynecologic Oncology* **151(1),** 166–175 (2018).

117. Adami HO, Lambe M, Persson I, Ekbom A, Adami HO, Hsieh CC, Trichopoulos D, Ekbom A, Lambe M, Leon D, Janson PO. Parity, age at first childbirth, and risk of ovarian cancer. *The Lancet* **344(8932),** 1250–1254 (1994).

118. Stewart C, Ralyea C, Lockwood S. Ovarian Cancer: An Integrated Review. *Seminars in Oncology Nursing* **35(2),** 151–156 (2019).

119. Crispens MA. Endometrial and ovarian cancer in lynch syndrome. *Clinics in colon and rectal surgery* **25(2),** 97–102 (2012).

120. Armstrong DK, Alvarez RD, Bakkum-Gamez JN, Barroilhet L, Behbakht K, Berchuck A, Chen LM, Cristea M, DeRosa M, Eisenhauer EL, Gershenson DM, Gray HJ, Grisham R, Hakam A, Jain A, Karam A, Konecny GE, Leath CA, Liu J, Mahdi H, Martin L, Matei D, McHale M, McLean K, Miller DS, O'Malley DM, Percac-Lima S, Ratner E, Remmenga SW, Vargas R, Werner TL, Zsiros E, Burns JL, Engh AM. Ovarian Cancer, Version 2.2020, NCCN Clinical Practice Guidelines in Oncology. *Journal of the National Comprehensive Cancer Network* **19(2),** 191–226 (2021).

121. Arora T, Mullangi S, Lekkala MR. Ovarian Cancer. *StatPearls, PMID: 33620837* (2021).

122. Mathieu KB, Bedi DG, Thrower SL, Qayyum A, Bast RC Jr. Screening for ovarian cancer: imaging challenges and opportunities for improvement. *Ultrasound Obstet Gynecol* **51(3),** 293–303 (2018).

123. Chan JK, Urban R, Capra AM, Jacoby V, Osann K, Whittemore A, Habel LA. Ovarian cancer rates after hysterectomy with and without salpingo-oophorectomy. *Obstetrics Gynecology* **123(1),** 65–72 (2014).

124. Zheng P, Zheng P, Chen G. Conditional Survival of Advanced Epithelial Ovarian Cancer: A Real-World Data Retrospective Cohort Study From the SEER Database. *Frontiers in Medicine* **8** (2021).

125. Cook SA, Tinker AV. PARP Inhibitors and the Evolving Landscape of Ovarian Cancer Management: A Review. *BioDrugs* **33(3),** 255–273 (2019).

126. Eskander RN, Randall LM. Bevacizumab in the treatment of ovarian cancer. *Biologics* **5,** 1–5 (2011).

127. George A, McLachlan J, Tunariu N, Della Pepa C, Migali C, Gore M, Kaye S, Banerjee S. The role of hormonal therapy in patients with relapsed high-grade ovarian carcinoma: a retrospective series of tamoxifen and letrozole. *BMC Cancer* **456** (2017).

128. de Bree E, Michelakis D, Stamatiou D, Romanos J, Zoras O. Pharmacological principles of intraperitoneal and bidirectional chemotherapy. *Pleura Peritoneum* **2(2),** 47–62 (2017).

129. Prat, Jaime. Ovarian carcinomas: five distinct diseases with different origins, genetic alterations, and clinicopathological features. *Virchows Archiv* **460,** 237–249 (2012).

130. Peres LC, Cushing-Haugen KL, Anglesio M, Wicklund K, Bentley R, Berchuck A, Kelemen LE, Nazeran TM, Gilks CB, Harris HR, Huntsman DG, Schildkraut JM, Rossing MA, Köbel M, Doherty JA. Histotype classification of ovarian carcinoma: A comparison of approaches. *Gynecologic Oncology* **151(1),** 53–60 (2018).

131. Seidman JD, Horkayne-Szakaly I, Haiba M, Boice CR, Kurman RJ, Ronnett BM. The histologic type and stage distribution of ovarian carcinomas of surface epithelial origin. *International Journal of Gynecological Pathology* **23(1),** 41–4 (2004).

132. Romero I & Bast Jr RC. Minireview: human ovarian cancer: biology, current management, and paths to personalizing therapy. *Endocrinology* **153(4),** 1593–602 (2012).

133. Reid BM, Permuth JB, Sellers TA. Epidemiology of ovarian cancer: a review. *Cancer biology & medicine* **14(1),** 9–32 (2017).

134. Vang R, Shih IeM, Kurman RJ. Ovarian low-grade and high-grade serous carcinoma: pathogenesis, clinicopathologic and molecular biologic features, and diagnostic problems. *Advances in Anatomic Pathology* **16(5),** 267–82 (2009).

135. Soslow RA. Histologic subtypes of ovarian carcinoma: an overview. *International Journal of Gynecological Pathology* **27(2),** 161–74 (2008).

136. Lydia Gaba. What is Ovarian Cancer? accessed 28.03.2024. `https://www.clinicbarcelona.org/en/assistance/diseases/ovarian-cancer` (2020).

137. Ravindran F, Choudhary B. Ovarian Cancer: Molecular Classification and Targeted Therapy. *IntechOpen* (2021).

138. Klymenko Y, Kim O, Stack MS. Complex Determinants of Epithelial: Mesenchymal Phenotypic Plasticity in Ovarian Cancer. *Cancers (Basel)* **9(8),** 104 (2017).

139. Naora H & Montell DJ. Ovarian Cancer Metastasis: Integrating insights from disparate model organisms. *Nature Reviews Cancer* **5,** 355–366 (2005).

140. Shield K, Ackland ML, Ahmed N, Rice GE. Multicellular spheroids in ovarian cancer metastases: Biology and pathology. *Gynecologic Oncology* **113(1),** 143–148 (2009).

141. Rickard BP, Conrad C, Sorrin AJ, Ruhi MK, Reader JC, Huang SA, Franco W, Scarcelli G, Polacheck WJ, Roque DM, Del Carmen MG, Huang HC, Demirci U, Rizvi I. Malignant Ascites in Ovarian Cancer: Cellular, Acellular, and Biophysical Determinants of Molecular Characteristics and Therapy Response. *Cancers (Basel)* **13(17)** (2021).

142. Nieman KM, Kenny HA, Penicka CV, Ladanyi A, Buell-Gutbrod R, Zillhardt MR, Romero IL, Carey MS, Mills GB, Hotamisligil GS, Yamada SD, Peter ME, Gwin K, Lengyel E. Adipocytes promote ovarian cancer metastasis and provide energy for rapid tumor growth. *Nature Medicine* **17(11),** 1498–1503 (2011).

143. Pradeep S, Kim SW, Wu SY, Nishimura M, Chaluvally-Raghavan P, Miyake T, Pecot CV, Kim SJ, Choi HJ, Bischoff FZ, Mayer JA, Huang L, Nick AM, Hall CS, Rodriguez-Aguayo C, Zand B, Dalton HJ, Arumugam T, Lee HJ, Han HD, Cho MS, Rupaimoole R, Mangala LS, Sehgal V, Oh SC, Liu J, Lee JS, Coleman RL, Ram P, Lopez-Berestein G, Fidler IJ, Sood AK. Hematogenous metastasis of ovarian cancer: rethinking mode of spread. *Cancer Cell* **26(1),** 77–91 (2014).

144. Tanaka K, Shimada Y, Nishino K, Yoshihara K, Nakano M, Kameyama H, Enomoto T, Wakai T. Clinical Significance of Mesenteric Lymph Node Involvement in the Pattern of Liver Metastasis in Patients with Ovarian Cancer. *Annals of Surgical Oncology* **28(12),** 7606–7613 (2021).

145. Schoutrop E, Moyano-Galceran L, Lheureux S, Mattsson J, Lehti K, Dahlstrand H, Magalhaes I. Molecular, cellular and systemic aspects of epithelial ovarian cancer and its tumor microenvironment. *Seminars in Cancer Biology* **86(3),** 207–223 (2022).

146. Poveda A, Kaye SB, McCormack R, Wang S, Parekh T, Ricci D, Lebedinsky CA, Tercero JC, Zintl P, Monk BJ. Circulating tumor cells predict progression free survival and overall survival in patients with relapsed/recurrent advanced ovarian cancer. *Gynecological oncology* **122(3),** 567–72 (2011).

147. Tsuji T, Ibaragi S, Hu GF. Epithelial-mesenchymal transition and cell cooperativity in metastasis. *Cancer Research* **69(18),** 7135–9 (2009).

148. Panorchan P, Thompson MS, Davis KJ, Tseng Y, Konstantopoulos K, Wirtz D. Single-molecule analysis of cadherin-mediated cell-cell adhesion. *Journal of Cell Science* **119(1),** 66–74 (2006).

149. Sawada K, Mitra AK, Radjabi AR, Bhaskar V, Kistner EO, Tretiakova M, Jagadeeswaran S, Montag A, Becker A, Kenny HA, Peter ME, Ramakrishnan V, Yamada SD, Lengyel E. Loss of E-cadherin promotes ovarian cancer metastasis via alpha 5-integrin, which is a therapeutic target. *Cancer Research* **68(7),** 2329–39 (2008).

150. Tian X, Liu Z, Niu B, Zhang J, Tan TK, Lee SR, Zhao Y, Harris DC, Zheng G. E-cadherin/β-catenin complex and the epithelial barrier. *Journal of Biotechnology* (2011).

151. Kim WK, Kwon Y, Jang M, Park M, Kim J, Cho S, Jang DG, Lee WB, Jung SH, Choi HJ, Min BS, Il Kim T, Hong SP, Paik YK, Kim H. β-catenin activation down-regulates cell-cell junction-related genes and induces epithelial-to-mesenchymal transition in colorectal cancers. *Scientific Reports* **9(1)** (2019).

152. Yuan Z, Li Y, Zhang S, Wang X, Dou H, Yu X, Zhang Z, Yang S, Xiao M. Extracellular matrix remodeling in tumor progression and immune escape: from mechanisms to treatments. *Molecular Cancer* **22(1)** (2023).

153. Śliwa A, Szczerba A, Pięta PP, Białas P, Lorek J, Nowak-Markwitz E, Jankowska A. A Recipe for Successful Metastasis: Transition and Migratory Modes of Ovarian Cancer Cells. *Cancers (Basel)* **16(4),** 783 (2024).

154. Szymczak AL, Vignali DA. Development of 2A peptide-based strategies in the design of multicistronic vectors. *Expert Opinion on Biological Therapy* **5(5),** 627–38 (2005).

155. Zanoni M, Piccinini F, Arienti C, Zamagni A, Santi S, Polico R, Bevilacqua A, Tesei A. 3D tumor spheroid models for in vitro therapeutic screening: a systematic approach to enhance the biological relevance of data obtained. *Scientific Reports* **6(19103)** (2016).

156. Livak KJ & Schmittgen TD. Analysis of relative gene expression data using real-time quantitative PCR and the 2(-Delta Delta C(T)) Method. *Methods* **25(4),** 402–8 (2001).

157. Coman C, Solari FA, Hentschel A, Sickmann A, Zahedi RP, Ahrends R. Simultaneous Metabolite, Protein, Lipid Extraction (SIMPLEX): A Combinatorial Multimolecular Omics Approach for Systems Biology. *Molecular & cellular proteomics* **15(4),** 1453–1466 (2016).

158. Schindelin J, Arganda-Carreras I, Frise E, Kaynig V, Longair M, Pietzsch T, Preibisch S, Rueden C, Saalfeld S, Schmid B, Tinevez JY, White DJ, Hartenstein V, Eliceiri K, Tomancak P, Cardona A. Fiji: an open-source platform for biological-image analysis. *Nature Methods* **9(7),** 676–82 (2012).

159. Rakina M, Kazakova A, Villert A, Kolomiets L, Larionova I. Spheroid Formation and Peritoneal Metastasis in Ovarian Cancer: The Role of Stromal and Immune Components. *International Journal of Molecular Sciences* **23(11)** (2022).

160. Liao J, Qian F, Tchabo N, Mhawech-Fauceglia P, Beck A, Qian Z, Wang X, Huss WJ, Lele SB, Morrison CD, Odunsi K. Ovarian cancer spheroid cells with stem cell-like properties contribute to tumor generation, metastasis and chemotherapy resistance through hypoxia-resistant metabolism. *PLoS One* **9(1)** (2014).

161. Flörkemeier I, Antons LK, Weimer JP, Hedemann N, Rogmans C, Krüger S, Scherließ R, Dempfle A, Arnold N, Maass N, Bauerschlag DO. Multicellular ovarian cancer spheroids: novel 3D model to mimic tumour complexity. *Scientific Reports* **14(1)** (2024).

162. Baldanzi G, Bettio V, Malacarne V, Graziani A. Diacylglycerol Kinases: Shaping Diacylglycerol and Phosphatidic Acid Gradients to Control Cell Polarity. *Front Cell Dev Biol* **4(140)** (2016).

163. Hanna S, El-Sibai M. Signaling networks of Rho GTPases in cell motility. *Cell Signalling* **25(10),** 1955–61 (2013).

164. Shang S, Hua F, Hu ZW. The regulation of β-catenin activity and function in cancer: therapeutic opportunities. *Oncotarget* **8(20),** 33972–33989 (2017).

165. Munshi A, Hobbs M, Meyn RE. Clonogenic cell survival assay. *Methods in Molecular Medicine* **110,** 21–28 (2005).

166. Huergo MA, Pasquale MA, González PH, Bolzán AE, Arvia AJ. Growth dynamics of cancer cell colonies and their comparison with noncancerous cells. *Phys Rev E Stat Nonlin Soft Matter Phys* **85(1)** (2012).

167. Stadler M, Scherzer M, Walter S, Holzner S, Pudelko K, Riedl A, Unger C, Kramer N, Weil B, Neesen J, Hengstschläger M, Dolznig H. Exclusion from spheroid formation identifies loss of essential cell-cell adhesion molecules in colon cancer cells. *Scientific Reports* **8(1),** 1151 (2018).

168. Casey RC, Burleson KM, Skubitz KM, Pambuccian SE, Oegema TR Jr, Ruff LE, Skubitz AP. Beta 1-integrins regulate the formation and adhesion of ovarian carcinoma multicellular spheroids. *The American Journal of Pathology* **159(6),** 2071–80 (2001).

169. Lesjak MS, Marchan R, Stewart JD, Rempel E, Rahnenführer J, Hengstler JG. EDI3 links choline metabolism to integrin expression, cell adhesion and spreading. *Cell Adhesion & Migration* **8(5),** 499–508 (2014).

170. Bergers G, Fendt SM. he metabolism of cancer cells during metastasis. *Nature Reviews Cancer* **21(3),** 162–180 (2021).

171. Bhattacharya A, Alam K, Roy NS, Kaur K, Kaity S, Ravichandiran V, Roy S. Exploring the interaction between extracellular matrix components in a 3D organoid disease model to replicate the pathophysiology of breast cancer. *J Exp Clin Cancer Res* **42(1),** 343 (2023).

172. Williams ME, Howard D, Donnelly C, Izadi F, Parra JG, Pugh M, Edwards K, Lutchman-Sigh K, Jones S, Margarit L, Francis L, Conlan RS, Taraballi F, Gonzalez D. Adipocyte derived exosomes promote cell invasion and challenge paclitaxel efficacy in ovarian cancer. *Cell Communication and Signaling* **22(1),** 443 (2024).

173. Wu C, Dong S, Huang R, Chen X. Cancer-Associated Adipocytes and Breast Cancer: Intertwining in the Tumor Microenvironment and Challenges for Cancer Therapy. *Cancers (Basel)* **15(3),** 726 (2023).

174. Li Z, Fang X, Wang S. Omentum provides a special cell microenvironment for ovarian cancer. *Cancer Reports* **6(10)** (2023).

175. Motohara T, Masuda K, Morotti M, Zheng Y, El-Sahhar S, Chong KY, Wietek N, Alsaadi A, Carrami EM, Hu Z, Artibani M, Gonzalez LS, Katabuchi H, Saya H, Ahmed AA. An evolving story of the metastatic voyage of ovarian cancer cells: cellular and molecular orchestration of the adipose-rich metastatic microenvironment. *Oncogene* **38(16),** 2885–2898 (2019).

176. Emwas AH. The strengths and weaknesses of NMR spectroscopy and mass spectrometry with particular focus on metabolomics research. *Methods in Molecular Biology* **1277,** 161–93 (2015).

177. Antoniewicz MR. A guide to 13C metabolic flux analysis for the cancer biologist. *Experimental and Molecular Medicine* **50(4),** 1–13 (2018).

178. Nguyen VHL, Hough R, Bernaudo S, Peng C. Wnt/β-catenin signalling in ovarian cancer: Insights into its hyperactivation and function in tumorigenesis. *Journal of Ovarian Research* **12(1),** 122 (2019).

179. Ge J, Burnier L, Adamopoulou M, Kwa MQ, Schaks M, Rottner K, Brakebusch C. RhoA, Rac1, and Cdc42 differentially regulate αSMA and collagen I expression in mesenchymal stem cells. *Journal of Biological Chemistry* **293(24),** 9358–9369 (2018).

180. Madan S, Uttekar B, Chowdhary S, Rikhy R. Mitochondria Lead the Way: Mitochondrial Dynamics and Function in Cellular Movements in Development and Disease. *Front Cell Dev Biol* **9** (2022).

181. Herst PM, Berridge MV. Cell surface oxygen consumption: a major contributor to cellular oxygen consumption in glycolytic cancer cell lines. *Biochim Biophys Acta* **1767(2),** 170–7 (2007).

182. Chandrasekharan N, Simmons DL. The cyclooxygenases. *Genome Biology* **5(241)** (2004).

183. Toomey DP, Murphy JF, Conlon KC. COX-2, VEGF and tumour angiogenesis. *Surgeon* **7(3),** 174–80 (2009).

184. Williams CS, Tsujii M, Reese J, Dey SK, DuBois RN. Host cyclooxygenase-2 modulates carcinoma growth. *The Journal of Clinical Investigation,* 1589–94 (2000).

185. Zheng Y, Brash AR. On the role of molecular oxygen in lipoxygenase activation: comparison and contrast of epidermal lipoxygenase-3 with soybean lipoxygenase-1. *Journal of Biological Chemistry* **285(51),** 39876–87 (2010).

186. Ding XZ, Hennig R, Adrian TE. Lipoxygenase and cyclooxygenase metabolism: new insights in treatment and chemoprevention of pancreatic cancer. **2(10),** 1476–4598 (2003).

187. Weisser H, Göbel T, Melissa Krishnathas G, Kreiß M, Angioni C, Sürün D, Thomas D, Schmid T, Häfner AK, Kahnt AS. Knock-out of 5-lipoxygenase in overexpressing tumor cells-consequences on gene expression and cellular function. *Cancer Gene Therapy* **30(1),** 108–123 (2023).

188. Qausain S, Basheeruddin M. Unraveling the Peroxidase Activity in Peroxiredoxins: A Comprehensive Review of Mechanisms, Functions, and Biological Significance. *Cureus* **16(8)** (2024).

189. Khan AA, Rahmani AH, Aldebasi YH, Aly SM. Biochemical and pathological studies on peroxidases -an updated review. *Global Journal of Health Science* **6(5),** 87–98 (2014).

190. Nakamura H, Takada K. Reactive oxygen species in cancer: Current findings and future directions. *Cancer Science* **112(10),** 3945–3952 (2021).

191. Singh R, Manna PP. Reactive oxygen species in cancer progression and its role in therapeutics. *Exploration of Medicine* **3,** 43–57 (2022).

192. Wilson C, Terman JR, González-Billault C, Ahmed G. Actin filaments-A target for redox regulation. *Cytoskeleton* **73(10),** 577–595 (2016).

193. Balta E, Kramer J, Samstag Y. Redox Regulation of the Actin Cytoskeleton in Cell Migration and Adhesion: On the Way to a Spatiotemporal View. *Front Cell Dev Biol* **8** (2021).

194. Hobbs GA, Zhou B, Cox AD, Campbell SL. Rho GTPases, oxidation, and cell redox control. Small GTPases. *Small GTPases* **5** (2014).

195. Song Z, Ghochani M, McCaffery JM, Frey TG, Chan DC. Mitofusins and OPA1 mediate sequential steps in mitochondrial membrane fusion. *Molecular Biology of the Cell* **20(15),** 3525–32 (2009).

196. Nolden KA, Harwig MC, Hill RB. Human Fis1 directly interacts with Drp1 in an evolutionarily conserved manner to promote mitochondrial fission. *Journal of Biological Chemistry* **299(12)** (2023).

197. Burman JL, Pickles S, Wang C, Sekine S, Vargas JNS, Zhang Z, Youle AM, Nezich CL, Wu X, Hammer JA, Youle RJ. Mitochondrial fission facilitates the selective mitophagy of protein aggregates. *Journal of Cell Biology* **216(10),** 3231–3247 (2017).

198. Desai SP, Bhatia SN, Toner M, Irimia D. Mitochondrial localization and the persistent migration of epithelial cancer cells. *Biophysical Journal* **104(9),** 2077–88 (2013).

199. Chen W, Zhao H, Li Y. Mitochondrial dynamics in health and disease: mechanisms and potential targets. *Signal Transduction and Targeted Therapy* **8(1)** (2023).

200. Fung TS, Chakrabarti R, Higgs HN. The multiple links between actin and mitochondria. *Nat Rev Mol Cell Biol* **24(9),** 651–667 (2023).

201. Frohman MA. Role of mitochondrial lipids in guiding fission and fusion. *Journal of Molecular Medicine* **93(3),** 263–9 (2015).

202. An Introduction to Reactive Oxygen Species. *www.agilent.com/lifesciences/biotek* (2022).

203. Kim H, Xue X. Detection of Total Reactive Oxygen Species in Adherent Cells by 2',7'-Dichlorodihydrofluorescein Diacetate Staining. *Journal of Visualized Experiments* **160** (2020).

204. Mukhopadhyay P, Rajesh M, Yoshihiro K, Haskó G, Pacher P. Simple quantitative detection of mitochondrial superoxide production in live cells. *Biochem Biophys Res Commun* **358(1),** 203–8 (2007).

205. Duellman S, Shultz J, Vidugiris G, Cali J. A New Luminescent Assay for Detection of Reactive Oxygen Species. *Promega Corporation* (2013).

206. Picard M, Shirihai OS, Gentil BJ, Burelle Y. Mitochondrial morphology transitions and functions: implications for retrograde signaling? *Am J Physiol Regul Integr Comp Physiol* **304(6),** 393–406 (2013).

207. Aslan M, Hsu EC, Liu S, Stoyanova T. Quantifying the invasion and migration ability of cancer cells with a 3D Matrigel drop invasion assay. *Biology. Methods and Protocols* **6(1)** (2021).

208. Davidowitz RA, Iwanicki MP, Brugge JS. In vitro mesothelial clearance assay that models the early steps of ovarian cancer metastasis. *Journal of Visualized Experiments* **60** (2012).

209. Glotzbach A, Rohlf K, Gonscharow A, Lüke S, Demirci Ö, Begher-Tibbe B, Overbeck N, Reinders J, Cadenas C, Hengstler JG, Edlund K, Marchan R. EDI3 knockdown in ER-HER2+ breast cancer cells reduces tumor burden and improves survival in two mouse models of experimental metastasis. *Breast Cancer Research* **26(1),** 87 (2024).

210. Chasara RS, Ajayi TO, Leshilo DM, Poka MS, Witika BA. Exploring novel strategies to improve anti-tumour efficiency: The potential for targeting reactive oxygen species. *Heliyon* **9(9)** (2023).

211. Huang R, Chen H, Liang J, Li Y, Yang J, Luo C, Tang Y, Ding Y, Liu X, Yuan Q, Yu H, Ye Y, Xu W, Xie X. Dual Role of Reactive Oxygen Species and their Application in Cancer Therapy. *Journal of Cancer* **12(18),** 5543–5561 (2021).

Acknowledgements

I would like to express my sincere thanks to Prof. Dr. Jan G. Hengstler for providing me with the resources and opportunities to explore my research interests.

I would also like to extend heartfelt gratitude to Dr. Rosemarie Marchan and Dr. Karolina Edlund for your mentorship, great support, guidance, and encouragement throughout my PhD journey. Your insightful feedback and expertise have been invaluable in shaping my research. Thank you for letting me work on such a challenging, yet very interesting project. You always gave me the motivation to keep going despite the difficulties of the project!

Last but not least, I am grateful to my colleagues for their support and memorable work experience, which made this challenging journey much more enjoyable. I am happy that I can call some of you my friends after this time and that I have gained such reliable and great people for my life. Thank you all!

Meine höchste Dankbarkeit möchte ich meiner Familie und meinem Freund, Partner und Ehemann, Dima ausdrücken. Danke dafür, dass du immer für mich da warst!

Eidesstattliche Versicherung (Affidavit)

Gonscharow, Anastasia
Name, Vorname
(Surname, first name)

224616
Matrikel-Nr.
(Enrolment number)

Belehrung:

Wer vorsätzlich gegen eine die Täuschung über Prüfungsleistungen betreffende Regelung einer Hochschulprüfungsordnung verstößt, handelt ordnungswidrig. Die Ordnungswidrigkeit kann mit einer Geldbuße von bis zu 50.000,00 € geahndet werden. Zuständige Verwaltungsbehörde für die Verfolgung und Ahndung von Ordnungswidrigkeiten ist der Kanzler/die Kanzlerin der Technischen Universität Dortmund. Im Falle eines mehrfachen oder sonstigen schwerwiegenden Täuschungsversuches kann der Prüfling zudem exmatrikuliert werden, § 63 Abs. 5 Hochschulgesetz NRW.

Die Abgabe einer falschen Versicherung an Eides statt ist strafbar.

Wer vorsätzlich eine falsche Versicherung an Eides statt abgibt, kann mit einer Freiheitsstrafe bis zu drei Jahren oder mit Geldstrafe bestraft werden, § 156 StGB. Die fahrlässige Abgabe einer falschen Versicherung an Eides statt kann mit einer Freiheitsstrafe bis zu einem Jahr oder Geldstrafe bestraft werden, § 161 StGB.

Die oben stehende Belehrung habe ich zur Kenntnis genommen:

Official notification:

Any person who intentionally breaches any regulation of university examination regulations relating to deception in examination performance is acting improperly. This offence can be punished with a fine of up to EUR 50,000.00. The competent administrative authority for the pursuit and prosecution of offences of this type is the chancellor of the TU Dortmund University. In the case of multiple or other serious attempts at deception, the candidate can also be unenrolled, Section 63, paragraph 5 of the Universities Act of North Rhine-Westphalia.

The submission of a false affidavit is punishable.

Any person who intentionally submits a false affidavit can be punished with a prison sentence of up to three years or a fine, Section 156 of the Criminal Code. The negligent submission of a false affidavit can be punished with a prison sentence of up to one year or a fine, Section 161 of the Criminal Code.

I have taken note of the above official notification.

Dortmund, 13.03.2025
Ort, Datum
(Place, date)

Unterschrift
(Signature)

Titel der Dissertation:
(Title of the thesis):

Mitochondrial lysophosphatidic acid generating enzymes glycerol-3-phosphate acyltransferase 1 and acylglycerol kinase are associated with ovarian cancer cell migration.

Ich versichere hiermit an Eides statt, dass ich die vorliegende Dissertation mit dem Titel selbstständig und ohne unzulässige fremde Hilfe angefertigt habe. Ich habe keine anderen als die angegebenen Quellen und Hilfsmittel benutzt sowie wörtliche und sinngemäße Zitate kenntlich gemacht.
Die Arbeit hat in gegenwärtiger oder in einer anderen Fassung weder der TU Dortmund noch einer anderen Hochschule im Zusammenhang mit einer staatlichen oder akademischen Prüfung vorgelegen.

I hereby swear that I have completed the present dissertation independently and without inadmissible external support. I have not used any sources or tools other than those indicated and have identified literal and analogous quotations.

The thesis in its current version or another version has not been presented to the TU Dortmund University or another university in connection with a state or academic examination.*

*Please be aware that solely the German version of the affidavit ("Eidesstattliche Versicherung") for the PhD thesis is the official and legally binding version.

Dortmund, 13.03.2025
Ort, Datum
(Place, date)

Unterschrift
(Signature)

technische universität
dortmund

Fakultät für Chemie
und Chemische Biologie

Datum: 13.03.2025

An die/den Vorsitzende/n des Promotionsausschusses
der Fakultät für Chemie und Chemische Biologie der TU Dortmund

Eigenständigkeitserklärung für Dissertationen

nach der Ergänzung zur Promotionsordnung vom 29.10.2010
(Promotionsstudiengang) am 20.11.2023

Ich versichere hiermit an Eides statt, dass ich die vorliegende Dissertation mit dem folgenden Titel

Mitochondrial lysophosphatidic acid generating enzymes glycerol-3-phosphate
acyltransferase 1 and acylglycerol kinase are associated with ovarian cancer
cell migration.

selbstständig und ohne unzulässige fremde Hilfe verfasst habe. Ich habe keine anderen als die angegebenen Quellen und Hilfsmittel benutzt sowie wörtliche und sinngemäße Zitate kenntlich gemacht. Ich erkläre zudem, dass ich beim Einsatz von Schreib- und Bildwerkzeugen, die durch Künstliche Intelligenz (KI) unterstützt werden, diese in der Übersicht verwendeter Hilfsmittel mit ihrem Produktnamen, meiner Bezugsquelle sowie der spezifischen Methodik vollständig aufgeführt habe und, bei Übernahme von durch generative Schreibwerkzeuge erstellten Texten, die betreffenden Textstellen in der Arbeit als mit KI-generierter Unterstützung verfasst gekennzeichnet habe. Die Arbeit hat in gleicher oder ähnlicher Form noch keiner Prüfungsbehörde vorgelegen. Ich habe sichergestellt, dass durch die Verwendung generativer Modelle kein fremdes geistiges Eigentum verletzt wurde und ich kein wissenschaftliches Fehlverhalten etwa in Form von Plagiaten begangen habe.

Name: Gonscharow, Vorname Anastasia

Matrikelnummer: 224616

Datum, Unterschrift 13.03.2025